Intracellular chloride concentrations in glial cells under normal or pathological conditions

Inaugural-Dissertation

zur Erlangung des Doktorgrades an der
Fakultät für Mathematik und Naturwissenschaften
der Heinrich-Heine-Universität Düsseldorf

vorgelegt von

Elsa Miriam Justine Engels
aus Eschweiler

Jülich, Mai 2021

aus dem

Institute of Biological Information Processing,
Molekular- und Zellphysiologie (IBI-1)

des Forschungszentrums Jülich

Gedruckt mit der Genehmigung der
Fakultät für Mathematik und Naturwissenschaften
der Heinrich-Heine-Universität Düsseldorf

Berichterstatter:
1. Prof. Dr. Christoph Fahlke
2. Prof. Dr. Christine R. Rose
3. Prof. Dr. Christian Henneberger

Tag der mündlichen Prüfung: 27. Oktober 2021

„Wenn du das Ende von dem erreicht hast, was du wissen solltest,
stehst du am Anfang dessen, was du fühlen solltest.“

~ Khalil Gibran, 1883-1931 ~

Abstract

Glial cells represent a major cell population in the central nervous system (CNS). They supply nutrients and signalling molecules to adjacent neurons and regulate extracellular neurotransmitter and potassium concentrations ($[K^+]_{ext}$) (Deitmer and Rose 2010). High water permeability enables glial cells to rapidly change their cell volume. Pathological conditions, such as epilepsy, hepatic failure, hyponatremia, stroke, and traumatic brain injuries can result in glial cell swelling and cerebral edema (Feustel et al. 2004, Deng et al. 2014, Stokum et al. 2016, Gankam Kengne and Decaux 2018, Wilson and Mongin 2019). Chloride concentrations and their gradients are significant factors in volume regulation (McManus et al. 1995, Mongin 2016), initiation of apoptosis and the regulation of cell proliferation (Elorza-Vidal et al. 2019, Wilson and Mongin 2019), thereby making glial chloride homeostasis an important determinant of normal brain function.

Thus far, glial intracellular chloride concentrations ($[Cl^-]_{int}$) describing a range between 20 – 46 mM were mainly analysed in cultured cells and determined with different techniques and methods, (Kimelberg 1981, Kettenmann et al. 1987, Walz and Mukerji 1988, Bevensee et al. 1997, Bekar and Walz 2002). However, cultured glial cells are pulled out of their physiological environment and exhibit various differentiation phases. Measurements in acute brain slices (Marandi et al. 2002, Kaneko et al. 2004, Untiet et al. 2016, Untiet et al. 2017), appear to be better suited to describe glial chloride homeostasis under physiological conditions, because the natural environment of glial cells and specific neuron-glia interactions are preserved in this preparation.

The non-invasive fluorescence lifetime imaging microscopy (FLIM) with the chloride-sensitive dye MQAE (Gensch et al. 2015) is used to study various glial cell types in acute mouse brain slices. These experiments show a variety of $[Cl^-]_{int}$, which are substantially lower than $[Cl^-]_{int}$ in cerebellar Bergmann glial cells, estimated with the same method (Untiet et al. 2017). Moreover, the results demonstrate $[Cl^-]_{int}$ dynamics under pathophysiological conditions, known to disturb chloride homeostasis, like artificial evoked ischemia (present study: Engels et al., submitted) and episodic ataxia type 6 (present study: Kovermann et al. 2020; Kolobkova et al., in preparation).

This work demonstrates glial cell-specific regulations of $[Cl^-]_{int}$, which appear to be essential for cellular functions within the brain. Furthermore, it describes the functions of glial chloride transporters and channels in these processes.

Zusammenfassung

Gliazellen umfassen eine große Population an Zellen im zentralen Nervensystem. Sie versorgen benachbarte Neuronen mit Nährstoffen und Signalmolekülen und regulieren die extrazellulären Konzentrationen von Neurotransmittern und Kalium ($[K^+]_{ext}$) (Deitmer and Rose 2010). Eine erhöhte Wasserpermeabilität ermöglicht Gliazellen schnelle Zellvolumenänderungen. Pathologische Bedingungen, wie beispielsweise Epilepsie, Leberinsuffizienz, Hyponatriämie, Schlaganfälle, Schädel-Hirn-Trauma, Rückenmarks-verletzungen oder auch Hypoglykämie, stehen in einem Zusammenhang mit glialer Zellschwellung und Hirnödemen (Feustel et al. 2004, Deng et al. 2014, Stokum et al. 2016, Gankam Kengne and Decaux 2018, Wilson and Mongin 2019). Chloridkonzentrationen und deren Gradienten sind wichtige Faktoren für die Volumenregulation (McManus et al. 1995, Mongin 2016), Auslösung der Apoptose und die Regulation der Zellproliferation (Elorza-Vidal et al. 2019, Wilson and Mongin 2019) und machen demnach die gliale Chloridhomöostase zu einem bedeutenden Determinanten für eine normale Hirnfunktion.

Bis jetzt wurden gliale intrazelluläre Chloridkonzentrationen ($[Cl^-]_{int}$), die zwischen 20 und 46 mM variieren, weitestgehend in Zellkultur bestimmt und mit Hilfe unterschiedlicher Techniken und Methoden ermittelt (Kimelberg 1981, Kettenmann et al. 1987, Walz and Mukerji 1988, Bevensee et al. 1997, Bekar and Walz 2002). Kultivierte Gliazellen befinden sich jedoch nicht in ihrem natürlichen, zellulären Umfeld und bestehen aus unterschiedlichen Differenzierungsstadien. Messungen in akuten Gewebeschnitten (Marandi et al. 2002, Kaneko et al. 2004, Untiet et al. 2016, Untiet et al. 2017) erscheinen geeigneter zu sein, um die gliale Chlorid-Homöostase unter physiologischen Bedingung zu beschreiben, da hier die natürliche Umgebung von Gliazellen und Interaktionen zwischen Gliazellen und Neuronen erhalten bleiben.

Die nicht-invasive Fluoreszenzlebenszeit-Mikroskopie (FLIM) in Kombination mit dem chloridsensitiven Fluoreszenzfarbstoff MQAE (Gensch et al. 2015) ist zur Bestimmung unterschiedlicher glialer Zelltypen in akuten Mausgehirn-Gewebeschnitten verwendet worden. Die Experimente zeigen unterschiedliche $[Cl^-]_{int}$ auf, die deutlich geringer sind als $[Cl^-]_{int}$ in zerebellären Bergmann Gliazellen und mit der gleichen Methode ermittelt worden sind (Untiet et al. 2017). Die Ergebnisse ermöglichen eine Beschreibung der $[Cl^-]_{int}$-Dynamik unter pathophysiologischen Bedingungen, bei denen die Chloridhomöostase gestört ist, wie der artifiziell erzeugten Ischämie (Vorliegende Publikation: Engels et al., eingereicht) und der

Episodischen Ataxie Typ 6 (Vorliegende Publikationen: Kovermann et al. 2020; Kolobkova et al., in Vorbereitung).

Diese Arbeit weist glia-zellspezifische Regulationen der $[Cl^-]_{int}$ auf, die essentiell für zelluläre Aufgaben im Gehirn sind und beleuchtet die Funktionen von glialen Chloridtransportern und – Kanälen bei diesen Prozessen.

Contents

1 Introduction

1.1. Anatomy, functions and connections of the studied brain regions

1.1.1. Morphology of the hippocampus

The hippocampus is a highly conserved brain region, which shows similarities in developmental and connectivity characteristics in all vertebrates with a similar evolutionary origin. As a part of the limbic system, the hippocampus is also involved in processing of emotions and storage of new memory contents as well as transfer of memory compartments from short-term memory to long-term memory.

Due to the bilateral symmetry of the mammalian brain, the hippocampus is located in the medial temporal lobe of each cerebral hemisphere. Its appearance can be described as two U-shapes rotated into each other, the dentate gyrus (DG) and the hippocampus proper, subdivided into three fields, namely cornu ammonis (CA; CA1-3). Within the hippocampus, single unidirectional axons are involved in information processing. The major input of information comes from the entorhinal cortex via the performant path. Axons entering the hippocampus innervate DG granule cells, which are connected via their axons – mossy fibers – with pyramidal cells of the CA3 region. The CA3 pyramidal cells innervate the CA1 region via Schaffer collaterals. Finally, the output via CA1 pyramidal cells reaches the *subiculum* and the entorhinal cortex (Amaral and Witter 1989, Braak et al. 1996, Amaral et al. 2007).

The DG consists of an upper (*suprapyramidal*) and lower (*infrapyramidal*) blade of granule cells that are generated sequentially after birth. Morphologically, DG is structured in three layers. The outer *molecular layer*, located next to the entorhinal cortex, the *granule cell layer*, mostly composed of granule cells, and the *polymorphic layer*, located at the inner part of the *granule cell layer* and containing different neuronal and glial cell types. The CA regions consist of five different layers. The outer layer – *alveus* – contains axons of pyramidal cells and is separated from the *stratum pyramidale* by the thinner *stratum oriens*. The *pyramidal layer* or *stratum pyramidale* contains the cell bodies of pyramidal neurons and can be divided into four regions (CA1-3, CA4/hilus) according to different pyramidal cell morphologies, described by Lorente de Nó in 1934 (Lorente De Nó 1934, Amaral 1978). The CA2 region occupies a small area between CA1 and CA3 region. It is not just an extension of the CA3 region, and its role has not yet been fully clarified (Leroy et al. 2019). The *stratum radiatum* is located between the *stratum pyramidale* and the *stratum moleculare*. *Stratum lucidum* is only present in CA3

and is located between the *stratum pyramidale* and the *stratum moleculare* (O'Keefe and Nadel 1978).

Hippocampal neurotransmission is tightly controlled by various glial cells. In this study, the $[Cl^-]_{int}$ is determined for astrocytes of the *stratum radiatum* in CA1 and the *polymorphic layer* of the DG (yellow stars Figure 3.1) as well as radial glia-like cells (RGL), which are located in the subgranular zone of the DG layer (purple cells Figure 3.1). The aforementioned cells are primarily important in episodic ataxia 6 (EA6) since these cells express the excitatory amino acid transporter 1 (EAAT1), the gene product of *SLC1A3*, which is mutated in this disease (as shown in the present study: Kolobkova et al., in preparation).

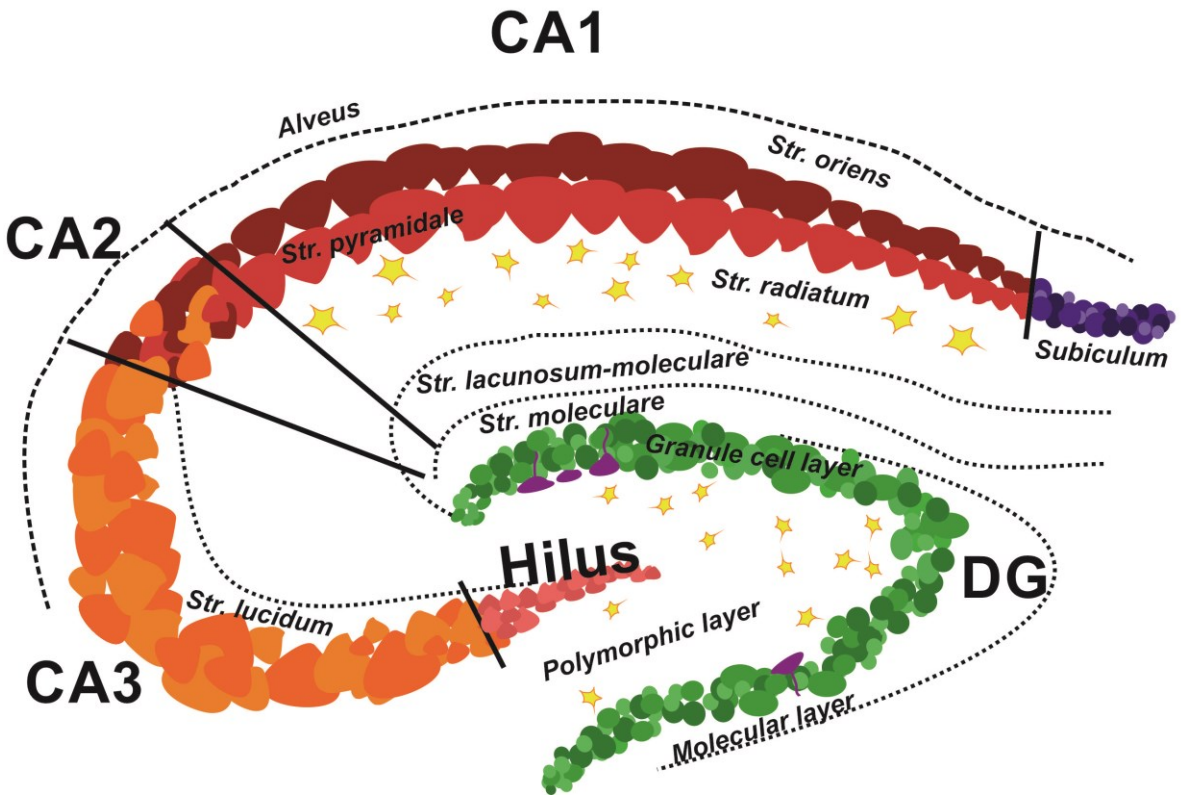

Figure 3.1: Schematic illustration of the hippocampus and its different morphological layers.
The unidirectional network of the hippocampus starts with the input from the entorhinal cortex, which forms connections to granule cells (contrasting green) in the dentate gyrus (DG) and pyramidal neurons in the cornu ammonis (CA) 3 subfield (contrasting orange), which send axons (Schaffer collateral) to pyramidal neurons (contrasting red) in CA1. Latter neurons project back to the entorhinal cortex. Astrocytes (yellow stars) of interest are located in the *stratum* (*Str.*) *radiatum* of CA1 and *polymorphic layer* of the DG as well at the inner edge of the *granule cell layer*– radial glia-like cells (RGL; purple cells).

1.1.2. Morphology of the cortex – neocortex

The cerebral cortex is the outer cell layer of the cerebrum. It consists of the grey matter hosting neuronal cell bodies and covers the white matter, which mostly hosts nerve fibers. 90% of the cerebral cortex consists of the neocortex, with the allocortex (olfactory system and hippocampus) representing the remaining 10% (Strominger N.L. 2012, Lee 2019). The folding complexity of the cortex, obtained by gyri and sulci, enlarges the cerebral surface while keeping the brain volume constant. Different, interconnected areas of the cortex are specialized to various functions, such as language and communication, receiving and processing sensory information, generating motoric commandos as well as learning and memory. The entire cortex can be divided into four lobes: *lobus temporalis*, *lobus frontalis*, *lobus parietali*s and *lobus occipitalis* (Sadava et al. 2011).

The differentiated mammalian cortex consists of six layers (Shepherd 2011) – from the outer to the inner: I *molecular layer*, II *external granular layer*, III *external pyramidal layer*, IV *internal granular layer*, V *internal pyramidal layer* and VI *multiform layer*. The molecular layer is the outermost cortical layer and develops first. It hosts a relatively low amount of cells and consists mainly of interneurons, stellate cells and basket cells. The *multiform layer* forms the innermost cortical layer and contains various nerve cells – the corticothalamic efferents. *Layer* II – V build the main core of the cortex and are irregular and variable layers throughout the development of mammals. The *external granular layer* consists of small granule cells that are connected to the granule cells of the *internal granular layer.* These cells innervate the *molecular layer*. Several pyramidal cells are also located in layer II. The *external pyramidal layer* mainly consists of pyramidal cells as well as the basket and stellate cells. Layers II and III are closely connected and it is nearly impossible to visually distinguish where layer II ends and layer III begins. The *internal granular layer*, like the *external granular layer*, consists only of basket and stellate cells that form cortical connections. The *internal pyramidal layer* is composed of big pyramidal cells that build subcortical connections to central areas of the brain and the spinal cord. Underneath these six layers lies the white matter with all its pathways and nerve fibers (Vogt 1903, Brodmann 1909, Nieuwenhuys 2013).

This thesis focuses on astrocytes of the neocortex layer II/III. Astrocytes in this layer can be distinguished from other groups by their orientation and broader branching, with branches oriented towards the cortical surface. In comparison to other astrocytes, they

occupy a greater volume and therefore allow more interactions with neighbouring synapses (Lanjakornsiripan et al. 2018).

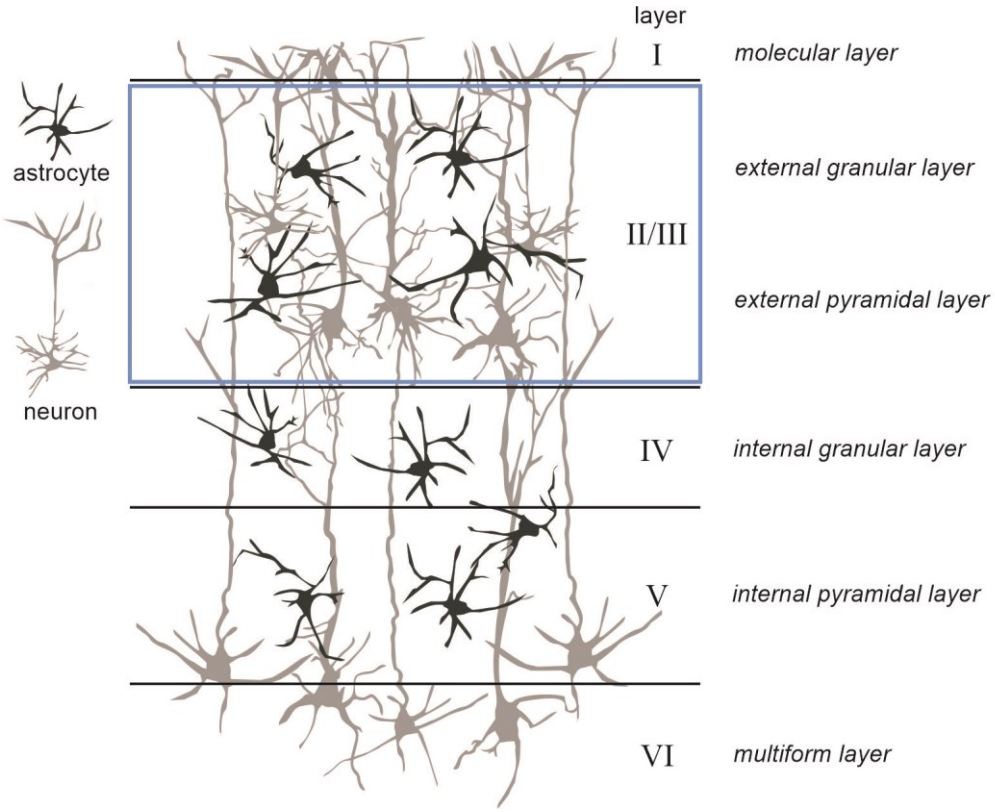

Figure 3.2: Schematic overview of cerebral cortex.
The diagram shows the cortical six-layer structure, starting with the *molecular layer* at the top downwards the following layers that can be differentiated from each other by their neuronal (light grey) cell types – granular cells, pyramidal cells, basket and stellate cells (layers labelled with *Roman numerals*). The $[Cl^-]_{int}$ is determined for astrocytes (dark grey) in layer II/III, highlighted by a blue box. This schematic overview is based on images from earlier publications (Vogt 1903, Brodmann 1909, Nieuwenhuys 2013).

1.1.3. Morphology of the cerebellum

The cerebellum is located in the *posterior cranium* and controls the fine adjustment and coordination of motion sequences. It is involved in implicit learning processes, such as language or movement. Cerebellar dysfunctions can lead to movement disorders, like ataxia and impaired motor coordination.

The cerebellum can be divided into two hemispheres, which are connected by the vermis. The grey matter is folded very tightly and form three lobes – anterior, posterior and the flocculonodular. These three lobes can be subdivided into ten lobes: anterior lobe in lobules I to V; posterior lobe in lobules VI to IX and flocculonodular lobe, in lobule X. The cerebellum hosts four principle neuron classes: granule cells, Purkinje cells, interneurons and

deep cerebellar cells. The lobes build a trilaminar structure composed of the *Purkinje cell layer*, hosting Purkinje neurons and Bergmann glia (BG) cells, located between the *internal granule layer* and the *outer molecular layer*. The last one consist of parallel and Purkinje cell fibers as well as processes of Bergmann glia (see Figure 3.4). The information circuity starts at the precerebellar system, where a group of surrounding nuclei sends projections (mossy fibers) to granule neurons. Purkinje cells receive inputs from parallel fibers of granule cells and from climbing fibers of inferior brainstem nuclei, which both form strong contacts with the dendrites of Purkinje cells. Finally, deep cerebellar cells are innervated by the axons of Purkinje cells and provide primary output from the cerebellar cortex (Chizhikov and Millen 2003, Tanaka et al. 2008, Sultan 2014).

1.2. Glial cell morphologies and their role in the CNS

The number of glial cells outnumbers the number of neurons (von Bartheld et al. 2016). Whereas glial cells were believed to mainly support and protect adjacent neurons (Ndubaku and de Bellard 2008), recent works have identified important active roles of glial cells in development, metabolic support for neurons, neuronal survival and differentiation, neuronal guidance, as well as in ion and neurotransmitter homeostasis (Ndubaku and de Bellard 2008, Jäkel and Dimou 2017). There are various subtypes of glial cells, including microglia, oligodendrocytes and astrocytes, all of which have different morphologies and specialised functions in the central nervous system (CNS).

The microglia act as immune system in the CNS by protecting the neuronal network against damaged or dying neurons and synapses as well as infections or injuries (Arcuri et al. 2017). They remove dead cells from biological tissue via phagocytosis, similarly to macrophages.

Oligodendrocytes wrap their processes around neuronal axons and thus provide electrical isolation of neuronal axons in the CNS, enabling fast saltatory transfer of action potentials along the sheathed axons.

Astrocytes have received their name because of their star-like structure. Their membranes contain various transporters, receptors and channels to maintain a healthy status of the neuronal environment. Furthermore, astrocytes are closely located to neurons and are of particular importance for the regulation of the neuronal environment. Due to their high potassium conductivity (Walz et al. 1984, Walz 2000, Kofuji and Newman 2004), they are

involved in buffering the extracellular potassium concentration, which increases during synaptic activity around neurons. Astrocytes express EAATs (Excitatory Amino Acid Transporters) and GATs (GABA Transporters) to take up glutamate or GABA (γ-aminobutyric acid) (Sattler and Rothstein 2006, Seifert et al. 2006, Eulenburg and Gomeza 2010). This ensures a rapid removal of neurotransmitters from the synaptic cleft to terminate synaptic transmission.

Glial cells in a living environment can be studied in a transgenic mouse line that expresses the enhanced green fluorescent protein (EGFP) under the control of the human glial fibrillary acid protein (GFAP) promotor (Nolte et al. 2001). However, in this animal, only a subset of glial cells in the CNS is marked (Lee et al. 2006, Kafitz et al. 2008). Within the glial cells expressing EGFP, there are subtypes with different expression levels of GFAP (Matthias et al. 2003, Kimelberg 2004). One subtype of glial cells exhibits bright EGFP fluorescence and expression of glutamate transporters (GluT), like EAAT1/GLAST and EAAT2/GLT-1 – GluT glial cells. The other subtype shows weak EGFP fluorescence and expresses glutamate receptors (GluR), such as AMPA receptors – GluR glial cells (Matthias et al. 2003, Jabs et al. 2005).

Another glial marker is the red fluorescent dye sulforhodamine 101 (SR101). This marker sufficiently stains astrocytes, which show typical electrophysiological properties of classical passive astrocytes (Nimmerjahn et al. 2004, Kafitz et al. 2008, Meier et al. 2008). The here used acute brain slices are stained with SR101 via bath loading (Kafitz et al. 2008) and only SR101 positive glial cells were analysed in this work.

1.2.1. Radial glia-like (RGL) cells in the hippocampus

Neurogenesis is defined as a process generating neurons from precursor cells and happens during embryonic development. However, further studies have shown that neurogenesis also occurs in the adult brain, in the subventricular zone of the lateral ventricles or in the subgranular zone of the DG (Kuhn et al. 1996, Eriksson et al. 1998, Bond et al. 2015). RGL cells are proliferating neuronal stem cells in the adult hippocampus, which is known to generate new astrocytes and granule neurons throughout the lifecycle of mammals. RGL cells express both astrocytic markers, such as EAAT1/GLAST and GFAP (Liour and Yu 2003, Jungblut et al. 2012), as well as embryonic neuronal stem cell markers, like BLBP (Brain lipid binding protein), Nestin and the transcription factor Sox2 (Eriksson et al. 1998, Berg et al. 2018).

RGL cells exhibit a single primary process that extensively branches within the *granule cell layer* and the *molecular layer* of the DG (Figure 3.3) (Gebara et al. 2016, Moss et al. 2016). Two populations of RGL cells – type α and type β, can be distinguished based on the length of their single primary processes (Gebara et al. 2016). For analysis, RGL cells can be visualized by staining with SR101 in acute brain slices. Although, SR101 stains RGL processes, distinguishing between primary processes was not possible in our experiments, and α- and β- RGL cell types were thus not investigated separately.

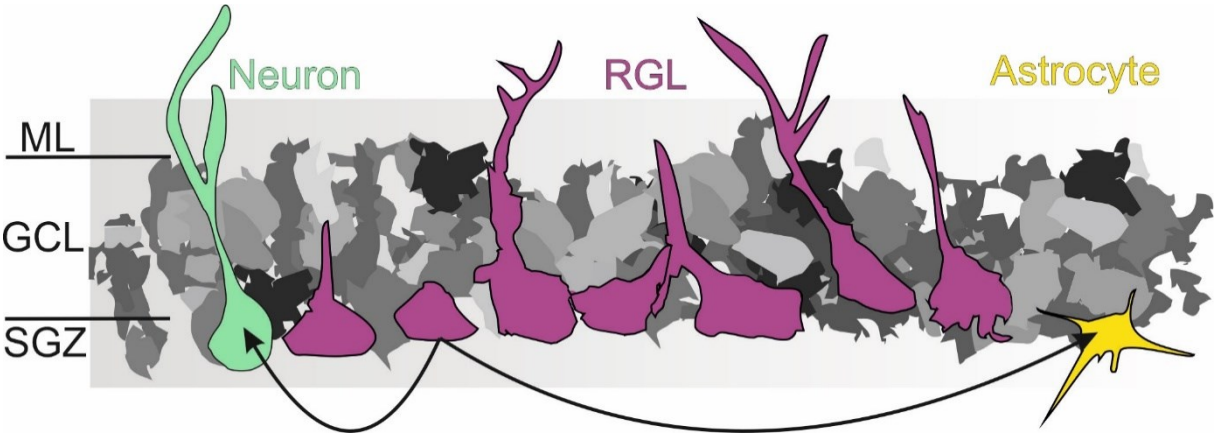

Figure 3.3: Schematic illustration of radial glia-like cells located in the subgranular zone (SGZ) of the DG.
RGL cells (purple) are proliferating progenitor cells and capable of generating new astrocytes (yellow) and neurons (green) in the DG. They exhibits single primary process extending through the *granule cell layer* (GCL) till the *molecular layer* (ML), where it branches and enwraps synapses, formed on the granule cell dendrites.

1.2.2. Bergmann glia (BG) in the cerebellar cortex

The cerebellar cortex consists of three different layers, the *molecular layer* (ML), the *Purkinje cell layer* (PCL) and the *granule cell layer* (GCL), exhibiting a notable heterogeneity of astroglia and oligodendroglia. The most well-known cells in the cerebellum are the unipolar BG, located next to Purkinje neurons in the PCL. Their highly branched processes extend radially along the ML and form tight contacts to Purkinje cell dendrites. In addition, their extensions are guidelines for granule cell migration in the developing cerebellum (see Figure 3.4) (Rakic 1971, Hatten et al. 1984, Yamada and Watanabe 2002). Like as with the hippocampus, neurogenesis takes place in the ventricular zone of the cerebellum that hosts radial glia, a precursor form of BG cells (Leung and Li 2018).

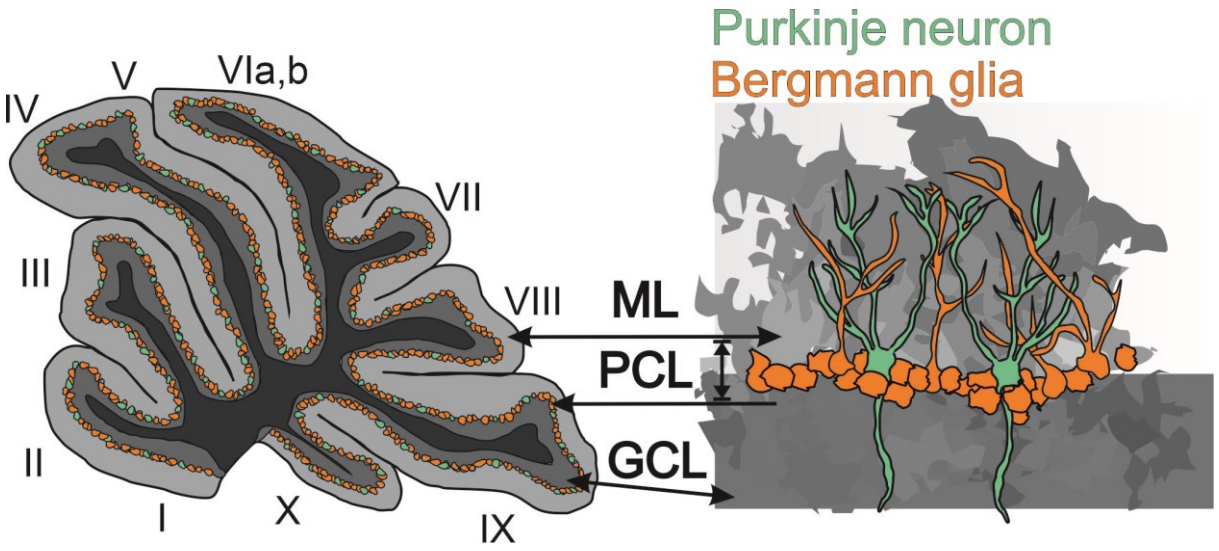

Figure 3.4: Structure of the cerebellum.
The scheme visualizes a parasagittal view of all ten lobes (I – X) and the three different cell layers of the cerebellum – *molecular layer* (ML), *Purkinje cell layer* (PCL) and the *granule cell layer* (GCL), which surrounds the inner white matter (black). Bergmann glial cells (orange) surround Purkinje neurons (green) and extend radial extensions, which enwrap synapses on Purkinje cell dendrites. The extensions of both cell types branch along the ML (Yamada and Watanabe 2002, Tanaka et al. 2008).

1.3. Physiological role of glial chloride concentrations

Chloride, the most abundant biological anion, can move across the cell membrane as well as membranes from intracellular compartments either via anion-selective channels or via passive or secondary-active transporters (Delpire and Staley 2014, Jentsch and Pusch 2018). $[Cl^-]_{int}$ contributes to the control of membrane potentials, to cell volume homeostasis as well as to initiation of apoptosis and the regulation of cell proliferation (McManus et al. 1995, Mongin 2016, Elorza-Vidal et al. 2019, Wilson and Mongin 2019).

During development, neurons and glial cells undergo a chloride switch from higher to lower $[Cl^-]_{int}$ (Delpire and Staley 2014, Untiet et al. 2017). The chloride switch correlates with the starting expression of EAAT1 and EAAT2 proteins in glial cells, (Schreiner et al. 2014). In neurons, it show a relationship with the GABA switch, which timely correlates with the functional change from an excitatory to an inhibitory GABA response of the postsynapse (Owens et al. 1996, Blaesse et al. 2009). In glial cells, $[Cl^-]_{int}$ is in a dynamic equilibrium between a coupled potassium-chloride efflux via KCC (Ringel and Plesnila 2008) and a chloride efflux via EAAT associated anion channels (Machtens et al. 2015, Fahlke et al. 2016), as well as chloride accumulation by the electroneutral NKCC1 (as shown in the present study Engels et al., submitted).

The distribution of water over plasma membranes is in equilibrium if intra- and extracellular solute concentrations (sodium, potassium, chloride and small organic molecules) are equally distributed, whereas osmotic gradients cause water influx or efflux. Changes in volume cause an activation of the following transporters and channels: $Na^+/K^+/2Cl^-$ cotransporter (NKCC1), $K^+/2Cl^-$ cotransporter (KCCs), Na^+/H^+ and $2Cl^-/HCO_3^-$ exchangers, aquaporin and volume regulated anion channel (VRAC) as well as Na^+ and Cl^- channels (see Figure 3.5). Acute cell swelling activates the KCCs that mediate the efflux of K^+ and Cl^- out of the cell with a corresponding water efflux to decrease cellular size. In case of cell shrinkage, the NKCC1 cotransporter, pumps $Na^+/K^+/2Cl^-$ into the cell. Additionally, the Na^+/H^+ and $2Cl^-/HCO_3^-$ exchangers as well as the Na^+ and Cl^- channels are activated to increase the intracellular solute concentration, which results in a water influx and increase in cell size (McManus et al. 1995, Kahle et al. 2015, Mongin 2016).

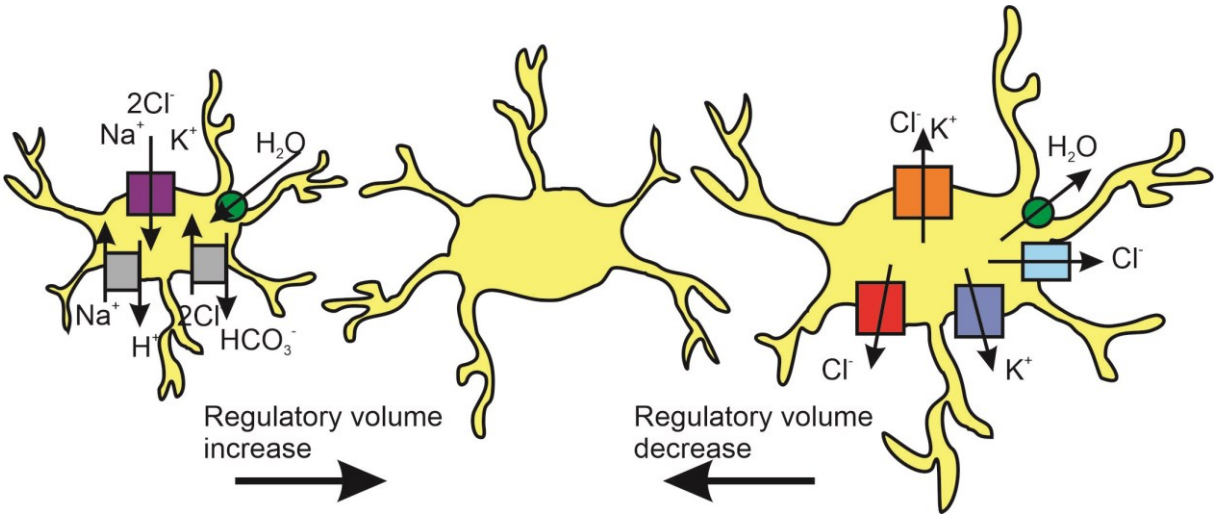

Figure 3.5: Schematic illustration of volume regulatory transporters in glial cells.
(Left) The cell volume can increase by activation of the bumetanide sensitive NKCC1 cotransporter (purple), which transports K^+, Na^+ and 2 Cl^- into the cell, facilitating water influx. Other transporters, following the same principle of water influx, are the Na^+/H^+ exchanger and Cl^-/HCO3 exchanger (grey). (Right) Cell swelling is corrected via controlled loss of K^+ and Cl^- via activated KCC cotransporters (orange), VRAC (light blue) as well as potassium (blue) and chloride (red) channels. The water flux is enabled by aquaporins (green circles) according to the direction of volume regulation. The scheme is made according to (McManus et al. 1995, Kahle et al. 2015, Mongin 2016).

The Gibbs-Donnan effect describes the unequal distribution of solute ions that can cross semipermeable membranes according to their concentrations. This distribution is influenced by impermeable charged ions/molecules. Each solution tries to establish an electrically neutral environment on each side of the membrane via an equal distribution of diffusible ions. However, the unequal distribution of impermeable charged ions/molecules

and the activity of the Na^+/K^+-ATPase create an electrochemical gradient over the membrane, so that one side of the membrane exhibits a stronger osmotic pressure. This leads to the prediction that the $[Cl^-]_{int}$ could be locally affected by impermeable anions, like negatively charged DNA/RNA under physiological pH or proteins.

1.4. Solute carrier family (SLC) transporter in the CNS

The Solute Carrier (SLC) group of membrane transporter proteins embraces 60 families of approximately 400 members that function as passive transporters, ion transporters or exchangers. They are involved in the transport of inorganic ions, amino acids, neurotransmitters, sugars, purine, fatty acids and other compounds across the cell membrane (Fredriksson et al. 2008). For chloride homeostasis the SLC transporters, NKCC1, KCC1-3, EAAT1/2 and GABA transporter type 1, seemed to be of special importance.

1.4.1. Cation coupled chloride cotransporter – NKCC and KCC

A characteristic of cation coupled chloride cotransport is the cotransport of Cl^- along with at least one of the two cations, either Na^+ and/or K^+ in electroneutral manner.

The SLC12 family members KCC1-3 (Ringel and Plesnila 2008) and the NKCC1 are expressed in astrocytes of the cortex, hippocampus and cerebellum (Yan et al. 2001a), while NKCC2 is kidney-specific (Russell 2000) and not relevant for this work. As mentioned above, KCCs are activated by cell swelling while NKCC1 is activated by cell shrinkage. Both processes introduce an osmotic imbalance and regulate the cell size via water efflux or influx. To achieve rapid changes in transporter activity as a fast response to changes in $[Cl^-]_{int}$, the activities of KCCs and NKCC1 are present in opposite phosphorylation states. Another difference between the transporters is that an increase in $[Cl^-]_{int}$ inhibits NKCC1 transport, while it activates KCCs transport (Russell 2000, Payne et al. 2003).

According to the following concentrations of a “typical” mammalian cell: intracellular $[Na^+] = 15$ mM and $[K^+] = 150$ mM; extracellular $[Na^+] = 140$ mM, $[K^+] = 5$ mM and $[Cl^-] = 130$ mM, the membrane transport of the electroneutral NKCCs and KCCs can be calculated using the chemical component of the electrochemical gradients of each ion:

[1.1] $$\Delta G = RT \ln \frac{c_1}{c_2},$$

R is the universal gas constant, T the temperature and c_1 and c_2 are the ion concentrations. NKCC1 transports Na^+, K^+ and Cl^- with a stoichiometry of $1Na^+:1K^+:2Cl^-$ (Russell 2000), so that the electrochemical gradient for this transport process is represented as the following sum [1.2](with the following abbreviations: intracellular $[Na^+] = [Na^+]_{int}$; intracellular $[K^+] = [K^+]_{int}$; intracellular $[Cl^-] = [Cl^-]_{int}$ and extracellular $[Na^+] = [Na^+]_{ext}$; extracellular $[K^+] = [K^+]_{ext}$; extracellular $[Cl^-] = [Cl^-]_{ext}$)

[1.2] $$\Delta G = \left(RT \ln \frac{[Na^+]_{int}}{[Na^+]_{ext}}\right) + \left(RT \ln \frac{[K^+]_{int}}{[K^+]_{ext}}\right) + 2\left(RT \ln \frac{[Cl^-]_{int}}{[Cl^-]_{ext}}\right)$$

The energetics of a transport can be described after mathematical conversion and simplification by the next equation [1.3] under equilibrium conditions, $\Delta G = 0$.

[1.3] $$[Cl^-]_{int} = [Cl^-]_{ext} \sqrt{\frac{[Na^+]_{ext} \times [K^+]_{ext}}{[Na^+]_{int} \times [K^+]_{int}}}$$

Subsequently, the NKCC1 would constantly accumulate ions into the cell under physiological conditions until $[Cl^-]_{int}$ is ≈ 72.5 mM and a thermodynamic equilibrium is established. On the other hand, KCCs transport $1K^+:1Cl^-$ (Russell 2000) in the opposite direction until $[Cl^-]_{int}$ drops down to ≈ 4.3 mM (calculated accordingly to the KCC stoichiometry). Due to their dependence on $[Na^+]$ and $[K^+]$, the activities of both cotransporters depend on the activity of the Na^+/K^+-ATPase, which will be reduced upon energy restriction.

1.4.2. Excitatory amino acid transporters (EAATs)

The SLC1 family includes the EAAT glutamate transporters that transport one glutamate, one H^+ and three Na^+ against one K^+ ion across the membrane (Zerangue and Kavanaugh 1996, Levy et al. 1998). The transporters are comprised of two domains, one stable localized domain, which establishes the multimerization of the trimeric proteins, and a dynamic region, which permits the substrate transport, by an elevator-like mechanism (Reyes et al. 2009). Additionally, the transporters function as anion-selective channels. These channels are opened during an intermediate state of the glutamate transport cycle so that chloride is released from cells due to the negative glial membrane potential (Machtens et al. 2015, Fahlke et al. 2016). In the mammalian brain, five different subtypes have been identified, EAAT1

(GLAST), EAAT2 (GLT-1), EAAT3 (EAAC1) EAAT4 and EAAT5 (Danbolt 2001). In mammals, these five proteins share 90% identity to comparative proteins of other mammalian species (Danbolt 2001). EAAT1 and EAAT2 are both expressed in glial cells but their expression levels vary between brain regions (Rothstein et al. 1994, Lehre and Danbolt 1998, Danbolt 2001). Analysis of EAAT expression levels as well as blocker experiments in RGL cells have proven that these cells also express EAAT1 and EAAT2 (Regan et al. 2007, Jungblut et al. 2012). The isoforms EAAT3 and EAAT4 are expressed in neuronal cell bodies and spines, respectively (Rothstein et al. 1994, Danbolt 2001). EAAT5 is restricted to retinal photoreceptors and bipolar cells (Lee et al. 2016).

Regan et al. (2007) showed that the majority of glial cells in the brain express a higher amount of EAAT1 if EAAT2 is not expressed in these cells. On the other hand, the expression of EAAT1 is suppressed, if EAAT2 is highly expressed in the same cell. Further studies have shown that the transcription of both, EAAT1 and EAAT2, undergoes developmental changes (Regan et al. 2007). Interestingly, the expression of EAAT1 and EAAT2 seems to be linked to the chloride switch in glial cells in CA1 and DG (Schreiner et al. 2014) and in cerebellar BG (Untiet et al. 2017).

1.4.3. GABA transporters (GATs)

GABA transporters (GATs) mediate the uptake of the inhibitory neurotransmitter GABA out of the synaptic cleft using Na^+ and Cl^- gradient (Guastella et al. 1990, Cammack et al. 1994, Hilgemann and Lu 1999). They terminate inhibitory synaptic transmission and prevent the spill over of extracellular GABA to neighbouring synapses (Borden 1996). To this date, four different forms of GATs have been described – GAT-1, GAT-2, GAT-3 and BGT-1 (Betaine/GABA transporter 1) and all belong to the SLC6 family. Northern blot and PCR analyses indicated that GAT-2 is expressed in the brain and the retina as well as in the liver, in which it is particularly abundant. BGT-1 was first identified in the kidney cells as a betaine transporter (Nakanishi et al. 1988). It was later shown that it also functions in GABA transport in the brain (Yamauchi et al. 1992, Borden 1996), although, its function is still under debate. GAT-1 is predominantly localized in neurons and GAT-3 in glial cells (Jin et al. 2011). The uptake of GABA is energetically linked to the gradients of Na^+ and Cl^- (Jiang et al. 2005, Eulenburg and Gomeza 2010). Willford et al. (2015) has suggested that the stoichiometry for all GABA transporter isoforms is

$3Na^+$:$1Cl^-$:1GABA and that forward and reverse transport modes of GABA are possible (Willford et al. 2015).

The predominantly inhibitory neurotransmitter GABA modulates the excitability of neurons according to the variations of chloride gradients, either via phasic or tonic inhibition. The phasic inhibition is triggered by the release of GABA from the presynapse that specifically binds at postsynaptically and perisynaptically located $GABA_A$ and $GABA_B$ receptors. In contrast, tonic inhibition is due to activation of extrasynaptic GABA receptors. This illustrates the modulatory role of GABA in synaptic transmission. The majority of extrasynaptic $GABA_A$ receptors contain α5-, α4- or δ-subunits and can detect micromolar concentrations of extracellular GABA ($[GABA]_{ext}$) (Glykys and Mody 2007, Belelli et al. 2009, Bryson et al. 2020). This work focuses on $GABA_A$ receptors since $GABA_B$ receptors are metabotropic receptors, which modulate the inhibition only indirectly.

1.5. Changes in $[Cl^-]_{int}$ can have adverse consequences for glial cells

1.5.1. Apoptotic cell death

Apoptosis is an active, programmed and tightly regulated cell death, which is activated through mitochondrial dysfunction (intrinsic pathway) or by the activation of cysteine-aspartic acid proteases, like caspase 3 (extrinsic pathway). Therefore, apoptosis can be precisely separated from necrosis, an unregulated and injury-induced cell death resulting in a cell volume increase. Changes in the ion homeostasis can cause cell shrinkage and apoptotic volume decrease (AVD). AVD is comprised of two phases: early-phase mitochondrial dysfunction and caspase-independent AVD and late-phase caspase-dependent apoptotic cell shrinkage, followed by loss of cell contacts and cell shape (Maeno et al. 2012).

Volume regulated K^+ and Cl^- channels can cause cell shrinkage (Maeno et al. 2000) and consequently could induce apoptosis. In thymocytes, it has been shown that the $[K^+]_{int}$ is reduced in apoptotic cells (Hughes et al. 1997). This indicates that the $[Na^+]_{int}$ could be higher than under physiological conditions (Bortner and Cidlowski 2003). These findings imply, that increased $[Na^+]_{int}$ and reduced $[K^+]_{int}$ are involved in cell volume regulations and signalling pathway to induce apoptosis. In addition, upregulated Cl^- efflux was described as basis of AVD in human endothelial cells (ECV304) (Porcelli et al. 2004). Further observations demonstrated that DIDS inhibition (Cl^- transport inhibitor) prevents AVD, as well as activation of caspase 3 and DNA fragmentation. This indicates that volume decrease trough Cl^- efflux is a trigger for

apoptosis (Ernest et al. 2008). Accordingly, all processes activated by cell shrinkage could induce a destabilization of the cell homeostasis, causing a collapse of the cells – apoptosis.

1.5.2. Episodic ataxia type 6 (EA6)

SLC1A3 encodes for the glial glutamate transporter EAAT1, which is responsible for the glutamate uptake from the synaptic cleft to avoid neurotoxicity (Harris et al. 2014). A missense mutation in *SLC1A3* causes EA6, which is characterized by epileptic seizures, ataxia and hemiplegia. The mutation predicts a substitution of proline by arginine at position 290 (P290R; p.Pro290Arg, 1047C>G; NP_004163) and was found in a 10-year-old boy. He showed developmental anomalies, such as a delay of the crawling and walking phase, the occurrence of periods with ataxia and slurred speech (Jen et al. 2005). The mutation P290R causes functional changes in EAAT1. It reduces the speed of conformational changes of the transporter associated with Na^+-binding and thereby decreases the glutamate transport rate, while increasing the open probability of the anion channel (Winter et al. 2012, Hotzy et al. 2013). Meanwhile, additional missense mutations in the *SLC1A3* gene were associated with EA6 (de Vries et al. 2009, Pyle et al. 2015, Choi et al. 2017a, Choi et al. 2017b, Iwama et al. 2018).

To understand how functional alterations of P290R EAAT1 cause the phenotype of EA6, a knock-in mouse model (*Slc1a3*$^{P290R/+}$) was generated. Mutant mice exhibit impaired motor coordination and epileptic seizures ((Kovermann et al. 2020) find this work attached to this thesis).

1.5.3. Ischemia

Brain ischemia is a frequent vascular complication and represents one of the main causes of disability and death in our aging population (Katan and Luft 2018). Ischemia is caused by a reduced blood supply and decreased oxygen availability. An ischemic lesion consists of a core region, with profound reduction of blood flow and irreversible cell death, surrounded by the peri-infarct zone, also referred to as penumbra. The penumbra is of main interest in research and therapy of ischemia. Cells in this area are exposed to a partially reduced blood flow over the ischemic threshold. When surrounded by healthy tissue, damaged cells can recover spontaneously if the cerebral blood flow returns after a certain timeframe. These mechanisms allow cells to recover and to rebuild physiological ion and glutamate distributions.

Reduced cerebral blood flow decreases the oxygen and glucose supply, which leads to disturbances in cellular metabolism and reduction of the ATP level. The Na^+/K^+-ATPase is a major consumer of ATP. Reduced ATP levels decrease Na^+ and K^+ gradients across neuronal and glial membranes and impair the activities of various secondary active transporters. This leads to an increase of $[K^+]_{ext}$ and decrease of $[Na^+]_{ext}$ causing membrane depolarization. Increased glutamate release and impaired uptake results in higher extracellular glutamate concentrations ($[glutamate]_{ext}$).

Anoxic depolarization describes a uncontrollable depolarization, induced by an increase of $[K^+]_{ext}$ (Hertz et al. 2015) and $[glutamate]_{ext}$ (Belov Kirdajova et al. 2020) as well as $[Na^+]_{int}$ (Gerkau et al. 2018) and $[Cl^-]_{int}$, which potentially results in glutamate-induced apoptosis or necrosis of neuronal cells (Zhang and Bhavnani 2006, Kritis et al. 2015).

NKCC1 was shown to be upregulated in neurons in the ischemic penumbra (Bhuiyan et al. 2017). Other experiments with cultured neurons demonstrated that the NKCC1 is stimulated by high $[K^+]_{ext}$ and $[glutamate]_{ext}$ (Yan et al. 2001b). This could indicate that the NKCC1 plays a key role in ischemia and that the fluxes of Na^+, K^+ and Cl^-, as well as water, are involved cell damage.

1.6. Chloride Imaging

1.6.1. Fluorescence lifetime imaging microscopy (FLIM)

To measure intracellular ion concentrations in living cells, various fluorescent indicators have been developed in recent years. The dynamics of the Cl^- homeostasis on cellular and subcellular levels can be studied by using the fluorescence lifetime imaging microscopy (FLIM) with the chloride sensitive quinolinium dye MQAE (1-(Ethoxycarbonylmethyl)-6-methoxy-quinolium bromide) (Gensch et al. 2015).

Fluorescence microscopy is based on the excitation of a fluorophore with light of defined energy (wavelength) from the ultraviolet, visible and near-infrared light spectrum ($h\nu$, where h is the Planck constant and ν the frequency of the photon) and the detection of the emitted photons of longer wavelengths (Stokes-shift).

In the last twenty years, FLIM has been established to examine absolute ion concentrations in cells (Marcu et al. 2014, Gensch et al. 2015). To measure $[Cl^-]_{int}$ the fluorescence lifetime (τ) is a more suitable parameter compared to fluorescence intensity, because the fluorescence lifetime determined for a fluorophore – here MQAE – is

independent of the amount of fluorophore molecules in one cell and the excitation light intensity. The fluorescence intensity of a fluorophore is directly proportional to the amount of fluorophore molecules. In cells, the amount of fluorophores cannot be controlled and is influenced by many factors. Therefore, it is unsuitable to determine the absolute $[Cl^-]_{int}$ from the fluorescence intensity of MQAE.

The fluorescence lifetime of a fluorophore τ is the time a fluorophore stays in the excited state (S_1) before it returns to its ground state (S_0) (Figure 3.6). The fluorescence lifetime equals ([1.4]) the reciprocal of the sum of rate constants of the deactivation processes of the excited electron, namely the non-radiative rate constant (internal conversion and vibrational relaxation; k_{nr}), the rate of dynamic (or collisional) quenching (k_q) and the radiative rate constant (the rate of emitting photons; k_f):

[1.4] $$\tau = \frac{1}{k_{nr} + k_q + k_f} .$$

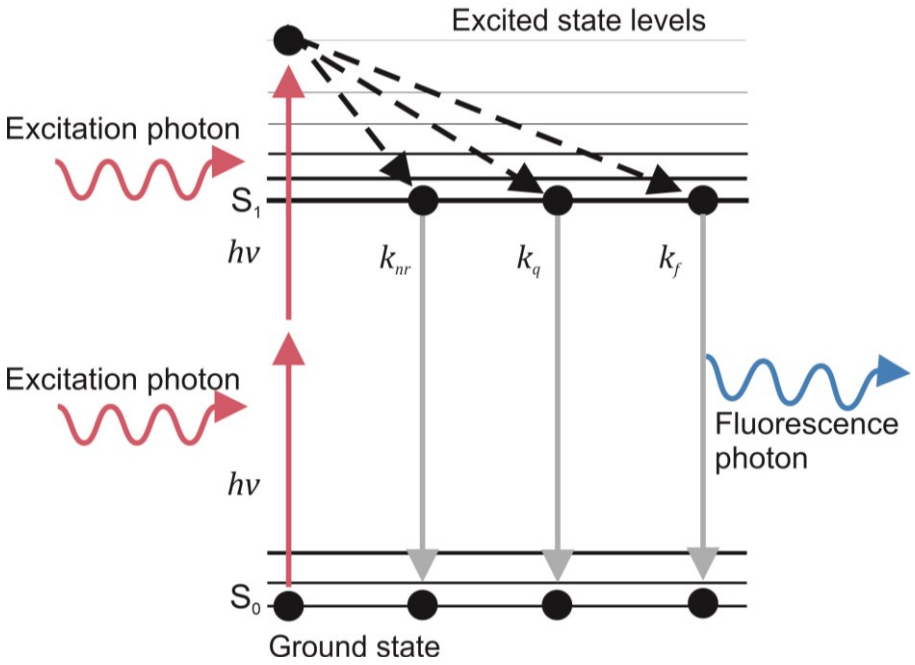

Figure 3.6: Jablonski diagram illustrating the two-photon excitation and possible relaxation ways of the fluorophore.
A fluorophore is excited via two-photon excitation (hv) from the ground state (S_0) to the excited state (S_1). In the S_1, the fluorophore stays for a specific time – the fluorescence lifetime (τ) – until it returns to S_0 either by non-radiative decay (k_{nr}) or by the emission of light (k_f). In the presence of quencher molecules, the excited fluorophore can collide with a quencher molecule (in this dissertation chloride). It then forms a short-lived collisional complex and the excited electron returns to the ground state S_0 without emission of a photon (k_q).

Fluorescence microscopy using two-photon excitation of chloride-sensitive dyes by femtosecond pulsed near-infrared light is a harmless and non-invasive technique to study chloride concentrations in acute brain slices. The two-photon excitation is based on simultaneous absorption of two low-energy photons by the molecule of interest (Zipfel et al. 2003, Berezin and Achilefu 2010) and enables the detection of glial cells at depths that are unreachable with one-photon excitation or confocal microscopy.

FLIM in combination with MQAE proves to be a more convenient tool to study $[Cl^-]_{int}$ in living cells of acute brain slices than chloride imaging with genetically encoded fluorescent sensors for chloride, like "Clomeleon" (Kuner and Augustine 2000). This Cl^- sensor has some disadvantages, as it suffers from divergent light scattering due to different wavelengths, tissue deepness and age dependency (Oheim et al. 2001) as well as the sensitivity of the fluorescent protein towards pH changes (Kuner and Augustine 2000).

1.6.2. Measuring fluorescence lifetimes with the time-correlated single photon counting technique

To determine the fluorescence lifetime in the time-domain, the technique of time-correlated single-photon counting (TCSPC, Simple-Tau 152; Becker&Hickl) is applied. With this technique, fluorophores of a probe – solution, cell or tissue – are excited with short pulses (typical: 50-200 fs) of photons of defined energy (wavelength) impinging on the sample at high repetition frequency (typical: 80 MHz). The photon detector works in single photon counting mode and registers a photon with very accurate timing. Excitation power is dimmed so that less than one photon per excitation pulse is detected. The time between excitation and detection of the emitted photon is measured and plotted in a histogram. This step is repeated 10^5 – 10^8 times to achieve a sufficient amount of detected photons in the photon arrival time histogram. This histogram can be described by the best fit of a sum of exponential functions, from which the average fluorescence lifetime (τ_{ave}; [1.5] with τ_x = lifetime of the exponential component; a_x= respective amplitude) can be calculated (as shown in the present study Engels et al., submitted; section: Fluorescence lifetime imaging microscopy (FLIM); Figure 3.7).

[1.5] $$\tau_{ave} = \frac{a_1 * \tau_1 + a_2 * \tau_2}{a_1 + a_2}$$

The fluorescence lifetime was measured with an upright scanning fluorescence microscope and averaged over a total scanning time of 40 s or 80 s (as shown in the present study Engels et al., submitted; section: Fluorescence lifetime imaging microscopy (FLIM)). Using scanning fluorescence microscopes, the arrival time of one single photon and a focused laser beam scanning a defined area are used to create a 3-dimensional matrix, in which for each pixel of the scanned area the fluorescence signal and the fluorescence decay is stored.

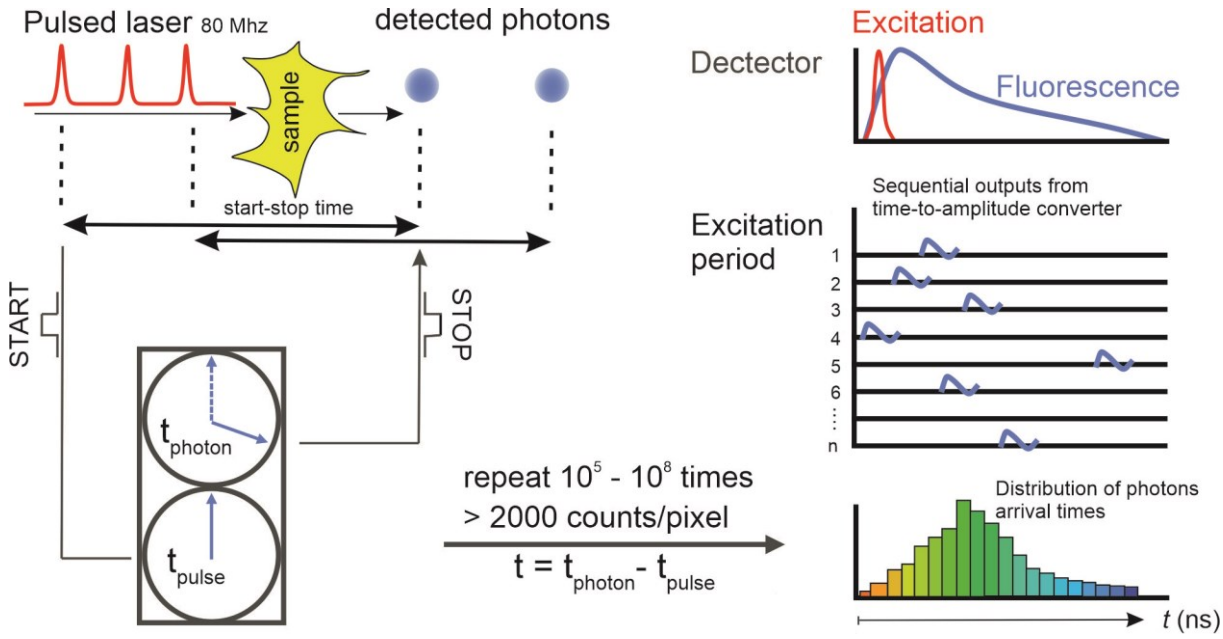

Figure 3.7: Schematics of the time-correlated single photon counting mechanism.
Using a pulsed laser, the fluorophore is excited and starts the detection of the fluorescence lifetime (START t_{pulse}) which is stopped by the detection of the emitted photon (STOP t_{photon}). During the time of measurements, this process is repeated 10^5 – 10^8 and all detected photons (> 2000 counts/pixel) are collected in a histogram to calculate the τ_{ave}. Scheme was drawn according to (Becker 2005).

1.6.3. The chloride-sensitive fluorescent dye MQAE

Chloride accumulation or deprivation in cells can be studied by using fluorescent quinolinium-derivatives, like the chloride-sensitive dye MQAE, in combination with two-photon excitation FLIM microscopy. The dye is a well-suited Cl^- sensor to determine cytoplasmic chloride concentrations (Verkman et al. 1989, Biwersi and Verkman 1991, Kaneko et al. 2004, Untiet et al. 2017) because of its chloride sensitivity, which is based on dynamic collisional quenching.

MQAE, like all quinolinium-derivates, has a specific Stern-Volmer constant (K_{SV}) and fluorescence lifetime in the absence of chloride (τ_0) which depends on the surrounding environment, i.e. the abundance of other molecules that quench the fluorescence of MQAE.

In the various glial cells, different amounts of other negatively charged atoms and molecules are present, which can contribute as additional quenchers. The majority of chloride transport blockers are fluorescent in the ultraviolet range and are negatively charged under physiological pH. Therefore, they could contribute to the measured fluorescence with a different fluorescence lifetime or could quench the fluorescence of MQAE by themselves, which both impair the accuracy of this approach (Figure 3.8a). Furthermore, dimethylsulfoxid (DMSO) - a commonly used solvent for many organic chemical substances including the four blocker molecules used in this work – can also act as a quencher of MQAE fluorescence.

Time-resolved detection of the fluorescence lifetime decays of MQAE (3 mM) in presence of varying DMSO concentrations (0 – 0.2% v/v) were determined in cuvette measurements using fluorescence spectrophotometer with time-resolved detection (Fluotime100, Picoquant, Berlin, Germany) based on a picoHarp300 unit by utilizing a pulsed diode laser (Laser Picoquant LDH- P-C-375; emission: 375 nm; pulse width: <40 ps; used repetition frequency: 20 MHz) as an excitation source. Fluorescence decay curves as a function of time (t) were measured by time-correlated single-photon counting that enables the determination of fluorescence decay components with fluorescence lifetimes greater than 100 ps. Decay curves were analysed by iterative reconvolution of the instrument response function, IRF(t), with an exponential model function, M(t), using the FluoFit software (version 4.5.3.0; Picoquant). Cuvette experiments demonstrated that DMSO indeed acts as a quencher with increasing concentrations. Its Stern-Volmer plot yields a straight line and the Stern-Volmer constant of DMSO is estimated as 8.73 M^{-1} (Figure 3.8 b). Further cuvette experiments have shown, that the blocker Bumetanide, *R*-(+)-DIOA and DL-TBOA (Figure 3.8a) influences the MQAE fluorescence lifetime (faster decay) while no emission from the blockers with spectra different from MQAE was detected.

Since in FLIM measurements of acute brain slices under the microscope the intracellular concentration of DMSO and the various blockers cannot be determined nor controlled I decided to test the influence of blocker and DMSO for every single blocker in the acute brain slice and for every glial cell type. The blocker UCPH-101 comprises no COOH group and does not quench the MQAE lifetime (Figure 3.8c). Further MQAE calibrations in the presence and absence of UCPH-101 were performed in neocortical astrocytes. The physiological calibration with or without UCPH-101 point out similar results for the observed $[Cl^-]_{int}$ and confirm that UCPH-101 dissolved in DMSO does not additional effect MQAE

lifetime. To determine accurate $[Cl^-]_{int}$ further calibrations in the presence of Bumetanide, *R*-(+)-DIOA and DL-TBOA have to carried out (as shown in the present study Engels et al., submitted; section: Fluorescence lifetime imaging microscopy (FLIM) Figure 4). The fluorescence lifetime of MQAE is inversely proportional to the chloride concentration (Verkman 1990, Kaneko et al. 2002, Gensch et al. 2015) and enables determination of $[Cl^-]_{int}$ over a broad range. To achieve this, MQAE fluorescence lifetime changes need to be accurately calibrated within the cells or brain region of interest.

Altogether, MQAE allows measurements of $[Cl^-]_{int}$ after a cell specific calibration in acute brain slices, because of the following properties: high Cl^- affinity, independent from dye/fluorophore concentration, insensitive to HCO_3^- concentration, very little photobleaching and insensitivity to changes of the pH (Verkman et al. 1989, Koncz and Daugirdas 1994, Kaneko et al. 2002, Kovalchuk and Garaschuk 2012, Arosio and Ratto 2014).

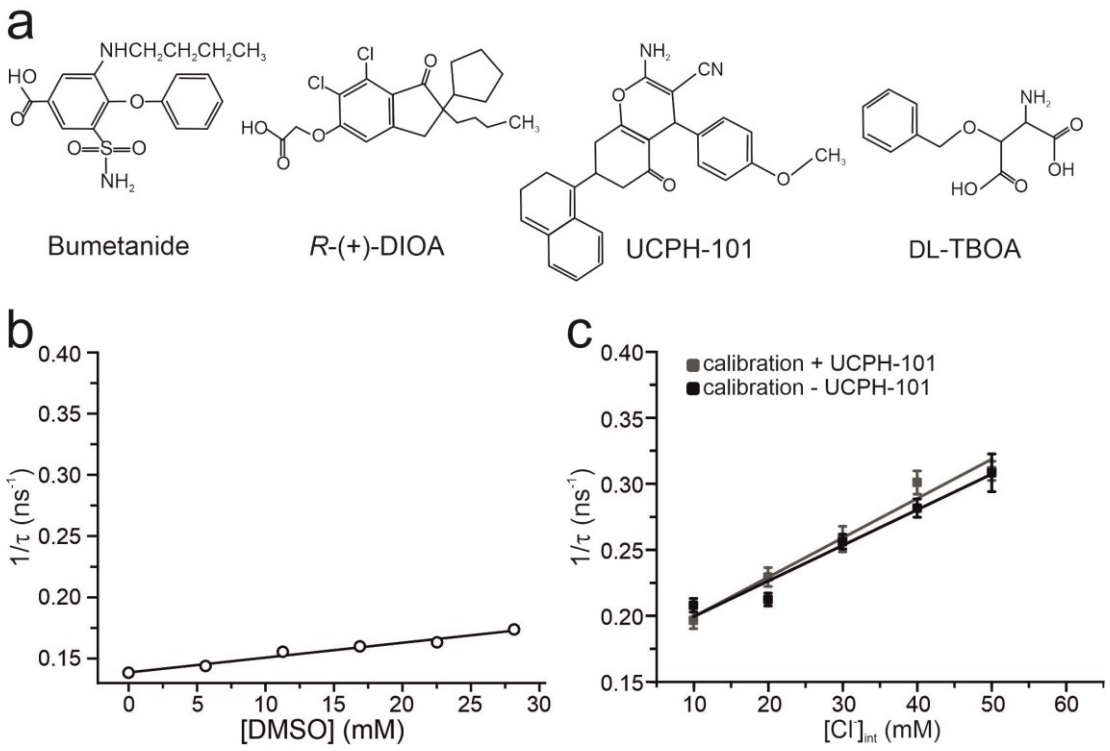

Figure 3.8: Potential, additional quencher of MQAE lifetime. (a) Chemical structure of Bumetanide, *R*-(+)-DIOA, UCPH-101 and DL-TBOA. (b) Stern-Volmer analysis of 3 mM MQAE dissolved in 0 mM Cl^- in the presence of different DMSO concentrations (0 – 0.2% v/v; 0 – 28.16 mM; K_{SV} = 8.73 M^{-1} and τ_0 = 7.23 ns). The fluorescence lifetime was determined by collecting fluorescence intensity decays with 10000 counts in the maximum (excitation: 380 nm; emission: 460 nm). (c) MQAE calibration in neocortical astrocytes in presence (grey; K_{SV} = 17.59 M^{-1} and τ_0 = 5.90 ns) and absence (black; K_{SV} = 15.7 M^{-1} and τ_0 = 5.81 ns) of UCPH-101 (for comparability experiments were performed in the same animal).

1.7. Aim of this dissertation

Chloride is the main compensatory ion for the movement of cations, like K^+ and Na^+ in living cells. $[Cl^-]_{int}$ is an important determinant of many cellular functions, like volume regulating processes, neurotransmitter uptake, maturation of glial cells and excitability of neurons, but $[Cl^-]_{int}$ is still barely investigated. A number of transporters, such as the NKCC1, KCCs and EAATs, are involved in chloride fluxes over the plasma membrane. The differences in function and expression level of these chloride channels/transporters result in a high variability in $[Cl^-]_{int}$. This is the reason why mechanisms underlying intracellular Cl^- homeostasis are insufficiently understood.

In literature, chloride concentrations in glial cells had been mainly determined in cell culture (Kimelberg 1981, Kettenmann et al. 1987, Walz and Mukerji 1988, Bevensee et al. 1997, Bekar and Walz 2002). The first measurements of chloride concentrations in glial cells in an intact natural environment, acute brain slices, have been done recently in our lab (Untiet et al. 2017).

The goal of this work was to determine further physiological $[Cl^-]_{int}$ of glial cells in the hippocampus (CA1, DG and RGL cells) and neocortex (layer II/III). Furthermore, the $[Cl^-]_{int}$ of glial cells was measured after chloride channel/transporter inhibition/blocking to determine the function of different channels/transporters in the intracellular Cl^- homeostasis. In addition, the influence of pathophysiological conditions, like chemical ischemia and episodic ataxia were examined in acute tissue slices.

To determine $[Cl^-]_{int}$ the fluorescence lifetime imaging microscopy and the chloride sensitive dye MQAE was used. This technique served as main component, as well as a support to electrophysiological recordings, immunohistochemistry or protein expression results, respectively, of the mentioned publications.

2 Publications and Manuscripts

2.1.1. Published manuscript

Increased glutamate transporter-associated anion currents cause glial apoptosis in episodic ataxia 6

Peter Kovermann*, Verena Untiet*, Yulia Kolobkova*, Miriam Engels, Stephan Baader, Karl Schilling and Christoph Fahlke

* These authors contributed equally

Pages: 31 – 47

Journal: BRAIN COMMUNICATIONS 2020: Volume 2, Issue 1 2020 Page 1 of 17 published on 4 March 2020

DOI: 10.1093/braincomms/fcaa022

Contribution: I did FLIM measurements of BG in acute tissue slices of the cerebellum and analysed the obtained data. I was involved in the presentation of the results in figure 4 (D-F) as well as in the interpretation of the data and the revision of the manuscript.

doi:10.1093/braincomms/fcaa022 BRAIN COMMUNICATIONS 2020: Page 1 of 17 | 1

BRAIN COMMUNICATIONS

Increased glutamate transporter-associated anion currents cause glial apoptosis in episodic ataxia 6

Peter Kovermann,[1,†] Verena Untiet,[1,*,†] Yulia Kolobkova,[1,†] Miriam Engels,[1] Stephan Baader,[2] Karl Schilling[2] and Christoph Fahlke[1]

[†] These authors contributed equally to this work.

* Present address: Center for Translational Neuromedicine, Divison of Glial Disease and Therapeutics, Københavns Universitet, 2200 København N, Denmark.

Episodic ataxia type 6 is an inherited neurological condition characterized by combined ataxia and epilepsy. A severe form of this disease with episodes combining ataxia, epilepsy and hemiplegia was recently associated with a proline to arginine substitution at position 290 of the excitatory amino acid transporter 1 in a heterozygous patient. The excitatory amino acid transporter 1 is the predominant glial glutamate transporter in the cerebellum. However, this glutamate transporter also functions as an anion channel and earlier work in heterologous expression systems demonstrated that the mutation impairs the glutamate transport rate, while increasing channel activity. To understand how these changes cause ataxia, we developed a constitutive transgenic mouse model. Transgenic mice display epilepsy, ataxia and cerebellar atrophy and, thus, closely resemble the human disease. We observed increased glutamate-activated chloride efflux in Bergmann glia that triggers the apoptosis of these cells during infancy. The loss of Bergmann glia results in reduced glutamate uptake and impaired neural network formation in the cerebellar cortex. This study shows how gain-of-function of glutamate transporter-associated anion channels causes ataxia through modifying cerebellar development.

1 Institut für Biologische Informationsprozesse, Molekular- und Zellphysiologie (IBI-1), Forschungszentrum Jülich, 52428 Jülich, Germany
2 Anatomisches Institut, Anatomie und Zellbiologie, Rheinische Friedrich-Wilhelm Universität Bonn, 53115 Bonn, Germany

Correspondence to: Peter Kovermann, Institut für Biologische Informationsprozesse, Molekular- und Zellphysiologie (IBI-1), Forschungszentrum Jülich, 52428 Jülich, Germany.
E-mail: p.kovermann@fz-juelich.de
Correspondence may also be addressed to: Christoph Fahlke. E-mail: c.fahlke@fz-juelich.de

Keywords: glutamate transporters; chloride homeostasis; Bergmann glia; glial apoptosis; episodic ataxia

Abbreviations: BLBP = brain lipid-binding protein; CASP3 = caspase 3; CF = climbing fibre; CV = covariances; $[Cl^-]_{int}$ = internal chloride concentration; EAAT1 = excitatory amino acid transporter 1; EAs = episodic ataxias; EGFP = enhanced green fluorescent protein; GFAP = glial fibrillary acidic protein; GLAST = glutamate–aspartate transporter; MQAE = 1-(ethoxycarbonylmethyl)-6-methoxy-quinolinium bromide; TUNEL = terminal dUTP nick-end labelling; WT = wild type

Received July 1, 2019. Revised January 24, 2020. Accepted February 2, 2020. Advance Access publication March 4, 2020

Graphical Abstract

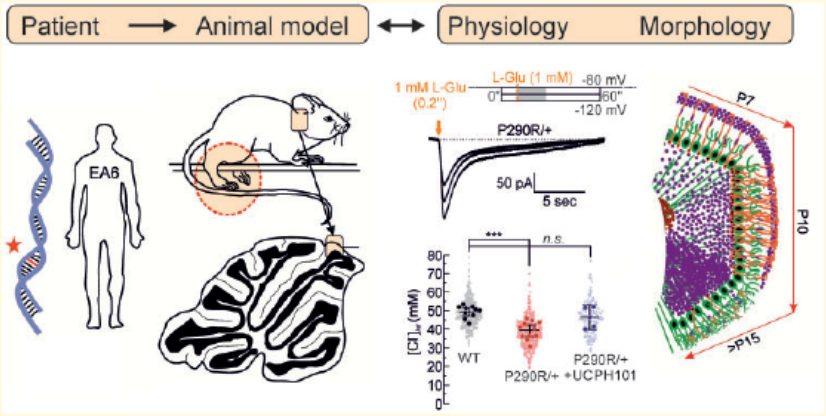

Introduction

Episodic ataxias (EAs) are rare neurological syndromes characterized by paroxysmal cerebellar incoordination, variably combined with epilepsy, dystonia and migraine-like headache (Jen *et al.*, 2007). Eight variants of autosomal dominant EAs (EA1–8) have been defined with different genetic origins. EA6 has been reported in only seven families, with clinical symptoms differing from those of other EA forms by the addition of long-lasting attacks of ataxia and epilepsy and the absence of myokymia, nystagmus and tinnitus. Mutations in *SLC1A3*, encoding the glial excitatory amino acid transporter 1 (EAAT1), the human homologue of the glutamate–aspartate transporter (GLAST) (Storck *et al.*, 1992), were identified in all seven families (Jen *et al.*, 2005; de Vries *et al.*, 2009; Pyle *et al.*, 2015; Choi *et al.*, 2017a, *b*; Iwama *et al.*, 2018).

A heterozygous *SLC1A3* missense mutation predicting arginine replacement of a proline residue in transmembrane domain 5 of *h*EAAT1 (P290R) was identified in a 10-year-old boy, who had suffered from episodes of ataxia, epilepsy and hemiplegia throughout his childhood (Jen *et al.*, 2005). The patient also experienced attacks of headache, visual field neglect and hemiplegia for at least twice the duration of those in other EA patients. Magnetic resonance imaging scan showed mild cerebellar atrophy, and electroencephalography revealed subclinical seizure activity in one episode and epileptiform discharges in another one (Jen *et al.*, 2005). EAATs function as both secondary-active glutamate transporters and anion channels (Fahlke *et al.*, 2016) and P290R substitution exerts opposing effects on these functions in heterologous expression systems. It reduces the speed of conformational changes associated with Na^+ association/dissociation with the outward-facing EAAT1, thereby decreasing the glutamate transport rate and increasing the open probability of the anion channel (Winter *et al.*, 2012; Hotzy *et al.*, 2013).

To investigate how changes in glial glutamate transporter function cause the neurological symptoms of EA6, we used a constitutive heterozygous mouse model carrying the targeted missense mutation in EAAT1/GLAST (*Slc1a3*$^{P290R/+}$).

Materials and methods

Animals

Wild-type (WT), homozygous GLAST knock-out (*Slc1a3*$^{-/-}$) and heterozygous GLAST mutant (*Slc1a3*$^{P290R/+}$) mice of both sexes with the genetic backgrounds, C57BL/6N (WT, *Slc1a3*$^{P290R/+}$) and 129/SvJ (WT, *Slc1a3*$^{-/-}$, *Slc1a3*$^{P290R/+}$) and FVB/N [Tg(GFAP–EGFP)14Mes/J], were studied at ages between P5 and P800 (Supplementary Material). Mouse studies in this study conform with the Animal Research: Reporting of *In Vivo* Experiments guidelines (McGrath *et al.*, 2010).

Motor coordination testing

Motor coordination was tested in the ledge test (Guyenet *et al.*, 2010) by manually placing WT and mutant mice on a 1-cm wide ledge and encouraging them to walk along the ledge for 2′ by gentle nudges (Supplementary Material). Rotarod testing was performed by placing female mice (~P50) on an accelerating rotarod (Ugo-Basile, Italy) and measuring latencies to fall off the rotating rod. Mice usually underwent a short training and were subjected to three test sessions within two consecutive days (Day 1, 10:00–12:00 h and 14:00–16:00 h; Day 2, 10:00–12:00 h) after the successful completion of this training.

Each session consisted of three trials 10′ apart (Supplementary Material).

Visualization and quantification of specific cell types and components

Details about staining procedures and used antibodies are provided in the Supplementary Material and in Supplementary Table 2.

Preparation of acute cerebellar slices

After anesthetizing animals (P7–P900) with isoflurane and rapid decapitation, brains were placed in ice-cold oxygenated Ringer's solution A (125 mM NaCl, 2.5 mM KCl, 1.25 mM NaH_2PO_4, 26 mM $NaHCO_3$, 0.5 mM $CaCl_2$, 5 mM $MgCl_2$, 20 mM $C_6H_{12}O_6$, 5% CO_2 and 95% O_2). Sagittal cerebellar slices (250-µm thick) were cut using a microtome ($\upsilon = 60$ Hz, amplitude = 1 mm) and transferred to a gauze slice holder in oxygenated Ringer's solution A for 30′ at 37°C and 90′ to Ringer's solution B (125 mM NaCl, 2.5 mM KCl, 1.25 mM NaH_2PO_4, 26 mM $NaHCO_3$, 2 mM $CaCl_2$, 1 mM $MgCl_2$ and 25 mM $C_6H_{12}O_6$) at room temperature (RT). During experiments, the slices were constantly perfused with oxygenated Ringer's solution B or oxygenated artificial cerebrospinal fluid (125 mM NaCl, 2.5 mM KCl, 1.25 mM NaH_2PO_4, 26 mM $NaHCO_3$, 2 mM $CaCl_2$, 1 mM $MgCl_2$). All experiments with acute slices were completed within 8 h after brain removal.

Cl^- current recordings in Bergmann glia cells

We performed whole-cell recordings of Bergmann glia cell anion currents in acute cerebellar slices of mice between P9 and P14 under continuous perfusion with artificial cerebrospinal fluid at RT supplemented with 1 µM 6-cyano-7-nitroquinoxaline-2,3-dione (Tocris Bioscience, Germany) using an EPC10 USB amplifier with PatchMaster software (HEKA Elektronik). Bergmann glia cells were visually identified by morphology and location in the Purkinje neuron layer. The pipette solution contained 145 mM KCl, 1 mM $MgCl_2$ and 10 mM HEPES/KOH (pH 7.2). Cells were held at membrane potentials of −80/−100/−120 mV, and glutamate-activated anion currents were elicited by the application of Na glutamate (1 mM) by a pressure-driven perfusion system (PDES-DXH; NPI Electronic GmbH, Germany) coupled to standard micropipettes (Hilgenberg, Germany) placed 10–20 µm from the cell somata. A maximum of one Bergmann glia cell was tested per slice.

Fluorescence lifetime imaging microscopy

We measured the internal chloride concentration ($[Cl^-]_{int}$) of Bergmann glia cells by 1-(ethoxycarbonylmethyl)-6-methoxy-quinolinium bromide (MQAE) fluorescence lifetime imaging microscopy with an upright fluorescence microscope (A1 MP, Nikon, Netherlands) equipped with a 25× water immersion objective (Gensch *et al.*, 2015; Untiet *et al.*, 2017). Acute cerebellar slices were incubated with 3.5 mM MQAE in Ringer's solution B for 30′. MQAE fluorescence is collisional quenched by Cl^- ions, resulting in a linear relationship between the inverse fluorescence lifetime and $[Cl^-]_{int}$ (Verkman, 1990):

$$\frac{\tau_0}{\tau} = 1 + K_{SV}\ [Cl^-]_{int}, \quad (1)$$

where τ is the MQAE fluorescence lifetime at a given $[Cl^-]_{int}$, τ_0 is the MQAE fluorescence lifetime in the absence of chloride and K_{SV} is the cell type-specific Stern–Volmer constant. After calibration in Bergmann glia cells using the 2-ionophore calibration experiments (Untiet *et al.*, 2017), $[Cl^-]_{int}$ for single-cell soma was calculated from the mean fluorescence lifetime of all pixels within a defined region of interest. $[Cl^-]_{int}$ are given as mean ± 95% confidence interval (CI) from 3–4 individual animals per time point and genotype.

Apoptosis assays

Bergmann glia cells were identified in acute cerebellar slices from the progeny of GFAP-conjugated enhanced green fluorescent protein (GFAP–EGFP) reporter mice [FVB/N(GFAP–EGFP)14MES/J] crossbred with *Slc1a3*$^{P290R/+}$ mutants. After anesthetizing animals with isoflurane and rapid decapitation, brains were transferred into 4% paraformaldehyde in phosphate buffer (30′, 4°C). Cerebella were then washed in phosphate buffer (30′, RT) and incubated in phosphate buffer supplemented with 10% $C_{12}H_{22}O_{11}$ (60′, RT) and 30% $C_{12}H_{22}O_{11}$ (12 h, 4°C) before embedding in NEG50 (Thermo Fisher Scientific, USA) and cut into sagittal slices (18 µm thick), using a HM560 microtome (MICROM, Germany). Slices were incubated with antibody against rabbit anti-active caspase 3 (CASP3) to label apoptotic cells. For immunochemical analysis, slices were incubated in CTA (5% ChemiBLOCKER—Merck-Millipore, 0.5% TritonX-100—Sigma Aldrich, 0.05% NaN_3, v/v) for 10′ and then overnight in CTA with primary antibody at RT. Secondary antibodies were applied in CTA for 60′. Apoptosis was quantified by averaging the number of CASP3-positive Bergmann glia cells per brain slice for each tested animal. Terminal dUTP nick-end labelling (TUNEL) of fragmented DNA in cerebellar nuclei was performed as a control for Bergmann glial apoptosis as described in Supplementary Material. Details about used antibodies/kits are listed in Supplementary Table 2.

Cell-attached recordings from Purkinje neurons

We visually identified Purkinje neurons in acute brain slices based on size and location between the granule cell layer and the molecular layer. For electrophysiological recordings, pipettes (4–6 MΩ) were filled with a Ringer-like solution (140 mM NaCl, 4 mM KCl and 10 mM HEPES/KOH, pH 7.4) and slices were constantly perfused with oxygenated artificial cerebrospinal fluid (125 mM NaCl, 2.5 mM KCl, 2 mM $CaCl_2$, 2 mM $MgCl_2$, 1.25 mM NaH_2PO_4 and 26 mM $NaHCO_3$) during the course of the experiment. Cell-attached patches were formed at neuron somata, and currents were recorded at RT between 30" and 10' in voltage-clamp mode at 0 mV (EPC10 amplifier; HEKA Elektronik). Data were analysed offline using Clampfit event-analysis functions (Molecular Devices, USA).

Statistical analysis

All statistical parameters were calculated with SigmaPlot (Systat Software GmbH), OriginPro (OriginLab Corp.) or Excel (Microsoft Corp.). Data are presented as means ($\bar{x}$), medians ($\tilde{x}_{0.5}$) ± CI (95% confidence interval) or σ (standard deviation) from individual animals. Ages are provided as postnatal days. Data were analysed using Mann–Whitney *U*-tests or two-way ANOVA tests and Kruskal–Wallis ANOVA on ranks with Holm–Sidak or Dunn's *post hoc* testing. *P*-values ≤ 0.05 were considered statistically significant with $^{*}P \leq 0.05$, $^{**}P \leq 0.01$, $^{***}P \leq 0.001$; all *P*-values are provided in Supplementary Table 3.

Data availability

The source data that support the findings of this study are available from the corresponding author upon reasonable request.

Results

Slc1a3$^{P290R/+}$ mice suffer from epilepsy and ataxia

Knock-in *Slc1a3*$^{P290R/+}$ mice (*Slc1a3*^{tm1P290RCfa}) were initially generated by homologous recombination in the C57BL/6N background (Supplementary Material and Supplementary Fig. 1). Heterozygous mice suffered from spontaneous generalized seizures and death during the weaning period with a peak between postnatal days (P) P25– and P30 (Fig. 1A, grey), and we therefore backcrossed the mutation into the 129/SvJ strain, as a similar procedure has been successfully used to generate another animal model of severe epilepsy (Yu *et al.*, 2006). This change in genetic background reduced lethal seizure activity by ~70% ($n = 39/150$, C57/129Sv) and delayed the onset of the seizure period and the peak time of premature deaths to P35–P55 (Fig. 1A, red and Supplementary Video 1). We monitored WT and *Slc1a3*$^{P290R/+}$ mice and scored fitness with respect to general condition, behavioural aspects and EA6 associated pathology (Supplementary Table 1). Mutant male mice exhibited a severe phenotype with maximum scores between P40 and P80, whereas female *Slc1a3*$^{P290R/+}$ mice showed a milder constitutive phenotype (Supplementary Fig. 2).

We assessed motor coordination by observing the *Slc1a3*$^{P290R/+}$ animals walking along the ledge of a cage (Fig. 1B) (Guyenet *et al.*, 2010). Ledge tests showed significantly more paw slips per step number in mutant animals (Fig. 1C and Supplementary Video 2), with no difference between sexes ($n = 8/12/12/11$, WT$^{♂}$/WT$^{♀}$/Mut$^{♂}$/Mut$^{♀}$). Gait coordination was additionally tested by measuring the time animals can walk on a rotating horizontal rod (Jones and Roberts, 1968) (Fig. 1D–F). Figure 1D shows averaged time series of consecutive rotarod sessions (labelled I–III) for WT and mutant animals on Kaplan–Meier curves (Kaplan and Meier, 1958). These values were corrected for episodes, in which mice did not walk forward, but rotated with the rotarod by holding on to it (spin failures, Supplementary Material; Fig. 1E and Supplementary Fig. 3A). In initial tests, we observed a much higher frequency of such episodes for mutant male than animals for mutant female animals and, therefore, restricted rotarod testing to female animals (Supplementary Material). Compared with WT mice, mutant mice remained shorter times on the rotating rod and started significantly earlier to make mistakes ($n = 8/7$ animals, WT/Mut, Fig. 1F and Supplementary Fig. 3B). In the third trial, all WT performed the task without falling off and without spin failures, whereas 4/7 *Slc1a3*$^{P290R/+}$ animals still either fall off or rotated with the waltz (Fig. 1D–F and Supplementary Fig. 3). In conclusion, *Slc1a3*$^{P290R/+}$ animals exhibit a robust EA6 phenotype with epilepsy and ataxia, thus resembling the phenotype of humans carrying the same mutation.

Cerebellar Bergmann glia cells from *Slc1a3*$^{P290R/+}$ mice degenerate during the second and third postnatal weeks

As EAAT1/GLAST is highly expressed in cerebellar Bergmann glia cells (Rothstein *et al.*, 1994; Torp *et al.*, 1994; Chaudhry *et al.*, 1995; Watase *et al.*, 1998), alterations in these cells likely represent initial steps in cerebellar dysfunction in *Slc1a3*$^{P290R/+}$ mice. Figure 2A shows representative confocal images from the cerebellar cortex of WT and mutant mice (P20), immunostained with antibodies against glial fibrillary acidic protein (GFAP) and against brain lipid-binding protein (BLBP). Anti-BLBP permits the visualization of Bergmann glia soma (Feng *et al.*, 1994), whereas anti-GFAP stains Bergmann glia

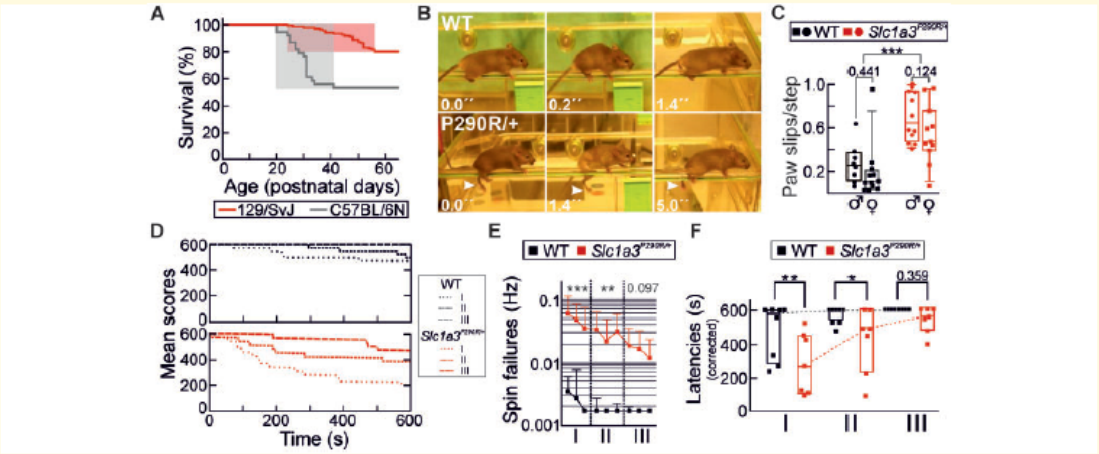

Figure 1 ***Slc1a3*$^{P290R/+}$ mice suffer from epilepsy and ataxia.** Image **A** depicts survival rates for C57BL/6 (grey) and 129/SvJ (red) *Slc1a3*$^{P290R/+}$ mice over time, with shaded areas indicating periods with pronounced seizure activity. Representative screen shots (**B**) from video recordings of WT and *Slc1a3*$^{P290R/+}$ mice moving on a ledge indicate that transgenic mice tend to slip (arrowheads) from the ledge with their hindlimbs. The whisker plot (**C**) shows the median paw slip numbers per step for adult (P50) WT (black) or *Slc1a3*$^{P290R/+}$ (red) mice of both sexes (circles, ♂; squares, ♀). The analysis revealed no detectable sex differences in Ledgetest performance ($P = 0.110$) but pronounced differences between genotypes in both sexes ($n = 8/12/12/11$, WT$^{♂}$/WT$^{♀}$/Mut$^{♂}$/Mut$^{♀}$, $P \leq 0.001^{♂}/P = 0.001^{♀}$). The averaged time series of mean scores (**D**) for three consecutive rotarod trial sessions (I–III) with adult female WT (black) or *Slc1a3*$^{P290R/+}$ (red) mice at P50 point to differences between WT and mutant animals. The increased mean spin failure frequencies (**E**) for WT or *Slc1a3*$^{P290R/+}$ ($P = 0.011$) and the decreased rotarod latencies to fall (**F**) indicate that *Slc1a3*$^{P290R/+}$ mice suffer from ataxia ($n = 8/7$, WT/Mut, $P = 0.031$). Data are shown as whisker-box plots with medians [whisker: 5th to 95th percentile, box: 25th to 75th percentiles, single (**C**) and repeated measure (**E** and **F**) two-way ANOVA and Holm–Sidak *post hoc* test]; $^{*}P \leq 0.05$, $^{**}P \leq 0.01$, $^{***}P \leq 0.001$; all *P*-values for this figure are provided in Supplementary Table 3.

fibres. In WT animals, Bergmann glia cells with typical unipolar morphology, i.e. soma in the Purkinje neuron layer and extensions in the molecular layer, were readily observed; however, such structures were absent in *Slc1a3*$^{P290R/+}$ mice at P20. We identified Bergmann glia cell fibres as GFAP-positive processes in the cerebellar molecular layer, which originate from Purkinje neuron layers, and counted them in WT and mutant animals between P5 and P800. Prior to P10, WT and mutant animals had similar fibre numbers, indicating the normal development of Bergmann glia in *Slc1a3*$^{P290R/+}$ mice to this age. However, between P10 and P20, a pronounced age-dependent reduction in Bergmann glia cell fibre numbers occurred in *Slc1a3*$^{P290R/+}$ cerebella (Fig. 2B). GFAP-positive Bergmann glia fibres were reduced in all cerebellar regions, while glial development remained unaffected in the hippocampus and the cerebral cortex (data not shown). The number of Bergmann glia cell soma and fibres was reduced by a similar percentage (Fig. 2C), indicating loss of Bergmann glia cells and not mere retraction of fibres in the *Slc1a3*$^{P290R/+}$ cerebellum. Whereas the Bergmann glial cells were reduced by >70% in the Purkinje layer of mutant animals, the number of glial cells only slightly increased in the molecular layer (Fig. 2C). Immunostaining of cerebellar slices and western blotting of cerebellar lysates against the Bergmann glia markers BLBP, S100β and GLAST showed decreased numbers of Bergmann glia cell somata (Supplementary Fig. 4A and B) and reduced relative protein expression of the markers (Supplementary Fig. 4C and D and Supplementary Material). These results indicate Bergmann glia cell death rather than mislocalization of glial cells to the molecular layer. In *Slc1a3*$^{-/-}$ (*Slc1a3*^{tm1Ktu}, GLAST knock-out) mice, the density of Bergmann glia cell fibres was not different from WT at P50 (Fig. 2B), demonstrating that loss of EAAT1/GLAST glutamate transporter does not result in Bergmann glia cell degeneration at this age (Watase *et al.*, 1998).

Altered cell distribution in the cerebellar cortex of *Slc1a3*$^{P290R/+}$ mice

Slc1a3$^{P290R/+}$ animals vary widely in cerebellar morphology, ranging from increased density of granule cells in the molecular layer (Fig. 2D–F and Supplementary Fig. 5A–F) to massive degeneration associated with foamy syncytial structures (Supplementary Fig. 5G and H). In contrast, adult WT cerebella are characterized by a defined layered structure with virtually no granule cells in the molecular layer. Since fibres from Bergmann glia cells

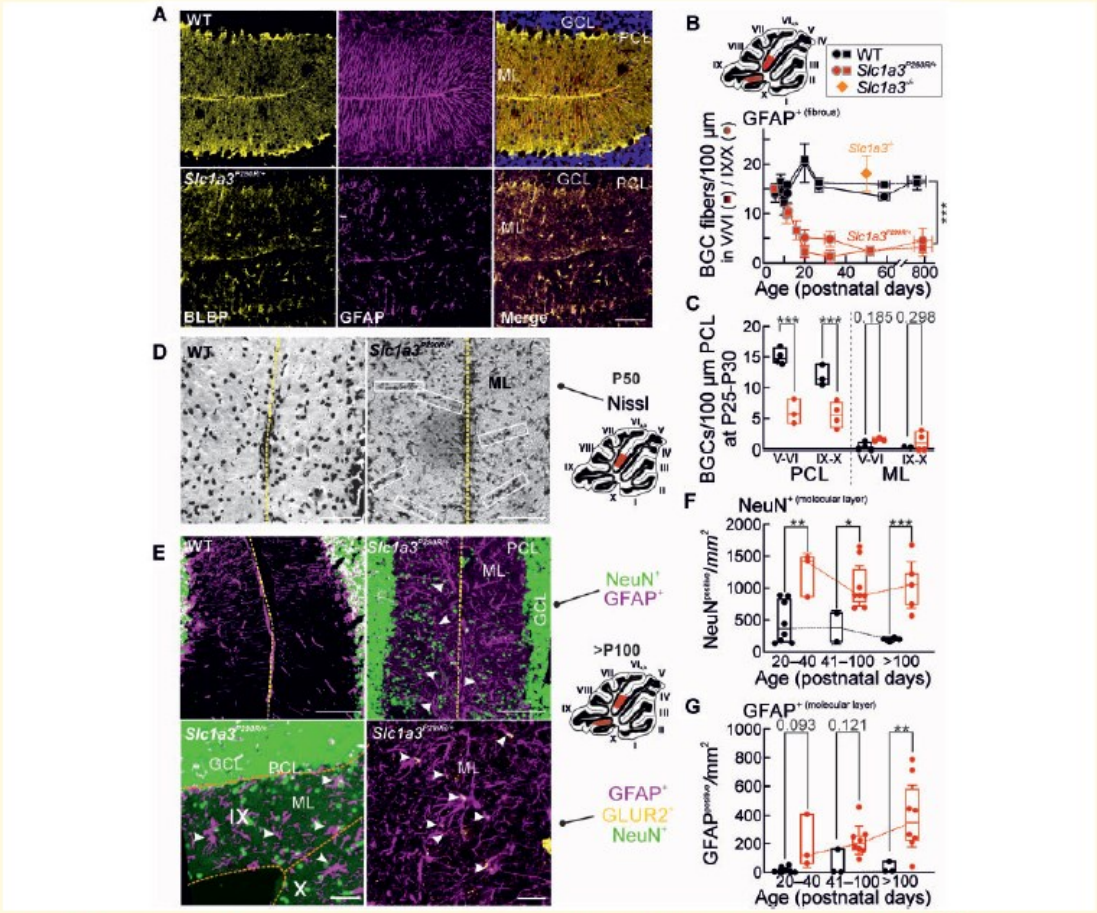

Figure 2 Degeneration of Bergmann glia cells and cellular reorganization of the cerebellar cortex in *Slc1a3*$^{P290R/+}$ mice. Representative confocal images (**A**) of paraffin-embedded cerebellar WT (*top*) or *Slc1a3*$^{P290R/+}$ (*bottom*) slices show the vermis region of lobe V/VI immunostained for BLBP (yellow) and GFAP (P20, magenta) and indicate age-dependent changes in the numbers of Bergmann glia cell fibres (**B**) in the MLs of WT (black), *Slc1a3*$^{-/-}$ (orange) or *Slc1a3*$^{P290R/+}$ (red) cerebella. The data represent mean numbers of GFAP^{positive} fibres per 100 µm PCL in individual animals ($n = 25/32$ animals, WT/Mut). Bergmann glial cell numbers were counted (**C**) in the PCL and in the ML and indicated that the median cell loss is much higher than the number of ectopic cells in the ML. Cerebellar regions stained for Nissl (**D**, P50) or stained for NeuN (**E**, >P100, green) indicate regions with anomalous enrichment of NeuN^{positive} cells (**E**, arrowheads). The white boxes depict linear arrangements of Nissl-stained nuclei within the ML of *Slc1a3*$^{P290R/+}$ mice (**D**). The whisker-box plots (**F** and **G**) show increased density of NeuN^{positive} cells (F, $n = 14/16$ animals, WT/Mut) and increased density of GFAP^{positive} cells (G, $n = 14/19$ animals, WT/Mut) in mutant lobes V/VI. Astrocytes mislocalize to the ML in mutant cerebella; confocal images of the nodular region (**E**, *bottom*) of an *Slc1a3*$^{P290R/+}$ animal (>P100) immunostained for GFAP (magenta) and NeuN (green) indicate multipolar astrocytes in the ML from mutant animals (**E**, *bottom*, left). Colocalization (white) of GLUR2 (yellow) with GFAP (magenta) in the ML (**E**, *bottom*, right) of an *Slc1a3*$^{P290R/+}$ mouse shows that GFAP^{positive} multipolar astrocytes do not emerge from the Bergmann glia cell pool (see also Supplementary Fig. 6). The density of GFAP^{positive} multipolar cells in the MLs increases over time in *Slc1a3*$^{P290R/+}$ mice but not in WT mice. Scale bars: 100 µm (**A**), 50 µm (**D**) and 50/25 µm (**E**, *top*/*bottom*). Numbers of Bergmann glia fibres over time (**B**) are shown as means ± SEM of individual animals, and genotype-specific differences over time were analysed with two-way ANOVA and Holm–Sidak *post hoc* testing. Data in **C**, **F** and **G** are shown as whisker-box plots (whisker: ± CI, box: 25th to 75th percentiles with each data point representing the values obtained from one individual animal; two-way ANOVA and Holm–Sidak *post hoc* tests); *$P \leq 0.05$, **$P \leq 0.01$ and ***$P \leq 0.001$; all *P*-values for this figure are provided in Supplementary Table 3. GCL, granule cell layer; ML, molecular layer; PCL, Purkinje cell layer.

and from their progenitors serve as migration pathways for cerebellar granule cells in the developing cerebellum (Rakic, 1971; Hatten *et al.*, 1984), changes in Bergmann glia function might result in the mislocalization of granule cells. In mutant cerebella without severe degeneration, we regularly observed mislocalized cells that are recognized by antibodies against NeuN, a specific nuclear marker for cerebellar granule cells (Mullen *et al.*, 1992; Weyer and Schilling, 2003) (Fig. 2D and E). We conclude that mutant EAAT1/GLAST expression impairs granule cell migration to the internal granule cell layer during development.

We also observed multipolar astrocytes in the molecular layer of *Slc1a3*$^{P290R/+}$ cerebella, which did not only differ from Bergmann glia cells in localization of their cell somas but also in morphology (Fig. 2E and G). We co-stained slices with antibodies against glutamate receptors 1 and 2 (GLUR1, GLUR2) and GFAP (Fig. 2E and Supplementary Fig. 6A), since GLUR2 is expressed in astrocytes, but not in Bergmann glia cells (Keinanen *et al.*, 1990; Iino *et al.*, 2001; Droste *et al.*, 2017). Colocalization of GLUR2 and GFAP antibodies indicates that most of the ectopic glial cells were astrocytes rather than transformed Bergmann glia cells. We performed additionally immunostaining against glial proteins BLBP and S100β that distinguishes radial glia—expressing BLBP and S100β—and astrocytes—expressing S100β alone (Supplementary Fig. 6B) and provides additional evidence for the invasion of reactive astrocytes into the molecular layer. Invasion of reactive astrocytes is a typical repair mechanism of the central nervous system (Sofroniew, 2005; Anderson *et al.*, 2014).

P290R expression alters the morphology and number of Purkinje neuron synapses in the cerebellum

Purkinje neurons form glutamatergic synapses with parallel fibres or climbing fibres (CFs), and Bergmann glia cells not only provide a scaffold for the outgrowth of Purkinje neuron dendritic trees but also ensheath newly developing synapses (Palay and Chan-Palay, 1974; Grosche *et al.*, 1999; Yamada *et al.*, 2000; Lordkipanidze and Dunaevsky, 2005). Ultrastructural analyses illustrate that most of these synapses are almost completely surrounded by Bergmann glia cell processes in WT animals. This close wrapping of Purkinje neuron synapses by Bergmann glia cells could not be observed in the molecular layer of *Slc1a3*$^{P290R/+}$ animals (Supplementary Fig. 7).

During development the number of CFs in contact with a certain Purkinje neuron is reduced to one, and these changes are associated with the formation of parallel fibre synapses (Woodward *et al.*, 1974; Crepel, 1982; Mariani, 1982). To test for developmental changes in mutant animals, we quantified glutamatergic and GABAergic synapses in mutant animals by immunostaining parallel fibre synapses with anti-VGLUT1, CF synapses with anti-VGLUT2 (Miyazaki *et al.*, 2003) or anti-GAD65/67 antibodies, which label GABAergic synapses (Fig. 3 and Supplementary Material) in animals between P30 and P65. All tested cerebellar regions of mutant animals had an increased density of VGLUT1-positive clusters of presynaptic boutons (Fig. 3A and B), while VGLUT2-positive clusters are reduced in all tested cerebellar regions of mutant animals (Fig. 3A and C). The density of GAD65/67-positive synapses was slightly reduced in the region between lobules V and VI of mutant animals, whereas nodular regions had similar GAD65/67-positive cluster densities in both WT and mutant animals (Fig. 3A and D). Taken together, these findings demonstrate that expression of P290R modifies synaptic morphology and connections in the cerebellum.

Increased P290R anion current is associated with glia cell apoptosis

P290R enhances EAAT1 anion currents in heterologous expression systems (Winter *et al.*, 2012), so that *Slc1a3*$^{P290R/+}$ Bergmann glia cells are expected to exhibit increased EAAT1/GLAST anion currents. We measured glutamate-elicited Cl^- currents using whole-cell patch clamping of Bergmann glia cells from acute brain slices of mice between P9 and P14 by applying brief pulses (200 ms) of glutamate (1 mM) at a holding potential near to their reversal potential (−80 mV). In these experiments, the pipette solution contained 145 mM KCl, 1 mM $MgCl_2$ and 10 mM HEPES/KOH (pH 7.2). Bergmann glial cells were visually identified and distinguished from multipolar astrocytes—that are present in *Slc1a3*$^{P290R/+}$ molecular layers (Fig. 2E and G and Supplementary Fig. 6)—based on their size and location in proximity to Purkinje neurons. In a few cases, we inadvertently established the whole-cell configuration with neuronal cells, which could be easily distinguished from glial cells by their firing activity and discarded. Glutamate application elicited inward currents that were significantly increased in Bergmann glia cells from *Slc1a3*$^{P290R/+}$ mice (Fig. 4A, 60.7 ± 26.2/120.3 ± 63.2 pA, ±CI, $n = 3/6$ animals, WT/Mut, $P = 0.024$). Since P290R modifies the voltage dependence of EAAT1 anion currents and causes prominent activation by hyperpolarization (Winter *et al.*, 2012), we also compared glutamate-elicited currents of WT and *Slc1a3*$^{P290R/+}$ Bergmann glia cells at −100 and −120 mV with their respective currents at −80 mV. Hyperpolarization caused only minor current increases in WT Bergmann glia cells but significantly enhanced glutamate-elicited currents in *Slc1a3*$^{P290R/+}$ Bergmann glia cells (Fig. 4B and C).

Since EAAT1/GLAST anion channels are major determinants of the internal Cl^- concentration ($[Cl^-]_{int}$) in Bergmann glia cells (Untiet *et al.*, 2017), it was

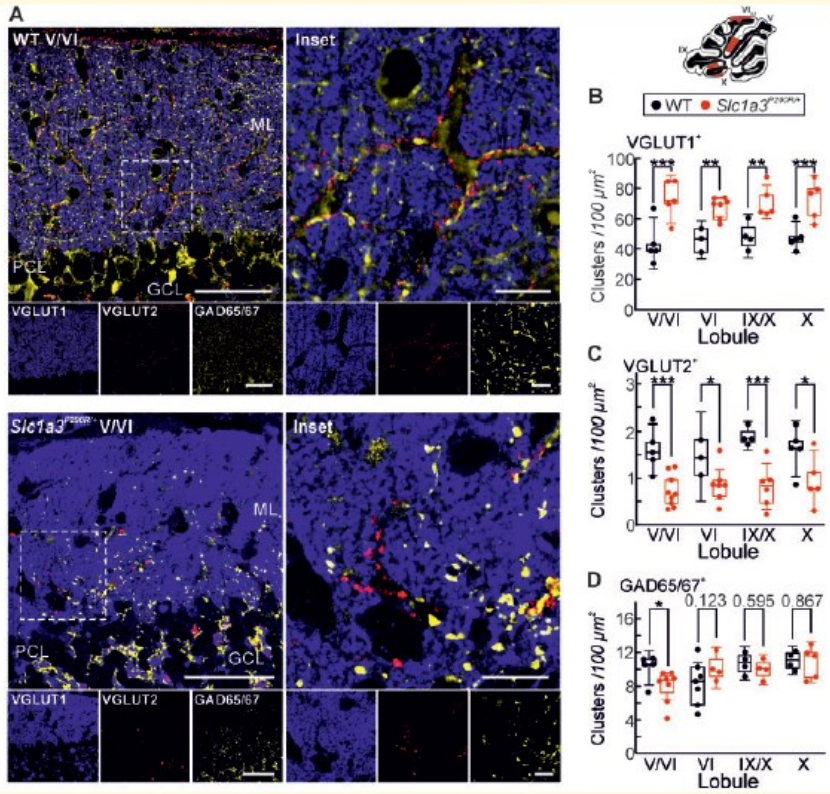

Figure 3 Altered synapse densities in *Slc1a3*$^{P290R/+}$ cerebella. Representative confocal images of WT and *Slc1a3*$^{P290R/+}$ cerebellar MLs (**A**) immunostained for the vesicular glutamate transporters VGLUT1 (blue, parallel fibres) and VGLUT2 (red, CFs) or for glutamate decarboxylase isoforms 65 and 67 (GAD65/67, yellow). Image **A** shows overviews and magnified insets. Median densities of glutamatergic VGLUT1^{positive} (**B**) and glutamatergic VGLUT2^{positive} (**C**) clusters of synaptic boutons are different in WT and mutant animals, whereas the densities of GABAergic clusters (**D**) are similar [$n = 3$–5/5–7 in **B**; $n = 3$–5/5–9 animals in **C**; $n = 4$–7/4–8 animals in **D** (WT/Mut)]. Scale bars (**A**): overviews, 50 µm; insets, 10 µm. Data in **B**–**D** are shown as whisker-box plots with medians (whisker: ±CI, box: 25th to 75th percentiles with each data point representing the mean density from an individual animal; two-way ANOVA and Holm–Sidak *post hoc* test); $^{*}P \leq 0.05$, $^{**}P \leq 0.01$ and $^{***}P \leq 0.001$; all *P*-values for this figure are provided in Supplementary Table 3. GCL, granule cell layer; ML, molecular layer; PCL, Purkinje cell layer.

mandatory to test how increased EAAT1/GLAST anion currents affect $[Cl^-]_{int}$ in *Slc1a3*$^{P290R/+}$ Bergmann glia cells. We performed fluorescence lifetime imaging microscopy using the Cl^--sensitive dye MQAE in acute cerebellar slices (Untiet *et al.*, 2017) between P4 and P14 (Materials and methods, Fig. 4D–F). $[Cl^-]_{int}$ was lower in *Slc1a3*$^{P290R/+}$ mice than in WT, and incubation of *Slc1a3*$^{P290R/+}$ slices with the EAAT1/GLAST blocker 2-amino-5,6,7,8-tetrahydro-4-(4-methoxyphenyl)-7-(naphthalen-1-yl)-5-oxo-4*H*-chromene-3-carbonitrile (10 µM) increased the $[Cl^-]_{int}$ to values close to those of WT (Fig. 4F). In Bergmann glia cells, $[Cl^-]_{int}$ is in a dynamic equilibrium between Cl^- accumulation via NKCC transporters and Cl^- efflux through EAAT anion channels (Untiet *et al.*, 2017). Changes in numbers or transport rates of each protein shift the equilibrium and modify $[Cl^-]_{int}$. Reduced $[Cl^-]_{int}$ thus provides additional evidence for increased Cl^- efflux in *Slc1a3*$^{P290R/+}$ Bergmann glia cells.

We observed small difference in $[Cl^-]_{int}$ between WT and mutant mice also in the first postnatal week, i.e. before onset of glutamatergic innervation. EAAT1/GLAST is expressed at these ages (Schreiner *et al.*, 2014), and EAAT anion channels are not exclusively activated by external glutamate but also assume a basal activity under glutamate-free conditions or with internal glutamate (Fahlke *et al.*, 2016). Increased activity of P290R EAAT1/GLAST anion channels thus fully accounts for altered $[Cl^-]_{int}$ also at ages below P7.

$[Cl^-]_{int}$ was smaller in *Slc1a3*$^{P290R/+}$ than in WT Bergmann glia cells but still larger than expected for passive distribution. Thus, activation of EAAT1/GLAST and

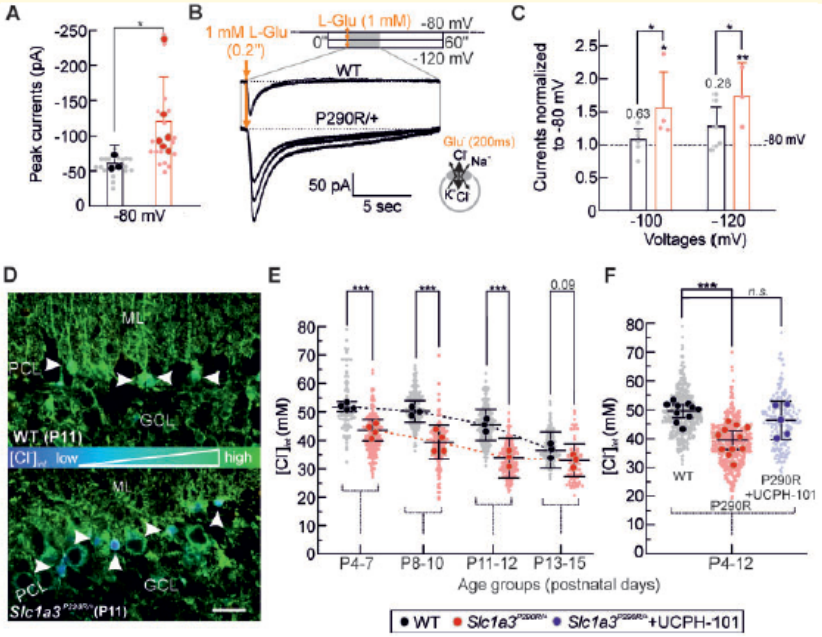

Figure 4 Enhanced EAAT1/GLAST chloride currents in *Slc1a3*$^{P290R/+}$ Bergmann glia cells. Bar graph **A** depicts pooled mean peak whole-cell current responses of Bergmann glia (−80 mV) to brief pulses (200 ms) of 1 mM L-Glu from experiments with acute cerebellar brain slices (± CI, $n = 3/6$ animals, big circles, WT/Mut). Individual tested cells are shown as shaded small circles. In **B**, representative glutamate-induced Bergmann glia cell whole-cell currents are shown for three different holding potentials for WT and mutant cells. A bar graph **C** summarizes Bergmann glia peak current responses of individual WT and *Slc1a3*$^{P290R/+}$ cells for the voltages −100 and −120 mV, normalized to their respective currents at −80 mV (± CI, $n = 6/3–4$ cells, WT/Mut). Representative FLIM recordings of cerebellar cortices (**D**) from WT and *Slc1a3*$^{P290R/+}$ mice at P11 reveal decreased $[Cl^-]_{int}$ in mutant Bergmann glia cells (arrows). $[Cl^-]_{int}$ is colour-coded according to the colour bar between images (scale bar: 25 µm). Point plots (**E**) depict mean $[Cl^-]_{int}$ during the first and second weeks of development for individual animals (big circles). $[Cl^-]_{int}$ of Bergmann glial cells was measured in WT and in *Slc1a3*$^{P290R/+}$ slices. Figure **F** summarizes data from the period with genotype-specific differences in the absence and in the presence of the EAAT1/GLAST-specific antagonist UCPH-101 (Abrahamsen *et al.*, 2013). In **A** and **C**, data points are means ± CI from individual animals (**A**, Mann–Whitney *U*-test) or cells (**C**, two-way ANOVA with repeated measures and Holm–Sidak *post hoc* tests). Data in **E** and **F** are presented and statistically analysed as means ± CI of individual animals [big circles, two-way ANOVA with Holm–Sidak *post hoc* test (**E**); Kruskal–Wallis ANOVA on ranks with Dunn's *post hoc* test vs WT control (**F**)]. Distribution of measured individual cells is depicted in the background (**A**, **E** and **F**, small circles); $^*P \leq 0.05$, $^{**}P \leq 0.01$ and $^{***}P \leq 0.001$; all *P*-values for this figure are provided in Supplementary Table 3. GCL, granule cell layer; ML, molecular layer; PCL, Purkinje cell layer.

EAAT2/GLT-1 anion channels at the onset of glutamatergic synaptic transmission during the second postnatal week (Watanabe and Kano, 2011) results in Cl^- efflux from Bergmann glia cells in both *Slc1a3*$^{P290R/+}$ and WT animals. These currents are larger in *Slc1a3*$^{P290R/+}$ as in WT animals and might cause cell shrinking and apoptosis of mutant Bergmann glia cells (Porcelli *et al.*, 2004; Ernest *et al.*, 2008). We crossed reporter mice with GFAP–EGFP with *Slc1a3*$^{P290R/+}$ animals, stained cerebellar tissue from P9–P15 with antibodies for active caspase-3 (CASP3) and identified apoptotic glial cells by the colocalization of EGFP and CASP3 (Fig. 5A and B). Figure 5B shows the numbers of apoptotic cells from WT and *Slc1a3*$^{P290R/+}$ brain slices during postnatal development, demonstrating significantly increased levels of apoptotic events in mutant cerebella (Fig. 5B, left) and significantly more apoptotic Bergmann glial cells (Fig. 5B, right) between P10 and P13 in the animal model. Since CASP3 activation was also reported during normal development (Oomman *et al.*, 2005), we additionally tested the apoptosis marker TUNEL in GFAP–EGFP-expressing mice of both genotypes (Gavrieli *et al.*, 1992). We observed substantially more TUNEL signals in mutant than in WT cerebella (Fig. 5C). In mutant animals, TUNEL colocalizes with the nuclei of cells expressing GFAP–EGFP in the Purkinje cell layer, indicating glia apoptosis (Fig. 5D and E). The number of apoptotic Bergmann glia cells detected by TUNEL/GFAP–EGFP colocalization was comparable to the CASP3 assay between P10 and P13 (CASP3: 10.2 ± 2.9, TUNEL: 20.2 ± 15.1, means ± CI, $n = 15/7$ mutant animals, CASP3/TUNEL). We also observed increased numbers of TUNEL and of CASP3 signals that did not colocalize with

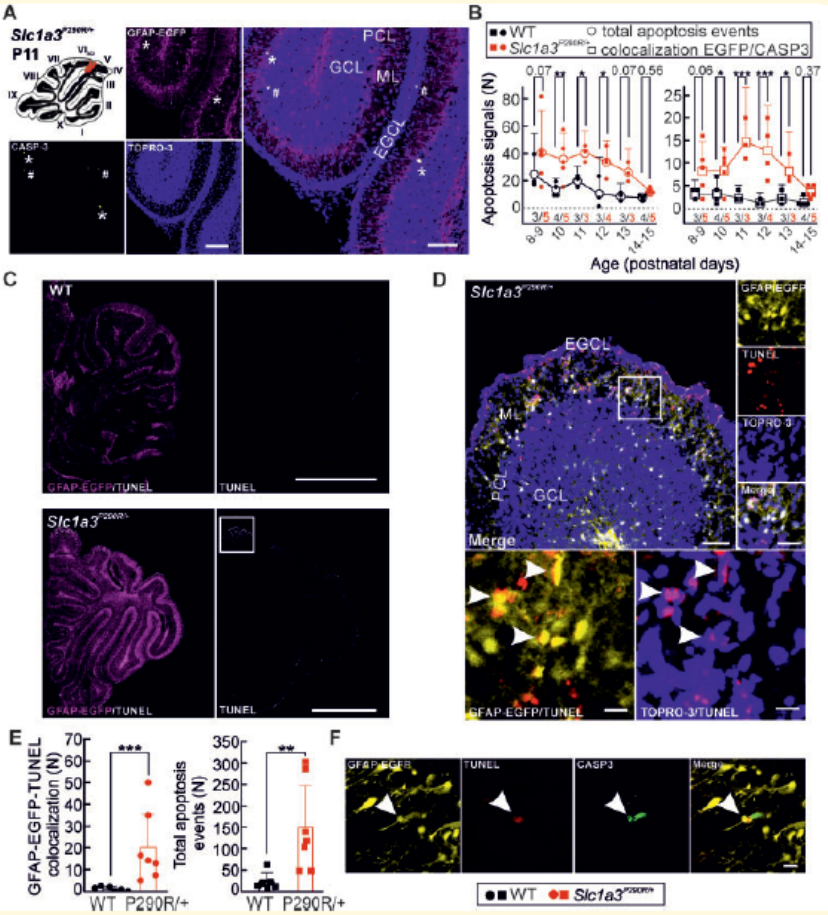

Figure 5 *Slc1a3*$^{P290R/+}$ Bergmann glia cell loss is caused by apoptosis during the second postnatal week. Apoptosis of Bergmann glia cells visualized by confocal imaging (**A**) of an *Slc1a3*$^{P290R/+}$ cerebellar cortex immunostained for GFAP and CASP3 (scale bars: 50 µm) with colocalization of CASP3/GFAP–EGFP (asterisks) and CASP3 (hash) signals in a transgenic mouse. Point plots of mean numbers of total CASP3^{positive} cells and CASP3^{positive} Bergmann glia of individual animals over time (**B**) demonstrate increased numbers of apoptotic Bergmann glia cells in *Slc1a3*$^{P290R/+}$ animals during the second postnatal week. Confocal images from whole sagittal cerebellar slices stained for fragmented DNA (**C**, EGFP/TUNEL) and magnified views from region of interest (**D**) of mutant cerebellum as indicated in **C**. Merged views of EGFP/TUNEL and of TOPRO-3/TUNEL show the overlap of GFAP–EGFP and TUNEL signals, and the localization of TUNEL signals in the nuclei (**C**, arrowheads). Bar graphs in **B** show the mean numbers (±CI) of apoptotic signals (left) and the mean numbers of EGFP/CASP3 colocalized signals (right) per individual animal ($n = 3$–5 animals per genotype and age group, two-way ANOVA with Holm–Sidak *post hoc* test). Bar graphs in **E** show the mean total numbers of TUNEL signals for individual animals ($n = 6/7$, WT/Mut, left) and the mean numbers (±CI) of GFAP–EGFP/TUNEL colocalized signals for the same animals (right). Statistical analyses were done with Kruskal–Wallis ANOVA on ranks and Dunn's *post hoc* test for colocalized signals (left) and total apoptosis events (right), separately. Confocal image (**F**) shows the colocalization of EGFP/TUNEL/CASP3. Scale bars: 100 µm (**A**), 1 mm (**C**); 100, 25 and 10 µm (**D**); and 10 µm (**F**); *$P \leq 0.05$, **$P \leq 0.01$ and ***$P \leq 0.001$; all *P*-values for this figure are provided in Supplementary Table 3. EGCL, external granule cell layer, GCL, granule cell layer, ML, molecular layer, PCL, Purkinje cell layer.

GFAP (Fig. 5A and B–E, CASP3: 33.6 ± 6.2, TUNEL: 149.4 ± 96.8, means ± CI, $n = 15/7$ mutant animals, CASP3/TUNEL). These signals might be due to earlier apoptosis events of Bergmann glial cells or due to apoptosis of other cell types, such as migrating granule cells in the external granule cell layer.

Abnormal spiking properties of *Slc1a3*$^{P290R/+}$ Purkinje neurons

Cerebellar Purkinje neurons represent the only neuronal output of the cerebellar cortex (Marr, 1969). In the absence of synaptic input, they fire action potentials with

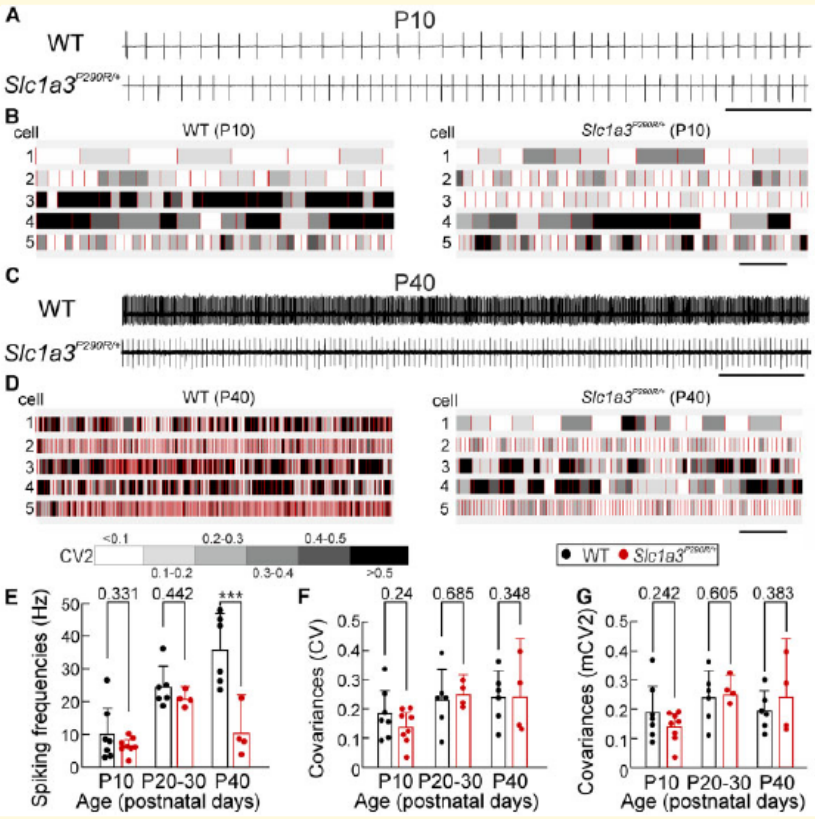

Figure 6 ***Slc1a3*$^{P290R/+}$ Purkinje neurons display abnormal spiking properties.** Current traces obtained from cell-attached patch clamp recordings (**A** and **C**) show patterns of spontaneous firing from individual Purkinje neurons in acute slices from juvenile (**A**, P10) or adult (**C**, P40) WT or *Slc1a3*$^{P290R/+}$ mice. Burst plots (**B** and **D**) of representative Purkinje neuron spike trains for juvenile (**B**) or adult (**D**) WT or *Slc1a3*$^{P290R/+}$ mice. Spikes are shown as red bars and interspike intervals in grey scale according to the temporary covariance (CV2). Purkinje neuron mean simple spike frequencies (**E**) differ between P40 WT and mutant animals, whereas mean absolute CVs (**F**) and mean CVs of interspike intervals (**G**) are similar in WT and mutant animals. Pooled data are shown as bars with means ± CI, with **E**–**G** representing mean values from the same animals (P10, $n = 7/8$; P20–30, $n = 6/4$; P40, $n = 6/4$ animals, WT/Mut, two-way ANOVA with Holm–Sidak *post hoc* tests; $^{***}P \leq 0.001$); all *P*-values for this figure are provided in Supplementary Table 3.

precisely regulated interspike intervals (Bell and Grimm, 1969; Arancillo *et al.*, 2015) and changes in the frequency and in the temporal precision of interspike intervals are known to impair motor coordination (Hoebeek *et al.*, 2005; Walter *et al.*, 2006; Alvina and Khodakhah, 2010; Jayabal *et al.*, 2017). We measured spontaneous simple spiking activity with cell-attached patch clamp recordings (Donato *et al.*, 2006) in vermal regions in lobes V/VI, VI–VIII and VIII/IX of acute WT and mutant cerebellar slices. Representative recordings from WT and *Slc1a3*$^{P290R/+}$ mice at P10 (Fig. 6A) and P40 (Fig. 6C) demonstrate typical biphasic spikes, corresponding to inward and outward currents during action potentials (Womack and Khodakhah, 2002). In Purkinje neurons from WT animals, the spontaneous spiking frequency increases during development from 10.1 ± 7.9 Hz at P10 to 35.8 ± 11.8 Hz at P40 (±CI, $n = 7/6$ animals). In *Slc1a3*$^{P290R/+}$ animals, the developmental acceleration was less pronounced, resulting in significantly slower firing in mutant Purkinje neurons at P40 (10.4 ± 11.9 Hz, ±CI, $n = 4$ animals) (Fig. 6E).

To compare the temporal precision of simple spiking activities, we calculated ISI covariances (CV) and intrinsic variabilities (CV2) for WT and mutant Purkinje neurons (Holt *et al.*, 1996). For all tested ages, CV and CV2 were not different between WT and mutant Purkinje neurons (Fig. 6F and G). The CV values observed in *Slc1a3*$^{P290R/+}$ animals were in good agreement with other reports studying acute slices at similar temperatures (Wulff *et al.*, 2009; Jayabal *et al.*, 2017). Smaller CV values (<0.1) were only reported in acute slices from older mice (Jayabal *et al.*, 2016) or in studies at physiological

temperatures (Hansen *et al.*, 2013). We conclude that the developmental acceleration of simple spike frequencies (McKay and Turner, 2005) is absent in *Slc1a3*$^{P290R/+}$, probably due to progressive glia and neuron degeneration.

Loss of Bergmann glia modifies climbing fibre regulation of Purkinje neuron activity in *Slc1a3*$^{P290R/+}$ mice

Bergmann glial processes ensheath glutamatergic synapses between CFs and Purkinje neurons (Supplementary Fig. 7), and glutamate uptake into Bergmann glial processes helps reducing glutamate spill-over from the synaptic cleft after the simultaneous release of multiple synaptic vesicles (Wadiche and Jahr, 2001). The CF–Purkinje neuron synapse thus represents a system well suited to study the functional consequences of EAAT1/GLAST dysfunction and Bergmann glia degeneration on glutamatergic synaptic transmission in the cerebellum.

CF activity typically interrupts simple spike activity for periods up to several hundred milliseconds, the so-called CF pauses (Eccles *et al.*, 1966; Bell and Grimm, 1969; Latham and Paul, 1971; Sato *et al.*, 1992). These pauses play a role in signal transmission to the deep cerebellar nuclei during learning processes (Otis *et al.*, 2012). We measured the lengths of these pauses in WT and *Slc1a3*$^{P290R/+}$ Purkinje neurons after pulses with supersaturating glutamate concentrations at ages below P30. At these ages, simple spike activity was similar for WT and mutant Purkinje neurons (Fig. 6E). Figure 7A depicts representative responses from WT and mutant Purkinje neurons to glutamate application, and in Fig. 7B, aligned simple spike events were plotted vs time with corresponding histograms of aligned events binned at 100 ms, before and after the glutamate puff. In WT Purkinje neurons, the glutamate application evokes a short period of augmented spike firing, followed by a short depressed phase as described earlier (Tang *et al.*, 2017). While the baseline simple spike activities are recovered within several seconds after the pulse in WT Purkinje neurons (1.2 ± 0.7 s) in most cases, silent periods were significantly longer in *Slc1a3*$^{P290R/+}$ Purkinje neurons (39.2 ± 57.2 s, ±CI, $n = 10/3$ animals, $P = 0.011$, Fig. 7C). We conclude that glutamate uptake is severely reduced in *Slc1a3*$^{P290R/+}$ mice and results in altered synaptic transmission between CFs and Purkinje neurons.

Cerebellar degeneration in *Slc1a3*$^{P290R/+}$ mice

We reasoned that the absence of Bergmann glia cells might result in cerebellar atrophy and compared the sizes of WT and *Slc1a3*$^{P290R/+}$ cerebella in old mice (i.e. >P180). Quantification of cerebellar transversal areas revealed smaller values in all tested *Slc1a3*$^{P290R/+}$ than in corresponding WT animals (Fig. 8A), due to a reduction in all cerebellar regions (Fig. 8B). We observed similar alterations in mutant female and male mice ($n = 5/5$ animals, Mut$^{♂}$/Mut$^{♀}$, $P = 0.55$) and thus pooled results from both sexes in subsequent analyses. The mean size was reduced by $37 \pm 13\%$ ($\pm\sigma$, $n = 10/10$ animals, WT/Mut) in *Slc1a3*$^{P290R/+}$, and 6 out of 10 cerebella were reduced by >35% in transversal sizes. Nissl staining of slices from whole vermis regions of mutant mice shows fewer cerebellar lobes and a smaller total sagittal plane, with smaller granule cell layers and molecular layer areas (Fig. 8C and D). There was no obvious size reduction in white matter area of *Slc1a3*$^{P290R/+}$ slices ($n = 4/4$ animals, WT/Mut, Fig. 8D). We additionally compared the number of Purkinje cells and the thickness of molecular layers from younger WT and mutant animals (P27–60) from lobes VI and X. There was no difference in molecular layer thickness between genotypes ($P = 0.391$). The number of Purkinje cells was significantly reduced in the external region of mutant lobes VI ($4.4 \pm 0.5/3.7 \pm 1.3$ Purkinje neurons/100 µm, ±CI, $n = 8/11$, WT/Mut, $P = 0.003$), but not in the other tested regions (Supplementary Fig. 8). We conclude that loss of Bergmann glia cells leads to generalized cerebellar degeneration in *Slc1a3*$^{P290R/+}$ mice, likely because Bergmann glial apoptosis impairs glutamate removal and causes excitotoxic Purkinje neuron death.

Discussion

EA type 6 is an inherited condition characterized by impaired motor coordination with epilepsy and migraine-like headache. Thus far, all reported cases have been associated with mutations in *SLC1A3* (Jen *et al.*, 2005; de Vries *et al.*, 2009; Pyle *et al.*, 2015; Choi *et al.*, 2017*a*, *b*; Iwama *et al.*, 2018), but how these mutations cause the specific clinical phenotype of EA is still insufficiently understood. To answer this question, we used a knock-in mouse model expressing EAAT1/GLAST carrying a mutation recently described in a human patient (Jen *et al.*, 2005). *Slc1a3*$^{P290R/+}$ mice suffer from epileptic attacks, ataxia and cerebellar atrophy and thus exhibit similar neurological symptoms as the patient with the same mutation. Disease-associated *SLC1A3* mutations were initially assumed to modify glutamate transport rates and to affect synaptic transmission via decreased glutamate uptake. However, comparison of the neurological symptoms of *Slc1a3*$^{P290R/+}$ and the corresponding knock-out animal *Slc1a3*$^{-/-}$—that lacks completely EAAT1/GLAST-mediated glutamate uptake and only suffers from moderate impairment of motor coordination (Watase *et al.*, 1998; Perkins *et al.*, 2016)—argues against this assumption. We here demonstrate that the expression of P290R EAAT1 reduces glutamate uptake by a different mechanism: gain-of-function of EAAT1/GLAST Cl^- currents significantly impairs

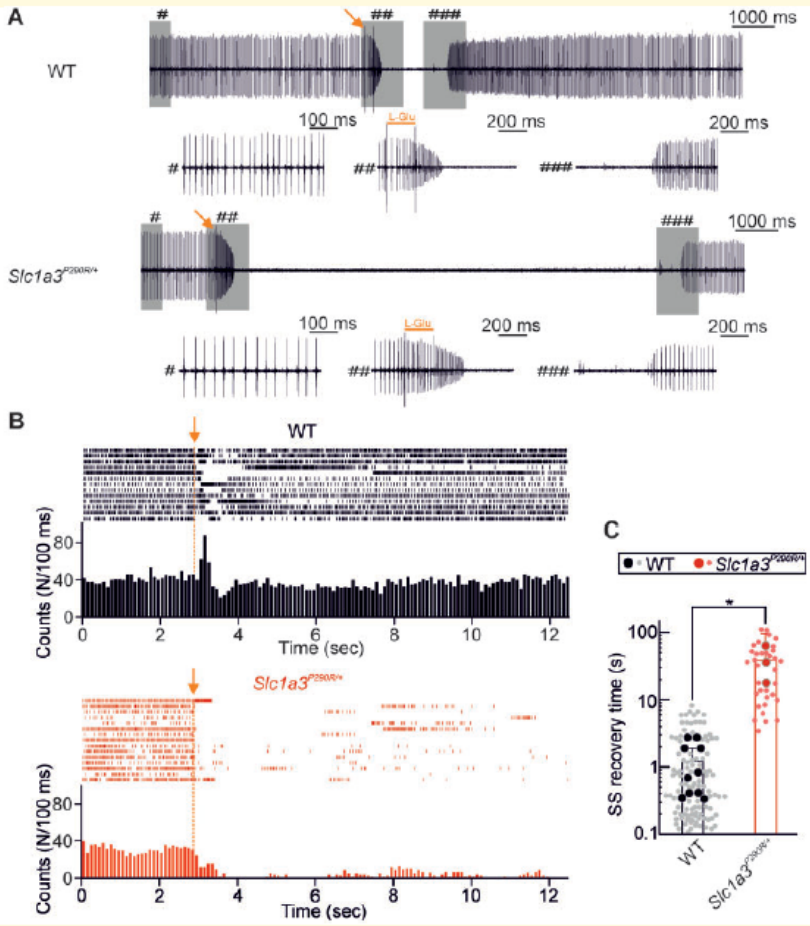

Figure 7 Increased CF pause durations in *Slc1a3*$^{P290R/+}$ Purkinje neurons. Current traces from cell-attached patch clamp recordings of Purkinje neuron somata (**A**) show representative simple spike activities of WT and *Slc1a3*$^{P290R/+}$ Purkinje neurons before and after glutamate puff application (arrow). Pooled burst plots with corresponding histograms (**B**) from individual responses of WT and *Slc1a3*$^{P290R/+}$ Purkinje neurons show substantial prolonged recovery periods (**C**) for Purkinje neurons from *Slc1a3*$^{P290R/+}$ mice. Burst plots (**B**) are constructed from glutamate puff responses of $n = 7/3$ Purkinje neurons (WT/Mut), and histograms are binned at 100 ms. Bar plot (**C**) shows recovery times as means ± CI from mean pause lengths values observed in $n = 10/3$ individual animals (WT/Mut, big circles, Mann–Whitney *U*-test) and pooled glutamate responses from all tested cells (small circles). Lengths of scale bars are indicated in **A**; *$P \leq 0.05$; *P*-value for this figure is provided in Supplementary Table 3.

cerebellar glutamate homeostasis by causing Bergmann glia degeneration.

P290R causes gain-of-function of *h*EAAT1 anion channel activity in heterologous expression systems (Winter *et al.*, 2012), and we found significantly increased glutamate-induced anion currents in *Slc1a3*$^{P290R/+}$ Bergmann glia cells. Although Bergmann glia $[Cl^-]_{int}$ was slightly lower in mutant than in WT, these values were significantly larger than expected for passive distributions (Fig. 4). Increased P290R EAAT1/GLAST anion channel activity will thus result in enhanced Cl^- efflux and excessive cell shrinkage in *Slc1a3*$^{P290R/+}$ Bergmann glia cells upon establishment of glutamatergic synaptic signalling in the second postnatal week. Cl^- loss and cell shrinkage can trigger apoptosis (Walev *et al.*, 1995; Friis *et al.*, 2005), and EAAT1/GLAST anion channel gain-of-function can thus account for glial apoptosis in *Slc1a3*$^{P290R/+}$ at ages between P9 and P14 (Figs 4 and 5). We were not able to show cell shrinkage in mutant animals directly, most likely since cell shrinkage leads to apoptosis in a fast and irreversible manner. EAAT1/GLAST is highly expressed in glial cells in the cerebellum,

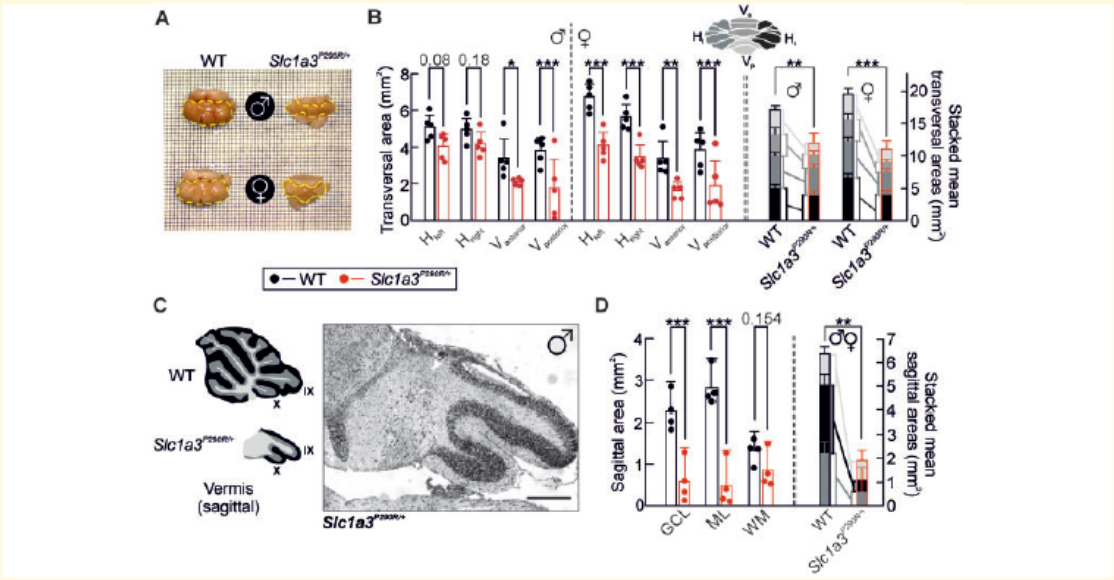

Figure 8 Cerebellar degeneration in old *Slc1a3*$^{P290R/+}$ mice. Overall views of fixed brains (**A**) from adult WT or *Slc1a3*$^{P290R/+}$ mice (>P180) of both sexes on a grid surface (grid size: 0.25 mm^2) show degeneration of cerebella from transgenic animals. Bar graphs (**B**) show details of size decreases by comparing different cerebellar areas for male and female animals, and stacked bars with summed areas of WT and *Slc1a3*$^{P290R/+}$ cerebella show overall cerebellar size decreases for both sexes. Sagittal views of Nissl-stained vermis region (**C**) from a male 2.5-year-old (P921) *Slc1a3*$^{P290R/+}$ mouse. Insets demonstrate the orientation of the slice and the vermis layer structures for WT and *Slc1a3*$^{P290R/+}$ mice. Quantification of mean sagittal size distributions (**D**) of vermal cerebellar layers in elderly WT and mutant mice (~P600–P950) of both sexes shows that ML and granule cell layer denote substantial mass decreases, but not WM, and stacked bars with summed areas of WT and *Slc1a3*$^{P290R/+}$ cerebella show overall sagittal cerebellar size decreases. Bar graphs in **B** and **D** denote mean area sizes ±CI and in stacked bars; sizes are presented as means ± SEM. Each mean was calculated from $n = 5^{♂}5^{♀}/5^{♂}5^{♀}$ (**B**) and $n = 4/4$ (**D**) animals (WT/Mut). Data of both sexes were separately analysed with two-way ANOVA and Holm–Sidak *post hoc* tests. Colour coding of cerebellar areas/layers is indicated in the insets in **C** and **D**. Scale bar: 250 µm (**C**); $^*P \leq 0.05$, $^{**}P \leq 0.01$ and $^{***}P \leq 0.001$; all *P*-values for this figure are provided in Supplementary Table 3. H, hemisphere; V, vermis; GCL, granule cell layer; ML, molecular layer; WM, white matter.

so Bergmann glia cell apoptosis is likely to be the first stage of cerebellar degeneration (Figs 2 and 5).

We observed Bergmann glial apoptosis with two markers, TUNEL and CASP3 (Fig. 5). Recent reports (Oomman *et al.*, 2004; Oomman *et al.*, 2005) described a constitutive expression of CASP3 in a large percentage of rat Bergmann glial cells, whereas other apoptosis markers as TUNEL or Annexin V were absent. We could only detect CASP3 expression in apoptotic cells in mutant animals, but not in WT Bergmann glial cells, suggesting species-specific roles of CASP3 in mouse and rat.

Spontaneous spiking of Purkinje neurons is controlled by feed-forward inhibition by interneurons (Marr, 1969; Midtgaard, 1992; Hausser and Clark, 1997; Wulff *et al.*, 2009) and thus represents a marker for the integrity of the cerebellar network. Although Purkinje neuron activity was comparable in young WT and mutant animals, degenerative processes result in lower frequency spiking in adult *Slc1a3*$^{P290R/+}$ mice (Fig. 6). Similar changes in Purkinje neuron activity were observed in another ataxia animal model, the ataxin 2 (*Atxn2*) mouse carrying a mutation of ataxin 2 [ATXN2^{Q127}: Tg(Pcp2-ATXN2*127Q)#Plt/0] found in patients with spinocerebellar ataxia type 2. These animals exhibited cerebellar degeneration and decreased Purkinje neuron firing rates, with no major difference in firing precision (Hansen *et al.*, 2013).

Purkinje neurons receive glutamatergic inputs from olivary CFs, with synaptic activity usually followed by a period without spontaneous spiking (Eccles *et al.*, 1966; Bell and Grimm, 1969; Latham and Paul, 1971; Sato *et al.*, 1992), the so-called CF pause. The prominent Bergmann glia degeneration in *Slc1a3*$^{P290R/+}$ causes a significant reduction in glutamate uptake in these animals that results in increased CF pause durations in Purkinje neurons of these mice (Fig. 7). Changes in CF pause durations are a common finding in mouse models for ataxia and hemiplegic migraine, for example in a migraine mouse model carrying a mutation in *Cacna1a* (Gao *et al.*, 2012) or in ataxic mice lacking BK channels (Cheron *et al.*, 2009).

Slc1a3$^{P290R/+}$ animals exhibit the degradation of Bergmann glia in the cerebellum, but not of glial cells in other brain regions such as hippocampus or cortex. This difference is likely due to separate expression levels of EAAT1/GLAST and/or distinct $[Cl^-]_{int}$ in Bergmann glia. Insertion of the homologous P>R mutation into *Drosophila* EAAT1 (Eaat1$^{P>R}$) or expression of mutant human EAAT1 caused episodic paralyzes with compromised astrocyte morphology and developmental impairment in *Drosophila* larvae (Parinejad *et al.*, 2016). This phenotype was mimicked by the overexpression of K^+-Cl^- cotransporter and could be rescued by Na^+-K^+-$2Cl^-$ cotransporter expression. These findings highlight the physiological importance of $[Cl^-]_{int}$ homeostasis for glial function but also identify differences between mouse Bergmann glia cells and *Drosophila* glial cells: Bergmann glial apoptosis is an initial stage of cerebellar degeneration in *Slc1a3*$^{P290R/+}$ mice, while Eaat1$^{P>R}$ larvae have impaired astrocyte infiltration but no degeneration. Glial cells express various Cl^--coupled transporters, whose function might be modified by reduced $[Cl^-]_{int}$ in *Slc1a3*$^{P290R/+}$ mice. Glial GATs are Na^+/Cl^-/GABA transporters, and the observed changes in $[Cl^-]_{int}$ would cause a reduction in resting [GABA] by ~20% between P10 and P12. Cl^-/HCO_3^- exchange might modify intracellular pH in *Slc1a3*$^{P290R/+}$glia. However, since the main alteration in *Slc1a3*$^{P290R/+}$ is a dramatic reduction in the number of Bergmann glia cells, all these predicted changes are minor compared with the morphological changes.

So far, five different brain disorders have been associated with *SLC1A3* mutations: EA (Jen *et al.*, 2005; de Vries *et al.*, 2009; Choi *et al.*, 2017*a*; Iwama *et al.*, 2018), migraine (Kovermann *et al.*, 2017); Tourette syndrome (Adamczyk *et al.*, 2011), attention-deficit hyperactivity disorder and autism (van Amen-Hellebrekers *et al.*, 2016). Although the underlying physiological mechanisms are insufficiently understood, these conditions might share fundamental pathophysiological processes: a sequence variant predicting E219D, found in some individuals with Tourette syndrome (Adamczyk *et al.*, 2011), increases the relative probability of surface membrane insertion for human EAAT1 and *SLC1A3* duplication is likely to increase EAAT1 expression in attention-deficit hyperactivity disorder and autism. In these diseases, increased EAAT1 numbers in the surface membrane are expected to enhance glutamate-activated anion currents in glial cells. It is tempting to speculate that these changes might alter glial function and neuronal migration, resulting in changes in neuronal network formation and function.

EAAT glutamate transporters are prototypical dual function proteins that mediate secondary-active glutamate transport and anion conductance. Although the structural basis of these two different transport processes has been established (Machtens *et al.*, 2015), the physiological impact of linking these distinct functions remains less clear. It is now clear that EAATs play a major role in regulating glial $[Cl^-]_{int}$ in the mammalian central nervous system (Untiet *et al.*, 2017) and in glial differentiation in *Drosophila* (Parinejad *et al.*, 2016). Our work illustrates how changes in EAAT1 anion channel activity can have dramatic consequences on differentiation and integrity of the cerebellum. It has been known for decades that glial and neuronal EAATs have differences in anion channel activity (Wadiche *et al.*, 1995). Our findings highlight the impact of low glial EAAT anion channel activity on glial Cl^- homeostasis. Animals carrying a heterozygous P290R mutation have only moderately increased EAAT-mediated anion currents but exhibit dramatic changes in cerebellar differentiation and profound cerebellar degeneration. Hence, glial EAATs must be optimized for both effective secondary-active transport and low anion channel activity.

Supplementary material

Supplementary material is available at *Brain Communications* online.

Acknowledgements

We are grateful to Christoph Aretzweiler, Marcel Böttcher and Tanja Mertens, for technical assistance with genotyping and care of animals and to Dr Niels Danbolt for providing *Slc1a3*$^{-/-}$ knock-out animals. We acknowledge Nikola Kornadt-Beck for help with legal aspects of animal breeding, Stefanie Ramrath for help in preparing sections for ultrastructural analyses and Drs Thomas Gensch, Arnd Baumann and Anja Mataruga for helpful discussions.

Funding

This work was supported by the German Ministry of Education and Research (E-RARE network Treat-ION, BMBF 01GM1907C to C.F.) and by the German Research Foundation (FOR 2795; FA 301/13-1 to Ch.F.).

Competing interests

The authors report no competing interests.

References

Abrahamsen B, Schneider N, Erichsen MN, Huynh TH, Fahlke C, Bunch L, et al. Allosteric modulation of an excitatory amino acid transporter: The subtype-selective inhibitor UCPH-101 exerts sustained inhibition of EAAT1 through an intramonomeric site in the trimerization domain. J Neurosci 2013; 33: 1068–87.

Adamczyk A, Gause CD, Sattler R, Vidensky S, Rothstein JD, Singer H, et al. Genetic and functional studies of a missense variant in a

glutamate transporter, SLC1A3, in Tourette syndrome. Psychiat Genet 2011; 21: 90–7.
Alvina K, Khodakhah K. The therapeutic mode of action of 4-aminopyridine in cerebellar ataxia. J Neurosci 2010; 30: 7258–68.
Anderson MA, Ao Y, Sofroniew MV. Heterogeneity of reactive astrocytes. Neurosci Lett 2014; 565: 23–9.
Arancillo M, White JJ, Lin T, Stay TL, Sillitoe RV. *In vivo* analysis of Purkinje cell firing properties during postnatal mouse development. J Neurophysiol 2015; 113: 578–91.
Bell CC, Grimm RJ. Discharge properties of Purkinje cells recorded on single and double microelectrodes. J Neurophysiol 1969; 32: 1044–55.
Chaudhry FA, Lehre KP, van Lookeren Campagne M, Ottersen OP, Danbolt NC, Storm-Mathisen J. Glutamate transporters in glial plasma membranes: highly differentiated localizations revealed by quantitative ultrastructural immunocytochemistry. Neuron 1995; 15: 711–20.
Cheron G, Sausbier M, Sausbier U, Neuhuber W, Ruth P, Dan B, et al. BK channels control cerebellar Purkinje and Golgi cell rhythmicity *in vivo*. PLoS One 2009; 4: e7991.
Choi KD, Jen JC, Choi SY, Shin JH, Kim HS, Kim HJ, et al. Late-onset episodic ataxia associated with *SLC1A3* mutation. J Hum Genet 2017a; 62: 443–6.
Choi KD, Kim JS, Kim HJ, Jung I, Jeong SH, Lee SH, et al. Genetic variants associated with episodic ataxia in Korea. Sci Rep 2017b; 7: 13855.
Crepel F. Regression of functional synapses in the immature mammalian cerebellum. Trends Neurosci 1982; 5 (Suppl C): 266–9.
de Vries B, Mamsa H, Stam AH, Wan J, Bakker SL, Vanmolkot KR, et al. Episodic ataxia associated with EAAT1 mutation C186S affecting glutamate reuptake. Arch Neurol 2009; 66: 97–101.
Donato R, Page KM, Koch D, Nieto-Rostro M, Foucault I, Davies A, et al. The ducky^{2J} mutation in *Cacna2d2* results in reduced spontaneous Purkinje cell activity and altered gene expression. J Neurosci 2006; 26: 12576–86.
Droste D, Seifert G, Seddar L, Jadtke O, Steinhauser C, Lohr C. Ca^{2+}-permeable AMPA receptors in mouse olfactory bulb astrocytes. Sci Rep 2017; 7: 44817.
Eccles JC, Llinas R, Sasaki K. The excitatory synaptic action of climbing fibres on the Purkinje cells of the cerebellum. J Physiol 1966; 182: 268–96.
Ernest NJ, Habela CW, Sontheimer H. Cytoplasmic condensation is both necessary and sufficient to induce apoptotic cell death. J Cell Sci 2008; 121: 290–7.
Fahlke C, Kortzak D, Machtens JP. Molecular physiology of EAAT anion channels. Pflugers Arch 2016; 468: 491–502.
Feng L, Hatten ME, Heintz N. Brain lipid-binding protein (BLBP): a novel signaling system in the developing mammalian CNS. Neuron 1994; 12: 895–908.
Friis MB, Friborg CR, Schneider L, Nielsen MB, Lambert IH, Christensen ST, et al. Cell shrinkage as a signal to apoptosis in NIH 3T3 fibroblasts. J Physiol 2005; 567: 427–43.
Gao Z, Todorov B, Barrett CF, van Dorp S, Ferrari MD, van den Maagdenberg AM, et al. Cerebellar ataxia by enhanced $Ca_V2.1$ currents is alleviated by Ca^{2+}-dependent K^+-channel activators in *Cacna1a* (S218L) mutant mice. J Neurosci 2012; 32: 15533–46.
Gavrieli Y, Sherman Y, Ben-Sasson SA. Identification of programmed cell death *in situ* via specific labeling of nuclear DNA fragmentation. J Cell Biol 1992; 119: 493–501.
Gensch T, Untiet V, Franzen A, Kovermann P, Fahlke C. Determination of intracellular chloride concentrations by fluorescence lifetime imaging. In: Becker W, editor. Springer Series Chem. Basel, CH: Springer International Publishing Switzerland; 2015.
Grosche J, Matyash V, Moller T, Verkhratsky A, Reichenbach A, Kettenmann H. Microdomains for neuron-glia interaction: parallel fiber signaling to Bergmann glial cells. Nat Neurosci 1999; 2: 139–43.
Guyenet SJ, Furrer SA, Damian VM, Baughan TD, La Spada AR, Garden GA. A simple composite phenotype scoring system for evaluating mouse models of cerebellar ataxia. J Vis Exp 2010; 39: 1787.
Hansen ST, Meera P, Otis TS, Pulst SM. Changes in Purkinje cell firing and gene expression precede behavioral pathology in a mouse model of SCA2. Hum Mol Genet 2013; 22: 271–83.
Hatten ME, Liem RK, Mason CA. Two forms of cerebellar glial cells interact differently with neurons *in vitro*. J Cell Biol 1984; 98: 193–204.
Hausser M, Clark BA. Tonic synaptic inhibition modulates neuronal output pattern and spatiotemporal synaptic integration. Neuron 1997; 19: 665–78.
Hoebeek FE, Stahl JS, van Alphen AM, Schonewille M, Luo C, Rutteman M, et al. Increased noise level of Purkinje cell activities minimizes impact of their modulation during sensorimotor control. Neuron 2005; 45: 953–65.
Holt GR, Softky WR, Koch C, Douglas RJ. Comparison of discharge variability *in vitro* and *in vivo* in cat visual cortex neurons. J Neurophysiol 1996; 75: 1806–14.
Hotzy J, Schneider N, Kovermann P, Fahlke C. Mutating a conserved proline residue within the trimerization domain modifies Na^+ binding to excitatory amino acid transporters and associated conformational changes. J Biol Chem 2013; 288: 36492–501.
Iino M, Goto K, Kakegawa W, Okado H, Sudo M, Ishiuchi S, et al. Glia-synapse interaction through Ca^{2+}-permeable AMPA receptors in Bergmann glia. Science 2001; 292: 926–9.
Iwama K, Iwata A, Shiina M, Mitsuhashi S, Miyatake S, Takata A, et al. A novel mutation in *SLC1A3* causes episodic ataxia. J Hum Genet 2018; 63: 207–11.
Jayabal S, Chang HH, Cullen KE, Watt AJ. 4-aminopyridine reverses ataxia and cerebellar firing deficiency in a mouse model of spinocerebellar ataxia type 6. Sci Rep 2016; 6: 29489.
Jayabal S, Ljungberg L, Watt AJ. Transient cerebellar alterations during development prior to obvious motor phenotype in a mouse model of spinocerebellar ataxia type 6. J Physiol 2017; 595: 949–66.
Jen JC, Graves TD, Hess EJ, Hanna MG, Griggs RC, Baloh RW; the CINCH Investigators. Primary episodic ataxias: diagnosis, pathogenesis and treatment. Brain 2007; 130: 2484–93.
Jen JC, Wan J, Palos TP, Howard BD, Baloh RW. Mutation in the glutamate transporter EAAT1 causes episodic ataxia, hemiplegia, and seizures. Neurology 2005; 65: 529–34.
Jones BJ, Roberts DJ. The quantitative measurement of motor inco-ordination in naive mice using an accelerating rotarod. J Pharm Pharmacol 1968; 20: 302–4.
Kaplan EL, Meier P. Nonparametric estimation from incomplete observations. J Am Ass 1958; 53: 34.
Keinanen K, Wisden W, Sommer B, Werner P, Herb A, Verdoorn TA, et al. A family of AMPA-selective glutamate receptors. Science 1990; 249: 556–60.
Kovermann P, Hessel M, Kortzak D, Jen JC, Koch J, Fahlke C, et al. Impaired K^+ binding to glial glutamate transporter EAAT1 in migraine. Sci Rep 2017; 7: 13913.
Latham A, Paul DH. Spontaneous activity of cerebellar Purkinje cells and their responses to impulses in climbing fibres. J Physiol 1971; 213: 135–56.
Lordkipanidze T, Dunaevsky A. Purkinje cell dendrites grow in alignment with Bergmann glia. Glia 2005; 51: 229–34.
Machtens JP, Kortzak D, Lansche C, Leinenweber A, Kilian P, Begemann B, et al. Mechanisms of anion conduction by coupled glutamate transporters. Cell 2015; 160: 542–53.
Mariani J. Extent of multiple innervation of Purkinje cells by climbing fibers in the olivocerebellar system of *weaver*, *reeler*, and *staggerer* mutant mice. J Neurobiol 1982; 13: 119–26.
Marr D. A theory of cerebellar cortex. J Physiol 1969; 202: 437–70.
McGrath JC, Drummond GB, McLachlan EM, Kilkenny C, Wainwright CL. Guidelines for reporting experiments involving animals: the ARRIVE guidelines. Brit J Pharmacol 2010; 160: 1573–6.
McKay BE, Turner RW. Physiological and morphological development of the rat cerebellar Purkinje cell. J Physiol 2005; 567: 829–50.

Midtgaard J. Stellate cell inhibition of Purkinje cells in the turtle cerebellum *in vitro*. J Physiol 1992; 457: 355–67.
Miyazaki T, Fukaya M, Shimizu H, Watanabe M. Subtype switching of vesicular glutamate transporters at parallel fibre-Purkinje cell synapses in developing mouse cerebellum. Eur J Neurosci 2003; 17: 2563–72.
Mullen RJ, Buck CR, Smith AM. NeuN, a neuronal specific nuclear protein in vertebrates. Development 1992; 116: 201–11.
Oomman S, Finckbone V, Dertien J, Attridge J, Henne W, Medina M, et al. Active caspase-3 expression during postnatal development of rat cerebellum is not systematically or consistently associated with apoptosis. J Comp Neurol 2004; 476: 154–73.
Oomman S, Strahlendorf H, Finckbone V, Strahlendorf J. Non-lethal active caspase-3 expression in Bergmann glia of postnatal rat cerebellum. Brain Res Dev Brain Res 2005; 160: 130–45.
Otis TS, Mathews PJ, Lee KH, Maiz J. How do climbing fibers teach? Front Neural Circuits 2012; 6: 95.
Palay S-L, Chan-Palay V. Cerebellar cortex. Berlin, Heidelberg: Springer; 1974.
Parinejad N, Peco E, Ferreira T, Stacey SM, van Meyel DJ. Disruption of an EAAT-mediated chloride channel in a *Drosophila* model of ataxia. J Neurosci 2016; 36: 7640–7.
Perkins EM, Suminaite D, Clarkson YL, Lee SK, Lyndon AR, Rothstein JD, et al. Posterior cerebellar Purkinje cells in an SCA5/SPARCA1 mouse model are especially vulnerable to the synergistic effect of loss of beta-III spectrin and GLAST. Hum Mol Genet 2016; 25: 4448–61.
Porcelli AM, Ghelli A, Zanna C, Valente P, Ferroni S, Rugolo M. Apoptosis induced by staurosporine in ECV304 cells requires cell shrinkage and upregulation of Cl^- conductance. Cell Death Differ 2004; 11: 655–62.
Pyle A, Smertenko T, Bargiela D, Griffin H, Duff J, Appleton M, et al. Exome sequencing in undiagnosed inherited and sporadic ataxias. Brain 2015; 138: 276–83.
Rakic P. Neuron-glia relationship during granule cell migration in developing cerebellar cortex. A Golgi and electronmicroscopic study in *Macacus rhesus*. J Comp Neurol 1971; 141: 283–312.
Rothstein JD, Martin L, Levey AI, Dykes-Hoberg M, Jin L, Wu D, et al. Localization of neuronal and glial glutamate transporters. Neuron 1994; 13: 713–25.
Sato Y, Miura A, Fushiki H, Kawasaki T. Short-term modulation of cerebellar Purkinje cell activity after spontaneous climbing fiber input. J Neurophysiol 1992; 68: 2051–62.
Schreiner AE, Durry S, Aida T, Stock MC, Ruther U, Tanaka K, et al. Laminar and subcellular heterogeneity of GLAST and GLT-1 immunoreactivity in the developing postnatal mouse hippocampus. J Comp Neurol 2014; 522: 204–24.
Sofroniew MV. Reactive astrocytes in neural repair and protection. Neuroscientist 2005; 11: 400–7.
Storck T, Schulte S, Hofmann K, Stoffel W. Structure, expression, and functional analysis of a Na^+-dependent glutamate/aspartate transporter from rat brain. Proc Natl Acad Sci USA 1992; 89: 10955–9.
Tang T, Xiao J, Suh CY, Burroughs A, Cerminara NL, Jia L, et al. Heterogeneity of Purkinje cell simple spike-complex spike interactions: zebrin- and non-zebrin-related variations. J Physiol 2017; 595: 5341–57.
Torp R, Danbolt NC, Babaie E, Bjoras M, Seeberg E, Storm-Mathisen J, et al. Differential expression of two glial glutamate transporters in the rat brain: an *in situ* hybridization study. Eur J Neurosci 1994; 6: 936–42.
Untiet V, Kovermann P, Gerkau NJ, Gensch T, Rose CR, Fahlke C. Glutamate transporter-associated anion channels adjust intracellular chloride concentrations during glial maturation. Glia 2017; 65: 388–400.
van Amen-Hellebrekers CJ, Jansen S, Pfundt R, Schuurs-Hoeijmakers JH, Koolen DA, Marcelis CL, et al. Duplications of *SLC1A3*: Associated with ADHD and autism. Eur J Med Genet 2016; 59: 373–6.
Verkman AS. Development and biological applications of chloride-sensitive fluorescent indicators. Am J Physiol 1990; 259: C375–88.
Wadiche JI, Amara SG, Kavanaugh MP. Ion fluxes associated with excitatory amino acid transport. Neuron 1995; 15: 721–8.
Wadiche JI, Jahr CE. Multivesicular release at climbing fiber-Purkinje cell synapses. Neuron 2001; 32: 301–13.
Walev I, Reske K, Palmer M, Valeva A, Bhakdi S. Potassium-inhibited processing of IL-1 beta in human monocytes. EMBO J 1995; 14: 1607–14.
Walter JT, Alvina K, Womack MD, Chevez C, Khodakhah K. Decreases in the precision of Purkinje cell pacemaking cause cerebellar dysfunction and ataxia. Nat Neurosci 2006; 9: 389–97.
Watanabe M, Kano M. Climbing fiber synapse elimination in cerebellar Purkinje cells. Eur J Neurosci 2011; 34: 1697–710.
Watase K, Hashimoto K, Kano M, Yamada K, Watanabe M, Inoue Y, et al. Motor discoordination and increased susceptibility to cerebellar injury in GLAST mutant mice. Eur J Neurosci 1998; 10: 976–88.
Weyer A, Schilling K. Developmental and cell type-specific expression of the neuronal marker NeuN in the murine cerebellum. J Neurosci Res 2003; 73: 400–9.
Winter N, Kovermann P, Fahlke C. A point mutation associated with episodic ataxia 6 increases glutamate transporter anion currents. Brain 2012; 135: 3416–25.
Womack M, Khodakhah K. Active contribution of dendrites to the tonic and trimodal patterns of activity in cerebellar Purkinje neurons. J Neurosci 2002; 22: 10603–12.
Woodward DJ, Hoffer BJ, Altman J. Physiological and pharmacological properties of Purkinje cells in rat cerebellum degranulated by postnatal x-irradiation. J Neurobiol 1974; 5: 283–304.
Wulff P, Schonewille M, Renzi M, Viltono L, Sassoe-Pognetto M, Badura A, et al. Synaptic inhibition of Purkinje cells mediates consolidation of vestibulo-cerebellar motor learning. Nat Neurosci 2009; 12: 1042–9.
Yamada K, Fukaya M, Shibata T, Kurihara H, Tanaka K, Inoue Y, et al. Dynamic transformation of Bergmann glial fibers proceeds in correlation with dendritic outgrowth and synapse formation of cerebellar Purkinje cells. J Comp Neurol 2000; 418: 106–20.
Yu FH, Mantegazza M, Westenbroek RE, Robbins CA, Kalume F, Burton KA, et al. Reduced sodium current in GABAergic interneurons in a mouse model of severe myoclonic epilepsy in infancy. Nat Neurosci 2006; 9: 1142–9.

2.2.1. Submitted manuscript

Glial chloride homeostasis under transient ischemic stress

Miriam Engels, Manu Kalia, Sarah Rahmati, Laura Petersilie, Nils Pape, Peter Kovermann, Michel J.A.M. van Putten, Christine R. Rose, Hil G.E. Meijer, Thomas Gensch, Christoph Fahlke

Pages: 49 – 94

Status: submitted

Contribution: I was involved in the planning and the practical implementation of all chloride measurements. For the following figures, I calibrated, measured and determined $[Cl^-]_{int}$, examined statistical analysis, created imaging pictures and prepared the figures: Chloride imaging in acute hippocampal and neocortical slices (Fig. 2 and 3), modification of glial resting $[Cl^-]_{int}$ and chloride dependence of MQAE fluorescence lifetimes by chemical blocker (Fig. 4), modification of glial resting $[Cl^-]_{int}$ after energy restriction (Fig. 6) and its modification by specific chloride- and EAAT-transport blocker under energy restriction (Fig. 7 and 8). I rearranged to the text structure the figures illustrating minimum photon numbers for the determination of fluorescence (Fig. 1), ATP levels under chemical ischemia (Fig.5), astrocytic cell swelling (Fig. 9) and mathematical modelling results (Fig. 10). I was involved in the interpretation of the data and the writing of the first manuscript draft.

Glial chloride homeostasis under transient ischemic stress

Abbreviated title: **Glial chloride concentrations in ischemic stress**

Miriam Engels[1], Manu Kalia[2,3], Sarah Rahmati[1,#], Laura Petersilie[3], Nils Pape[3], Peter Kovermann[1], Michel J.A.M. van Putten[4], Christine R. Rose[3], Hil G.E. Meijer[2], Thomas Gensch[1], Christoph Fahlke[1,*]

1 Institute of Biological Information Processing, Molekular- und Zellphysiologie (IBI-1), Forschungszentrum, Wilhelm-Johnen-Straße, 52428 Jülich, Germany,

2 Applied Analysis, Department of Applied Mathematics, University of Twente, Drienerlolaan 5, 7522 NB Enschede, The Netherlands,

3 Institute of Neurobiology, Heinrich Heine University, Universitätsstraße 1, 40225 Düsseldorf, Germany,

4 Department of Clinical Neurophysiology, University of Twente, Drienerlolaan 5, 7522 NB Enschede, The Netherlands

current address: University of Bordeaux, CNRS, Interdisciplinary Institute for Neuroscience, IINS, 146 Rue Léo Saignat, 33076 Bordeaux, France

*Address correspondence to Christoph Fahlke, Institute of Biological Information Processing, Molekular- und Zellphysiologie (IBI-1), Forschungszentrum Jülich, 52425 Jülich, Germany

Email: c.fahlke@fz-juelich.de

Number of pages: 41

Number of tables: 1

Number of figures: 10

Number of words for abstract: 250

Number of words for introduction: 546

Number of words for discussion: 1892

Conflict of interest statement: The authors declare no conflict of interest

ACKNOWLEDGMENTS

This work was supported by the Deutsche Forschungsgemeinschaft (DFG, German Research Foundation) to C.R.R. (Ro2327/12-1 and 14-1) and Ch.F. (FA 301/13-1) as part of the Research Unit FOR 2795 (Synapses under stress).

Abstract

Pathological conditions such as ischemia, infections, or traumatic brain injury can cause glial cell swelling. Both swelling and regulatory volume decreases depend on the intracellular chloride concentration ($[Cl^-]_{int}$). Despite its high relevance for brain ion and volume homeostasis, experimental data for glial $[Cl^-]_{int}$ are lacking for most brain regions. We measured $[Cl^-]_{int}$ in hippocampal and neocortical astrocytes and in hippocampal radial glia-like cells (RGL) in acute murine brain slices using fluorescence lifetime imaging microscopy with the chloride-sensitive dye MQAE. We observed substantial heterogeneity in $[Cl^-]_{int}$, ranging from 14.0 ± 2.0 mM in neocortical astrocytes to 28.4 ± 3.0 mM in dentate gyrus astrocytes. Chloride accumulation by the Na^+-K^+-$2Cl^-$ cotransporter (NKCC1) and chloride outward transport (efflux) through K^+-Cl^- co-transporters (KCC1–KCC3) and excitatory amino acid transporter (EAAT) anion channels control $[Cl^-]_{int}$ to variable extent in distinct brain regions. In hippocampal astrocytes, blocking NKCC1 increased $[Cl^-]_{int}$, whereas KCC or EAAT anion channel inhibition had little effect. In contrast, neocortical astrocytic or RGL $[Cl^-]_{int}$ was very sensitive to block of chloride outward transport, but not to NKCC1 inhibition. Mathematical modeling demonstrated that higher numbers of NKCC1 and KCC transporters can account for lower $[Cl^-]_{int}$ in neocortical astrocytes. Energy depletion mimicking ischemia for up to 10 min did not result in pronounced changes in $[Cl^-]_{int}$ in any of the tested glial cell types. However, $[Cl^-]_{int}$ changes occurred under ischemic conditions after blocking selected anion transporters. We conclude that stimulated chloride accumulation and chloride efflux can compensate for each other under transient energy deprivation. (250 words)

Significance Statement

Many cellular functions are regulated by transmembrane chloride transport, but the mechanisms underlying intracellular chloride homeostasis remain insufficiently understood. Here, we measured glial $[Cl^-]_{int}$ in different brain regions in acute brain slices. We found substantial and unexpected heterogeneity and identified differences in anion transporter expression as basis of this heterogeneity. Although glial anion transporters utilize electrochemical gradients, which change upon energy restriction, we did not find significant changes in $[Cl^-]_{int}$ upon transient ischemic stress. We demonstrate that stimulated chloride accumulation and chloride efflux compensate for each other, ensuring constant $[Cl^-]_{int}$ and preventing cell volume changes under these conditions. Our results will provide much needed quantitative information to understand and to model brain ion and water homeostasis in health and diseases.

Introduction

Glial cells fulfill many important functions in the mammalian central nervous system. First, they supply nutrient and signaling molecules to neurons and regulate extracellular K^+ concentrations (Deitmer and Rose, 2010). Second, glial secondary-active transport systems control resting synaptic neurotransmitter concentrations to optimize the spatiotemporal resolution of synaptic transmission. Glial cells have higher water permeability than neurons, making them prone to faster changes in cell volume caused by physiological variations in external and internal osmolarity (Andrew et al., 2007; MacAulay and Zeuthen, 2010; Nagelhus and Ottersen, 2013; Papadopoulos and Verkman, 2013). Since changes in osmotically active solute concentrations are intimately associated with glial key functions, mechanisms for volume regulation are especially important for this class of cells.

Various pathological conditions (such as epilepsy, hepatic failure, hyponatremia, stroke, and traumatic brain and spinal cord injuries) can result in dysregulation of astrocytic cell volume; astrocyte swelling can result in cytotoxic brain edema (Stokum et al., 2016; Wilson and Mongin, 2018). By reducing the extracellular volume, glial swelling has the potential to modify metabolite and neurotransmitter diffusion. Glial swelling and changes in ionic concentrations may subsequently result in an increased net water transport across the blood brain barrier, causing cerebral edema and increased intracranial pressure (ICP). Increased intracranial pressure can result in life-threatening conditions such as tissue damage and reduced blood flow. In ischemic infarcts, cerebral edema strongly impacts the functional outcome.

Volume recovery after cell swelling is based on water efflux driven by the synchronized outward movement of K^+, Cl^-, and HCO_3^- without affecting the transmembrane voltage (Kahle et al., 2015; Mongin, 2016; Delpire and Gagnon, 2018; Wilson and Mongin, 2018; Toft-Bertelsen et al., 2021). Activation of two classes of ion transporters, the Na^+-K^+-$2Cl^-$ cotransporter NKCC1 and the Na^+/H^+-exchanger NHE1, are necessary for volume increases

after osmotic or metabolic shrinkage (Song et al., 2020). Intracellular accumulation of NaCl and KCl drives the inward movement of water (Lang et al., 1998; Mongin and Orlov, 2001; Pasantes-Morales, 2016). Regulatory volume changes require chloride fluxes across the membrane (Mongin, 2016), making the intracellular chloride concentration ($[Cl^-]_{int}$) a primary determinant of volume regulation (Dijkstra et al., 2016).

Here we used fluorescence lifetime imaging microscopy (FLIM) with the chloride-sensitive dye MQAE (Kaneko et al., 2004; Kovalchuk and Garaschuk, 2012; Gensch et al., 2015; Untiet et al., 2017) to study $[Cl^-]_{int}$ in glial cells under both control conditions and conditions that mimic ischemic energy restriction. We determined the resting $[Cl^-]_{int}$ in four types of glial cells (hippocampal astrocytes in the dentate gyrus (DG) and cornu ammonis region 1 (CA1), hippocampal radial glia-like (RGL) cells, and neocortical astrocytes) in acute brain slices and, remarkably, observed regional heterogeneity in glial ion concentration. Using specific blockers, we identified the key chloride transport proteins that determined glial chloride homeostasis and assessed their contribution to $[Cl^-]_{int}$ and cell volume in the tested brain regions. Although chloride transport depends on processes that are affected during ischemia, we observed only slight absolute changes in $[Cl^-]_{int}$ upon transient chemical ischemia. Further, to explain our results, we used a mathematical model describing $[Cl^-]_{int}$ of glial cells as a dynamic equilibrium of chloride fluxes. (515/650 words)

Material and Methods

Animals

We used SV129 mice of both sexes at postnatal day P20–P45 for chloride measurements. Organotypic brain slices for ATP imaging were prepared from P6–P8 Balb/C mice (both sexes), and cell volume measurements were performed on slices obtained from P14–18 Balb/C mice (both sexes). Animals were housed under standard conditions in the animal facility of Forschungszentrum Jülich (SV129) or Heinrich Heine University Düsseldorf (Balb/C) according to institutional guidelines under a 12-h light/dark cycle and in small groups with food and water provided *ad libitum*. All experiments complied with the German Law for Protection of Animals and European Community Council Directive 2010/63/EU and were approved by the regulatory authorities, the FZJ/HHU and Landesamt für Natur, Umwelt und Verbraucherschutz of Nordrhein-Westfalen, and Central Unit for Animal Research and Animal Welfare Affairs of the Heinrich Heine University Düsseldorf, in accordance with institutional act number O50/05.

Preparation of acute brain slices

After decapitation under isoflurane anesthesia brains were rapidly removed and placed in oxygenated, ice-cold preparation solution containing (in mM) 125 NaCl, 2.5 KCl, 1.25 NaH_2PO_4, 26 $NaHCO_3$, 0.5 $CaCl_2$, 5 $MgCl_2$, 25 glucose. Sagittal hippocampal or coronal cortical slices (250 µm thickness) were cut with a microtome (Microm HM650V, Thermo Scientific, Walldorf, Germany; frequency 60 Hz, amplitude 1 mm, drive 10) and transferred to a gauze slice holder in oxygenated Ringer's solution at 37°C (Untiet et al., 2017). Glial cells were stained with sulforhodamine 101 (SR101, Sigma-Aldrich, St. Louis, MO, USA) in a preparation ringer solution that contained 2 µM SR101 for 20 min at 37°C (Kafitz et al., 2008), followed by a 10 min incubation in standard oxygenated Ringer's solution with (in mM) 125

NaCl, 2.5 KCl, 1.25 NaH_2PO_4, 26 $NaHCO_3$, 2 $CaCl_2$, 1 $MgCl_2$, 20 glucose, at 37°C. The stained acute tissue slices were stored at room temperature (20 – 22°C) for at least 30 min before use. Slices were constantly perfused with oxygenated (carbogen; 95% O_2 / 5% CO_2) standard Ringer's solution. All experiments were performed within 5 – 8 h of brain removal.

DL-threo-β-benzyloxyaspartic acid (DL-TBOA; 100 µM; Tocris Bioscience, Bristol, UK), *R*-(+)-butylindazone, (dihydroindenyl)oxy alkanoic acid (*R*-(+)-DIOA, 100 µM, Sigma-Aldrich, Merck, Darmstadt, Germany) or 3-butylamino-4-phenoxy-5-sulfamoyl benzoic acid (bumetanide; 40 µM, Sigma-Aldrich, Merck, Darmstadt, Germany) were added to both the incubation (20-min incubation) and perfusion solutions. In contrast, 2-amino-5,6,7,8-tetrahydro-4-(4-methoxyphenyl)-7-(naphthalen-1-yl)-5-oxo-4*H*-chromene-3-carbonitrile (UCPH-101, Abcam, Cambridge, UK) inhibits excitatory amino acid transporter 1 (EAAT1/GLAST) with very slow unblocking kinetics (Abrahamsen et al., 2013) and is not washed out within the imaging experiment duration (around 30 min). Hence, in relevant experiments, brain slices were incubated with for 20 µM UCPH-101 for 20 min and then perfused with standard Ringer's solution without UCPH-101 for imaging.

Fluorescence lifetime imaging microscopy (FLIM)

Brain slices were incubated in oxygenated standard Ringer's solution containing 3.5 mM 1-(ethoxycarbonylmethyl)-6-methoxyquinolinium bromide (MQAE, Sigma-Aldrich, Merck, Darmstadt, Germany) (Verkman, 1990) for 30–40 min at room temperature and then transferred to an imaging chamber attached to an upright fluorescence microscope. Experiments were performed using two different imaging systems: roughly half used an A1 MP microscope (Nikon, Amsterdam, The Netherlands) equipped with a 25× water immersion objective (NA1.1; working distance (WD) 2 mm; XYZ, Nikon) and a mode-locked Titan-Sapphire laser (Mai Tai DeepSee, Newport Spectra Physics; Irvine, CA; output power 2.3 W at 750 nm); the other half used a LSM880 microscope (Zeiss, Jena, Germany) equipped with a 20× water immersion

objective (NA 1.0, WD 2.1 mm; XYZ, Zeiss) linked to a tunable laser (InSight X3, Newport Spectra Physics, Darmstadt, output power 1.9 W at 750 nm). Two-photon excitation (λ_{exc} = 750 nm) was carried out at 80 MHz with either 100 fs light pulses or 120 fs light pulses, with identical results. Mean fluorescence lifetimes were measured using multidimensional time-correlated single-photon counting (TCSPC) in a volume of 0.08 µm^3 per individual pixel, resulting in a three-dimensional resolution of approximately 1.3 µm in the *z*-axis and 0.35 µm in the *x*- and *y*-axes (Zipfel et al., 2003).

Six to eight images were taken for each measurement, starting at a depth of about 30 µm from the upper cutting edge and reaching not further than approximately 100 µm into the slice. For all brain regions studied, only glial cells that were clearly stained by SR101, sufficiently loaded with MQAE, and showed region-specific characteristic morphology and location were included in the analysis. Following two-photon (Nikon A1 MP microscope: 900 nm) or one-photon (Zeiss LSM880 confocal microscope: 561 nm) excitation, emitted SR101 fluorescence was filtered using an appropriate bandpass filter (Nikon A1 MP: 595AF60, 565–637 nm; Omega Optical, Brattleboro, VT, USA) or a GaAsP detector (Zeiss, LSM880) with a freely selectable emission detection band (570–700 nm). A single region of interest (ROI) was defined for each glial soma, and the fluorescence lifetime of cells was calculated as the average fluorescence lifetime of all pixels in the ROI. Fluorescence was filtered by separating MQAE fluorescence (peak emission: 460 nm) from autofluorescence (bandpass 445bp90: 400–490 nm; Omega Optical, Brattleboro, VT, USA) and recorded with a GaAsP hybrid photodetector (HPM-100-40, Becker & Hickl, Berlin, Germany) with non-descanned detection. TCSPC electronics (SPC-152; Becker & Hickl, Berlin, Germany) and acquisition software were used for FLIM as previously described (Kaneko et al., 2004; Untiet et al., 2017)).

Fluorescence lifetime images were generated using SPCImage 6.0–8.3 (Becker & Hickl, Berlin, Germany). Fluorescence decays were fitted with bi-exponential functions (Kaneko et

al., 2004; Gilbert et al., 2007; Funk et al., 2008; Untiet et al., 2017)), and the average fluorescence lifetime (τ_{ave})

$$\tau_{ave} = \frac{a_1 * \tau_1 + a_2 * \tau_2}{a_1 + a_2}$$

was used to calculate $[Cl^-]_{int}$ values (τ_x = lifetime of the exponential component; a_x= respective amplitude).

Fitting the sum of exponentials to fluorescence decay curves from TCSPC experiments can result in systematic errors for low photon counts (Maus et al., 2001). To define conditions that circumvent this limitation of FLIM-based concentration measurements, we systematically studied the consequences of low photon numbers with the two-photon fluorescence microscopes with FLIM modality used for measuring glial $[Cl^-]_{int}$ (Figure 1). We determined fluorescence lifetimes in MQAE droplets with $[Cl^-]$ of 15, 40, or 100 mM and obtained fluorescence lifetimes identical to the fluorescence lifetime determined independently with a cuvette-based fluorescence lifetime spectrophotometer at high photon numbers (> 1000 photons) (TimeHarp 100, PicoQuant, Berlin, Germany). Further increasing the photon counts did not modify the fluorescence lifetime. When modifying the photon number of fluorescence intensity decays (FIDs) by changing binning options, smaller binning reduced the photon numbers per decay and significantly decreased fluorescence lifetimes (Figure 1a). We combined binning with varying the excitation power and found that — for less than 1000 photons per FID — the estimated fluorescence lifetime deviates by up to 25% from the correct value (Figure 1b). In similar experiments with two other chloride concentrations with shorter fluorescence lifetimes (40 mM NaCl and100 mM NaCl) similar, but less pronounced effects of low photon numbers were observed (Figure 1b). In experiments with astrocytes in the CA1 region a similar effect of low photon counts was observed under conditions that result in low photon counts (Figure 1d, I: 4.22 ns (296 photons per FID); II: 4.24 ns (269 photons per FID); III: 4.15 ns (473 photons per FID)). These lifetimes predict incorrectly higher chloride

concentrations (I: 30.8 mM; II: 30.3 mM; III: 32.1 mM). When the same area was measured with a longer acquisition time and photon numbers per FID well above 1000, we obtained the expected fluorescence lifetimes (Figure 1c, I: 4.88 ns (4817 photons per FID); II: 4.96 ns (3941 photons per FID); III: 4.73 ns (6240 photons per FID), as well as chloride concentrations (I: 19.3 mM; II: 18.1 mM; III: 21.6 mM) near to the mean of $[Cl^-]_{int}$ estimated for hippocampal (CA1) astrocytes (Figure 2i). Therefore, we chose to use a minimum number of 2000 photons per FID in all of our experiments. We usually summed fluorescence lifetimes over nine pixels and assigned the resulting value to the central pixel (bin factor 1). In a few cases, in which the number of photons per pixel was below the critical value of 2000 counts (Figure 1a), we used a bin factor of 2 (i.e. we summed photon distributions over the surrounding 25 pixels).

For calibration (Figures 2g and 3c) acute tissue slices were incubated in HEPES-buffered solutions containing (in mM) 140 K^+, 10 Na^+, 10 HEPES, 10–60 Cl^-, 80–130 gluconate, adjusted to 310 mOsm/L with K–gluconate and to pH 7.4 with KOH, supplemented with 20 µM nigericin (sodium salt; Sigma-Aldrich, Merck, Darmstadt, Germany) and 20 µM tributyltin (chloride salt; Sigma-Aldrich, Merck, Darmstadt, Germany) (Chao et al., 1989; Bevensee et al., 1997; Kaneko et al., 2004; Kovalchuk and Garaschuk, 2012). Since MQAE is quenched much less effective by HCO_3^- than by Cl^- (Kaneko et al., 2004), intracellular bicarbonate is not expected to contribute to the MQAE lifetime and was therefore ignored in calibration experiments. MQAE fluorescence is quenched not only collisionally by chloride ions (Verkman, 1990), but also by the chemical blockers used in our experiments. Consequently, to account for changes in fluorescence lifetimes, we performed additional calibrations after 20-min incubation with blockers (Figure 4b,d,f,h). The importance of these additional calibration was proven by differences in $[Cl^-]_{int}$ calculated using the original calibration (without blocker) compared with corrected values after additional calibration. Re-calibration of MQAE lifetimes with three blockers (bumetanide, *R*-(+)-DIOA, and DL-TBOA) is necessary to accurately assess the roles of specific chloride transporters/channels in setting

the $[Cl^-]_{int}$. Since MQAE self-quenching reduces the fluorescence lifetime (at fixed $[Cl^-]$) with increasing [MQAE] (Kaneko et al., 2002; Gensch et al., 2015), we performed calibration experiments using the same MQAE loading protocols as in the actual measurements.

Transient energy restriction in the ischemic penumbra was mimicked by removing glucose from standard Ringer's solution and adding 5 mM sodium azide and 2 mM 2-deoxy-D-glucose (Sigma-Aldrich) (Gerkau et al., 2018). Slices were perfused for 2, 5, or 10 min with the ischemia cocktail, and then continuously perfused with oxygenated standard Ringer's solution during imaging. Ischemia measurements were always performed as the first experiments of the day, with two to five slices tested for different ischemic periods (2, 5, or 10 min). Fluorescence lifetimes were determined with scanning times of at least 40 s or 80 s. Slices with insufficient MQAE loading or strong slice movement during scanning were not included in the analysis. During fluorescence lifetime imaging we approximated glial cell volumes by defining a circular ROI surrounding the glial soma from confocal images and assuming a spherical shape for the glial cell. This approximation did not reveal significant changes in volume under any tested condition (data are not shown).

ATP imaging

Imaging of intracellular ATP was performed in organotypic brain slice cultures of the hippocampus and adjacent cortex, which were prepared following an established protocol (Stoppini et al., 1991; Lerchundi et al., 2019). Briefly, Balb/C mice were decapitated at P6-8, and brains were cut into 250 µm-thick slices using a microtome (HM 650 V; Thermo Fisher Scientific, Waltham, MA, USA) after transfer to oxygenated, ice-cold preparation saline (in mM): 130 NaCl, 2.5 KCl, 2 $CaCl_2$, 1 $MgCl_2$, 1.25 NaH_2PO_4, 26 $NaHCO_3$, 10 glucose. Slices were kept on Biopore membranes (Millicell standing insert, Merck Millipore, Burlington, VT, USA) in an incubator at the interface between humidified carbogen (95% O_2/ 5% CO_2) and culture medium at 36.5°C. After 1-3 days in culture, 0.5 µl of a vector (AAV5/2) carrying the

code for ATeam1.03^{YEMK} ("ATeam") (Imamura et al., 2009) under the control of astrocytic-specific promotor GFAP was applied to the top of a slice as described before (Lerchundi et al., 2019). Slices were maintained in the incubator for at least six more days before performing experiments.

Transduced slices were imaged at an epifluorescence microscope (Nikon Eclipse FN-I, Nikon GmbH Europe, Düsseldorf, Germany) equipped with a monochromator (Poly-V; Thermo Scientific/FEI, Planegg, Germany). Slices were perfused with oxygenated Ringer solution containing (in mM): 138 NaCl, 2.5 KCl, 2 $CaCl_2$, 1 $MgCl_2$, 1.25 NaH_2PO_4, 18 $NaHCO_3$ and 10 glucose; warmed to 33 ± 1 °C. ATeam was excited at 435 nm and fluorescence collected from regions of interest manually drawn around cell bodies. Emission was split at 500 nm (WVIEW GEMINI optic system; Hamamatsu Photonics, Herrsching, Germany) onto two band pass filters (483/32: imaging of eCFP/donor; 542/27: imaging of Venus/acceptor), and the fluorescence ratio (Venus/eCFP) calculated for individual somata.

Cell volume measurements based on maximum intensity projections

P14–P18 mice (both sexes) were killed by CO_2 anesthesia and decapitation. The brains were removed and placed in oxygenated, ice-cold preparation saline (in mM: 125 NaCl, 2.5 KCl, 0.5 $CaCl_2$, 6 $MgCl_2$, 1.25 NaH_2PO_4, 26 $NaHCO_3$, and 20 glucose). Parasagittal brain slices (250 µm) were obtained using a vibratome (Microm HM 650V, Thermo Scientific, Planegg, Germany or 7000smz-2, n.p.i.Tamm, Germany). Brain slices were incubated for 20 min at 34°C in standard oxygenated Ringer's solution. During the incubation period, SR101 (0.5–1 µM) was added to selectively stain astrocytes (Kafitz, Meier, Stephan, & Rose, 2008). After staining, brain slices were maintained in standard Ringer's solution at room temperature until use.

During experiments, brain slices were continuously perfused with standard Ringer's solution at room temperature. Hypo-osmotic stress was induced by reducing the NaCl concentration of standard Ringer's solution to 75 mM, thereby decreasing the osmolarity from

about 310 to 220 mOsm/L. Chemical ischemia was induced by perfusing slices with glucose-free standard Ringer's solution containing 5 mM NaN_3 and 2 mM 2-deoxy-D-glucose (Gerkau et al., 2018). A motorized confocal laser scanning microscope (Nikon Eclipse C1: Fluor 60×/1.00W, software EZ-C1 3.91 Nikon Instruments, Düsseldorf, Germany) was used to document SR101 fluorescence. Z-stacks were taken at 0.6 µm increments and maximum intensity projections were calculated in ImageJ. Images were deconvolved using Huygens Professional Software (Scientific Volume Imaging, Hilversum, The Netherlands).

Modeling $[Cl^-]_{int}$ under transient ischemia

To simulate ischemia-induced changes in $[Cl^-]_{int}$, we modified a recently developed model (Kalia et al., 2021) that describes the temporal evolution of intra- and extracellular Na^+, K^+, Ca^{2+}, Cl^-, and glutamate concentrations at the tripartite synapse during the transient blockade of Na^+/K^+-ATPase in neurons and astrocytes. The model describes the temporal evolution of the molar amounts of Na^+, K^+, Cl^-, Ca^{2+}, and glutamate in neuronal, astrocyte, and extracellular compartments using the following differential equations:

$$\begin{cases} \dfrac{d}{dt}N_X^i = -\dfrac{1}{z_X F}\sum_j I_j^{X,i}, \\ \dfrac{d}{dt}W_i = \lambda_i \sum_X ([X]_i - [X]_e), \\ \dfrac{d}{dt}q = \alpha_q (1-q) - \beta_q q, \end{cases}$$

where N_X^i denotes the molar amount (i.e. the number moles of X in compartment i), z_X denotes the valence of ion X, and F denotes Faraday's constant. The term $I_j^{X,i}$ describes currents mediated by the transporter j with respect to ion X in compartment I with gating variable q. The compartments are allowed to swell and shrink in response to osmotic gradients across the membrane. Volumes W of glia and neurons and molar ionic amounts were used to determine the ion concentrations shown in Figure 10.

This model differs from the earlier version (Kalia et al., 2021) by integrating KCC transporters as the Cl^- transport system in the astrocytic plasma membrane, in addition to the NKCC1 and Cl^- leak channels. We assumed that the transport number J_{KCC} changes proportionally to the driving force of this coupled transporter, as follows:

$$J_{KCC}^{\alpha} = P_{KCC}^{\alpha} \frac{RT}{F} \ln\left(\frac{[K^+]_e[Cl^-]_e}{[K^+]_i[Cl^-]_i}\right).$$

We did not explicitly model the glial anion conductances generated by EAAT anion channels: these anion efflux pathways are represented as components of the anion leak conductance of the modeled glial cells.

Experimental Design and Statistical Analysis

Extent of systematic fluorescence lifetime deviation: We used 3-mm-sized droplets of MQAE (3 mM) dissolved in an aqueous solution of 15, 40, or 100 mM chloride and imaged a 100-µm wide area located 50 µm inside the droplet. The photon number of FIDs are modified by changing either the acquisition time, excitation energy, or applied binning options. For binning, we summed the FIDs of pixels surrounding the central pixel FIDs, and assigned the FID sum as a new, binned FID to the central pixel.

MQAE calibration: We calibrated MQAE fluorescence lifetimes in all glial cell types in absence and presence of chemical blockers (bumtenaide, DL-TBOA, or *R*-(+)-DIOA) are done (Kovalchuk and Garaschuk, 2012). Mean fluorescence lifetimes were measured for five to eight predefined chloride concentrations (10–60 mM; n = 3 animals/chloride concentration, > 10 cells/mouse/chloride concentration). Error bars indicate the standard deviation (mean ± SD), in positive and negative direction (analyzed in OriginPro 2018G; OriginLab Corporation, Northampton, USA). A linear fit of $[Cl^-]$ dependence of these values provides K_{SV} and τ_0. The corresponding adjusted coefficient of determination (R^2_{adj}) of all linear fits was calculated as:

$$R^2_{adj} = 1 - \frac{(1 - R^2) * (n - 1)}{n - k - 1}$$

where R^2 describes the percentage of the variation for a dependent variable that is explained by independent variables in a regression model, n is the number of observations and k is the number of independent variables. The R^2_{adj} values are provided in the correlating figure legends.

Chloride concentration: $[Cl^-]_{int}$ were calculated form τ_{ave} determined within a single region of interest (ROI) defined for each glial soma in Fiji (Schindelin et al., 2012) using the calibration curve obtained for the respective glia cell in presence/absence of a particular blocker. In figures, box plots present data (mean ± 1.5 IQR (Interquartile range)) as mean values from individual animals (black points) and single cells (small, shaded dots) without outlier exclusion (drawn in OriginPro 2018G; OriginLab Corporation, Northampton, USA). In the text, $[Cl^-]_{int}$ are given as the mean ± SD values from animals. For statistical analysis, one-way ANOVA tests with Holm–Sidak *post hoc* testing were used to determine *p*-values. Each experiment was performed with at least four different animals.

ATP levels: Analysis was performed off-line employing OriginPro 9 Software (OriginLab Corporation, Northhampton, MA, USA.). Changes in intracellular ATP levels are expressed as % changes in the Venus/eCFP fluorescence ratio, normalized to the baseline fluorescence ratio ("ΔATeam ratio (%)"). Data were statistically analyzed either by t-test or by one-way ANOVA followed by *post hoc* Bonferroni test. Each experiment was performed with at least three different animals.

Cell volume measurements: Changes in cell volume were evaluated based on maximum intensity projections (Risher et al., 2009). For this, line profiles in scaled images were taken at the smallest extension (width) of astrocyte somata. Gray values were then normalized to the maximum, and the full width at half maximum (FWHM) was calculated using Origin Pro2018b (OriginLab 18 Corporation, Northampton, USA). Datasets were analyzed using a Shapiro–Wilk normality test. One-way repeated measures ANOVA with Bonferroni *post hoc* testing was used

to compare data obtained in a single experimental series. Each experiment included at least five different animals.

For all experiments: p-values of ≤ 0.05 were considered statistically significant with $*p<0.05$, $**p<0.01$, $***p<0.001$. The exact p-values are provided in the results or relevant not significant results are marked with n.s. (not significant).

Results

Glial cells show regional variability in $[Cl^-]_{int}$

Figure 2 shows fluorescence intensity (Figure 2a,c,e) and fluorescence lifetime (Figure 2b,d,f) images of acute MQAE-loaded hippocampal slices following two-photon excitation. CA1 and DG astrocytes and RGL cells were identified based on SR101 fluorescence and their characteristic morphology and localization. CA1 astrocytes were imaged in the stratum radiatum and DG astrocytes in the polymorphic layer at the interface between granule cell layers. The RGL subpopulation of glial cells are easily identified by SR101 staining owing to their characteristic unipolar morphology, with a single main extension projecting through the granule cell layer, and cell body located in the subgranular zone of the DG (Mori et al., 2006; Brunne et al., 2010; Jungblut et al., 2012). They also express stem cell markers and can differentiate into either granule neurons or astrocytes (Berg et al., 2018). As glial cells accumulate MQAE to a greater extent than neurons, fluorescence intensity (Figure 2a,c,e) can also be used to identify glia in MQAE-loaded brain slices.

MQAE fluorescence is collisionally quenched by Cl^- ions, resulting in an inverse linear relationship between fluorescence lifetime and chloride concentration (Verkman, 1990):

$$\frac{\tau_0}{\tau} = 1 + K_{SV}[Cl^-]_{int}$$

where τ is the MQAE fluorescence lifetime at a given $[Cl^-]_{int}$, τ_0 is the MQAE fluorescence lifetime in the absence of chloride, and K_{SV} is the Stern–Volmer constant. MQAE is not only

quenched by Cl^-, so to account for the effects of other quenchers K_{SV} must be determined for each cell type. We calibrated MQAE lifetimes for various $[Cl^-]_{int}$ that were preset by permeabilizing the cell membrane with nigericin and tributyltin and then incubating cells in solutions containing 140 mM K^+ and the chosen $[Cl^-]$ (Chao et al., 1989; Bevensee et al., 1997; Kaneko et al., 2004; Gensch et al., 2015; Untiet et al., 2017). Linear regression analysis of the average fluorescence lifetime at different chloride concentrations ($[Cl^-]_{int}$) derived the K_{SV} and τ_0 for the three types of hippocampal astrocytes (Figure 2g, Table 1). Using the obtained K_{SV} values, we calculated average $[Cl^-]_{int}$ values (Figure 2i) of 28.4 ± 3.0 mM in 222 DG astrocytes (n = 18 slices, N = 8 animals), 20.6 ± 2.5 mM in 529 CA1 astrocytes (n = 42 slices, N = 17 animals), and 20.3 ± 0.7 mM in 596 RGL cells (n = 24 slices, N = 5 animals).

We next measured astrocytic $[Cl^-]_{int}$ in layer II/III of the neocortex (Figure 3d). The K_{SV} for MQAE in neocortical astrocytes (Table 1) is in the same range as the K_{SV} values obtained for hippocampal CA1 astrocytes and RGL cells. However, the mean $[Cl^-]_{int}$ is much smaller in neocortical astrocytes (14.0 ± 2.0 mM in 365 neocortical astrocytes, n = 19 slices, N = 6 animals) than in hippocampal astrocytes.

Taken together, these findings show a marked regional variation in resting $[Cl^-]_{int}$ in astrocytes. Moreover, $[Cl^-]_{int}$ of RGL cells are lower than of cerebellar Bergmann glia, another class of radial glial cells (Untiet et al., 2017).

Distinct chloride transport processes predominate in hippocampal and neocortical astrocytes

We recently demonstrated that chloride accumulation via the NKCC1 electroneutral cation–chloride cotransporter and chloride efflux through EAAT anion channels control $[Cl^-]_{int}$ of Bergmann glia cells (Untiet et al., 2017). EAATs are secondary-active glutamate transporters that can also function as anion channels (Fairman et al., 1995; Wadiche et al., 1995; Machtens et al., 2015; Fahlke et al., 2016). Glial cells additionally express the K^+-Cl^- co-transporters

KCC1 and KCC3 (Mount et al., 1999; Yan et al., 2001; Ringel and Plesnila, 2008) that mediate coupled potassium-chloride efflux; however, we did not observe major changes in Bergmann glia $[Cl^-]_{int}$ upon application of the specific KCC blocker *R*-(+)-DIOA (Untiet et al., 2017).

We assessed the function of these transporters in hippocampal and neocortical glia by measuring $[Cl^-]_{int}$ in the presence of specific inhibitors: i.e. 40 µM bumetanide (NKCC1 blocker) (Payne et al., 2003), 100 µM *R*-(+)-DIOA (KCC1–3 blocker) (Mercado et al., 2000), 20 µM UCPH-101 (EAAT1/GLAST blocker) (Abrahamsen et al., 2013), or 100 µM DL-TBOA (non-specific EAAT blocker) (Shimamoto et al., 1998) (Figure 4a,c,e,f). This approach is complicated by blocker fluorescence and blocker quenching of MQAE fluorescence that modify MQAE lifetimes and prevent an accurate determination of $[Cl^-]_{int}$ from standard calibration results. Therefore, we performed MQAE calibration in the presence of bumetanide, DL-TBOA, or *R*-(+)-DIOA (Figure 4b,d,f,h), and observed substantial variation in characteristic Stern–Volmer parameters for MQAE (Table 1).

These experiments distinguished two classes of glia cells, with clear differences in chloride transport. Whereas bumetanide decreased the $[Cl^-]_{int}$ to 10.9 ± 3.1 mM in CA1 (155 astrocytes n = 14 slices, N = 5 animals, p = 7.91E-08, one-way ANOVA with Holm–Sidak *post hoc* test) and 19.9 ± 1.5 mM in DG (122 astrocytes, n = 13 slices, N = 5 animals, p = 5.51E-05, one-way ANOVA with Holm–Sidak *post hoc* test), it had no significant effect on the $[Cl^-]_{int}$ of neocortical astrocytes or RGL cells. *R*-(+)-DIOA increased $[Cl^-]_{int}$ in neocortical astrocytes to 26.6 ± 8.7 mM (185 astrocytes, n = 14 slices, N = 5 animals, p = 1.37E-04, one-way ANOVA with Holm–Sidak *post hoc* test) and RGL cells to 27.9 ± 4.2 mM (132 cells, n = 14 slices, N = 5 animals, p = 1.15E-04, one-way ANOVA with Holm–Sidak *post hoc* test), but had no effect on the $[Cl^-]_{int}$ of CA1 or DG astrocytes. UCPH-101 increased $[Cl^-]_{int}$ most prominently in neocortical astrocytes (21.9 ± 2.3 mM; 141 astrocytes, n = 13 slices, N = 5 animals, p = 0.008, one-way ANOVA with Holm–Sidak *post hoc* test) and less effectively in CA1 astrocytes (25.0 ± 1.7 mM; 174 astrocytes, n = 15 slices, N = 5 animals, p = 0.003, one-way ANOVA with

Holm–Sidak *post hoc* test) and RGL cells (24.4 ± 2.5 mM; 393 astrocytes, $n = 29$ slices, $N = 7$ animals, $p = 0.013$, one-way ANOVA with Holm–Sidak *post hoc* test), but had little effect on the $[Cl^-]_{int}$ of DG astrocytes. DL-TBOA blocks both glial glutamate transporters (EAAT1/GLAST and EAAT2/GLT-1) and increased $[Cl^-]_{int}$ to a greater extent than UCPH-101 in neocortical astrocytes (25.5 ± 4.1 mM; 163 astrocytes, $n = 13$ slices, $N = 5$ animals, $p =$ 3.37E-04, one-way ANOVA with Holm–Sidak *post hoc* test) and significantly increased the $[Cl^-]_{int}$ of RGL cells (32.8 ± 2.7 mM; 105 astrocytes, $n = 12$ slices, $N = 5$ animals, $p =$ 1.09E-08, one-way ANOVA with Holm–Sidak *post hoc* test). DL-TBOA had no apparent effect on astrocytic $[Cl^-]_{int}$ in the hippocampus.

We conclude that differences in the resting $[Cl^-]_{int}$ of different astroglial cell types are associated with variation in the expression of Cl^- import and export/efflux pathway proteins.

Chemical ischemia has only slight effects on glial $[Cl^-]_{int}$

Secondary-active transporters exploit existing concentration gradients of certain substrates to transport other substrates against their chemical gradients. NKCC and KCC transporters are driven by Na^+ and/or K^+ gradients established by the ubiquitous Na^+-K^+-ATPase (Verkhratsky et al., 2020). Na^+-K^+-ATPase consumes one ATP per transport cycle, making cellular ATP levels a critical determinant of extra- and intracellular $[Na^+]$ and $[K^+]$. The majority of ATP is produced by oxidative phosphorylation, so that oxygen restriction reduces cellular ATP energy production within short time. Reduced ATP may increase $[Na^+]_{int}$ and $[K^+]_{out}$ (Hertz et al., 2015; Gerkau et al., 2017), reduce the membrane potential and thus modify transport processes involved in the chloride homeostasis of glia cells.

Ischemic stroke, resulting from insufficient cerebral perfusion, is a leading cause of disability and death in our aging population. The consequences of ischemia depend on severity of cell damage: extensive cell death occurs in the core ischemic zone, whereas cells in the ischemic penumbra may recover after reperfusion. We studied the effects of transient energy

restriction in the ischemic penumbra by first removing glucose, blocking oxidative phosphorylation with sodium azide, and blocking glycolysis with 2-deoxy-D-glucose (Gerkau et al., 2018). We then measured $[Cl^-]_{int}$ under perfusion with oxygenated standard Ringer's solution. To quantify the degree of inhibition of cellular ATP production, we expressed the ATP-sensitive fluorescence resonance energy transfer (FRET)-based sensor ATeam1.03^{YEMK} in astrocytes in organotypic brain slices (Lerchundi et al., 2019) (Figure 5a). After exposure to sodium azide and 2-deoxy-D-glucose (Figure 5b), the ATeam ratio was reduced by 18.2% ± 7.0% (21 cells, n = 3 slices, N = 3 animals) within 0.5 min, by 43.6 ± 7.0% (27 cells, n = 4 slices, N = 4 animals, p = 2.225E-16, one-way ANOVA with Bonferroni *post hoc* test) after 2 min and by 55.1 ± 5.8% (18 cells, n = 3 slices, N = 3 animals, p = 8.539E-7, one-way ANOVA with Bonferroni *post hoc* test) after 5 min (Figure 5c). This finding confirms that chemical block of oxidative phosphorylation and glycolysis effectively reduces the cellular ATP content.

Figure 6 shows changes in the glial $[Cl^-]_{int}$ after chemical ischemia for 2, 5, and 10 min. In CA1 astrocytes and RGL cells, the $[Cl^-]_{int}$ remained constant at all three time points. In DG astrocytes, we observed a transient increase at 2 min (p = 0.007, one-way ANOVA with Holm–Sidak *post hoc* test) after chemical ischemia that returned to physiological levels at 5 or 10 min. In neocortical astrocytes, an increase in $[Cl^-]_{int}$ occurred after 10 min of chemical ischemia (p = 0.008, one-way ANOVA with Holm–Sidak *post hoc* test). To define the contribution of specific chloride transporters to glial $[Cl^-]_{int}$ control during chemical ischemia, we measured the combined effect of restricted ATP supply and specific chloride transport blockers (Figure 7 and Figure 8). In neocortical astrocytes, bumetanide alone had no effect, but bumetanide pre-treatment decreased $[Cl^-]_{int}$ after chemical ischemia (Figure 7g, 2min: p = 6.53E-04, 5 min p = 9.78E-04, one-way ANOVA with Holm–Sidak *post hoc* test), consistent with additional upregulation of Cl^- efflux/outward transport pathways. As *R*-(+)-DIOA caused a dramatic increase of $[Cl^-]_{int}$ under ischemic conditions (Figure 7h, 10min: p = 0.002, one-way ANOVA with Holm–Sidak *post hoc* test), but UCPH-101 (Figure 8g, 2min: p = 0.006, one-way ANOVA

with Holm–Sidak *post hoc* test) and DL-TBOA did not (Figure 8h), we conclude that both NKCC1 and KCCs are activated during ischemia in neocortical astrocytes. These transporters mediate chloride transport in opposite directions and thus partially compensate for each other, resulting in only a limited increase in the $[Cl^-]_{int}$ under energy restriction. Similar, but less pronounced effects were observed in RGL cells (Figure 7e,f and Figure 8e,f, (f) 5min: $p = 0.005$, one-way ANOVA with Holm–Sidak *post hoc* test). Surprisingly, chemical ischemia had no pronounced effect on $[Cl^-]_{int}$ in CA1 and in DG astrocytes after pre-treatment with specific transport blockers (CA1: Figure 7a and b, 2min: $p = 0.005$, one-way ANOVA with Holm–Sidak *post hoc* test, Figure 8a and b; DG: Figure 7c, Figure 8c and d). Only in DG astrocytes we observed an increase of the mean $[Cl^-]_{int}$ at 10 min after ischemic conditions and a pre-treatment with *R*-(+)-DIOA (Figure 7d, $p = 1.94E-05$, one-way ANOVA with Holm–Sidak *post hoc* test).

Astrocytic volume changes during energy restriction

Cl^- is the main physiological anion and is a major determinant of cell swelling and regulatory volume changes. The largely unaltered $[Cl^-]_{int}$ is not expected to cause significant changes in volume during transient energy restriction. To confirm this observation, we next stained acute tissue slices of the neocortex with SR101 to label astrocytes and generated maximum intensity projections from Z-stacks (0.6 µm increments) by confocal microscopy (Figure 9a,c). Chemical ischemia for up to 10 min (measured with 5 min delay) did not change the mean width of astrocyte somata (Figure 9b, 18 cells, $n = 5$ slices, $N = 5$ animals; control-ischemia: $p = 0.275$; ischemia-recovery: $p = 0.619$; control-recovery: $p = 0.894$, one-way ANOVA with Bonferroni *post hoc* test) or cause strong delocalization or deformation of astrocytic extensions (Figure 9a). Notably, some cells swelled, whereas the soma size of others decreased (Figure 9b). As a control, we transiently perfused slices with hypo-osmotic saline (220 mOsm/L) for 10 min. Hypo-osmotic stress resulted in a significant increase in the width of astrocyte somata from 5.3 ± 0.8 µm to 6.0 ± 1.1 µm (Figure 9d, 16 cells, $n = 13$ slices, $N = 7$ animals; control-hypo: $p =$

1.77E-05; hypo-recovery: p = 2.54E-09; control-recovery: p = 0.008, one-way ANOVA with Bonferroni *post hoc* test), which was fully reversible (Figure 9c,d). In addition, primary and secondary astrocyte processes were strongly displaced (Figure 9c).

Taken together, these results indicate that neocortical layer II/III astrocytes respond heterogeneously to transient chemical ischemia, but that the overall population does not undergo major changes in somatic volume.

Mathematical modeling reveals how differences in anion transporter numbers can cause cell-specific responses to transient ischemia

To understand how differences in anion transporter expression might shape the response to transient energy restriction, we used a recently developed quantitative model of a glutamatergic synapse to identify key determinants of synaptic failure during energy deprivation (Kalia et al., 2021). To account for the clear effects of *R*-(+)-DIOA-dependent KCC block on $[Cl^-]_{int}$, the model was expanded by inserting KCC co-transporters as an additional Cl^- transport system into astrocytes.

Figure 10 shows simulations of ischemia-related changes in $[Cl^-]_{int}$ in cortical and in DG astrocytes. We chose these two types of astrocytes because they represent two extremes in both resting $[Cl^-]_{int}$ and changes in $[Cl^-]_{int}$ following the selective inhibition of anion transporters. Ischemia was simulated by blocking Na^+-K^+-ATPase in both neurons and astrocytes to 50% of baseline pumping capacity. In the model, astrocytes were subjected to energy deprivation for 5 or 10 min and then allowed to recover for 15 or 10 min, respectively (Figure 10b; gray shading). Alternatively, astrocytes are treated with bumetanide (to block NKCC1), *R*-(+)-DIOA (to block astrocytic KCCs), or DL-TBOA (to block neuronal and astrocyte EAAT) for 20 min (green region), followed by energy deprivation for 10 min (gray block), and then another 30 min of transport block after energy restoration (Figure 10c).

As NKCC1 is the dominant Cl^- influx pathway and KCC the dominant Cl^- efflux pathway in our model, we manipulated resting $[Cl^-]_{int}$ and changes of $[Cl^-]_{int}$ in response to energy restriction by varying the efflux rates of these two co-transporters. Figure 10a shows a log–log plot of the NKCC1 and KCC flux rates. Within this two-parameter space, we found two distinct regions corresponding to our $[Cl^-]_{int}$ measured in cortical and DG astrocytes: cortical results were well described by higher KCC expression (approximately 10 times) in astrocytes than in neurons; and results for DG astrocytes were well described by lower expression of both NKCC1 (about 10 times lower than in the cortex) and KCC (about 100 times lower than neuronal KCC). These adjustments gave correct predictions for resting $[Cl^-]_{int}$ in the two different brain regions and for the ischemic response in the absence or presence of blockers (Figure 10b,c). In response to transient ischemia for 5 or 10 min, DG hippocampal astrocytes had only a slight response to transient energy restriction. In contrast, cortical astrocytes underwent a transient increase in $[Cl^-]_{int}$ that was fully reversible by restoring primary-active Na+-K+-transport after 5 min (but not after 10 min) of energy restriction (Figure 10b). These findings are in good agreement with our experimental results (Figure 6).

Bumetanide triggered Cl^- efflux in both brain regions (cortex and DG), but the effect on $[Cl^-]_{int}$ was more pronounced for cortical astrocytes (-67% change relative to baseline; Figure 10c, upper panel) than for DG astrocytes (-5% relative to baseline; Figure 10c, lower panel). The subsequent induction of ischemia caused a sharp increase in $[Cl^-]_{int}$ in cortical astrocytes, that was partially reversed when normal ATPase function was restored. In DG astrocytes, the predicted $[Cl^-]_{int}$ was largely unaffected by bumetanide treatment. *R*-(+)-DIOA caused massive Cl^- influx into the cortex (+300% of baseline), which was further enhanced by ischemic conditions and not reversed by energy restoration. In contrast, *R*-(+)-DIOA caused only minor changes in $[Cl^-]_{int}$ in DG astrocytes. The effect of DL-TBOA was simulated by blocking both neuronal and astrocyte glutamate transport and partially blocking astrocytic Cl^- leak currents. In the cortex, DL-TBOA caused a sharp increase in $[Cl^-]_{int}$, followed by a plateau (at +200% of

baseline). In contrast, in the DG, DL-TBOA caused a slow rise to +5% of baseline at the end of the ischemic block. The EAAT anion conductance is modeled as part of a glial resting anion conductance (leak conductance). Since the exact contribution of EAAT anion channels to the total resting anion conductance is unknown, we varied the degree of resting conductance blockade by DL-TBOA, but found no discernible differences. These findings suggest that DL-TBOA mostly affects neuronal and glial glutamate transport, whereas changes in the glial resting conductance have only minor effects on $[Cl^-]_{int}$.

These results are in good agreement with our experimental results (shown in Figure 7 and Figure 8). We conclude that region-specific differences in glial chloride homeostasis can be explained by differences in the expression of specific inward and outward chloride transporters.

Discussion

We used fluorescence lifetime imaging microscopy to study chloride homeostasis in hippocampal and neocortical glial cells in acute brain slices. We observed region- and cell-type specific $[Cl^-]_{int}$ under both control conditions and chemical ischemia. The resting $[Cl^-]_{int}$ of astrocytes in the hippocampal CA1 (20.6 ± 2.5 mM) was lower than in DG astrocytes (28.4 ± 3.0 mM), but higher than in neocortical astrocytes (14.0 ± 2.0 mM). The $[Cl^-]_{int}$ in RGL cells (20.3 ± 0.7 mM) was comparable to values in CA1 astrocytes. These values are significantly lower than previously determined for cerebellar Bergmann glia cells (Untiet et al., 2017) and lower than those reported for glial cells in culture (Kimelberg, 1981; Smith et al., 1981; Kettenmann et al., 1987; Walz and Mukerji, 1988; Bevensee et al., 1997; Bekar and Walz, 2002). Blocking NKCC1 with bumetanide decreased the $[Cl^-]_{int}$ in hippocampal astrocytes, but not in neocortical astrocytes or RGL cells (Figure 4 a,c,e,d). Whereas blockers of KCCs and EAAT chloride outward transport/efflux pathways did not affect the $[Cl^-]_{int}$ in DG astrocytes, K^+-Cl^- co-transport as well as EAAT1/GLAST- and EAAT2/GLT-1-mediated anion currents were found to substantially contribute to $[Cl^-]_{int}$ in RGLs and neocortical astrocytes. In CA1 astrocytes, inhibition of EAAT anion channels, but not of KCCs, significantly changed the $[Cl^-]_{int}$. These results indicate that chloride accumulation by NKCC1, as well as chloride outward transport by KCCs and outward flux via two glial EAAT isoforms, EAAT1/GLAST and EAAT2/GLT-1, control glial $[Cl^-]_{int}$. The observed alterations in chloride concentration after blocking EAAT anion channels emphasize the importance of glutamate transporters for chloride homeostasis (Untiet et al., 2017; Kovermann et al., 2020).

We used the quinolinium-based fluorescent indicator MQAE to study cytoplasmic $[Cl^-]$ (Verkman, 1990; Biwersi and Verkman, 1991; Woll et al., 1996; Kaneko et al., 2004; Untiet et al., 2016). Quinolinium-based fluorescent indicators are unaffected by H^+ and OH^- (Verkman et al., 1989; Koncz and Daugirdas, 1994) and collisionally quenched by Cl^-, resulting in a linear

inverse relationship between fluorescence lifetime and chloride concentration (Verkman, 1990; Gensch et al., 2015) and allowing accurate measurements over a broad range of $[Cl^-]$. All cells contain additional quenchers of MQAE, and to account for differing levels of MQAE quenchers, we performed specific calibrations for all cell types studied (Figure 2g, Figure 3c, Table 1). The differences in calibration curves between DG astrocytes and the other tested glial cells illustrate the importance of calibrating every cell type in which $[Cl^-]_{int}$ will be determined.

We showed that chemical blockade of oxidative and non-oxidative phosphorylation resulted in significantly decreased cellular [ATP] (Figure 5). ATP shortage results in increased external $[K^+]$ (Hertz et al., 2015) and [glutamate] (Belov Kirdajova et al., 2020) and increased internal $[Na^+]$ (Gerkau et al., 2017). We expected these changes to modify the transport activities of NKCC1 and KCCs, as well as the open probability of EAAT anion channels, thereby changing glial $[Cl^-]_{int}$. However, despite this prediction, chemical ischemia did not cause major changes in glial $[Cl^-]_{int}$ (Figure 6). The use of specific blockers allowed the identification of changes in chloride transport during energy restriction and their effect on chloride homeostasis. In neocortical astrocytes, the reduction in $[Cl^-]_{int}$ caused by bumetanide was greater under ischemic conditions (Figure 7g; 2 min: 8.1 ± 1.3 mM; 5 min: 8.3 ± 0.7; 10 min: 9.6 ± 1.3 mM) than under control conditions. In the same cells, and ischemia caused the $[Cl^-]_{int}$ to increase (2 min: 43.4 ± 20.3 mM; 5 min: 52.2 ± 27.9 mM; 10 min 64.3 ± 12.8 mM) in the presence of the *R*-(+)-DIOA KCC blocker (Figure 7h). These results indicate that under ischemic conditions, KCC-mediated outward transport compensates for an increase in NKCC1-mediated inward transport. In DG astrocytes and RGL cells, major changes in $[Cl^-]_{int}$ were only observed after 10 min of ischemia in the presence of *R*-(+)-DIOA (Figure 7d 10 min: 48.2 ± 10.9 mM; 7f 10 min: 33.0 ± 9.0 mM). Under all other experimental conditions, ischemia-mediated changes in transport properties remained below the experimental resolution limit in hippocampal astrocytes and RGL cells. In all cases, blocking EAAT anion channels under ischemic conditions had only minor effects on $[Cl^-]_{int}$ (Figure 8), indicating that changes in

EAAT anion current amplitudes are not major contributors to chloride homeostasis under ischemia.

We observed marked differences in $[Cl^-]_{int}$ between the studied glial cells, ranging from 14 mM to 28 mM. The use of a mathematical model that describes ionic changes in the tripartite synapse under ischemia permitted to propose a surprisingly simple cellular basis of the different responses of glial $[Cl^-]_{int}$ in cortex and hippocampus. We could reproduce glia type-specific differences in resting $[Cl^-]_{int}$ as well as in ischemia and transport-block induced changes of this parameter by modifying expression levels of NKCC1 and KCCs (Figure 10). Our results suggest that expression levels of these two chloride transport systems are much higher in the cortex than in the hippocampus. High levels of NKCC1 in neocortical astrocytes thus result in lower $[Cl^-]_{int}$ than low levels in DG astrocytes. In our modeling, $[Cl^-]_{int}$ was assumed to be in dynamic equilibrium between Cl^- inward and outward movement. This simplifying view neglects the role of water co-transport through chloride channels and transporters and the importance of fixed charges inside and outside the cell in setting intracellular $[Cl^-]$ (Delpire and Staley, 2014; Glykys et al., 2014). However, although this simplification prevents exact quantification of relative numbers of CCC transporters in distinct glia types, it still permits predicting changes in $[Cl^-]_{int}$ upon block of distinct chloride transporters.

Glia express GAT1 and GAT3 GABA transporters that couple the movement of GABA to the transport of Na^+ and Cl^- ions (Zomot et al., 2007; Zhou and Danbolt, 2013). The observed differences in $[Cl^-]_{int}$ predict that external resting [GABA] is about 50% lower in the cortex than in the DG region. The physiological relevance of this difference is not currently understood. Since a regulatory volume decrease requires Cl^- efflux (Grinstein et al., 1982; Mongin, 2016; Wilson and Mongin, 2018), neocortical astrocytes appear to be less competent in regulating volume. They are also more sensitive to energy restriction. Only minor changes in $[Cl^-]_{int}$ were seen in DG astrocytes in response to energy restriction. In contrast, under the

same conditions the $[Cl^-]_{int}$ increased significantly in cortical astrocytes, which was rapidly reversed when the energy supply was restored after 5 min (Figure 10b).

NKCC1 transport is regulated by external $[K^+]$ and internal $[Na^+]$ and $[Cl^-]$, as well as by cell shrinkage and by activation of metabotropic glutamate receptors (Delpire, 2000; Payne et al., 2003). Increased external $[K^+]$ and internal $[Na^+]$ are well established under experimental ischemic conditions, making elevated external $[K^+]$ a likely first step in NKCC1 activation. The resulting changes in $[Cl^-]_{int}$ are counteracted by KCCs: after *R*-(+)-DIOA pre-treatment, we observed increased $[Cl^-]_{int}$ followed by cell swelling upon ischemia. Comparison of the experimental (Figure 4,6-8) and modeling results (Figure 10) indicates that $[Cl^-]_{int}$ changes upon transient energy restriction can be fully described without assuming regulatory changes in the number of active transporters. Mere adjustment of NKCC1 and KCC transport rates by changing the driving force via altered ion concentrations predicts $[Cl^-]_{int}$ that are in good agreement with our experimental results. We assume that increased EAAT anion channel activity due to higher [glutamate] and changes in the membrane potential due to rises in $[K^+]_{ext}$ largely compensate for each other (Rossi et al., 2007; Rakers et al., 2017). Glial cells are generally agreed to swell under severe energy restriction, thus driving edema during brain ischemia (Andrew et al., 2007; Risher et al., 2009). Since volume changes require water fluxes based on electroneutral electrolyte fluxes, cell swelling is not possible without Cl^- flux and changes in $[Cl^-]_{int}$. Under transient energy restriction, we observed major changes in neither $[Cl^-]_{int}$ (Figure 6) nor cell volume (Figure 9). Since we have measured $[Cl^-]_{int}$ only in glial somata so far, we cannot predict how $[Cl^-]_{int}$ will vary in glial extensions under energy restrictions.

In summary, we have quantified intracellular $[Cl^-]$ in hippocampal and cortical astrocytes as well as in radial-like glia cells in acute brain slices under resting conditions and transient energy restriction. We observed distinct $[Cl^-]_{int}$ in different glia cell types under resting conditions and no major changes during chemical ischemia. Thus, glia cells can control

internal chloride concentrations and support cell volume stability under transient energy deprivation.

References

Abrahamsen B, Schneider N, Erichsen MN, Huynh TH, Fahlke C, Bunch L, Jensen AA (2013) Allosteric modulation of an excitatory amino acid transporter: the subtype-selective inhibitor UCPH-101 exerts sustained inhibition of EAAT1 through an intramonomeric site in the trimerization domain. J Neurosci 33:1068-1087.

Adamczyk A, Gause CD, Sattler R, Vidensky S, Rothstein JD, Singer H, Wang T (2011) Genetic and functional studies of a missense variant in a glutamate transporter, SLC1A3, in Tourette syndrome. Psychiat Gen 21:90-97.

Andrew RD, Labron MW, Boehnke SE, Carnduff L, Kirov SA (2007) Physiological evidence that pyramidal neurons lack functional water channels. Cereb Cortex 17:787-802.

Bekar LK, Walz W (2002) Intracellular chloride modulates A-type potassium currents in astrocytes. Glia 39:207-216.

Belov Kirdajova D, Kriska J, Tureckova J, Anderova M (2020) Ischemia-triggered glutamate excitotoxicity from the perspective of glial cells. Front Cell Neurosci 14:51.

Berg DA, Bond AM, Ming GL, Song H (2018) Radial glial cells in the adult dentate gyrus: what are they and where do they come from? F1000Research 7:277.

Bevensee MO, Apkon M, Boron WF (1997) Intracellular pH regulation in cultured astrocytes from rat hippocampus. II. Electrogenic Na/HCO3 cotransport. J Gen Physiol 110:467-483.

Biwersi J, Verkman AS (1991) Cell-permeable fluorescent indicator for cytosolic chloride. Biochemistry 30:7879-7883.

Brunne B, Zhao S, Derouiche A, Herz J, May P, Frotscher M, Bock HH (2010) Origin, maturation, and astroglial transformation of secondary radial glial cells in the developing dentate gyrus. Glia 58:1553-1569.

Chao AC, Dix JA, Sellers MC, Verkman AS (1989) Fluorescence measurement of chloride transport in monolayer cultured cells. Mechanisms of chloride transport in fibroblasts. Biophys J 56:1071-1081.

Chivukula AS, Suslova M, Kortzak D, Kovermann P, Fahlke C (2020) Functional consequences of SLC1A3 mutations associated with episodic ataxia 6. Hum Mutat 41, 1892-1905

Deitmer JW, Rose CR (2010) Ion changes and signalling in perisynaptic glia. Brain Res Rev 63:113-129.

Delpire E (2000) Cation-chloride cotransporters in neuronal communication. News Physiol Sci 15:309-312.

Delpire E, Gagnon KB (2018) Water homeostasis and cell volume maintenance and regulation. Curr Top Membr 81:3-52.

Delpire E, Staley KJ (2014) Novel determinants of the neuronal Cl(-) concentration. J Physiol 592:4099-4114.

Dijkstra K, Hofmeijer J, van Gils SA, van Putten MJ (2016) A biophysical model for cytotoxic cell swelling. J Neurosci 36:11881-11890.

Fahlke C, Kortzak D, Machtens JP (2016) Molecular physiology of EAAT anion channels. Pflugers Arch 468:491-502.

Fairman WA, Vandenberg RJ, Arriza JL, Kavanaugh MP, Amara SG (1995) An excitatory amino-acid transporter with properties of a ligand-gated chloride channel. Nature 375:599-603.

Funk K, Woitecki A, Franjic-Würtz C, Gensch T, Möhrlen F, Frings S (2008) Modulation of chloride homeostasis by inflammatory mediators in dorsal root ganglion neurons. Mol Pain 4:32.

Gensch T, Untiet V, Franzen A, Kovermann P, Fahlke C (2015) Determination of intracellular chloride concentrations by Fluorescence Lifetime Imaging. In: Advanced Time-Correlated Single Photon Counting Applications, pp 189-211: Springer.

Gerkau NJ, Rakers C, Petzold GC, Rose CR (2017) Differential effects of energy deprivation on intracellular sodium homeostasis in neurons and astrocytes. J Neuroscience Res 95:2275-2285.

Gerkau NJ, Rakers C, Durry S, Petzold GC, Rose CR (2018) Reverse NCX attenuates cellular sodium loading in metabolically compromised cortex. Cereb Cortex 28:4264-4280.

Gilbert D, Franjic-Würtz C, Funk K, Gensch T, Frings S, Möhrlen F (2007) Differential maturation of chloride homeostasis in primary afferent neurons of the somatosensory system. Int J Dev Neurosci 25:479-489.

Glykys J, Dzhala V, Egawa K, Balena T, Saponjian Y, Kuchibhotla KV, Bacskai BJ, Kahle KT, Zeuthen T, Staley KJ (2014) Local impermeant anions establish the neuronal chloride concentration. Science 343:670-675.

Grinstein S, Clarke CA, Dupre A, Rothstein A (1982) Volume-induced increase of anion permeability in human lymphocytes. J Gen Physiol 80:801-823.

Guella I, McKenzie MB, Evans DM, Buerki SE, Toyota EB, Van Allen MI, Epilepsy Genomics S, Suri M, Elmslie F, Deciphering Developmental Disorders S, Simon MEH, van Gassen KLI, Héron D, Keren B, Nava C, Connolly MB, Demos M, Farrer MJ (2017) De Novo Mutations in YWHAG Cause Early-Onset Epilepsy. Am J Hum Genet 101:300-310.

Hertz L, Gerkau NJ, Xu J, Durry S, Song D, Rose CR, Peng L (2015) Roles of astrocytic Na^+,K^+-ATPase and glycogenolysis for K^+ homeostasis in mammalian brain. J Neurosci Res 93:1019-1030.

Imamura H, Nhat KP, Togawa H, Saito K, Iino R, Kato-Yamada Y, Nagai T, Noji H (2009) Visualization of ATP levels inside single living cells with fluorescence resonance energy transfer-based genetically encoded indicators. Proc Natl Acad Sci USA 106:15651-15656.

Jen JC, Wan J, Palos TP, Howard BD, Baloh RW (2005) Mutation in the glutamate transporter EAAT1 causes episodic ataxia, hemiplegia, and seizures. Neurology 65:529-534.

Jungblut M, Tiveron MC, Barral S, Abrahamsen B, Knöbel S, Pennartz S, Schmitz J, Perraut M, Pfrieger FW, Stoffel W, Cremer H, Bosio A (2012) Isolation and characterization of living primary astroglial cells using the new GLAST-specific monoclonal antibody ACSA-1. Glia 60:894-907.

Kafitz KW, Meier SD, Stephan J, Rose CR (2008) Developmental profile and properties of sulforhodamine 101--Labeled glial cells in acute brain slices of rat hippocampus. J Neurosci Meth 169:84-92.

Kahle KT, Khanna AR, Alper SL, Adragna NC, Lauf PK, Sun D, Delpire E (2015) K-Cl cotransporters, cell volume homeostasis, and neurological disease. Trends Mol Med 21:513-523.

Kalia M, Meijer HGE, Van Gils SA, van Putten MJ, Rose CR Ion dynamics at the tripartite synapse. bioRxiv doi: 10.1101/2021.03.19.436129v1

Kaneko H, Putzier I, Frings S, Gensch T (2002) Determination of intracellular chloride concentration in dorsal root ganglion neurons by fluorescence lifetime imaging. In: Calcium-activated chloride channels (Fuller CM, ed), pp 163-185 San Diego: Elsevier Academic Press

Kaneko H, Putzier I, Frings S, Kaupp UB, Gensch T (2004) Chloride accumulation in mammalian olfactory sensory neurons. J Neurosci 24:7931-7938.

Kettenmann H, Backus KH, Schachner M (1987) gamma-Aminobutyric acid opens Cl-channels in cultured astrocytes. Brain Res 404:1-9.

Kimelberg HK (1981) Active accumulation and exchange transport of chloride in astroglial cells in culture. Biochim Biophys Acta 646:179-184.
Koncz C, Daugirdas JT (1994) Use of MQAE for measurement of intracellular [Cl^-] in cultured aortic smooth muscle cells. Am J Physiol 267:H2114-2123.
Kovalchuk Y, Garaschuk O (2012) Two-photon chloride imaging using MQAE in vitro and in vivo. Cold Spring Harb Protoc 2012:778-785.
Kovermann P, Hessel M, Kortzak D, Jen JC, Koch J, Fahlke C, Freilinger T (2017) Impaired K^+ binding to glial glutamate transporter EAAT1 in migraine. Sci Rep 7:13913.
Kovermann P, Untiet V, Kolobkova Y, Engels M, Baader S, Schilling K, Fahlke C (2020) Increased glutamate transporter-associated anion currents cause glial apoptosis in episodic ataxia 6. Brain Commun 2, fcaa022.
Lang F, Lepple-Wienhues A, Paulmichl M, Szabó I, Siemen D, Gulbins E (1998) Ion channels, cell volume, and apoptotic cell death. Cell Physiol Biochem 8:285-292.
Lerchundi R, Kafitz KW, Winkler U, Färfers M, Hirrlinger J, Rose CR (2019) FRET-based imaging of intracellular ATP in organotypic brain slices. J Neurosci Res 97:933-945.
MacAulay N, Zeuthen T (2010) Water transport between CNS compartments: contributions of aquaporins and cotransporters. Neuroscience 168:941-956.
Machtens JP, Kortzak D, Lansche C, Leinenweber A, Kilian P, Begemann B, Zachariae U, Ewers D, de Groot BL, Briones R, Fahlke C (2015) Mechanisms of anion conduction by coupled glutamate transporters. Cell 160:542-553.
Maus M, Cotlet M, Hofkens J, Gensch T, De Schryver FC, Schaffer J, Seidel CA (2001) An experimental comparison of the maximum likelihood estimation and nonlinear least-squares fluorescence lifetime analysis of single molecules. Anal Chem 73:2078-2086.
Mercado A, Song L, Vazquez N, Mount DB, Gamba G (2000) Functional comparison of the K^+-Cl^- cotransporters KCC1 and KCC4. J Biol Chem 275:30326-30334.
Mongin AA (2016) Volume-regulated anion channel--a frenemy within the brain. Pflugers Arch Eur J Phy 468:421-441.
Mongin AA, Orlov SN (2001) Mechanisms of cell volume regulation and possible nature of the cell volume sensor. Pathophysiology 8:77-88.
Mori T, Tanaka K, Buffo A, Wurst W, Kühn R, Götz M (2006) Inducible gene deletion in astroglia and radial glia--a valuable tool for functional and lineage analysis. Glia 54:21-34.
Mount DB, Mercado A, Song L, Xu J, George AL, Jr., Delpire E, Gamba G (1999) Cloning and characterization of KCC3 and KCC4, new members of the cation-chloride cotransporter gene family. J Biol Chem 274:16355-16362.
Nagelhus EA, Ottersen OP (2013) Physiological roles of aquaporin-4 in brain. Physiol Rev 93:1543-1562.
Papadopoulos MC, Verkman AS (2013) Aquaporin water channels in the nervous system. Nature Rev Neurosci 14:265-277.
Pasantes-Morales H (2016) Channels and volume changes in the life and death of the cell. Mol Pharmacol 90:358-370.
Payne JA, Rivera C, Voipio J, Kaila K (2003) Cation-chloride co-transporters in neuronal communication, development and trauma. Trends Neurosci 26:199-206.
Rakers C, Schmid M, Petzold GC (2017) TRPV4 channels contribute to calcium transients in astrocytes and neurons during peri-infarct depolarizations in a stroke model. Glia 65:1550-1561.
Ringel F, Plesnila N (2008) Expression and functional role of potassium-chloride cotransporters (KCC) in astrocytes and C6 glioma cells. Neurosci Lett 442:219-223.
Risher WC, Andrew RD, Kirov SA (2009) Real-time passive volume responses of astrocytes to acute osmotic and ischemic stress in cortical slices and in vivo revealed by two-photon microscopy. Glia 57:207-221.

Rossi DJ, Brady JD, Mohr C (2007) Astrocyte metabolism and signaling during brain ischemia. Nat Neurosci 10:1377-1386.

Schindelin J, Arganda-Carreras I, Frise E, Kaynig V, Longair M, Pietzsch T, Preibisch S, Rueden C, Saalfeld S, Schmid B, Tinevez JY, White DJ, Hartenstein V, Eliceiri K, Tomancak P, Cardona A (2012) Fiji: an open-source platform for biological-image analysis. Nature Meth 9:676-682.

Shimamoto K, Lebrun B, Yasuda-Kamatani Y, Sakaitani M, Shigeri Y, Yumoto N, Nakajima T (1998) DL-threo-beta -benzyloxyaspartate, a potent blocker of excitatory amino acid transporters. Mol Pharmacol 53:195-201.

Smith QR, Johanson CE, Woodbury DM (1981) Uptake of ^{36}Cl and ^{22}Na by the brain-cerebrospinal fluid system: comparison of the permeability of the blood-brain and blood-cerebrospinal fluid barriers. J Neurochem 37:117-124.

Song S, Luo L, Sun B, Sun D (2020) Roles of glial ion transporters in brain diseases. Glia 68:472-494.

Stergachis AB, Pujol-Giménez J, Gyimesi G, Fuster D, Albano G, Troxler M, Picker J, Rosenberg PA, Bergin A, Peters J, El Achkar CM, Harini C, Manzi S, Rotenberg A, Hediger MA, Rodan LH (2019) Recurrent SLC1A2 variants cause epilepsy via a dominant negative mechanism. Ann Neurol 85:921-926.

Stokum JA, Gerzanich V, Simard JM (2016) Molecular pathophysiology of cerebral edema. J Cereb Blood Flow Metab 36:513-538.

Stoppini L, Buchs PA, Muller D (1991) A simple method for organotypic cultures of nervous tissue. J Neurosci Methods 37:173-182.

Toft-Bertelsen TL, Larsen BR, Christensen SK, Khandelia H, Waagepetersen HS, MacAulay N (2021) Clearance of activity-evoked K^+ transients and associated glia cell swelling occur independently of AQP4: A study with an isoform-selective AQP4 inhibitor. Glia 69:28-41.

Untiet V, Kovermann P, Gerkau NJ, Gensch T, Rose CR, Fahlke C (2017) Glutamate transporter-associated anion channels adjust intracellular chloride concentrations during glial maturation. Glia 65:388-400.

van Amen-Hellebrekers CJ, Jansen S, Pfundt R, Schuurs-Hoeijmakers JH, Koolen DA, Marcelis CL, de Leeuw N, de Vries BB (2016) Duplications of SLC1A3: Associated with ADHD and autism. Eur J Med Genet 59:373-376.

Verkhratsky A, Untiet V, Rose CR (2020) Ionic signalling in astroglia beyond calcium. J Physiol 598:1655-1670.

Verkman AS (1990) Development and biological applications of chloride-sensitive fluorescent indicators. Am J Physiol 259:C375-388.

Verkman AS, Sellers MC, Chao AC, Leung T, Ketcham R (1989) Synthesis and characterization of improved chloride-sensitive fluorescent indicators for biological applications. Anal Biochem 178:355-361.

Wadiche JI, Amara SG, Kavanaugh MP (1995) Ion fluxes associated with excitatory amino acid transport. Neuron 15:721-728.

Walz W, Mukerji S (1988) KCl movements during potassium-induced cytotoxic swelling of cultured astrocytes. Exp Neurol 99:17-29.

Wilson CS, Mongin AA (2018) Cell volume control in healthy brain and neuropathologies. Curr Top Membr 81:385-455.

Woll E, Gschwentner M, Furst J, Hofer S, Buemberger G, Jungwirth A, Frick J, Deetjen P, Paulmichl M (1996) Fluorescence-optical measurements of chloride movements in cells using the membrane-permeable dye diH-MEQ. Pflugers Arch Eur J Phy 432:486-493.

Yan Y, Dempsey RJ, Sun D (2001) Expression of Na^+-K^+-Cl^- cotransporter in rat brain during development and its localization in mature astrocytes. Brain Res 911:43-55.

Zhou Y, Danbolt NC (2013) GABA and glutamate transporters in brain. Front Endocrinol 4:165.
Zipfel WR, Williams RM, Webb WW (2003) Nonlinear magic: multiphoton microscopy in the biosciences. Nature Biotechnol 21:1369-1377.
Zomot E, Bendahan A, Quick M, Zhao Y, Javitch JA, Kanner BI (2007) Mechanism of chloride interaction with neurotransmitter:sodium symporters. Nature 449:726-730.

Tables

Table 1. MQAE calibration under physiological conditions or in presence of bumetanide, DL-TBOA, or *R*-(+)-DIOA, results in substantial variation in K_{SV} and τ_0. Abbreviations: CA1 – cornu ammonis region 1; DG – dentate gyrus; RGL – radial glial-like cells; K_{SV} = Stern-Volmer constants; τ_0 = fluorescence lifetime in the absence of a quencher/chloride

Brain Region	CA1		DG		RGL		Cortex	
Parameter	K_{SV} in M^{-1}	τ_0 in ns	K_{SV} in M^{-1}	τ_0 in ns	K_{SV} in M^{-1}	τ_0 in ns	K_{SV} in M^{-1}	τ_0 in ns
physiological	18.56	6.63	16.85	7.02	20.66	6.67	18.11	6.24
Bumetanide (40 µm)	17.89	5.42	22.06	6.3	22.65	6.29	13.18	5.07
DL-TBOA (100 µm)	17.79	5.73	17.35	5.78	18.65	5.83	17.01	5.49
R-(+)-DIOA (100 µm)	15.99	5.51	17.69	5.71	17.42	5.62	18.29	5.54

Figures

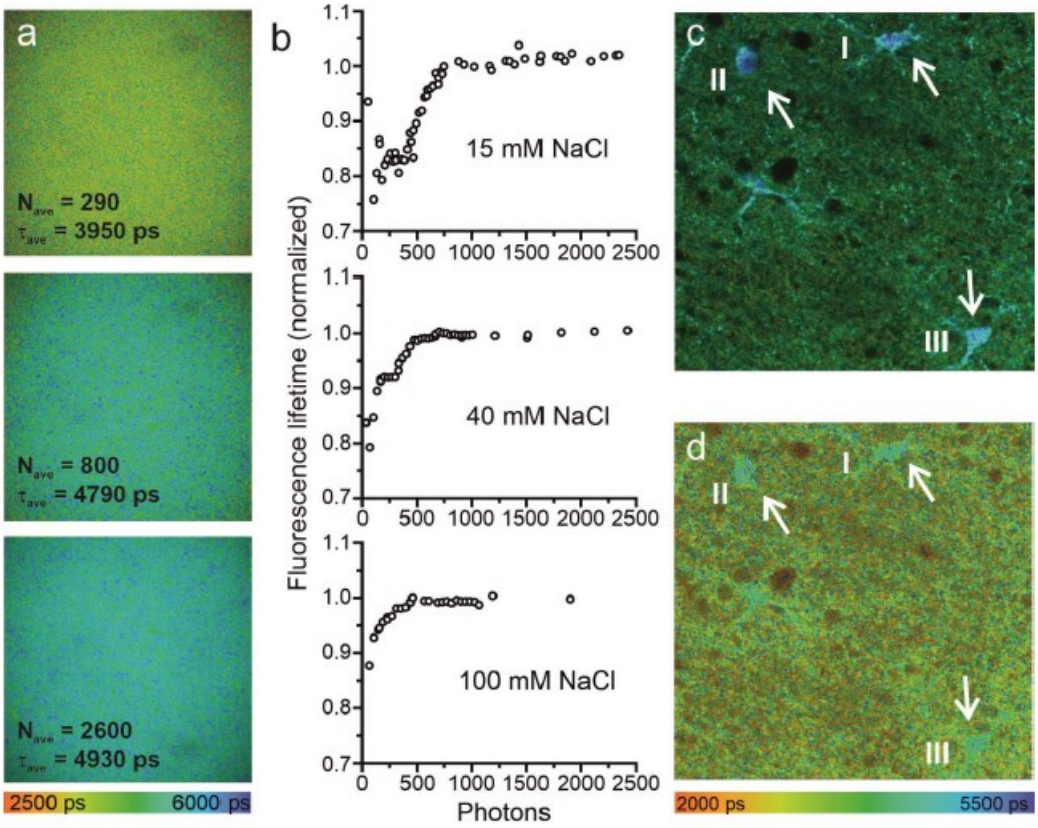

Figure 1. Minimum photon numbers for the determination of fluorescence lifetime by fitting fluorescence decays. (a) Fluorescence lifetime images of a droplet of 3 mM MQAE dissolved in a solution containing 15 mM NaCl. The three images were calculated from the same data set using different bin factors to generate single-pixel fluorescence intensity decays (FIDs) with varying photon numbers. (b) Fluorescence lifetimes of 3 mM MQAE (15 mM NaCl normalized to the limiting value of 4.95 ns; 40 mM NaCl normalized to the limiting value of 2.2 ns; 100 mM NaCl normalized to the limiting value of 1.15 ns) plotted as a function of photon numbers per FID. Photon numbers per FID varied by the excitation power, acquisition time, or bin factor. (c) Fluorescence lifetime image of a hippocampal brain slice (CA1 region). The average photon numbers for single-pixel FIDs in the three glia cells visible in the center of the image were 4817 (I), 3941 (II), and 6240 (III), resulting in expected fluorescence lifetimes: 4.88 ns (I), 4.96 ns (II), and 4.73 ns (III). (d) A second fluorescence lifetime image of the same brain slice area, measured with a reduced acquisition time and otherwise identical measurement conditions. Consequently, the respective FID photon numbers were significantly reduced to 296 (I), 269 (II), and 373 (III), resulting in a reduction of fluorescence lifetimes to 4.22 ns (I), 4.24 ns (II), and 4.15 ns (III).

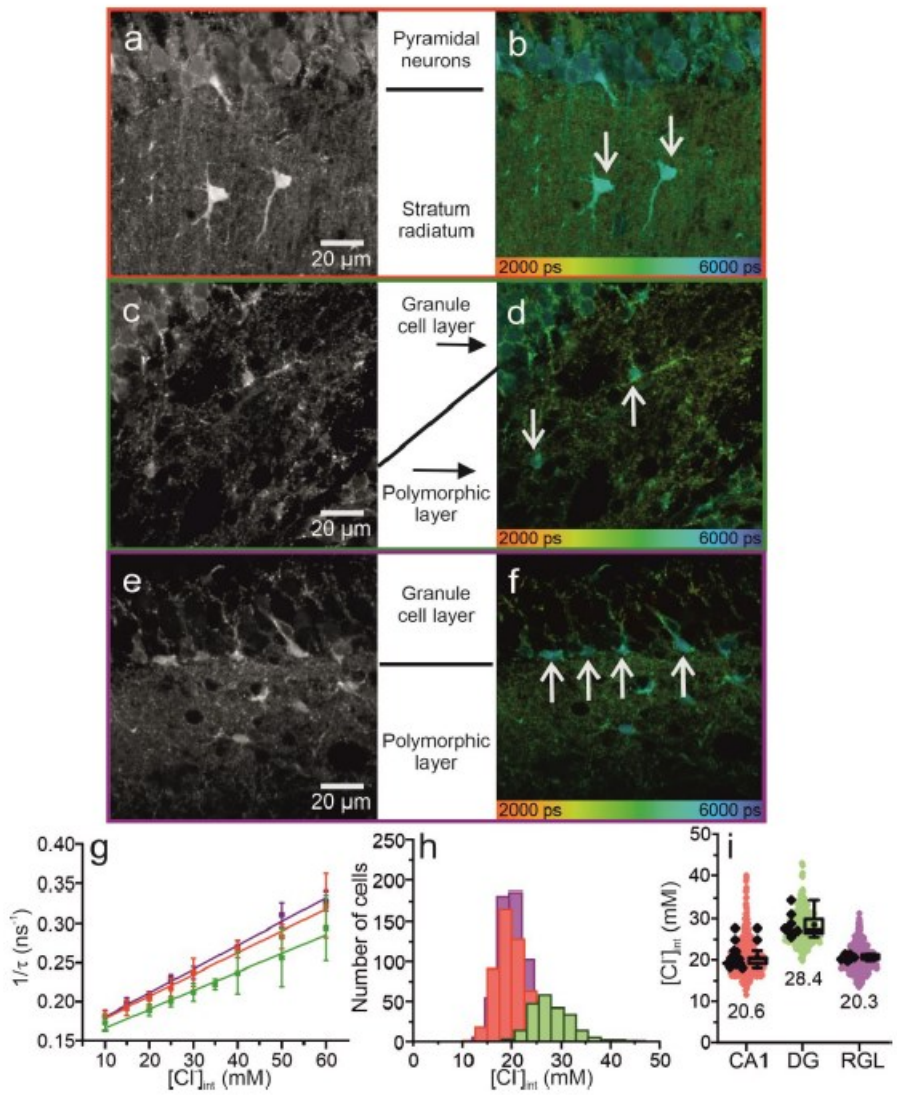

Figure 2. Chloride imaging in acute hippocampal slices. (a–f) Representative fluorescence intensity (a,c,e) and fluorescence lifetime (b,d,f) images of the CA1 (a and b) and DG (c and d) regions and RGL cells (e and f), with glial cells marked by arrows. Average fluorescence lifetimes (in ps) are color-coded. (g) Stern–Volmer plot of the chloride dependence of the MQAE fluorescence lifetime in hippocampal glia. Data points represent the inverse average fluorescence lifetime at different chloride concentrations, error bars indicate standard deviation, and solid lines represent a linear fit (10–60 mM; $N = 3$ animals/chloride concentration, > 10 cells/mouse/chloride concentration, mean ± SD, CA1: $R^2_{adj} = 0.991$; DG: $R^2_{adj} = 0.979$; RGL: $R^2_{adj} = 0.992$). (h,i) Physiological $[Cl^-]_{int}$ of all three glial cell types shown as a histogram (h) or box plot (i) (red – CA1, green – DG, purple – RGL). In the box plot (mean ± 1.5 IQR), black points are the mean $[Cl^-]_{int}$ from individual animals and colored points are the mean $[Cl^-]_{int}$ from individual cells. Abbreviations: CA1 – cornu ammonis region 1; DG – dentate gyrus; RGL – radial glial-like cells.

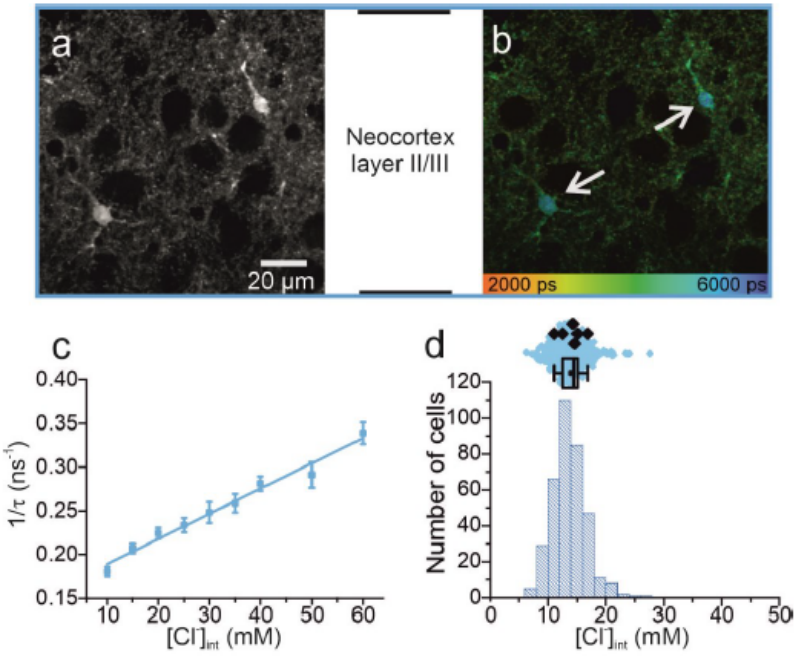

Figure 3. Chloride imaging in neocortical astrocytes. (a,b) Neocortical layer II/III representative fluorescence intensity (a) and fluorescence lifetime (b) images of neocortical astrocytes (marked by arrows). Average fluorescence lifetimes (in ps) are color-coded. (c) Stern–Volmer plot of the chloride dependence of the MQAE fluorescence lifetime in neocortical astrocytes. Data points represent the inverse average fluorescence lifetime measured at different chloride concentrations, error bars indicate the standard deviation, and solid lines represent a linear fit (10–60 mM; n = 3 animals/chloride concentration, > 10 cells/mouse/chloride concentration, mean ± SD, $R^2_{adj} = 0.976$). (d) Physiological $[Cl^-]_{int}$ in neocortical astrocytes, shown as a histogram and box plot. In the box plot (mean ± 1.5 IQR), black points are the mean $[Cl^-]_{int}$ from individual animals and colored points are the mean $[Cl^-]_{int}$ from individual cells.

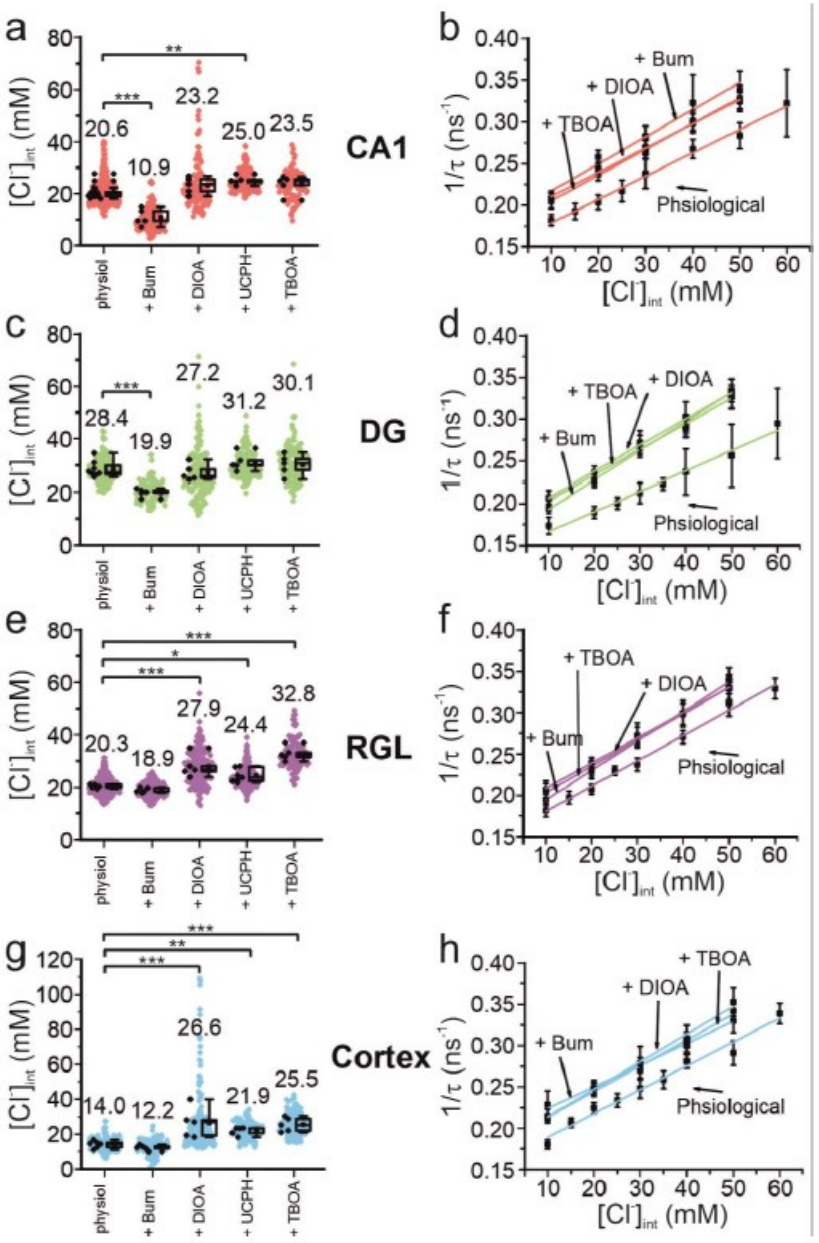

Figure 4. Modification of glial resting $[Cl^-]_{int}$ and chloride dependence of MQAE fluorescence lifetimes by indicated blocker. (a–h) $[Cl^-]_{int}$ of hippocampal astrocytes in the CA1 (a) and DG (c) regions, RGL cells (e), and neocortical glial cells (g) under physiological conditions or after treatment with blocker, as indicated. In the box plot (mean ± 1.5 IQR), black points are the mean $[Cl^-]_{int}$ from individual animals and colored points are the mean $[Cl^-]_{int}$ from individual cells. Stern–Volmer plots for glial cells in the CA1 (b) and DG (d) regions, RGL cells of the hippocampus (f), and neocortical glial cells (h). For each brain region, Stern–Volmer plots were created under physiological conditions and in the presence of bumetanide, *R*-(+)-DIOA, or DL-TBOA to visualize the influence of these blockers on MQAE florescence

lifetimes. Data points represent the inverse average fluorescence lifetime at different chloride concentrations, error bars indicate the standard deviation, and the solid lines represent a linear fit (10–60 mM; $n = 3$ animals/chloride concentration, > 10 cells/mouse/chloride concentration, mean ± SD, CA1$_{Bum}$: $R^2_{adj} = 0.963$, CA1$_{TBOA}$: $R^2_{adj} = 0.996$, CA1$_{DIOA}$: $R^2_{adj} = 0.993$; DG$_{Bum}$: $R^2_{adj} = 0.994$, DG$_{TBOA}$: $R^2_{adj} = 0.979$, DG$_{DIOA}$: $R^2_{adj} = 0.999$; RGL$_{Bum}$: $R^2_{adj} = 0.999$, RGL$_{TBOA}$: $R^2_{adj} = 0.992$, RGL$_{DIOA}$: $R^2_{adj} = 0.993$; Cortex$_{Bum}$: $R^2_{adj} = 0.983$, Cortex$_{TBOA}$: $R^2_{adj} = 0.991$, Cortex$_{DIOA}$: $R^2_{adj} = 0.989$). $^*p \leq 0.05$, $^{**}p \leq 0.01$, $^{***}p \leq 0.001$, one-way ANOVA with Holm–Sidak *post hoc* test; all *p*-values for this figure are mentioned in the results. Abbreviations: CA1 – cornu ammonis region 1; DG – dentate gyrus; RGL – radial glial-like cells; Physiol: physiological; Bum: bumetanide; DIOA: *R*-(+)-DIOA; UCPH: UCPH-101; TBOA: DL-TBOA.

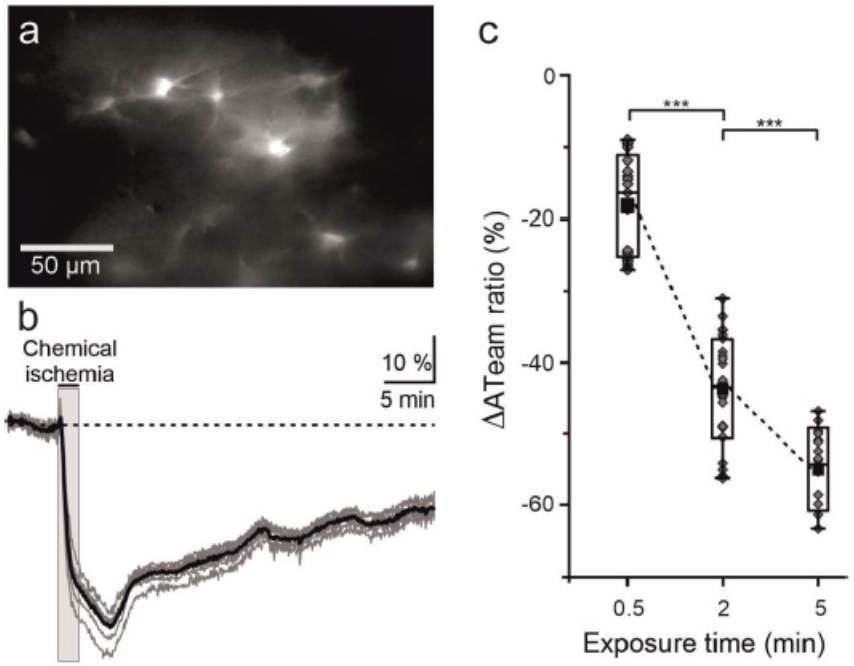

Figure 5. Chemical ischemia reduces astrocytic ATP levels. (a) Image of the fluorescence ratio of ATeam (Venus/eCFP), expressed under the control of the astrocyte-specific promotor GFAP in an organotypic brain tissue slice. (b) Normalized changes in astrocytic ATeam ratio following 2 min of chemical ischemia (chem. ischemia; gray area) indicate a decrease in intracellular ATP. Gray traces are from individual cells, and the black line represents an average of individual cells. (c) Normalized changes in the astrocytic ATeam ratio (ΔATeam ratio) following exposure of slices to chemical ischemia for 0.5, 2 or 5 min, shown as box and whisker plots. Means are shown as black squares, medians as black dotted lines, range (min–max) as black vertical lines, and standard deviations as boxes; single data points are shown in gray. $^{***}p \leq 0.001$, one-way ANOVA with Bonferroni *post hoc* test; all *p*-values for this figure are mentioned in the results.

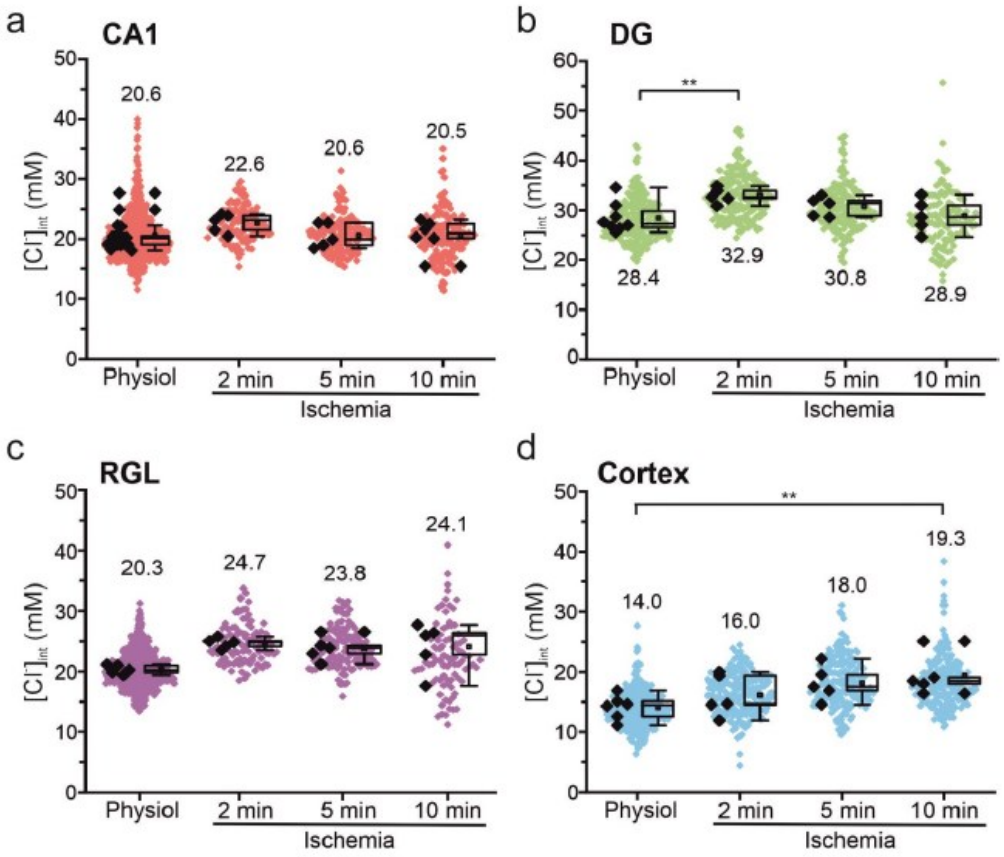

Figure 6. Modification of glial $[Cl^-]_{int}$ after energy restriction. (a–d) $[Cl^-]_{int}$ of hippocampal astrocytes in the CA1 (a) and DG (b) regions, of RGL cells (c), and of neocortical glial cells (d) under physiological conditions or after energy restriction for the indicated times. In the box plot (mean ± 1.5 IQR), black points represent mean $[Cl^-]_{int}$ from individual animals and colored points are the mean $[Cl^-]_{int}$ from individual cells. $^{**}p \leq 0.01$, one-way ANOVA with Holm–Sidak *post hoc* test; all *p*-values for this figure are mentioned in the results. Abbreviations: CA1 – cornu ammonis region 1; DG – dentate gyrus; RGL – radial glial-like cells; Physiol: physiological; Ischemia: Chemical ischemia.

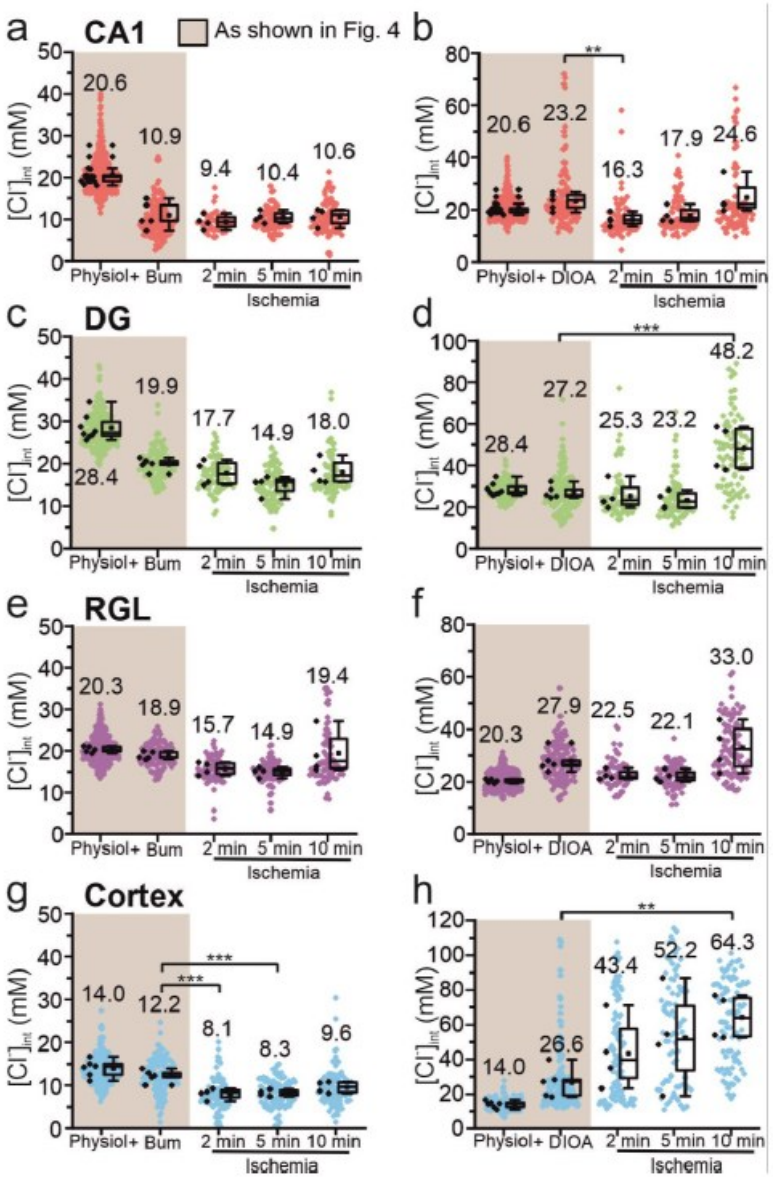

Figure 7. Modification of glial $[Cl^-]_{int}$ by a specific chloride transport blocker under energy restriction. (a–h) $[Cl^-]_{int}$ of hippocampal astrocytes in the CA1 (a,b) and DG (c,d) regions, of RGL cells (e,f), and of neocortical glial cells (g,h) under physiological conditions, in the presence of a specific chloride transport blocker (bumetanide or *R*-(+)-DIOA), or after energy restriction for the indicated times in the presence of the chloride transport blocker. In the box plot (mean ± 1.5 IQR), black points are the mean $[Cl^-]_{int}$ from individual animals and colored points are the mean $[Cl^-]_{int}$ from individual cells. $^{**}p \leq 0.01$ and $^{***}p \leq 0.001$, one-way ANOVA with Holm–Sidak *post hoc* test; all *p*-values for this figure are mentioned in the results. Abbreviations: CA1 – cornu ammonis region 1; DG – dentate gyrus; RGL – radial glial-like cells; Physiol: physiological; Ischemia: Chemical ischemia; Bum: bumetanide; DIOA: *R*-(+)-DIOA.

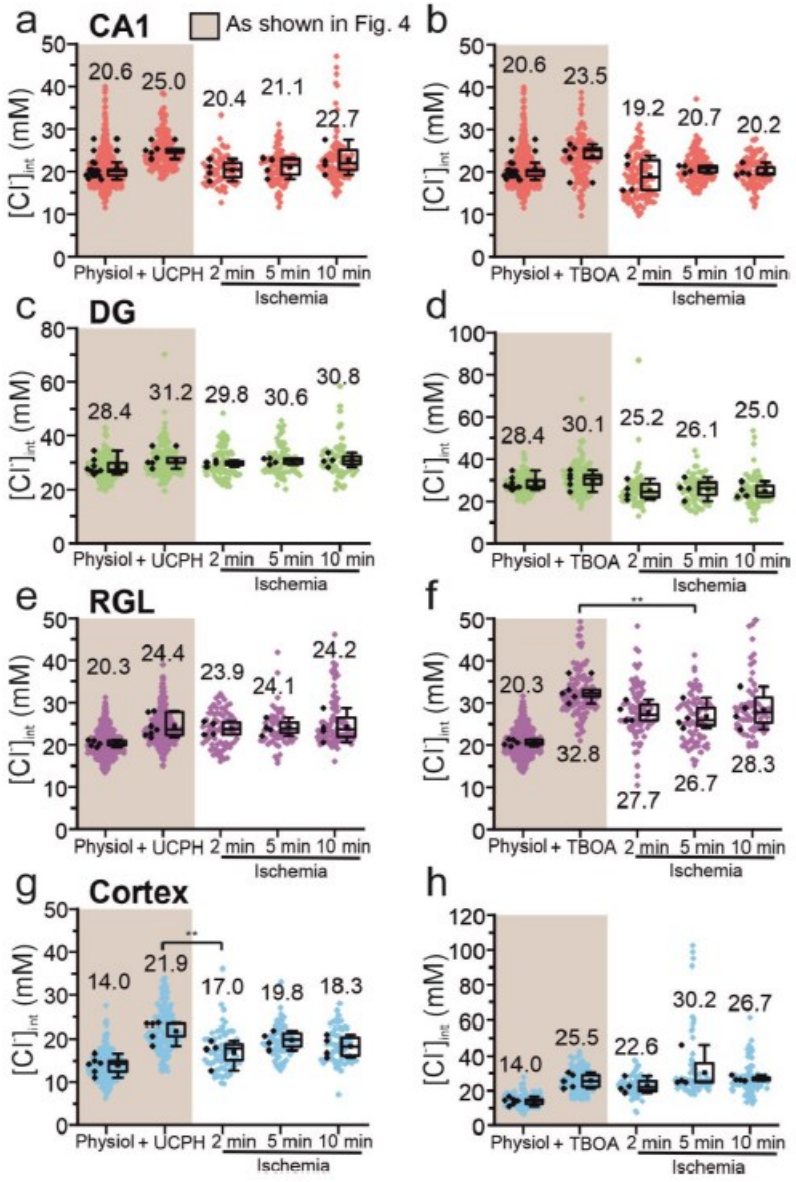

Figure 8. Modification of glial $[Cl^-]_{int}$ by a specific EAAT transporter blocker under energy restriction. (a–h) $[Cl^-]_{int}$ of hippocampal astrocytes in the CA1 (a,b) and DG (c,d) regions, RGL cells (e,f), and neocortical glial cells (g,h) under different conditions: physiological conditions, in the presence of a specific EAAT transporter blocker (UCPH-101 or DL-TBOA), and after energy restriction (ischemia) for the indicated times in the presence of the blocker. In the box plot (mean ± 1.5 IQR), black points are the mean $[Cl^-]_{int}$ from individual animals and colored points are the mean $[Cl^-]_{int}$ from individual cells. $^{**}p \leq 0.01$, one-way ANOVA with Holm–Sidak *post hoc* test; all *p*-values for this figure are mentioned in the results. Abbreviations: CA1 – cornu ammonis region 1; DG: dentate gyrus; RGL – radial glia-like cells; UCPH: UCPH-101; TBOA: DL-TBOA.

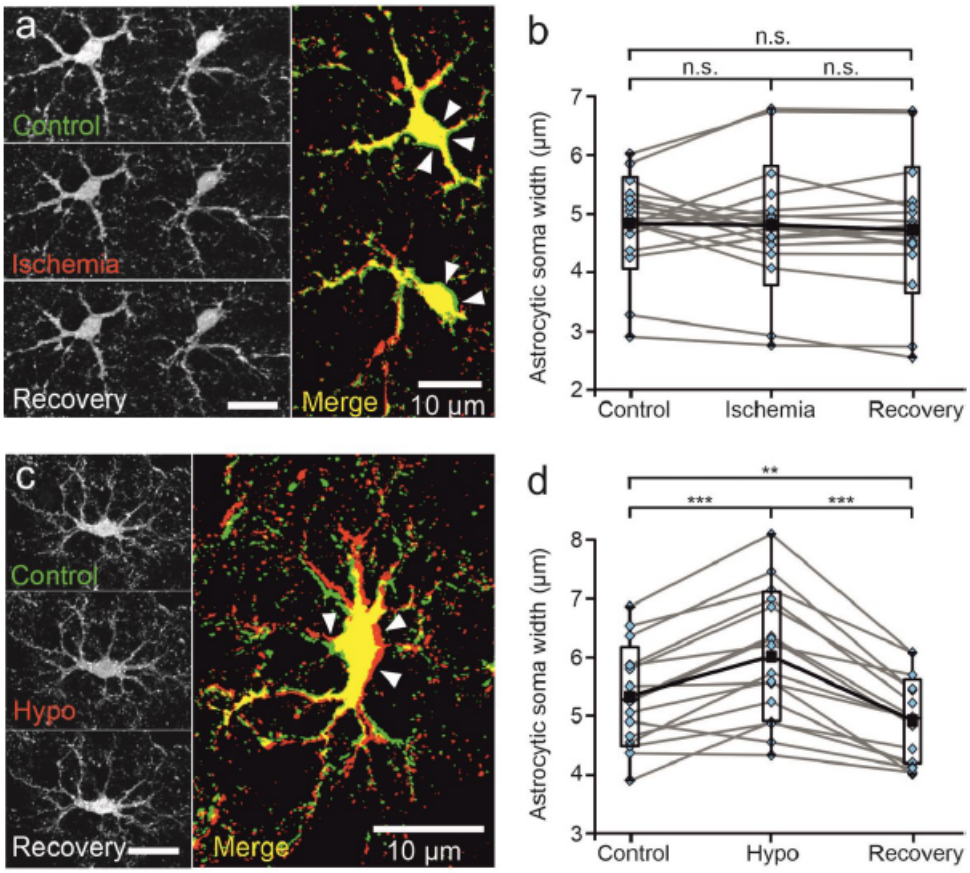

Figure 9. Astrocytes do not swell upon transient chemical ischemia. (a) Deconvolved confocal extended focus images showing SR101-labeled astrocytes in layer II/III of the mouse neocortex under control conditions, at 5 min after 10 min of chemical ischemia, and after 20 min of recovery. Arrowheads indicate areas of slight somatic shrinkage under chemical ischemia. The merged image is an overlay of the same cell under control (green) and ischemic (red) conditions (b) Box plots of astrocytic soma width (in µm; defined by FWHM of line profiles) under the conditions described in (a). (c) Deconvolved confocal extended focus images showing SR101-labeled astrocytes in layer II/III of the mouse neocortex under control conditions, at 5 min after a 10-min perfusion with hypo-osmotic saline (Hypo), and after 10 min of recovery (Recovery). The merged image is an overlay of the same cell under control (green) and hypo-osmotic (red) conditions. Arrowheads indicate areas of somatic swelling. (d) Box plots of astrocytic soma width (as described in (b)) under the conditions described in (c). Black squares are means, black lines are medians, vertical bars are ranges (min–max), and boxes are the standard deviation; single data points are shown in blue. n.s. $p \geq 0.05$, $^{**}p \leq 0.01$, $^{***}p \leq 0.001$, one-way ANOVA with Bonferroni *post hoc* test; all *p*-values for this figure are mentioned in the results. Abbreviation: n.s.: not significant.

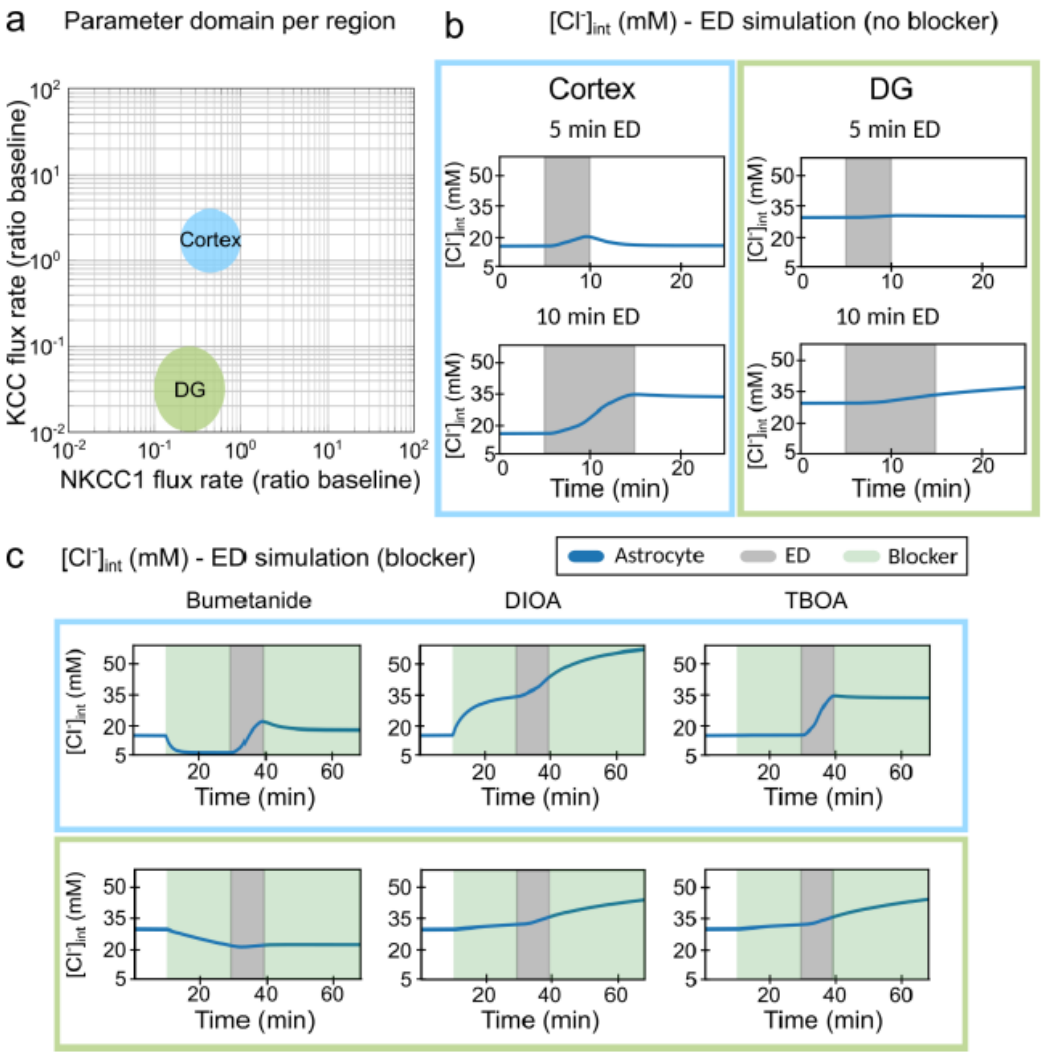

Figure 10. Differences in cortical and DG chloride homeostasis can be described by variation in KCC and NKCC1 expression levels. (a) Log–log plot of the KCC flux rate against the NKCC1 flux rate relative to baseline flux rates. Two distinct regions in this two-parameter space account for the results obtained with cortical (blue) or DG (green) $[Cl^-]_{int}$. (b) Predicted changes in astrocytic $[Cl^-]_{int}$ without blocker under conditions used in experiments. Left panel, cortex; right panel; DG. (c) The model was subjected to block of a specific chloride transport system (light green block: bumetanide, *R*-(+)-DIOA or DL-TBOA) for the first 30 min. At 20 min after the start of transport inhibition, transient ischemia was simulated by blocking neuronal and astrocyte Na^+-K^+-ATPase for 10 min (gray block), followed by energy restoration for 30 min in the presence of the mentioned blocker. Upper panel, cortex; lower panel, DG. Abbreviations: DG: dentate gyrus; ED: energy depletion; DIOA: *R*-(+)-DIOA; TBOA: DL-TBOA.

2.2.2. Manuscript in preparation

Impaired granule cell inhibition causes epilepsy in episodic ataxia 6

Yulia Kolobkova, Miriam Engels, Sabrina Behuet, Sebastian Bludau, Thomas Gensch, Christoph Fahlke*, Peter Kovermann*

* These authors contributed equally

Pages: 96 – 125

Status: in preparation

Contribution: I planned and did FLIM measurements of glial cells in hippocampal acute tissue slices (CA1 and RGL cells). For the figure 3 (B, D, E-F), I calibrated, measured and determined chloride concentrations, created imaging pictures and was involved in illustrating chloride measurement results. I was involved in the interpretation of the data and correction of the manuscript draft.

Impaired granule cell inhibition causes epilepsy in episodic ataxia 6

Yulia Kolobkova[1], Miriam Engels[1], Sabrina Behuet[2], Sebastian Bludau[2], Thomas Gensch[1], Christoph Fahlke[1,3,*], Peter Kovermann[1,3,*]

[1]Institute of Biological Information Processing, Molekular- und Zellphysiologie (IBI-1), Forschungszentrum Jülich GmbH, 52428 Jülich, Germany

[2]Institute of Neuroscience and Medicine, Strukturelle und funktionelle Organisation des Gehirns (INM-1), Forschungszentrum Jülich GmbH, 52428 Jülich, Germany

[3]These authors contributed equally

*Correspondence: p.kovermann@fz-juelich.de (P.K.), c.fahlke@fz-juelich.de (C.F.)

Running head: Impaired granule cell inhibition in episodic ataxia 6

Keywords: episodic ataxia, glutamate transporters, epilepsy, hippocampus, dentate gyrus, astrocytes, radial glia-like cells, granule cells, chloride homeostasis

Objective: A severe form of episodic ataxia type 6 is caused by the P290R mutation in glial EAAT1 glutamate transporters that reduces glutamate transport rates and enhances anion channel activity. We studied the cellular pathomechanisms of epileptic seizures in an animal model carrying the mutation.

Methods: Glutamatergic and GABAergic synaptic transmission in *Slc1a3*$^{P290R/+}$ mouse hippocampi were studied before and after epilepsy onset using whole-cell patch clamping in acute brain slices. We used fluorescence lifetime imaging microscopy with a chloride-sensitive dye to determine intracellular chloride concentrations in hippocampal glial cells. Protein expression was examined by immunohistochemistry and western blot analysis.

Results: Tonic GABAergic transmission was decreased in dentate gyrus granule cells from *Slc1a3*$^{P290R/+}$ mice before seizure onset (P20) whereas phasic GABAergic and glutamatergic transmission were unaltered in juvenile animals of the same age. Expression of the $GABA_AR$ δ subunit was unaltered in *Slc1a3*$^{P290R/+}$ mice, indicating that extrasynaptic GABA concentrations are decreased in juvenile mutant animals. EAAT1 (and its rodent homologue GLAST) are highly expressed in hippocampal radial glia-like cells (RGLs) that modulate neurotransmission in dentate gyrus. Intracellular chloride concentrations were reduced in *Slc1a3*$^{P290R/+}$ RGLs, indicating an increased driving force for GABA uptake via Cl^--dependent GABA transporters.

Interpretation: Increased activity of P290R EAAT1/GLAST chloride channels lowers internal chloride concentrations, thereby enhancing the driving force for GABA uptake by RGLs. Consequent reductions in ambient GABA concentrations and tonic inhibition cause granule cell hyperexcitability and epilepsy. Our study shows how increased EAAT1/GLAST chloride channel activity can cause epilepsy by modifying synaptic GABA concentrations.

250/250 words

INTRODUCTION

Mutations in *SLC1A3*—which encodes the glial excitatory amino acid transporter 1 (EAAT1)—are associated with episodic ataxia type 6 (EA6).[1-5] The P290R mutation that causes the exchange of proline for arginine at position 290 was recently identified in a patient with an unusually severe form of EA6 characterized by ataxia, hemiplegia, and epileptic seizures.[1] EAAT1 has a dual function as a glutamate transporter and anion channel,[6-8] and P290R was shown to impair glutamate transport and to enhance anion channel activity by EAAT1.[9]

To understand how this change in EAAT1 function caused neurological symptoms in the patient, we generated a knock-in mouse model (*Slc1a3*$^{P290R/+}$), which had impaired motor coordination and epileptic seizures.[10] We recently reported that ataxia in *Slc1a3*$^{P290R/+}$ mice is caused by Bergmann glia apoptosis triggered by increased glutamate-activated Cl^- efflux during infancy, and subsequent cerebellar degeneration.[10] However, cerebellar degeneration cannot account for the severe epileptic phenotype of *Slc1a3*$^{P290R/+}$ mice. Outside the cerebellum, EAAT1 and its rodent homologue GLAST are highly expressed in hippocampal radial glia-like cells (RGLs), a population of glial stem cells located in the subgranular zone of the dentate gyrus (DG) that can differentiate into either granule neurons or astrocytes.[11-13] Since RGLs are functionally and spatially coupled to granule cells,[14] functional changes in EAAT1/GLAST might modify synaptic transmission in DG neurons.

To understand the pathophysiological basis of the EA6 epileptic phenotype, we studied inhibitory and excitatory neurotransmission in the hippocampus of *Slc1a3*$^{P290R/+}$ mice. We observed decreased tonic γ-aminobutyric acid (GABA)ergic inhibition in DG granule cells, with unaltered expression of the $GABA_AR$ δ subunit. Therefore, the decrease in tonic inhibition is likely caused by reduced ambient GABA concentrations. Since internal chloride concentrations were decreased in RGLs from *Slc1a3*$^{P290R/+}$, we hypothesized that the driving force for GABA uptake by Na^+ and Cl^--driven GABA transporters is enhanced. The increased GABA uptake impairs tonic GABAergic currents, resulting in granule cell hyperexcitability and epilepsy.

MATERIALS & METHODS

Animals

Wild-type (WT) and mutant (*Slc1a3*$^{P290R/+}$) mice of both sexes in the 129/Sv genetic background were studied at ages between P10 and P800. Animals were housed under a 12 hour dark/light cycle. Our experiments conformed to Animal Research: Reporting of In Vivo Experiments guidelines[15] and were approved by the regulatory authorities, Forschungszentrum Jülich and Landesamt für Natur, Umwelt und Verbraucherschutz of North Rhine-Westphalia (reference numbers: 84-02.04.2014.A334, 81-04.04.2020.A441).

Patch clamp recordings

After anesthetizing animals with isoflurane and rapid decapitation, brains were placed in ice-cold Ringer's solution A (in mM: 125 NaCl, 2.5 KCl, 1.25 NaH_2PO_4, 26 $NaHCO_3$, 0.5 $CaCl_2$, 5 $MgCl_2$, 20 $C_6H_{12}O_6$) bubbled with 5% CO_2/95% O_2. Parasagittal 250 µm-thick slices were cut using a microtome (υ = 60 Hz, amplitude = 1 mm) and transferred to oxygenated Ringer's solution B (125 NaCl, 2.5 KCl, 1.25 NaH_2PO_4, 26 $NaHCO_3$, 2 $CaCl_2$, 1 $MgCl_2$, 25 $C_6H_{12}O_6$) for 30 minutes at 37°C, followed by 90 minutes at room temperature (RT).

We performed whole-cell recordings of hippocampal neurons from acute brain slices of mice aged between P20 and P55 using an EPC10 USB amplifier with PATCHMASTER software (HEKA Elektronik, Lambrecht, Germany). During recordings, slices were constantly perfused at room temperature with oxygenated Ringer's solution B supplemented with 1 µM tetrodotoxin (Tocris Bioscience, Bristol, UK) and 50 µM (2*R*)-amino-5-phosphovaleric acid (Tocris Bioscience). The pipette solution contained (in mM) 130 CsCl, 8 NaCl, 0.2 $MgCl_2$, 2 EGTA, 4 Mg-ATP, 0.3 Li-GTP, 1 QX-314, and 10 HEPES/CsOH (pH 7.2). Cells were clamped to -70 mV and GABAergic miniature inhibitory postsynaptic currents (mIPSCs) and tonic currents were recorded in the presence of 10 µM cyanquixaline (Tocris Bioscience). To estimate the amplitude of the $GABA_AR$-mediated tonic conductance, 30-second holding currents were compared under baseline conditions and after

3 minutes of continuous perfusion with 50 µM picrotoxin. α-amino-3-hydroxy-5-methyl-4-isoxazolepropionic acid (AMPA) receptor (AMPAR)-mediated miniature excitatory postsynaptic currents (mEPSCs) were recorded in the presence of 1 µM picrotoxin (Tocris Bioscience).

Fluorescence lifetime imaging microscopy

We measured the intracellular chloride concentration ($[Cl^-]_{int}$) of hippocampal astrocytes and RGLs by fluorescence lifetime imaging microscopy (FLIM) using two different imaging systems: an upright fluorescence microscope (A1 MP, Nikon, Amsterdam, Netherlands) equipped with a 25× water immersion objective[16] or a laser scanning microscope 880 (Zeiss, Jena, Germany) equipped with a 20× water immersion objective (NA 1.0, WD 2.1 mm, Zeiss) linked to a tunable laser (InSight X3, Newport Spectra Physics, Darmstadt, output power 1.9 W at 750 nm). Before imaging, acute slices were incubated in oxygenated Ringer's solution A containing 2 µM sulforhodamine 101 for 20 minutes at 37°C and then in sulforhodamine 101-free oxygenated Ringer's solution B for 10 minutes to stain astrocytes and RGLs. After 30 minutes at RT, single slices were incubated with the Cl-sensitive dye *N*-(ethoxycarbonylmethyl)-6-methoxyquinolinium bromide (MQAE; 3.5 mM) in Ringer's solution B for 30 minutes. MQAE fluorescence is collisionally quenched by Cl^- ions, resulting in a linear relationship between the inverse fluorescence lifetime and $[Cl^-]_{int}$[17]:

$$\frac{\tau_0}{\tau} = 1 + K_{SV}[Cl^-]_{int}$$

where τ is the MQAE fluorescence lifetime at a given $[Cl^-]_{int}$, τ_0 is the MQAE fluorescence lifetime in the absence of Cl^-, and K_{SV} is the cell type-specific Stern–Volmer constant. After calibration in astrocytes and RGLs using the 2-ionophore calibration method,[16] the $[Cl^-]_{int}$ for single-cell soma was calculated from the mean fluorescence lifetime of all pixels within a region of interest. To block EAAT1/GLAST activity, slices were incubated for 20 minutes in oxygenated Ringer's solution B supplemented with 20 µM of the EAAT1/GLAST blocker UCPH-101 (Abcam, Cambridge, UK).

Immunohistochemistry experiments

Brains were fixed in 4% paraformaldehyde in phosphate buffer (PB; in mM: 81 NaH_2PO_4, $2H_2O$, 9 $Na_2HPO_4 \cdot H_2O$, pH 7.4) for 30 minutes at 4°C. Subsequently, brains were washed in PB (30 minutes, RT) and incubated in PB containing 10% sucrose for 60 minutes at RT and then in PB containing 30% sucrose for 12 hours at 4°C. Hemispheres were embedded in NEG-50 frozen section medium (Thermo Fisher Scientific, Waltham, US) and cut into 14 µm-thick sagittal slices using an HM560 cryotome (Thermo Fisher Scientific). To prepare paraffin-embedded slices, brains were fixed in 4% paraformaldehyde for 5 days at 4°C. After dehydration in a graded ethanol series (50%, 70%, 90%, 100%), brains were embedded in paraffin and 5 µm-thick sagittal sections were cut.

Endogenous peroxidases were inactivated by incubation for 15 minutes at RT in a solution containing 21 mM $C_6H_8O_7$, 6 mM Na_2HPO_4, and 15% (v/v) H_2O_2. Epitopes were unmasked by boiling the sections for 20 minutes in 2 M Tris and 63 mM EDTA (pH 8.0). Sections were then blocked overnight at 4°C in 1% (w/v) bovine serum albumin in PB. Frozen and paraffin sections were incubated overnight at 4°C with primary antibodies specific for brain lipid-binding protein (BLBP), integrin α-M (CD11b), GABA transporter-3 (GAT-3), glial fibrillary acidic protein (GFAP), or GLAST (RRIDs: AB_10000325, AB_2650514, AB_304437, AB_1556315, AB_10829302) and then incubated for 45 minutes at RT in cyanine dye-conjugated secondary antibodies (RRIDs: AB_2340370, AB_2340460, AB_2340612, AB_2340813). Both primary and secondary antibodies were diluted in PB containing 5% ChemiBLOCKER (Merck Millipore, Darmstadt, Germany) and 1% Triton-X100. RGLs were quantified by counting the number of BLBP-, GLAST-, and GFAP-positive cells within single confocal planes, and GAT-3 fluorescence intensity was normalized to the BLBP fluorescence intensity for each cell.

Western blotting

Western blotting was performed using hippocampal lysates from at least three animals per genotype and age group. Whole hippocampi were frozen in liquid nitrogen after excision and homogenized at

4°C. The homogenate was centrifuged at 40,000*g* (45 minutes, 4°C) and the pellet was solubilized in 10 mM sodium phosphate (pH 8.0) containing 1% (w/v) sodium dodecyl sulfate, 40 µl/ml sodium deoxycholate, and protease inhibitors (5 minutes, RT) and centrifuged at 13,000*g* (10 minutes, 15°C).

Proteins were separated on 10–12% sodium dodecyl sulfate-gels and transferred to polyvinylidene fluoride membranes. After blocking (60 minutes in phosphate-buffered saline / 0.1% Tween-20 / 3% BSA, RT), membranes were incubated for 60 minutes at RT with primary antibodies specific for doublecortin (DCX), $GABA_AR$ δ subunit, GAT-3, or GLAST (RRIDs: AB_1586992, AB_2107256, AB_304437, AB_10829302); washed with phosphate-buffered saline / 0.1% Tween-20; and incubated with horseradish peroxidase-conjugated secondary antibody for 45 minutes at RT (RRIDs: AB_10981814, AB_228415, AB_228333). The membrane was washed again with phosphate-buffered saline / 0.1% Tween-20, and band intensities were quantified and normalized to α-actin or Na^+/K^+-ATPase background-corrected gray values.

Dendritic spine quantification

Golgi–Cox staining was performed as previously described.[18] A total of 3–11 individual 10 µm dendritic segments was quantified from each hippocampus. Only protrusions with a clearly discernible spine head and neck along the secondary and tertiary dendrites of granule cells and cornu ammonis 1 (CA1) pyramidal neurons were selected for analysis. Spine analysis was performed as previously described[19] using the freely available Reconstruct Software Version 1_1_0_0.[20] The linear spine density was calculated by dividing the total number of counted spines by the length of the sampled dendritic segment.

Quantitative receptor autoradiography

Quantitative receptor autoradiography of brains from P42–P47 mice was performed as previously described.[21] The mean densities of glutamatergic, GABAergic, and dopaminergic receptors were quantified in different brain regions and visualized via color-coding. Receptor densities (in fmol/mg

protein) were measured using the original, non-contrast-enhanced data sets in seven different brain regions: the motor and somatosensory cortices; the caudate putamen; the hippocampal subfields CA1, CA2/3, and DG; and the cerebellum. For each animal, brain area, and receptor type, three regions of interest were measured and average values were taken to represent the mean binding site density for each animal and brain area.

Statistical analysis

All statistical parameters were calculated with SigmaPlot (Systat Software) or OriginPro (OriginLab). Data are presented as the mean ($\bar{x}$) ± SEM or 95% confidence interval from individual animals (N). In several cases the number of individual cells is given (n). To compare groups with normal distributions, data were analyzed using 2-way analysis of variance (ANOVA) tests with Holm–Šidák or Bonferroni *post hoc* testing. Kruskal–Wallis ANOVA on ranks or Mann–Whitney *U*-tests were used for data that failed the Shapiro–Wilk test for normal distribution. *p*-values of ≤ 0.05 were considered statistically significant. The obvious phenotype and need for strict monitoring of *Slc1a3*$^{P290R/+}$ mice meant that blinding was not possible. The data that support the findings of this study are openly available in GitHub at https://github.com/peterkovermann/Data_Kolobkova_et_al 1.

RESULTS

Slc1a3$^{P290R/+}$ mice suffer from severe generalized epilepsy

Slc1a3$^{P290R/+}$ mice suffer from ataxia and severe epilepsy,[10] which closely resemble the neurological symptoms of the patient in whom the mutation was identified.[1] The mouse model was generated by homologous recombination in the C57BL/6 background,[10] but most of the mice did not survive the weaning period because of severe generalized epileptic seizures. However, backcrossing into the 129/Sv strain significantly increased the survival rate of mutant mice.[10]

In *Slc1a3*$^{P290R/+}$ mice, epileptic attacks usually consisted of multiple epileptic seizures lasting about 30 seconds each and separated by resting phases of 5–15 minutes (Fig 1A, Video S1). Attacks commonly started with a short period of agitation and tail lifting, followed by whole-body stretching and tremor or mild seizures. Severe seizures also involved the loss of startle reflexes for about 10 seconds (Fig 1B). We compared the general condition, some aspects of behavior, and EA6-associated pathology of 129/Sv WT and *Slc1a3*$^{P290R/+}$ mice.[10] Many *Slc1a3*$^{P290R/+}$ animals had to be euthanized due to severe epilepsy, which prevented the accurate quantification of mortality rates in this genotype. Male animals were significantly more susceptible to seizures and had earlier seizure onset than female animals (males/females: 29/23%, N = 139 / 152, $*p < 0.05$; Fig 1C and D). The peak period of seizure susceptibility was from the 3rd postnatal week until 2 months of age for both sexes and was associated with a significant reduction in body weight (Fig 1E). Animals that survived to the age of 2 months did not experience further epileptic attacks, suggesting that compensatory mechanisms develop in the adult mutant brain to counteract pro-epileptic activity.

Tonic GABAergic inhibition is decreased in *Slc1a3*$^{P290R/+}$ hippocampal granule cells

We next studied synaptic transmission in the hippocampus, a brain region involved in the pathogenesis of most genetic epilepsies.[22] Epilepsy usually originates from an imbalance between excitation and inhibition that is often caused by decreased efficiency of $GABA_AR$-mediated inhibition.[23] Therefore, we studied GABAergic transmission in the DG and CA1 regions through

whole-cell patch clamp recordings of acute hippocampal slices. Fig 2A shows representative $GABA_AR$-mediated mIPSCs in DG granule cells; these phasic synaptic inhibitory events occur through the transient activation of synaptic $GABA_ARs$. The mIPSC amplitudes, frequencies, and observed decay times did not differ between mutant and age-matched WT mice (Fig 2B to D).

The activation of extrasynaptic $GABA_ARs$ generates tonic currents,[24] which modulate neuronal excitation via hyperpolarization or shunting inhibition. Even minor changes in the amplitude of tonic inhibitory currents can have profound effects on neuronal excitability.[25] We isolated tonic GABAergic currents in whole-cell patch clamp recordings with the $GABA_AR$ inhibitor picrotoxin and measured their amplitude as the difference between the holding currents before and after picrotoxin inhibition (Fig 2E). Tonic $GABA_AR$-mediated currents had significantly lower amplitudes in *Slc1a3*$^{P290R/+}$ than in WT granule cells before the onset of the paroxysmal period (P20; Fig 2F). In contrast, tonic and phasic inhibition in CA1 pyramidal neurons were unchanged in *Slc1a3*$^{P290R/+}$ mice at this age (data not shown). After seizure onset, tonic and phasic inhibition in *Slc1a3*$^{P290R/+}$ mice were similar to the ones in age-matched WT mice (Fig 2B to D and F).

Tonic GABAergic currents in DG granule cells are primarily mediated by $GABA_ARs$ that contain a δ subunit.[24] To determine whether the reduction in tonic GABAergic current in *Slc1a3*$^{P290R/+}$ granule cells results from altered expression of the $GABA_AR$ δ subunit, we analyzed hippocampal lysates by western blotting; however, we found no significant differences in total δ-subunit protein between *Slc1a3*$^{P290R/+}$ and WT samples (Fig 2G). For these experiments, we used only male animals because δ-subunit expression is reported to change in female mice during the ovarian cycle.[26] We conclude that tonic inhibition of DG granule cells is decreased in *Slc1a3*$^{P290R/+}$ mice because of decreased ambient GABA levels.

Intracellular [Cl^-] is reduced in radial glia-like cells, but not in hippocampal astrocytes of *Slc1a3*$^{P290R/+}$ mice

In the hippocampus, EAAT1/GLAST is expressed in astrocytes[27] and in radial glia-like cells (RGLs) of the DG.[11–13] Both astrocytes and RGLs express GFAP, but only RGLs express high levels of BLBP. We studied the cellular environment of RGLs by immunostaining hippocampal slices, and observed that they are in close proximity to DG granule cells (Fig 3A).[14] Thus, RGLs are likely to be important for neurotransmitter clearance from the synaptic and extrasynaptic environment of granule cells, and changes in RGL neurotransmitter uptake might contribute to hippocampal hyperexcitability and epilepsy in *Slc1a3*$^{P290R/+}$ mice.

EAAT1 anion currents regulate the $[Cl^-]_{int}$ in Bergmann glia cells,[28] and enhanced P290R EAAT1 anion currents have been shown to decrease the $[Cl^-]_{int}$ in *Slc1a3*$^{P290R/+}$cerebellar Bergmann glia.[10] Since changes in the $[Cl^-]_{int}$ will modify the driving force for GABA uptake, we measured the RGL and astrocytic $[Cl^-]_{int}$ at postnatal days P20–P30 by fluorescence lifetime imaging microscopy using the chloride-sensitive dye MQAE (Fig 3B and D to F).[28] The RGLs of *Slc1a3*$^{P290R/+}$ mice have significantly lower $[Cl^-]_{int}$ compared with WT RGLs. Moreover, incubation of *Slc1a3*$^{P290R/+}$ slices with the EAAT1/GLAST blocker UCPH-101 (20 μM) increased the $[Cl^-]_{int}$ to values similar to those of WT animals (Fig 3B). In contrast, the $[Cl^-]_{int}$ was similar in astrocytes of the CA1 region in both WT and mutant animals (Fig 3D).

Changes in the $[Cl^-]_{int}$ increase the driving force of GAT-3, a secondary-active GABA transporter that utilizes Na^+ and Cl^- gradients to take up GABA into RGLs.[29] GAT-3 protein levels were increased in hippocampal lysates from *Slc1a3*$^{P290R/+}$ mice at the age of seizure onset. Coimmunostaining of glial GAT-3 and BLBP confirmed that GAT-3 is expressed in RGLs and co-localizes with BLBP in the somata and also the vertical processes that penetrate deep into the granule cell layer of the DG (Fig 3H). RGLs from *Slc1a3*$^{P290R/+}$ mice exhibit larger GAT-3 fluorescence intensities (normalized to BLBP fluorescence intensity) compared with those of WT mice (Fig 3I). We also observed that EAAT1/GLAST levels in hippocampal lysates from *Slc1a3*$^{P290R/+}$ mice are

reduced by 29% during the second postnatal week and by 44% at the age of seizure onset (Fig 3G). These results indicate a lower membrane density for mutant EAAT1, consistent with our previous findings of decreased P290R EAAT1/GLAST expression in heterologous expression systems and mutant cerebella.[8,10]

We conclude that gain of function in P290R EAAT1/GLAST anion channels reduces the $[Cl^-]_{int}$ in hippocampal RGLs. Decreased $[Cl^-]_{int}$ combined with increased GAT-3 expression in RGLs is expected to stimulate GABA uptake and reduce the tonic GABAergic currents.

Slc1a3$^{P290R/+}$ mice have fewer hippocampal RGLs and adult-born neurons

Gain of function in P290R EAAT1/GLAST anion channels triggers glial apoptosis in the _Slc1a3_$^{P290R/+}$ cerebellum.[10] To test whether similar alterations occur in the hippocampus of _Slc1a3_$^{P290R/+}$ mice, we counted hippocampal RGLs in _Slc1a3_$^{P290R/+}$ mice before and after seizure onset in immunohistochemical sections. Fig 4A shows representative confocal images from the subgranular zone of WT and mutant mice after immunostaining with antibodies against BLBP, GFAP, and GLAST. We observed similar RGL densities (counts per 100 µm of the DG subgranular zone length) in mutant and WT animals prior to the paroxysmal period (P20), but were significantly lower in mutant animals after seizure onset (P40; Fig 4B). RGL densities were comparable in WT and _Slc1a3_$^{-/-}$ (_Slc1a3_^{tm1Kta}, GLAST knock-out) mice at P30 (data not shown), indicating that decreased RGL density is a specific consequence of expression of the EAAT1/GLAST P290R mutant in _Slc1a3_$^{P290R/+}$.

Phagocytosis of GFAP-positive cells by CD11b-positive microglia was observed within the subgranular zone of _Slc1a3_$^{P290R/+}$ mice at P27 (Fig 4C). At this age, mutant hippocampi display both astrocytosis (characterized by the appearance of thicker astrocytic soma and processes) and microgliosis (indicated by increased CD11b expression) within the mutant hippocampi (Fig 4D and E). The density of granule cells remained unchanged (data not shown). Granule cells express DCX at the early stages of differentiation and migration. To follow the differentiation of RGLs into granule

cells, we quantified DCX expression via western blot analysis. DCX levels were reduced in *Slc1a3*$^{P290R/+}$ mice before, but not after, seizure onset (Fig 4F), suggesting that granule cell neurogenesis in the mutant hippocampus is reduced during the first 3 postnatal weeks. We conclude that P290R EAAT1/GLAST expression in RGLs impairs adult neurogenesis independently of epileptic activity.

Adult *Slc1a3*$^{P290R/+}$ mice exhibit increased hippocampal AMPAR density and reduced spine length and density

AMPA and N-methyl-D-aspartate ionotropic glutamate receptors play distinct roles in mediating epileptiform activity, with AMPARs considered of primary importance in initiating epileptiform discharges.[30] We studied AMPAR-mediated mEPSCs in CA1 pyramidal cells and DG granular cells from juvenile (P20) WT and *Slc1a3*$^{P290R/+}$ mice, and found no differences in the amplitudes, frequencies, or decay times in juvenile *Slc1a3*$^{P290R/+}$ (Fig 5A to D). In CA1 neurons (but not DG granular cells) from adult (P40) *Slc1a3*$^{P290R/+}$ mice, mEPSC amplitudes were slightly increased (Fig 5E and F), but frequencies and decay times were unchanged in both cell types (Fig 5G and H). Since AMPAR-mediated neurotransmission is unaltered before seizure onset, these changes do not contribute to the pathogenesis of epilepsy in *Slc1a3*$^{P290R/+}$mice but might help to sustain status epilepticus and initiate the abnormally prolonged seizures observed in mutant mice.

We next tested whether changes in neurotransmitter receptor expression confer resistance to seizures in adult *Slc1a3*$^{P290R/+}$ animals. We used quantitative autoradiography to measure AMPAR, $GABA_AR$, kainate receptor, N-methyl-D-aspartate receptor, and mGlu2/3R densities, and observed increased AMPAR densities in the caudatum putamen, motor and sensory cortices, and hippocampus of *Slc1a3*$^{P290R/+}$ mice at P45 (Fig 6A and B). In agreement with electrophysiological recordings from CA1 pyramidal cells (Fig 5F), AMPAR densities were increased in the CA1 region (Fig 6C) and reduced in the cerebellum of *Slc1a3*$^{P290R/+}$ animals (Fig 6D); the latter is probably caused by

progressive glial and neuronal degeneration.[10] Densities of all other receptors were unaffected in adult *Slc1a3*$^{P290R/+}$ mice (data not shown).

To test for possible compensatory morphological changes in hippocampal neurons that might suppress further epileptic activity, we analyzed Golgi–Cox-stained dendritic spines from granule cells and CA1 pyramidal cells after the paroxysmal period (>P70; Fig 6E). The analysis showed reduced spine lengths in secondary and tertiary dendrites in both DG and CA1 of *Slc1a3*$^{P290R/+}$ animals (Fig 6F), with reduced spine density only in the DG (Fig 6G). These results suggest that activity-dependent elimination of synaptic connections via spine retraction may counteract the hyperexcitability of hippocampal neurons in *Slc1a3*$^{P290R/+}$ animals.

DISCUSSION

A naturally occurring *SLC1A3* mutation (P290R) was originally reported to cause ataxia and epilepsy in a patient with EA6.[1] This mutation modifies the two transport functions of EAAT1 glutamate transporters in opposite ways: it reduces glutamate transport and enhances anion channel activity.[8] We used a knock-in animal model, the *Slc1a3*$^{P290R/+}$ mouse, to understand how these changes in transporter function cause the neurological symptoms of this form of EA6. Similar to the human patient,[10] *Slc1a3*$^{P290R/+}$ mice suffer from ataxia and epilepsy. We recently reported that ataxia is caused by cerebellar degeneration in these animals[10]. Since seizures directly arising from the cerebellum have so far only been described in patients with tumorous lesions,[31–33] we looked for changes in synaptic function in the hippocampus, a brain area known to trigger seizures,[34] in the mouse model. We found that tonic GABAergic currents were decreased in DG granule cells from *Slc1a3*$^{P290R/+}$ mice. The DG controls the excitability of the hippocampal network, and GABAergic tonic inhibition of DG granule cells appears to be especially important for this function.[35]

Changes in tonic GABAergic currents are common causes of epilepsy. GABAergic tonic currents are mediated by $GABA_AR$s that contain δ subunits, and genetic ablation of the δ subunit causes epilepsy in knock-out animals.[36] Moreover, mutations that decrease the mean open times and surface membrane insertion of $GABA_AR$ cause human epilepsies,[37] indicating that changes in tonic inhibitory currents are sufficient to trigger epilepsy. The important role of tonic inhibitory currents in epilepsy was further demonstrated by the decrease in seizure susceptibility due to the ovarian cycle-linked changes in δ-subunit abundance.[26] Interestingly, *Slc1a3*$^{P290R/+}$ females have significantly lower seizure susceptibility (Fig 1D), indicating that upregulation of the $GABA_AR$ δ subunit may confer protection against seizures at certain stages of the ovarian cycle. We observed decreased GABAergic tonic inhibition in *Slc1a3*$^{P290R/+}$ DG granule cells despite no change in $GABA_AR$ δ subunit levels, indicating that decreased ambient GABA levels around mutant granule cells are a *bona fide* cause of hippocampal hyperexcitability.

Since the P290R mutation affects the glia-specific glutamate transporter EAAT1/GLAST, impaired GABAergic tonic inhibition in *Slc1a3*$^{P290R/+}$ mice likely originates from functional alterations in glial cells. *Slc1a3*$^{-/-}$ mice (which completely lack EAAT1/GLAST-mediated glutamate uptake) generated with two different gene-targeting constructs were not epileptic,[38,39] suggesting that impaired EAAT1/GLAST glutamate uptake activity does not cause seizures. Thus, in *Slc1a3*$^{P290R/+}$ mice, epilepsy must be caused by gain of function in EAAT1/GLAST anion channels and not by impaired glutamate uptake. In support of this notion, *Slc1a3*$^{P290R/+}$ mice started to develop seizures only from the third postnatal week, despite EAAT1/GLAST protein levels in the hippocampus being significantly lower in the second postnatal week (Fig 3). In the hippocampus, only RGLs (not mature hippocampal astrocytes) exhibit high EAAT1/GLAST expression levels[11–13,26]. EAAT anion channels contribute to setting the resting $[Cl^-]_{int}$ in glial cells[28], and $[Cl^-]_{int}$ was found to be reduced only in the RGLs (not in CA1 astrocytes) of *Slc1a3*$^{P290R/+}$ mice. Selective EAAT1/GLAST blockade elevates the $[Cl^-]_{int}$ to WT values in *Slc1a3*$^{P290R/+}$ RGLs but not in *Slc1a3*$^{P290R/+}$ CA1 astrocytes, indicating that changes in the RGL $[Cl^-]_{int}$ were caused by the genetic modification of EAAT1/GLAST function.

Ambient GABA levels are maintained by GABA transporters that couple GABA uptake to Na^+ and Cl^- gradients,[29] and an earlier study demonstrated that the amplitude of tonic GABAergic currents is controlled by GABA uptake.[40] In *Slc1a3*$^{P290R/+}$ RGLs, the reduced $[Cl^-]_{int}$ decreases the steady-state extracellular GABA concentration by increasing the driving force for GABA transporters. Increased GAT-3 expression in *Slc1a3*$^{P290R/+}$ hippocampi (Fig 3) will also enhance the removal of GABA. At present, we can only speculate about the mechanism responsible for GAT-3 upregulation: for example, excessive GABA uptake into *Slc1a3*$^{P290R/+}$ RGLs due to reduced $[Cl^-]_{int}$ might result in higher $[Na^+]_{int}$, and consequently to higher $[Ca^{2+}]_{int}$ via Na^+/Ca^{2+} exchange,[41] leading to GAT-3 upregulation.[42]

Radial glia, such as Bergmann glia cells and RGLs, play a key role in the pathophysiology of EA6. The bodies of radial glia are located in the ventricular zone of the developing brain, and their long processes span the neural tube that guides the migration of immature neurons in early

development. However, whereas most neurogenesis in the developing cerebellum takes place in the embryo[43], the vast majority of the hippocampal granule cells (85% in the rat) are generated after birth, with the peak of proliferation at around P7.[44] Although *Slc1a3*$^{P290R/+}$ Bergmann glia undergoes shrinkage-induced apoptosis starting at the onset of glutamatergic synaptic transmission[10], we only observed moderate degeneration in hippocampal RGLs. This clearly indicates that RGLs are less prone to shrinkage and apoptosis at physiological glutamate levels. A possible reason for the different outcomes of P290R EAAT1/GLAST expression in the two cell types is that the $[Cl^-]_{int}$ is lower in RGLs than in Bergmann glia cells[28].

We found increased amplitudes of AMPAR-mediated mEPSCs in CA1 pyramidal cells in *Slc1a3*$^{P290R/+}$ animals after the 5th postnatal week (Fig 5), along with increased expression of hippocampal AMPARs (Fig 6). Epileptic discharges often promote the potentiation of AMPAR-mediated synaptic transmission to hippocampal neurons[45, 46], with excessive AMPAR-mediated glutamatergic excitation leading to epileptic synchronization. After *Slc1a3*$^{P290R/+}$ mice reached the age of ~2 months—when the survivors do not experience further epileptic seizures—we observed reduced spine density in DG granule cells and retraction of dendritic spines in the DG and CA1 regions. The plasticity of spines depends on the extracellular glutamate concentration, that is, high concentrations prevent the spine protrusion from seeking glutamate[47]. Seizure activity raises extracellular glutamate levels[48], which might result in the activity-dependent elimination of synaptic connections via spine retraction and, thereby, protect hippocampal neurons in *Slc1a3*$^{P290R/+}$ animals.

Fig 7 illustrates our current concept of the cellular pathogenesis of epilepsy in *Slc1a3*$^{P290R/+}$ animals. Increased Cl^- efflux from RGLs through mutant EAAT1/GLAST reduces the $[Cl^-]_{int}$ and facilitates GABA uptake through glial GAT-3. Lower ambient GABA around DG granule cells reduces GABAergic tonic currents, leading to DG hyperexcitability and epilepsy. Enhanced AMPAR-mediated transmission sustains epileptic discharges and initiates abnormally prolonged seizures in adult animals. Repetitive epileptic activity causes RGL loss and spine retraction of the principal hippocampal neurons, thereby terminating epileptic seizures at around 2 months of age.

The dual function of EAATs as secondary-active glutamate transporters and anion channels[6, 6-8] and the role of EAAT anion channels in setting the glial $[Cl^-]_{int}$[28] provide a functional link between glutamatergic and GABAergic synaptic transmission. Glutamate release from synapses will activate EAAT anion channels and stimulate GABA uptake by reducing the glial $[Cl^-]_{int}$, resulting in reduced $GABA_AR$ activity. The severe epileptic phenotype of *Slc1a3*$^{P290R/+}$ mice provides a pathophysiological example of this interaction. It is tempting to speculate that this mechanism also plays a role in maintaining the equilibrium between excitatory and inhibitory synaptic transmission under physiological, and other pathophysiological, conditions.

ACKNOWLEDGEMENTS

We are grateful to Christoph Aretzweiler, Marcel Böttcher, and Tanja Mertens, for technical assistance with the care and genotyping of animals, and to Niels Danboldt for providing the *Slc1a3*$^{-/-}$ knock-out animals. We acknowledge the help of Nikola Kornadt-Beck with the legal aspects of animal breeding and thank Jennifer Cremer for helpful discussions. We also thank the E-RARE network Treat-ION (BMBF 01GM1907C to Ch.F.) and the German Research Foundation (FOR 2795; FA 301/13–1 to Ch.F.) for funding.

AUTHOR CONTRIBUTIONS

Y.K., P.K., and Ch.F. designed the research; Y.K., M.E., Sa.B., Se.B., and P.K performed data acquisition and analysis; T.G. discussed the paper; and Y.K., P.K., and Ch.F. drafted the figures and the manuscript.

CONFLICT OF INTERESTS

The authors declare no conflict of interest.

REFERENCES

1. Jen JC, Wan J, Palos TP, et al. Mutation in the glutamate transporter EAAT1 causes episodic ataxia, hemiplegia, and seizures. Neurology 2005;65:529-534.
2. de Vries B, Mamsa H, Stam AH, et al. Episodic ataxia associated with EAAT1 mutation C186S affecting glutamate reuptake. Arch Neurol 2009;66:97-101.
3. Pyle A, Smertenko T, Bargiela D, et al. Exome sequencing in undiagnosed inherited and sporadic ataxias. Brain 2015;138:276-283.
4. Choi KD, Jen JC, Choi SY, et al. Late-onset episodic ataxia associated with *SLC1A3* mutation. J Hum Genet 2017;62:443-446.
5. Choi KD, Kim JS, Kim HJ, et al. Genetic variants associated with episodic ataxia in Korea. Sci Rep 2017;7:13855.
6. Wadiche JI, Amara SG, Kavanaugh MP. Ion fluxes associated with excitatory amino acid transport. Neuron 1995;15:721-728.
7. Fahlke C, Kortzak D, Machtens JP. Molecular physiology of EAAT anion channels. Pflugers Arch 2016;468:491-502.
8. Machtens JP, Kortzak D, Lansche C, et al. Mechanisms of anion conduction by coupled glutamate transporters. Cell 2015;160:542-53.
9. Winter N, Kovermann P, Fahlke C. A point mutation associated with episodic ataxia 6 increases glutamate transporter anion currents. Brain 2012;135:3416-3425.
10. Kovermann P, Untiet V, Kolobkova Y, et al. Increased glutamate transporter-associated anion currents cause glial apoptosis in episodic ataxia 6. Brain Comms 2020;2: fcaa022.
11. Brunne B, Zhao S, Derouiche A, et al. Origin, maturation, and astroglial transformation of secondary radial glial cells in the developing dentate gyrus. Glia. 2010;58:1553-1569.
12. Mori T, Tanaka K, Buffo A, et al. Inducible gene deletion in astroglia and radial glia – a valuable tool for functional and lineage analysis. Glia 2006;54:21-34.

13. Jungblut M, Tiveron MC, Barral S, et al. Isolation and characterization of living primary astroglial cells using the new GLAST-specific monoclonal antibody ACSA-1. Glia 2012;60:894-907.

14. Moss J, Gebara E, Bushong EA, et al. Fine processes of Nestin-GFP-positive radial glia-like stem cells in the adult dentate gyrus ensheathe local synapses and vasculature. Proc Natl Acad Sci U S A 2016;113:E2536-2545.

15. McGrath JC, Drummond GB, McLachlan EM, et al. Guidelines for reporting experiments involving animals: the ARRIVE guidelines. Br J Pharmacol 2010;160:1573-1576.

16. Untiet V, Moeller LM, Ibarra-Soria X, et al. Elevated cytosolic Cl^- concentrations in dendritic knobs of mouse vomeronasal sensory neurons. Chem Senses 2016;41:669-676.

17. Verkman AS. Development and biological applications of chloride-sensitive fluorescent indicators. Am J Physiol 1990;259:C375-388.

18. Zaqout S, Kaindl AM. Golgi-Cox staining step by step. Front Neuroanat 2016;10:38.

19. Risher WC, Ustunkaya T, Singh Alvarado J, Eroglu C. Rapid Golgi analysis method for efficient and unbiased classification of dendritic spines. PloS One 2014;9:e107591.

20. Fiala JC. Reconstruct: a free editor for serial section microscopy. J Microsc 2005;218:52-61.

21. Zilles K, Palomero-Gallagher N, Grefkes C, et al. Architectonics of the human cerebral cortex and transmitter receptor fingerprints: reconciling functional neuroanatomy and neurochemistry. Eur Neuropsychopharmacol 2002;12:587-599.

22. Avanzini G, Franceschetti S. Cellular biology of epileptogenesis. Lancet Neurol 2003;2:33-42.

23. Raimondo JV, Burman RJ, Katz AA, Akerman CJ. Ion dynamics during seizures. Front Cell Neurosci 2015;9:419.

24. Wlodarczyk AI, Sylantyev S, Herd MB, et al. GABA-independent $GABA_A$ receptor openings maintain tonic currents. J Neurosci 2013;33:3905-3914.

25. Mitchell SJ, Silver RA. Shunting inhibition modulates neuronal gain during synaptic excitation. Neuron 2003;38:433-445.

26. Maguire JL, Stell BM, Rafizadeh M, Mody I. Ovarian cycle-linked changes in GABA(A) receptors mediating tonic inhibition alter seizure susceptibility and anxiety. Nat Neurosci 2005;8:797-804.

27. Furuta A, Rothstein JD, Martin LJ. Glutamate transporter protein subtypes are expressed differentially during rat CNS development. J Neurosci 1997;17:8363-8375

28. Untiet V, Kovermann P, Gerkau NJ, et al. Glutamate transporter-associated anion channels adjust intracellular chloride concentrations during glial maturation. Glia 2017;65:388-400.

29. Lu CC, Hilgemann DW. GAT1 (GABA:Na^+:Cl^-) cotransport function. Steady state studies in giant *Xenopus* oocyte membrane patches. J Gen Physiol 1999;114:429-444.

30. Rogawski MA. AMPA receptors as a molecular target in epilepsy therapy. Acta Neurol Scand Suppl 2013;(197):9-18.

31. Martins WA, Paglioli E, Hemb M, Palmini A. Dysplastic cerebellar epilepsy: Complete seizure control following resection of a ganglioglioma. Cerebellum 2016;15:535-41.

32. Dagcinar A, Hilmi Kaya A, Ali Taşdemir H, et al. A fourth ventricular ganglioneurocytoma representing with cerebellar epilepsy: a case report and review of the literature. Eur J Paediatr Neurol 2007;11:257-260.

33. Strazzer S, Zucca C, Fiocchi I, et al. Epilepsy and neuropsychologic deficit in a child with cerebellar astrocytoma J Child Neurol 2006;21:817-820.

34. Lothman EW, Stringer JL, Bertram EH. The dentate gyrus as a control point for seizures in the hippocampus and beyond. Epilepsy Res Suppl 1992;7:301-13.

35. Coulter DA, Carlson GC. Functional regulation of the dentate gyrus by GABA-mediated inhibition. Prog Brain Res 2007;163:235-243.

36. Spigelman I, Li Z, Banerjee PK, et al. Behavior and physiology of mice lacking the GABAA-receptor delta subunit. Epilepsia 2002;43 Suppl 5:3-8.

37. Feng HJ, Kang JQ, Song L, et al. Delta subunit susceptibility variants E177A and R220H associated with complex epilepsy alter channel gating and surface expression of alpha4beta2delta GABAA receptors. J Neurosci 2006;26:1499-1506.

38. Watase K, Hashimoto K, Kano M, et al. Motor discoordination and increased susceptibility to cerebellar injury in GLAST mutant mice. Eur J Neurosci 1998;10:976-988.

39. Stoffel W, Korner R, Wachtmann D, Keller BU. Functional analysis of glutamate transporters in excitatory synaptic transmission of GLAST1 and GLAST1/EAAC1 deficient mice. Brain Res Mol Brain Res 2004;128:170–181.

40. Nusser Z, Mody I. Selective modulation of tonic and phasic inhibitions in dentate gyrus granule cells. J Neurophysiol 2002;87:2624-2628.

41. Doengi M, Hirnet D, Coulon P, et al. GABA uptake-dependent Ca(2+) signaling in developing olfactory bulb astrocytes. Proc Natl Acad Sci U S A 2009;106:17570-17575.

42. Shigetomi E, Tong X, Kwan KY, et al. TRPA1 channels regulate astrocyte resting calcium and inhibitory synapse efficacy through GAT-3. Nat Neurosci 2011;15:70-80.

43. Leto K, Arancillo M, Becker EB, et al. Consensus Paper: Cerebellar Development. Cerebellum 2016;15:789-828.

44. Nicola Z, Fabel K, Kempermann G. Development of the adult neurogenic niche in the hippocampus of mice. Front Neuroanat 2015;9:53.

45. Debanne D, Thompson SM, Gähwiler BH. A brief period of epileptiform activity strengthens excitatory synapses in the rat hippocampus in vitro. Epilepsia 2006;47:247-256.

46. Joshi S, Rajasekaran K, Sun H, et al. Enhanced AMPA receptor-mediated neurotransmission on CA1 pyramidal neurons during status epilepticus. Neurobiol Dis 2017;103:45-53.

47. Richards DA, Mateos JM, Hugel S, et al. Glutamate induces the rapid formation of spine head protrusions in hippocampal slice cultures. Proc Natl Acad Sci U S A 2005;102:6166-6171.

48. Meurs A, Clinckers R, Ebinger G, et al. Seizure activity and changes in hippocampal extracellular glutamate, GABA, dopamine and serotonin. Epilepsy Res 2008;78:50-59.

FIGURES

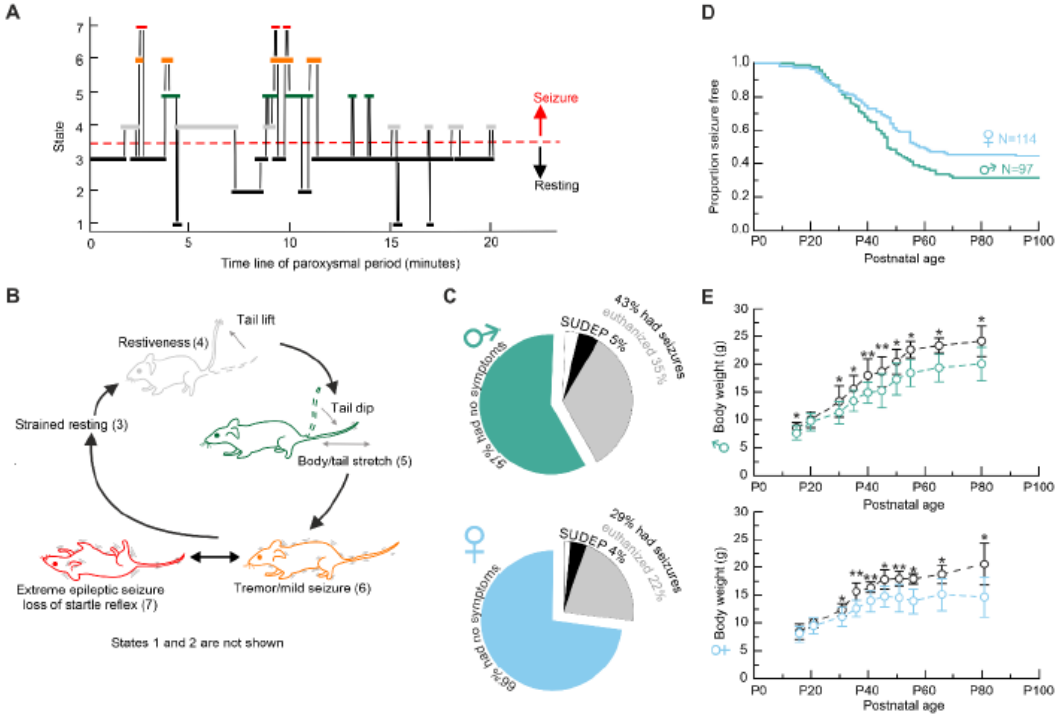

Figure 1: *Slc1a3*$^{P290R/+}$ mice suffer from tonic-clonic seizures. (A) Time line of the paroxysmal period of a representative epileptic seizure sequence from a *Slc1a3*$^{P290R/+}$ mouse (mut, also see the supplementary video), with color-coding of seizure states. 1 and 2 are resting states whereas 3 is a strained resting state (black). 4 shows a restiveness state (light grey). State 5 is characterized by body and tail stretch (green). State 6 represents tremor and mild seizure (yellow) and state 7—an extreme epileptic seizure with the loss of startle reflex (red). (B) Representative images of color-coded seizure states. (C) Percentages of mutant mice (♂ - green, ♀ - blue) affected by seizures or sudden unexpected death in epilepsy (SUDEP, N♂ = 79 / 65 and N♀ = 97 / 113, WT / mut). Mice with severe phenotype were euthanized based on predefined stop criteria.[10] (D) Seizure susceptibility of mutant mice by sex (♂ - green, ♀ - blue). Kaplan–Meier curve shows the proportion of seizure-free animals throughout the paroxysmal period for both sexes. (Log-rank statistic, $^{*}p < 0.05$). (E) Age dependence of body weight for wild-type (WT) and mutant mice (♂ - green, ♀ - blue). Each data point represents the mean weight ± standard deviation for N ≥ 3 animals. In total N♂ = 26 / 45 and N♀ = 22 / 35 (WT / mut) animals were analyzed with 2-way ANOVA and Holm–Šidák *post hoc* tests.

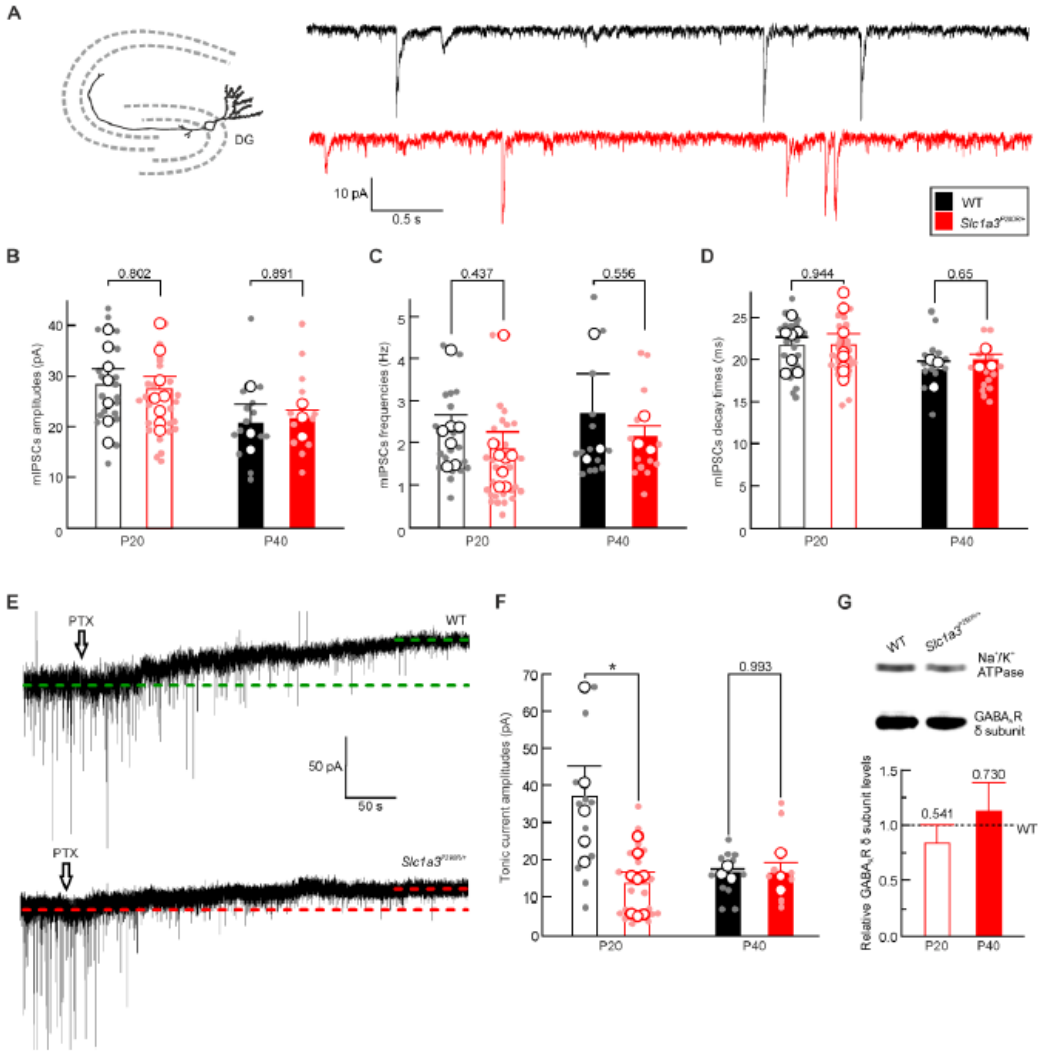

Figure 2: Reduced GABA$_A$R-mediated tonic inhibition in the hippocampal granule cells of *Slc1a3$^{P290R/+}$* mice. (A) Representative miniature inhibitory postsynaptic current (mIPSC) traces recorded from dentate gyrus (DG) granule cells of wild-type (WT) and *Slc1a3$^{P290R/+}$* (mut) mice at P20. (B) Pooled mean mIPSC amplitudes recorded from WT and mutant animals at P20 (before seizure onset) and P40 (after seizure onset). At P20, the mean mIPSC amplitudes were 28.4±8.0/27.4±7.2 pA (n=19/26 cells from N=7/8 animals, WT/mut). At P40, the mean mIPSC amplitudes of both genotypes were decreased to 16.3±5.4/18.4±10.4 pA (n=14/13, N=3/3, WT/mut). (C) Pooled mean frequencies of mIPSCs recorded from DG granule cells at P20 and P40. At P20, the mean mIPSC frequencies were 2.3±0.4/1.8±0.4 Hz (n=19/26, N=7/8, WT/mut). At P40, the mean mIPSC frequencies were 2.7±1.0/2.2±0.3 Hz (n=14/13, N=3/3, WT/mut) (D) Pooled mean decay times of mIPSCs recorded from DG granule cells at P20 and P40. At P20, the mean mIPSC decay times were 21.6±1.0/21.7±1.3 ms (n=19/26, N=7/8, WT/mut). At P40, the mean mIPSC decay times were 18.8±1.0/19.9±0.7 ms (n=13/14, N=3/3, WT/mut). (E) Representative tonic currents recorded from DG granule cells during picrotoxin (PTX, 50 µM) application. (F) Pooled mean amplitudes of tonic currents recorded from WT and mutant animals at P20 and P40. At P20, the mean amplitudes of tonic currents were 37.0±8.3/13.8±2.8 pA (n=11/18, N=5/8, WT/mut). At P40, the mean amplitudes of tonic currents were 16.4±7.1/16.4±6.7 pA (n=11/8, N=3/3, WT/mut). B–D and F present the means ± SEM of individual animals (N, big circles). (G) Western blot analysis of

$GABA_AR$ δ subunit expression in WT and mutant hippocampal tissue. Na^+/K^+-ATPase expression was used as the loading control. The graph shows the ratio of $GABA_AR$ δ subunit expression to Na^+/K^+-ATPase expression in WT (dashed line) and mutant hippocampi at P20 and P40. At P20, $GABA_AR$ δ subunit expression in the mutant hippocampi was 83±17% of that in the WT (N=3/4, WT/mut). At P40, $GABA_AR$ δ subunit expression in the *mutant* hippocampi slightly increased to 111±26% of that in the WT (N=3/3, WT/mut).

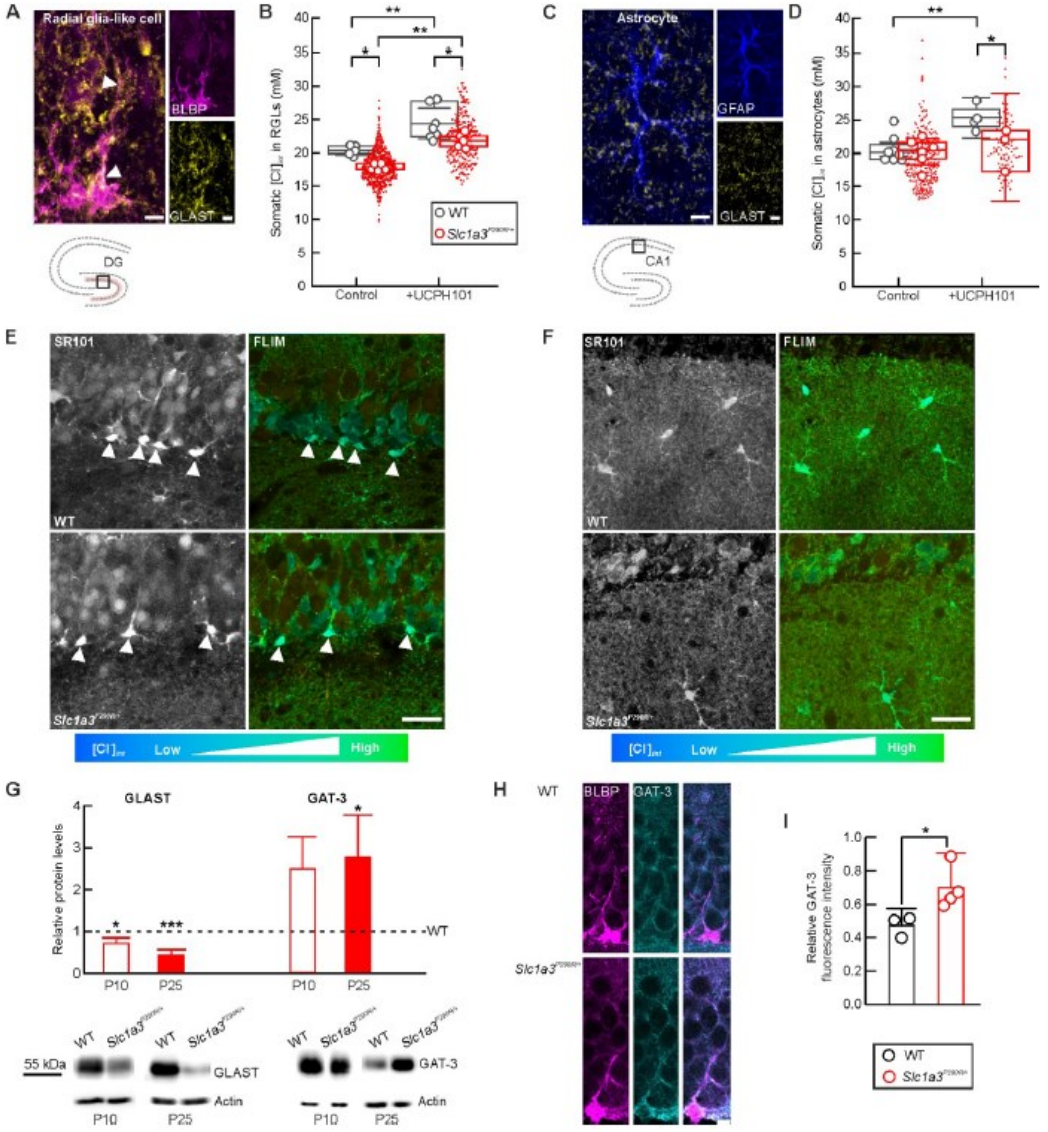

Figure 3: Reduced $[Cl^-]_{int}$ in *Slc1a3*$^{P290R/+}$ RGLs. (A) Representative confocal image of a BLBP-positive radial glia-like cell (RGL, magenta), with yellow-labeled EAAT1/GLAST. The main processes of EAAT1/GLAST-positive RGLs are indicated with arrowheads (scale bar: 5 µm). (B) Pooled mean $[Cl^-]_{int}$ in RGLs from individual wild-type (WT, gray circles; from Engels et al. 2021, submitted) and *Slc1a3*$^{P290R/+}$ animals (mut) at P20–P30. The $[Cl^-]_{int}$ were 20.3±0.9 / 17.5±0.6 mM (n=596/588 cells from N=5/5 animals, WT/mut). Application of the EAAT1/GLAST-specific

antagonist UCPH-101 increased the $[Cl^-]_{int}$ of RGLs to 24.4±2.3/21.4±1.4 mM (n=393/242, N=7/5, WT/mut). (C) Representative confocal image of a GFAP-positive (blue) astrocyte, with yellow-labeled EAAT1/GLAST (CA1 region, scale bar: 5 µm). (D) Pooled mean $[Cl^-]_{int}$ in CA1 astrocytes from individual WT (gray circles; from Engels et al. 2021, submitted) and mutant animals at P20–P30. Means of astrocytic $[Cl^-]_{int}$ were 20.6±1.7/20.3±2.2 mM (n=192/48, N=8/6, WT/mut). UCPH-101 increased the $[Cl^-]_{int}$ in WT astrocytes to 25.5±2.2 mM, but not in mutant astrocytes (20.6±8.0 mM, n=91/20, N=3/4, WT/mut). B and D present the means ± 95% confidence interval of individual WT (gray) and mutant (red) animals (2-way ANOVA and Holm–Šidák *post hoc* test). (E) Representative fluorescence lifetime imaging microscopy (FLIM) recordings in the hippocampal subgranular zone of WT and mutant mice at P25. Arrowheads show sulforhodamine 101-positive RGLs. (F) Representative FLIM recordings in the CA1 region of WT and mutant mice at P28. In E and F, the scale bar is 25 µm and $[Cl^-]_{int}$ is coded according to the color bar. (G) Western blot analysis of GLAST and GABA transporter-3 (GAT-3) in hippocampal tissue from WT and *Slc1a3*$^{P290R/+}$ animals. α-actin was used as loading control. The graph shows the expression ratios of GLAST and GAT-3 to α-actin in WT (dashed line) and mutant hippocampi at P10 and P25. At P10, GLAST expression in mutants was decreased to 71±13% of WT and GAT-3 expression in the mutants was increased to 249±77% of WT (N=4/4, WT/mut). At P25, GLAST expression in mutants was further decreased to 44±12% of WT and GAT-3 expression in the mutant hippocampi was still increased to 277±100% of WT (N=3/4, WT/mut, mean±SEM, 2-way ANOVA and Holm–Šidák *post hoc* tests). (H) Representative confocal images of BLBP-positive (magenta) RGLs expressing GAT-3 (cyan) from WT and mutant mice (scale bar: 10 µm). (I) Mean GAT-3 fluorescence intensities normalized to the BLBP fluorescences of individual cells. Data are presented as the means ± SEM from individual animals (N=3/4, WT/mut, Mann–Whitney *U*-test).

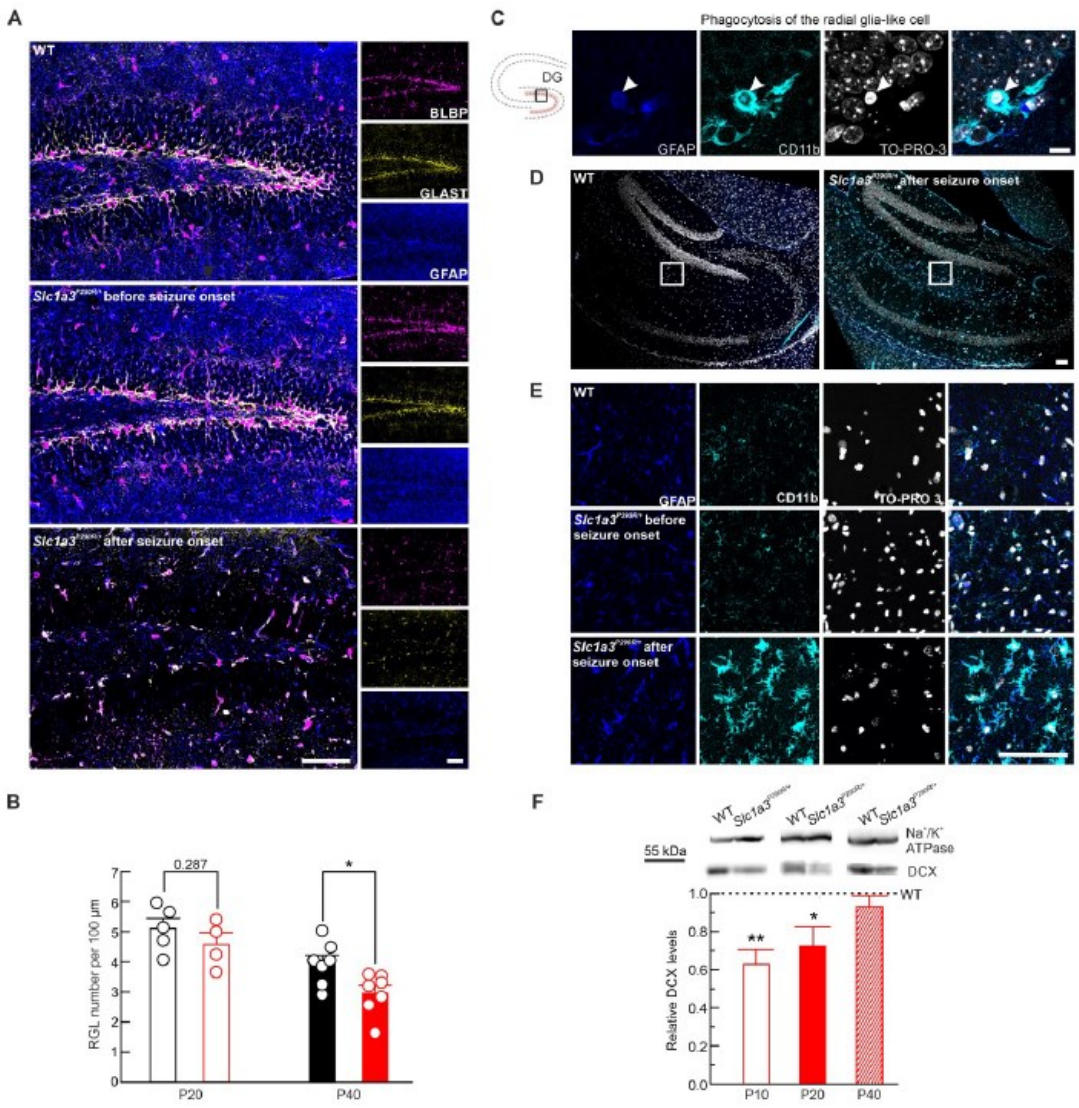

Figure 4: Hippocampal lesions in adult *Slc1a3*$^{P290R/+}$ mice.
(A) Representative confocal images of the dentate gyrus (DG) region from WT (P27, *top*) or *Slc1a3*$^{P290R/+}$ (mut, P23, *middle*; P27, *bottom*) animals immunostained for BLBP (magenta), GLAST (yellow), and GFAP (blue) indicate decreased radial glia-like cell (RGL) numbers after seizure onset in mutant animals (scale bar: 100 µm). (B) RGL density in wild-type (WT) and mutant animals at P20 and P40. At P20, the RGL numbers per 100 µm were 5.1±0.3/4.6±0.4 (N=5/4, WT/mut). At P40, the RGL numbers per 100 µm were 3.9±0.3/3.0±0.3 (N=7/4, WT/mut). (C) Representative confocal images show phagocytosis in the subgranular zone of mutant DG (P27). GFAP-positive (blue) cells have apoptotic condensed nuclei (TOPRO-3, gray) surrounded by CD11b-positive (cyan) microglial processes (scale bar: 10 µm). (D) Representative confocal overviews of WT and mutant hippocampi immunostained for GFAP and CD11b. Cell nuclei were labeled with TOPRO-3. (E) Stratum lacunosum-moleculare shown at a higher magnification. Note the thicker GFAP-positive main cellular processes of the reactive astrocytes and the increased number of branches with microglia within the mutant hippocampus, indicating astrocytosis and microgliosis in the mutant after seizures (P27, scale bars: 100 µm). (F) Western blots showing doublecortin (DCX) expression in the

hippocampal tissue of WT and mutant animals. Na^+/K^+-ATPase was used as the loading control. The graph shows the ratio of DCX to Na^+/K^+-ATPase expression in WT (dashed line) and mutant hippocampi at P10, P20, and P40. DCX expression in the mutant *Slc1a3*$^{P290R/+}$ hippocampi was 63±8% (P10, N=3/4), 72±10% (P25, N=3/5), and 94±6% (P40, N=3/3, WT/mut) of that in the WT. Data are presented as means ± SEM (2-way ANOVA and Holm–Šidák *post hoc* tests).

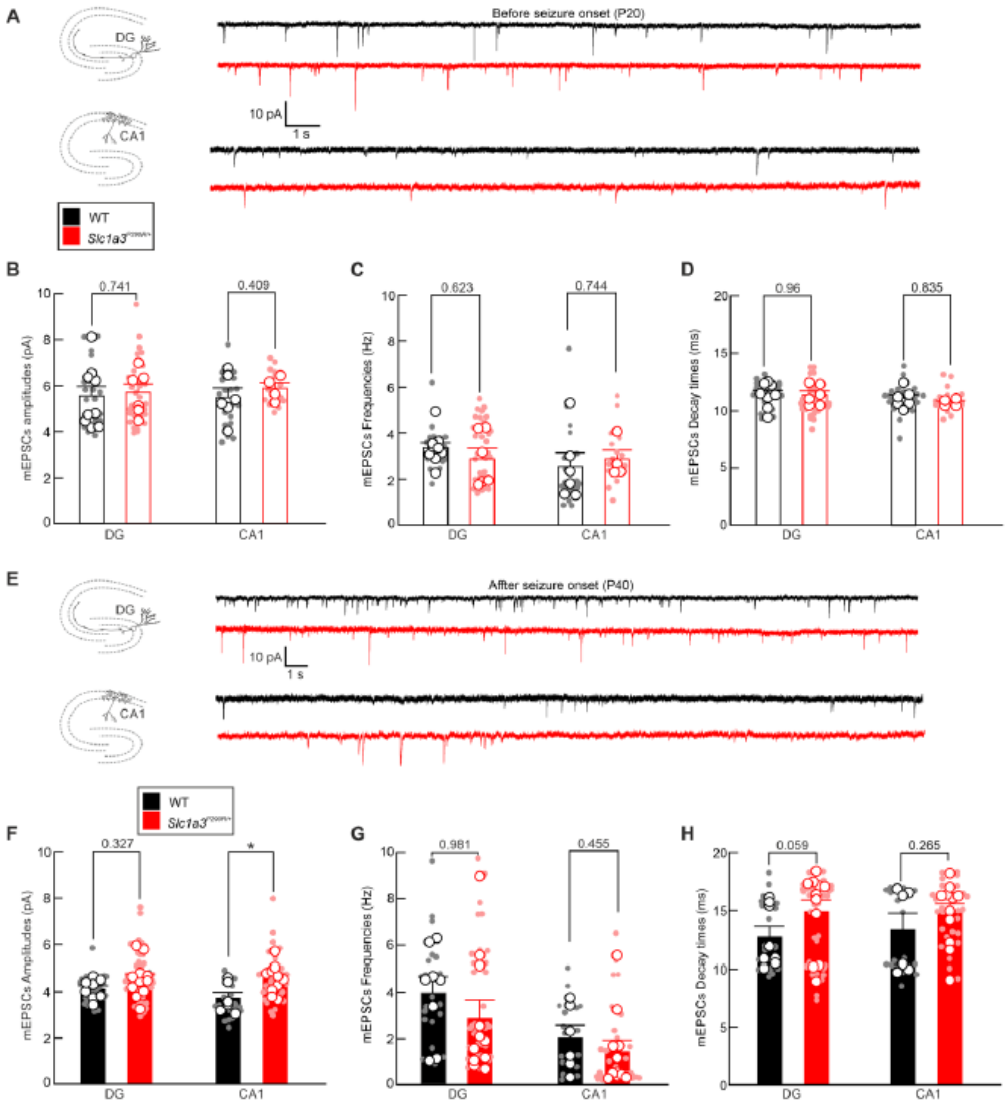

Figure 5: *Slc1a3*$^{P290R/+}$ mice have increased AMPAR-mediated currents.
(A) Representative miniature excitatory postsynaptic current (mEPSC) traces recorded from wild-type (WT) or *Slc1a3*$^{P290R/+}$(mut) dentate gyrus (DG), granule cells or CA1 pyramidal cells before seizure onset (P20). (B) Pooled mean amplitudes of mEPSCs recorded from WT and mutant DG granule cells and CA1 pyramidal cells at P20. The mean amplitudes were 5.5±0.5/5.7±0.4 pA in granule cells (n=17/28 cells from N=9/6 animals, WT/mut) and 5.5±0.4/5.8±0.3 pA in CA1 pyramidal cells (n=18/14, N=6/4; WT/mut). (C) Pooled mean frequencies of mEPSCs recorded from DG

granule cells and CA1 pyramidal cells at P20. The frequencies were 3.4±0.2/2.9±0.5 Hz (n=17/29, N=9/6, WT/mut) in granule cells and 2.5±0.6/2.8±0.4 Hz in CA1 pyramidal cells (n=18/14, N=6/4, WT/mut). (D) Pooled mean decay times of mEPSCs recorded from WT and mutant DG granule cells and CA1 pyramidal cells at P20. The decay times in granule cells were 11.4±0.4/11.3±0.3 ms (n=17/29, N=9/6, WT/mut) and 11.0±0.3/10.7±0.2 ms in CA1 pyramidal cells (n=18/14, N=6/4, WT/mut). (E) Representative mEPSC traces recorded from DG granule cells or CA1 pyramidal cells of WT and mutant mice after the seizure onset (P40). (F) Pooled mean amplitudes of mEPSCs recorded from DG granule cells and CA1 pyramidal cells at P40. The mEPSC amplitudes were 4.1±0.2/4.5±0.3 pA (n=20/33, N=8/11, WT/mut) in granule cells and 3.7±0.3/4.5±0.2 pA (n=16/25, N=6/10, WT/mut) in CA1 pyramidal cells. (G) Pooled mean frequencies of mEPSCs recorded from WT and mutant DG granule cells and CA1 pyramidal cells at P40. The mEPSC frequencies were 4.0±0.7/2.8±0.8 Hz (n=18/32, N=6/11, WT/mut) and 2.0±0.6/1.4±0.5 Hz (n=16/25, N=6/11) in CA1 pyramidal cells. (H) Pooled mean decay times of mEPSCs recorded from WT and mutant DG granule cells and CA1 pyramidal cells at P40. The mEPSC decay times were 12.6±0.9/14.9±1.0 ms (n=20/33, N=8/11) and 13.3±1.5/14.7±0.8 ms (n=16/25, N=6/11) in CA1 pyramidal cells. Data are presented as the means ± SEM from individual animals (2-way ANOVA and Holm–Šidák *post hoc* tests).

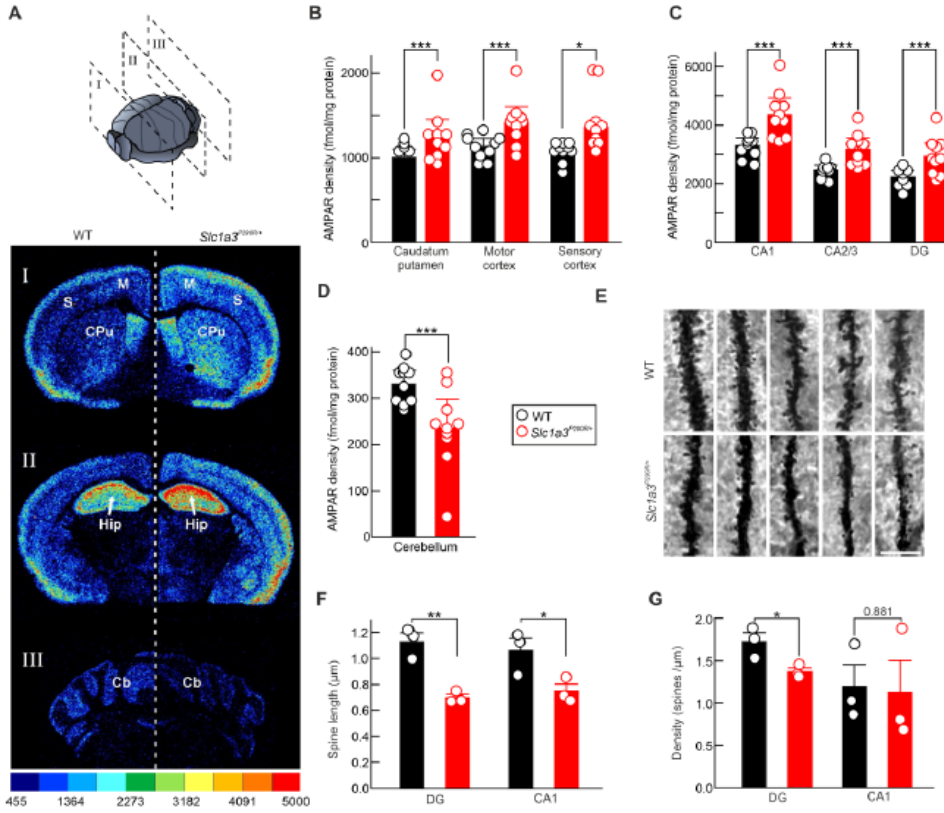

Figure 6: Hippocampal AMPAR densities and neuronal spine density are altered in adult *Slc1a3*$^{P290R/+}$ mice. (A) Contrast-enhanced color-coded AMPAR densities in the brain of wild-type (WT, *left*) and *Slc1a3*$^{P290R/+}$ mice (mut, *right*). Three cutting planes (**I–III**) show **I**, the caudate putamen (*Cpu*), motor cortex (*M*), and sensory (*S*) cortex; **II**, the hippocampus (*Hip*); and **III**, the cerebellum (*Cb*). The assigned color scale represents equally spaced density ranges in fmol/mg

protein. (B) – (D) AMPAR densities from the indicated brain regions. Data are presented as the mean densities ± 95% confidence interval (*N*=10/10 animals, WT/mut). In the caudate putamen, the AMPAR densities were 1004±101/1238±182 fmol/mg protein (WT/mut). The AMPAR densities in *M* and *S* cortices were 1133±87/1077±75 fmol/mg (*M/S*) in WT controls and 1412±165/1362±263 fmol/mg (*M/S*) in mutant animals. In the hippocampus, the AMPAR densities were 3292±252/2474±160/2227±204 fmol/mg, in WT controls and 4361±507/3173±353/2932±392 fmol/mg, in mutant animals (CA1 / CA2/3 / DG). Cerebellar AMPAR densities were 426±29/328±46 fmol/mg protein (WT/mut). (E) Representative Golgi–Cox-stained secondary and tertiary dendrites of WT and mutant granule cells (>P70, scale bar: 5 µm). (F) Pooled mean spine lengths in DG and CA1 neurons from WT and mutant animals. In the DG, the mean spine lengths were 1.13±0.07 /0.70±0.03 µm and in CA1, the spine lengths were 1.06±0.10/0.75±0.05 µm (WT/mut). (G) Pooled mean spine density measured in WT and mutant animals in DG and CA1 neurons. In DG neurons, the spine densities were 1.73±0.11/1.37±0.05 spines/µm and in CA1 1.20±0.26/1.12±0.4 spines/µm (WT/mut). F and G present data as means ± SEM for dendritic spines in 10 µm dendritic segments of DG granule cells and CA1 pyramidal cells from individual animals (N=3/3, WT/mut).

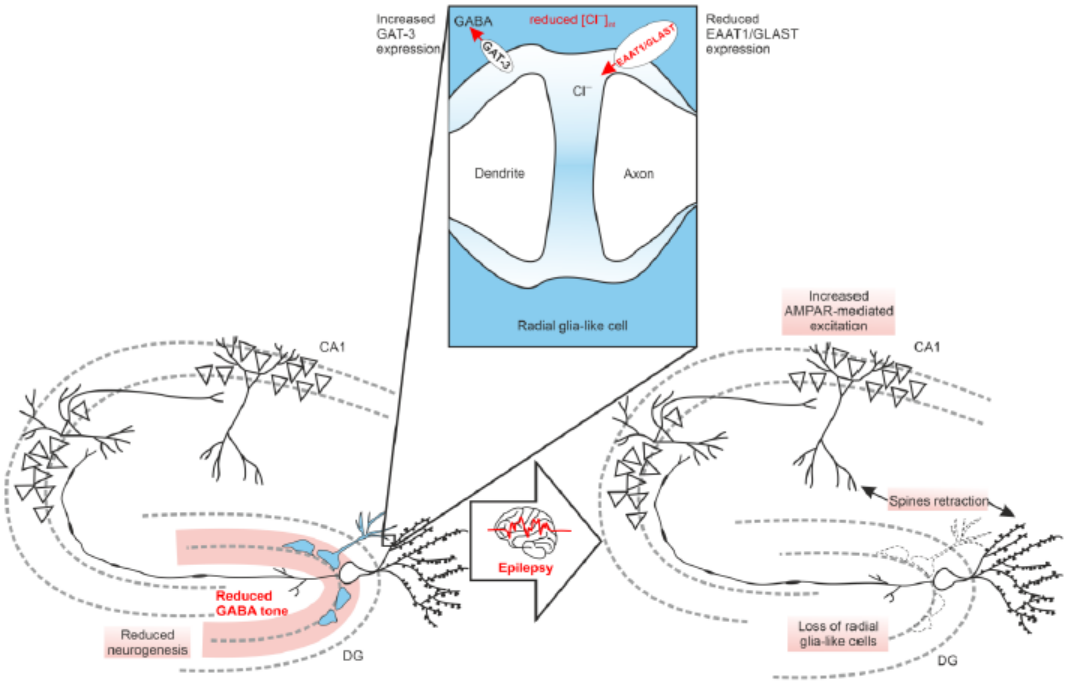

Figure 7: Hippocampal pathophysiology of EA6—from glial transporter dysfunction to seizures and morphological changes.
Increased Cl^- efflux from radial glia-like cells (RGLs) through mutant EAAT1/GLAST reduces the $[Cl^-]_{int}$, thereby stimulating GAT-3-mediated GABA uptake. Lower ambient GABA decreases tonic GABAergic currents in dentate gyrus (DG) granule cells, causing DG hyperexcitability and epilepsy. Later in adulthood, potentiated AMPAR-mediated transmission can sustain status epilepticus and initiate the abnormally prolonged seizures observed in mutant mice. Prolonged epileptic activity triggers RGLs loss and spine retraction in the principal hippocampal neurons.

3 Summary of results and conclusion

Two types of cells perform most CNS functions: neurons and glial cells, with glial cells outnumbering neurons. Glial cells support neurons, maintain their environment and regulate $[K^+]_{ext}$ and ambient neurotransmitter concentrations (Deitmer and Rose 2010). Chloride concentrations and their gradients are important determinants for volume regulation processes (McManus et al. 1995, Mongin 2016), initiation of apoptosis, the regulation of cell proliferation (Elorza-Vidal et al. 2019, Wilson and Mongin 2019) and neurotransmitter uptake (Zerangue and Kavanaugh 1996, Levy et al. 1998, Jiang et al. 2005, Eulenburg and Gomeza 2010). Defective volume regulation leads to glial cell swelling and cerebral edema in pathological conditions, such as epilepsy, hepatic failure, hyponatremia, stroke, and traumatic brain injuries (Feustel et al. 2004, Deng et al. 2014, Stokum et al. 2016, Gankam Kengne and Decaux 2018, Wilson and Mongin 2019), making glial chloride homeostasis an important determinant of normal brain function.

My thesis focuses on glial chloride homeostasis under normal conditions as well as in two different diseases, in a genetic human condition, EA6, and in early phases of brain ischemia, a vascular complication that frequently occurs in elderly patients and represents a major reason of disability or even death in our society.

FLIM measurements were used to determine $[Cl^-]_{int}$ of hippocampal astrocytes in the CA1 region (20.6 ± 2.5 mM) and the DG (28.4 ± 3.0 mM) in acute murine tissue slices, which are both higher than the value of neocortical astrocytes (14.0 ± 2.0 mM). $[Cl^-]_{int}$ in RGL cells (20.3 ± 0.7 mM) was comparable to those in CA1 astrocytes (as shown in the present study: Engels et al., submitted), but lower compared to other radial glial-like cells – BG (35.3 ± 0.3 mM) – in the cerebellum (Untiet et al. 2017). The results demonstrate that glial $[Cl^-]_{int}$ vary between different brain regions. These variations in $[Cl^-]_{int}$ might result in different volume regulation capacities and predict lower $[GABA]_{ext}$ at rest around neocortical glial cells compared to DG astrocytes or BG. The functional aspect of these variations in chloride homeostasis/$[Cl^-]_{int}$ is still unknown.

For a better understanding of the pathophysiology of EA6, a constitutive heterozygous knock-in mouse model (*Slc1a3*$^{P290R/+}$) was analysed (as shown in the present study: Kovermann et al., 2020). This mouse carries the same mutation as a reported patient with EA6, the P290R mutation of EAAT1 (Jen et al. 2005). In heterologous expressions systems, this mutation causes an increase in anion channel activity, a reduced glutamate transport and a reduction

of EAAT1 in the membrane by < 50% (Winter et al. 2012). *Slc1a3*$^{P290R/+}$ mice exhibit motor discoordination and spontaneous seizures similarly to human EA6 phenotype and thus represents a convincing animal model for this disease. Cl^- channels associated with EAAT1/GLAST are important determinants of the $[Cl^-]_{int}$ of BG (Untiet et al. 2017). FLIM experiments on BG of *Slc1a3*$^{P290R/+}$ show lower $[Cl^-]_{int}$ than in WT mice (as shown in the present study: Kovermann et al., 2020). The reduced concentration is related to an increase in Cl^- efflux in *Slc1a3*$^{P290R/+}$ mice, which can be associated with water efflux and volume decrease. Excessive Cl^- and water efflux leads to AVD (Porcelli et al. 2004, Ernest et al. 2008), which is accompanied with a detectable increase of the apoptosis indicator caspase 3 in cerebellar BG of *Slc1a3*$^{P290R/+}$ mice (as shown in the present study: Kovermann et al., 2020). The *Slc1a3*$^{P290R/+}$ mice suffer from a loss of BG in the cerebellum (as shown in the present study: Kovermann et al., 2020). Cerebella of juvenile *Slc1a3*$^{P290R/+}$ mice show a reduced amount of BG, which changes the activity of Purkinje neurons and leads to cerebellar degeneration and ataxia (as shown in the present study: Kovermann et al., 2020).

Until now, the seizures rising from the cerebellum could only be associated to tumorous lesions (Watase et al. 1998, Dagcinar et al. 2007, Martins et al. 2016). A few results in the literature describe the hippocampus and not the cerebellum as a brain region where epileptic seizures originate (Heinemann et al. 1992), which stresses the importance to study the hippocampus in our institute.

The DG is the first step in information processing and controls the excitability of the hippocampal network. Consequently, the tonic inhibition of the DG granule cells has an impact on the excitability within the hippocampal network. The inhibitory neurotransmitter GABA exerts a strong inhibitory signal influenced by extrasynaptic $GABA_A$ receptors (tonic inhibition), which leads to a reduction of the excitability of neurons. Pyramidal dendrites and granule cells of the hippocampus express high amounts of the $GABA_A$ receptor (Wisden et al. 1992, Sperk et al. 1997, Wainwright et al. 2000). Animal models of temporal lobe epilepsy show synaptic and extrasynaptic $GABA_A$ dysregulation, which may contribute to the hippocampal hyperexcitability, a hallmark of this disorder (Coulter and Carlson 2007). Furthermore, mutations in the $GABA_A$ receptor δ-subunit are associated with epilepsy in humans. Decreased channel open durations and changes expression amounts can effect seizure susceptibility (Dibbens et al. 2004, Feng et al. 2006, Coulter and Carlson 2007). In addition, the important role of tonic inhibitory currents for epilepsy is demonstrated by the

genetic ablation of δ-subunit knock-out animals (Spigelman et al. 2002). Measurements of GABAergic currents in granule cells of the DG show decreased currents in *Slc1a3*$^{P290R/+}$ mice compared to WT mice, although the protein level of the δ-subunit is unchanged in *Slc1a3*$^{P290R/+}$ mice. However, reduced GABA concentration in the extrasynaptic space results in hippocampal hyperexcitability (as shown in the present study: Kolobkova et al., in preparation). This leads to the assumption that the reduced tonic inhibition is caused by functional changes of *Slc1a3*$^{P290R/+}$ glial cells.

In the *Slc1a3*$^{P290R/+}$ mouse model seizures do not start before the third postnatal week. Before seizure onset, the expression level of EAAT1/GLAST in the hippocampus was lower compared to adult values (as shown in the present study: Kolobkova et al., in preparation)(Schreiner et al. 2014). The P290R-mediated reduced glutamate uptake (Winter et al. 2012) cannot fully explain epilepsy, since *Slc1a3*$^{-/-}$ mice completely lacking EAAT1/GLAST and hence EAAT1/GLAST-mediated glutamate uptake show no epileptic phenotype at juvenile ages (Watase et al. 1998, Stoffel et al. 2004). An important aspect here is that RGL cells express EAAT1/GLAST in a higher amount than astrocytes in the polymorphic layer of the DG (as shown in the present study: Kolobkova et al., in preparation or see attached supplementary results Figure 4.1) (Mori et al. 2006, Brunne et al. 2010, Jungblut et al. 2012).

Chloride measurements in WT and *Slc1a3*$^{P290R/+}$ mice showed lower $[Cl^-]_{int}$ in RGL cells of *Slc1a3*$^{P290R/+}$ mice than in CA1 and DG astrocytes (as shown in the present study: Kolobkova et al., in preparation; see attached supplementary results Figure 4.1). The results in astrocytic $[Cl^-]_{int}$ of CA1 and DG between WT and *Slc1a3*$^{P290R/+}$ mice showed no significant differences (see attached supplementary results Figure 4.1). Further experiments blocking EAAT1/GLAST with UCPH-101 described an increase in $[Cl^-]_{int}$ of RGL cells in *Slc1a3*$^{P290R/+}$ mice, while the $[Cl^-]_{int}$ of CA1 and DG astrocytes showed no detectable effect (as shown in the present study: Kolobkova et al., in preparation; see attached supplementary results Figure 4.1). A possible explanation for the lower hippocampal vulnerability in EA6 could be the negligible impact of the P290R mutation on CA1 and DG astrocytic $[Cl^-]_{int}$, since inhibition of EAAT1/GLAST Cl^- currents with UCPH-101 demonstrates no strong effect on the $[Cl^-]_{int}$ of *Slc1a3*$^{P290R/+}$ astrocytes. Taken together, these experiments demonstrate that the reduced $[Cl^-]_{int}$ in RGL cells of *Slc1a3*$^{P290R/+}$ mice is caused by the P290R mutation of EAAT1/GLAST (as shown in the present study: Kolobkova et al., in preparation).

The altered $[Cl^-]_{int}$ of RGL cells from *Slc1a3*$^{P290R/+}$ mice will affect the secondary active chloride-dependent GABA uptake (Eulenburg and Gomeza 2010) by increasing driving force of the GABA transporter resulting in reduced $[GABA]_{ext}$. A further reduction of the $[GABA]_{ext}$ is achieved by increased expression levels of GAT-3 in *Slc1a3*$^{P290R/+}$ RGL cells as demonstrated by immunohistochemistry experiments (as shown in the present study: Kolobkova et al., in preparation). A possible explanation for the increased GAT-3 expression is that lower $[Cl^-]_{int}$ of *Slc1a3*$^{P290R/+}$ RGL cells may lead to higher $[Na^+]_{int}$, that activates the Na^+/ Ca^{2+} exchanger. Consequently, elevation of the resting Ca^{2+} levels (Doengi et al. 2009) was shown to increase expression of GAT-3 (Shigetomi et al. 2011). Reduced $[GABA]_{ext}$ around DG granule cells explain the observed reduction in GABAergic tonic currents in *Slc1a3*$^{P290R/+}$ mice before seizure onset, which leads to DG hyperexcitability and epilepsy, as observed in the mouse model. Seizure activity at later stages are caused by enhanced AMPA receptor-mediated transmission as measured with autoradiography of radioactive neurotransmitters (as shown in the present study: Kolobkova et al., in preparation). Lastly, the P290R mutation causes a loss of RGL cells after seizure onset as well as spine retraction of neurons in the DG (as shown in the present study: Kolobkova et al., in preparation). These results help to understand the complex appearance of EA6. Whereas the increased chloride efflux leads to *Slc1a3*$^{P290R/+}$ BG apoptosis and cerebellar degeneration (as shown in the present study: Kovermann et al. 2020), *Slc1a3*$^{P290R/+}$ RGL cells show only moderate degeneration, (as shown in the present study: Kolobkova et al., in preparation), likely because of the lower $[Cl^-]_{int}$ in RGL cells.

$[Cl^-]_{int}$ thus turns out to be a main determinant of clinical symptoms in EA6. To study the role of $[Cl^-]_{int}$ in brain ischemia, I studied the effect of energy restriction on glial chloride homeostasis (Engels et al., (submitted)). $[Cl^-]_{int}$ was determined in different glial cell types, revealing marked differences in chloride homeostasis among each other.

Blocking the NKCC1 with bumetanide decreased $[Cl^-]_{int}$ in hippocampal CA1 and DG astrocytes, but without any striking effect in neocortical astrocytes and RGL cells. Inhibiting KCCs, the antagonists of NKCC1, with *R*-(+)-DIOA in hippocampal astrocytes show only minor changes in the $[Cl^-]_{int}$, but had clearly effects in neocortical astrocytes and RGL cells. The inhibition of EAAT1/GLAST with UCPH-101 increased the $[Cl^-]_{int}$ in RGL cells and hippocampal CA1 astrocytes. In addition, DG astrocytes showed a slight increase compared to the significant increase in neocortical astrocytes. DL-TBOA leads only in RGL cells and neocortical glial cells to a further increase of the $[Cl^-]_{int}$ (as shown in the present study: Engels et al.,

submitted). The distinct effects of chloride transporter/channel blockers in different brain regions suggested region-specific variability of chloride transporter/channel expression.

Chloride transporters/channels utilize driving forces that are influenced by metabolic stress. The ischemic penumbra can be mimicked by removing glucose from standard ringer solutions, blocking oxidative phosphorylation with sodium azide and glycolysis with 2-deoxy-D-glucose (Gerkau et al. 2018), to study modifications of glial $[Cl^-]_{int}$. We demonstrated that chemical ischemia reduce cellular ATP levels (as shown in the present study: Engels et al., submitted), and thus $[Na^+]_{ext}$ and $[K^+]_{int}$. These changes will modify the activity of the major glial chloride transporters, NKCC1 and the KCCs, as well as the open probability of EAAT anion channels changes. However, the glial $[Cl^-]_{int}$ was only slightly affected (as shown in the present study: Engels et al., submitted).

Since cell swelling will result in changes in $[Cl^-]_{int}$, our result indicates that there is little glial cell swelling under chemical ischemia. This notion was supported by glial volume measurements under chemical ischemia (10 min) (as shown in the present study: Engels et al., submitted).

These unexpected results guided further experiments to study the activity of different chloride transporter/channel during transient energy restriction. If neocortical astrocytes are treated with bumetanide the $[Cl^-]_{int}$ decreases further under ischemia conditions. Blocking KCCs after energy restriction results in dramatically higher and variable $[Cl^-]_{int}$. These two results indicate that the altered cation gradient due to ischemia activates the NKCC1 transporter, whose activity is compensated by ischemia-activated KCC transporters. Autopsy analysis of human brains shows that stroke or metabolic stress are possible explanations for upregulation of NKCC1 located in neurons (Bhuiyan et al. 2017). Blocking EAAT1/GLAST and EAAT2/GLT-1 anion channels under ischemic conditions did not result in substantial changes in $[Cl^-]_{int}$, demonstrating that these transporters and their anion channels have only a slight impact on the chloride homeostasis under ischemia (as shown in the present study: Engels et al., submitted).

A mathematical model established by Kalia et al. (Kalia et al. 2021) describes the distribution of Na^+, K^+, Cl^-, Ca^{2+} and glutamate, and volume changes at the tripartite synapse under metabolic stress. The model combined ion transport by several ion channels and transporters. Model parameters were chosen to account for experimental results in Engels et al. (submitted) and Na^+ measurements (Gerkau et al. 2018). The model of the tripartite

synapse under metabolic stress also includes the possibility to swell and contract in proportion to the osmolarity on both sides of the membrane. We focused on neocortical and DG astrocytes, as these two groups exhibit either a strong chloride accumulation in neocortical astrocytes or a weaker NKCC1 activity in DG astrocytes, as well as different impacts of KCC transporters. Simultaneously blocking neuronal and astrocyte Na^+/K^+-ATPase to 50% of baseline pumping capacity, mimicking the chemical ischemia protocol. Simulated astrocytes were exposed to a previous blocker incubation time of 20 min (as in the experiments presented in Engels et al., submitted) of bumetanide (blocks NKCC1), *R*-(+)-DIOA (blocks astrocyte KCCs) and DL-TBOA (blocks neuronal and astrocyte EAAT) and the chemical ischemia protocol plus a still active blockade of the transporter and channels. The results of the simulations nicely reproduced the observed experimental data (as shown in the present study: Engels et al., submitted). They demonstrate that the lower $[Cl^-]_{int}$ in neocortical astrocytes compared to astrocytes in the DG is caused by higher numbers of NKCC1 and KCCs. The effect of DL-TBOA during energy restriction was very small and similar to results under energy restriction, which only indicates a minor influence of EAAT1/2 anion channels on chloride homeostasis under transient ischemia. The results indicate that ischemia activates NKCC1-mediated inward transport, which is compensated by an increased KCC-mediated outward transport. As a result, astrocytes regulate their $[Cl^-]_{int}$ under metabolic stress and consequently attain cell volume stability under transient energy deprivation.

This dissertation demonstrates that glial chloride is not passively distributed, but rather actively established via transporters and channels and that $[Cl^-]_{int}$ varies among in different glial cell types and brain regions. Changes in chloride concentration due to a gain of function mutation of the glial EAAT1/GLAST can have a dramatic impact on ion homeostasis, cell volume and apoptosis, modifying extrasynaptic GABA concentrations and triggering seizures. In contrast, experiments on chloride homeostasis under transient energy restriction revealed that glial cells can control $[Cl^-]_{int}$ and support cell volume stability under such conditions.

4 Supplementary information

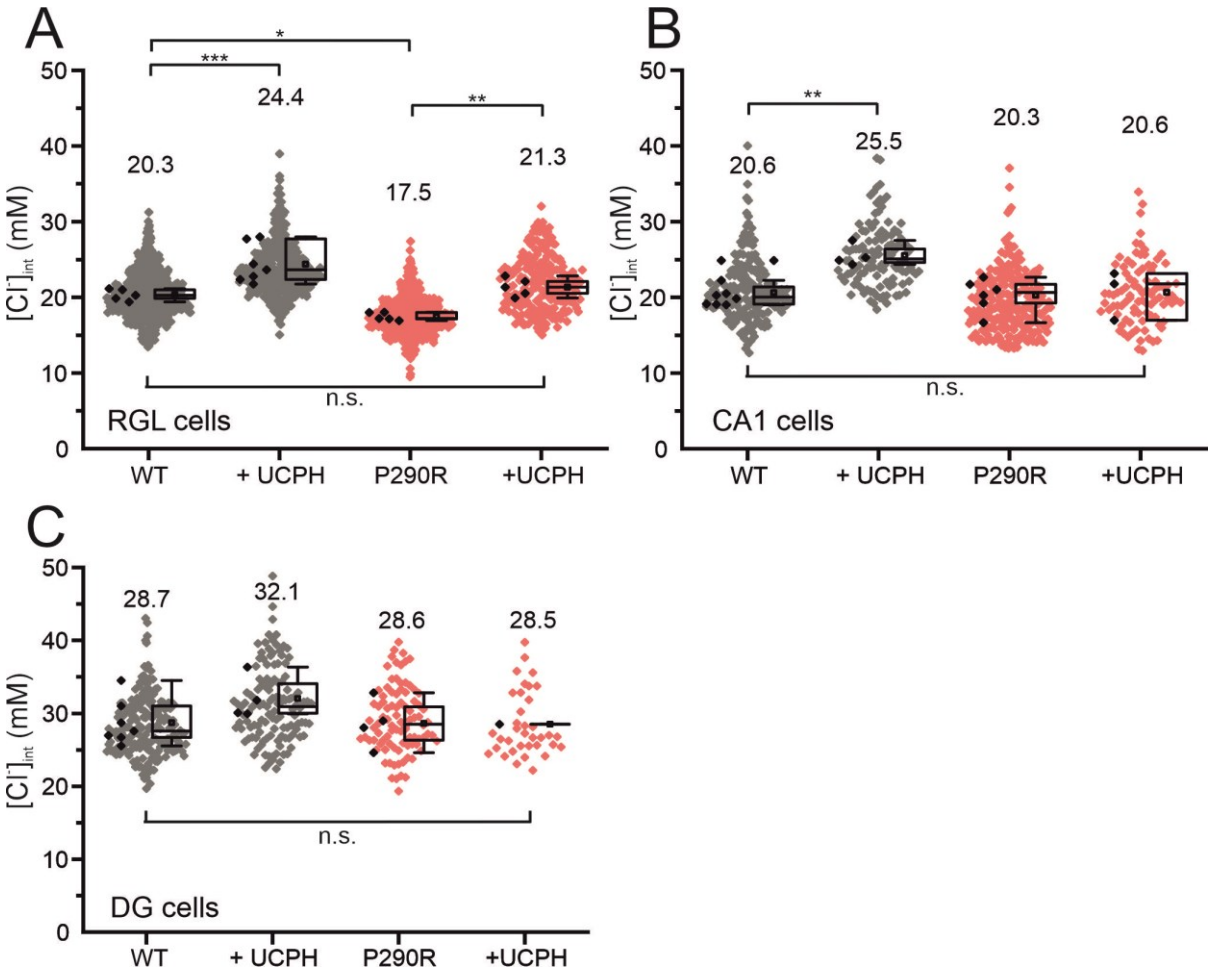

Figure 4.1: EAAT1/GLAST dependence of $[Cl^-]_{int}$ in RGLs and hippocampal glial cells – CA1 and DG in WT and *Slc1a3*$^{P290R/+}$ animals (P20-P30).

$[Cl^-]_{int}$ of hippocampal astrocytes in RGL cells (A) as well as hippocampal astrocytes in CA1 (B) and DG (C) under physiological conditions and after application of EAAT1/GLAST-specific antagonist UCPH-101 in WT (grey) and *Slc1a3*$^{P290R/+}$ mice (red). (A) The $[Cl^-]_{int}$ in RGL cells from *Slc1a3*$^{P290R/+}$ animals (17.5±0.5 mM, n=588 cells from N=5 animals) is significantly lower compared to the $[Cl^-]_{int}$ from WT animals (20.3±0.7 mM, n=596, N=5 animals). Application of UCPH-101 increases $[Cl^-]_{int}$ in WT and *Slc1a3*$^{P290R/+}$ RGL cells (24.4±2.5/21.3±1.2 mM, n=393/242, N=7/5, WT/Mut). (B) Mean $[Cl^-]_{int}$ is not different in CA1 astrocytes from WT and *Slc1a3*$^{P290R/+}$ animals (20.6±2.0/20.3±2.1 mM, n=192/248, N=8/6, WT/Mut). Note, that the UCPH-101 application does cause $[Cl^-]_{int}$ rise in WT astrocytes (25.5±1.4 mM, n=120, N=4) but not in *Slc1a3*$^{P290R/+}$ astrocytes (20.6±3.2 mM, n=91, N=3) as observed in *Slc1a3*$^{P290R/+}$ RGL cells. (C) So far $[Cl^-]_{int}$ of DG astrocytes show no difference between WT and *Slc1a3*$^{P290R/+}$ animals (28.7±3.1/28.6±3.4 mM, n=199/90, N=7/4, WT/Mut). Only in WT animals the $[Cl^-]_{int}$ increases due to UCPH-101 application (32.0±3.0 mM, n=126, N=4) and not in *Slc1a3*$^{P290R/+}$ animals (28.5±X mM, n=36, N=1). Box plots depict mean $[Cl^-]_{int}$ (mean ± 1.5 Interquartile range) from individual animals as black points and results from individual cells as grey (WT) or red (P290R) points. In the figure legend, $[Cl^-]_{int}$ are given as the mean ± standard deviation values from animals. A and B discussed results in Engels et al., submitted (WT) and Kolobkova et al., in preparation (WT + P290R). For statistical analysis, one-way ANOVA tests with Holm–Sidak *post hoc* testing were used to determine *p*-values. *$p \leq 0.05$, **$p \leq 0.01$ and ***$p \leq 0.001$; all *p*-values for this figure are provided in the following Supplementary Table 1. Abbreviations: RGL – Radial glial-like cells; CA1 – cornu ammonis region 1; DG – dentate gyrus; UCPH – UCPH-101; WT – WT animals; P290R – *Slc1a3*$^{P290R/+}$ animals

Supplementary Table 1 P-values

Sup. Fig. 1 RGL

One-way ANOVA	Significance α = 0.05 ?	Summary	P-value Holm-Sidak
WT - WT + UCPH	Yes	***	4.398E-4
WT - P290R	Yes	*	0.012
P290R - P290R + UCPH	Yes	**	0.001
WT - P290R+ UCPH	No	n.s.	0.333

alpha levels
0.00851
0.01021
0.01274
0.01695
0.02532
0.05

Sup. Fig. 1 CA1

One-way ANOVA	Significance α = 0.05 ?	Summary	P-value Holm-Sidak
WT - WT + UCPH	Yes	**	0.002
WT - P290R	No	n.s.	0.764
P290R - P290R + UCPH	No	n.s.	0.811
WT - P290R+ UCPH	No	n.s.	0.991

Sup. Fig. 1 DG

One-way ANOVA	Significance α = 0.05 ?	Summary	P-value Holm-Sidak
WT - WT + UCPH	No	n.s.	0.118
WT - P290R	No	n.s.	0.959
P290R - P290R + UCPH	No	n.s.	0.979
WT - P290R+ UCPH	No	n.s.	0.956

5 Abbreviations

AVD	Apoptotic volume decrease
BGT-1	Betaine/GABA transporter 1
BLBP	Brain lipid-binding protein
CA	Cornu ammonis
CA1-3	Cornu ammonis region 1-3
Cl^-	Chloride
$[Cl^-]_{ext}$	Extracellular chloride concentration
$[Cl^-]_{int}$	Intracellular chloride concentration
DG	Dentate gyrus
DMSO	Dimethylsulfoxid
EAAC 1	Excitatory amino acid carrier 1
EAAT 1-5	Excitatory Amino Acid Transporter 1-5
EA6	Episodic ataxia type 6
EGFP	Enhanced green fluorescent protein
FLIM	Fluorescence lifetime imaging microscopy
GABA	Gamma amino isobutyric acid/ γ-aminobutyric acid
$[GABA]_{ext}$	Extracellular GABA concentration
GAT-1/GAT-3	GABA transporter 1/3
GFAP	Glial fibrillary acid protein
GLAST	Glutamate–aspartate transporter Mammalian EAAT1
GLT-1	Glutamate transporter Mammalian EAAT2
GluR	Glutamate receptor
GluT	Glutamate transporter
$[glutamate]_{ext}$	Extracellular glutamate concentration
HCO^-_3	Bicarbonate
$h\nu$	h is the Planck constant; ν the frequency of the photon
K^+	Potassium
$[K^+]_{ext}$	Extracellular potassium concentration
$[K^+]_{int}$	Intracellular potassium concentration

k_f	Rate of spontaneous emission
k_{nr}	Constant to describe the non-radiative energy transition
k_q	Constant to describe the non-radiative energy transition in presence of a quencher (chloride)
KCC 1-3	Potassium chloride cotransporter 1-3
K_{SV}	Stern-Volmer constant
λ	Wavelength
mM	Millimolar
MQAE	1-(Ethoxycarbonylmethyl)-6-methoxy-quinolium bromide
Na^+	Sodium
$[Na^+]_{ext}$	Extracellular sodium concentration
$[Na^+]_{int}$	Intracellular sodium concentration
NKCC1	Sodium Potassium Chloride Cotransporter 1
nm	Nanometer
n.s.	Not significant
P290R	Substitution of Proline in the transmembrane domain 5 at position 290 by arginine
P	Status of significance
PX	Postnatal day X
S_0	Ground state
S_1	Excited state
SLC	Solute carrier family
Slc1a3^{P290R}/$^+$	EAAT1/GLAST (*Slc1a3*) heterozygous knock-in
Slc1a3$^-$/$^-$	EAAT1/GLAST (*Slc1a3*) knock-out
SR101	Sulforhodamine 101
τ	Fluorescence lifetime
TCSPC	Time Correlated Single Photon Counting
VRAC	Volume regulated anion channels
WT	Wildtype

6 References

Amaral, D. G. (1978). "A Golgi study of cell types in the hilar region of the hippocampus in the rat." J Comp Neurol **182**(4 Pt 2): 851-914.

Amaral, D. G. and M. P. Witter (1989). "The three-dimensional organization of the hippocampal formation: a review of anatomical data." Neuroscience **31**(3): 571-591.

Amaral, D. G., et al. (2007). "The dentate gyrus: fundamental neuroanatomical organization (dentate gyrus for dummies)." Prog Brain Res **163**: 3-22.

Arcuri, C., et al. (2017). "The Pathophysiological Role of Microglia in Dynamic Surveillance, Phagocytosis and Structural Remodeling of the Developing CNS." Front Mol Neurosci **10**: 191.

Arosio, D. and G. M. Ratto (2014). "Twenty years of fluorescence imaging of intracellular chloride." Front Cell Neurosci **8**: 258.

Becker, W. (2005). Advanced Time-Correlated Single Photon Counting Techniques, Springer-Verlag Berlin Heidelberg

Bekar, L. K. and W. Walz (2002). "Intracellular chloride modulates A-type potassium currents in astrocytes." Glia **39**(3): 207-216.

Belelli, D., et al. (2009). "Extrasynaptic GABAA receptors: form, pharmacology, and function." J Neurosci **29**(41): 12757-12763.

Belov Kirdajova, D., et al. (2020). "Ischemia-Triggered Glutamate Excitotoxicity From the Perspective of Glial Cells." Front Cell Neurosci **14**: 51.

Berezin, M. Y. and S. Achilefu (2010). "Fluorescence lifetime measurements and biological imaging." Chem Rev **110**(5): 2641-2684.

Berg, D. A., et al. (2018). "Radial glial cells in the adult dentate gyrus: what are they and where do they come from?" F1000Res **7**: 277.

Bevensee, M. O., et al. (1997). "Intracellular pH regulation in cultured astrocytes from rat hippocampus. II. Electrogenic Na/HCO3 cotransport." J Gen Physiol **110**(4): 467-483.

Bhuiyan, M. I. H., et al. (2017). "WNK-Cab39-NKCC1 signaling increases the susceptibility to ischemic brain damage in hypertensive rats." J Cereb Blood Flow Metab **37**(8): 2780-2794.

Biwersi, J. and A. S. Verkman (1991). "Cell-permeable fluorescent indicator for cytosolic chloride." Biochemistry **30**(32): 7879-7883.

Blaesse, P., et al. (2009). "Cation-chloride cotransporters and neuronal function." Neuron **61**(6): 820-838.

Bond, A. M., et al. (2015). "Adult Mammalian Neural Stem Cells and Neurogenesis: Five Decades Later." Cell Stem Cell **17**(4): 385-395.

Borden, L. A. (1996). "GABA transporter heterogeneity: pharmacology and cellular localization." Neurochem Int **29**(4): 335-356.

Bortner, C. D. and J. A. Cidlowski (2003). "Uncoupling cell shrinkage from apoptosis reveals that Na+ influx is required for volume loss during programmed cell death." J Biol Chem **278**(40): 39176-39184.

Braak, H., et al. (1996). "Functional anatomy of human hippocampal formation and related structures." Journal of Child Neurology **11**(4): 265-275.

Brodmann, K. (1909). "Vergleichende Lokalisationslehre der Grosshirnrinde in ihren Prinzipien dargestellt auf Grund des Zellenbaues." Verlag von Johann Ambrosius Barth.

Brunne, B., et al. (2010). "Origin, maturation, and astroglial transformation of secondary radial glial cells in the developing dentate gyrus." Glia **58**(13): 1553-1569.

Bryson, A., et al. (2020). "GABA-mediated tonic inhibition differentially modulates gain in functional subtypes of cortical interneurons." Proc Natl Acad Sci U S A **117**(6): 3192-3202.

Cammack, J. N., et al. (1994). "A GABA transporter operates asymmetrically and with variable stoichiometry." Neuron **13**(4): 949-960.

Chizhikov, V. and K. J. Millen (2003). "Development and malformations of the cerebellum in mice." Molecular Genetics and Metabolism **80**(1-2): 54-65.

Choi, K. D., et al. (2017a). "Late-onset episodic ataxia associated with SLC1A3 mutation." J Hum Genet **62**(3): 443-446.

Choi, K. D., et al. (2017b). "Genetic Variants Associated with Episodic Ataxia in Korea." Sci Rep **7**(1): 13855.

Coulter, D. A. and G. C. Carlson (2007). "Functional regulation of the dentate gyrus by GABA-mediated inhibition." Prog Brain Res **163**: 235-243.

Dagcinar, A., et al. (2007). "A fourth ventricular ganglioneurocytoma representing with cerebellar epilepsy: a case report and review of the literature." Eur J Paediatr Neurol **11**(5): 257-260.

Danbolt, N. C. (2001). "Glutamate uptake." Prog Neurobiol **65**(1): 1-105.

de Vries, B., et al. (2009). "Episodic ataxia associated with EAAT1 mutation C186S affecting glutamate reuptake." Arch Neurol **66**(1): 97-101.

Deitmer, J. W. and C. R. Rose (2010). "Ion changes and signalling in perisynaptic glia." Brain Res Rev **63**(1-2): 113-129.

Delpire, E. and K. J. Staley (2014). "Novel determinants of the neuronal Cl(-) concentration." J Physiol **592**(19): 4099-4114.

Deng, J., et al. (2014). "Expression of aquaporin 4 and breakdown of the blood-brain barrier after hypoglycemia-induced brain edema in rats." PLoS One **9**(9): e107022.

Dibbens, L. M., et al. (2004). "GABRD encoding a protein for extra- or peri-synaptic GABAA receptors is a susceptibility locus for generalized epilepsies." Hum Mol Genet **13**(13): 1315-1319.

Doengi, M., et al. (2009). "GABA uptake-dependent Ca(2+) signaling in developing olfactory bulb astrocytes." Proc Natl Acad Sci U S A **106**(41): 17570-17575.

Elorza-Vidal, X., et al. (2019). "Chloride Channels in Astrocytes: Structure, Roles in Brain Homeostasis and Implications in Disease." Int J Mol Sci **20**(5).

Eriksson, P. S., et al. (1998). "Neurogenesis in the adult human hippocampus." Nat Med **4**(11): 1313-1317.

Ernest, N. J., et al. (2008). "Cytoplasmic condensation is both necessary and sufficient to induce apoptotic cell death." J Cell Sci **121**(Pt 3): 290-297.

Eulenburg, V. and J. Gomeza (2010). "Neurotransmitter transporters expressed in glial cells as regulators of synapse function." Brain Res Rev **63**(1-2): 103-112.

Fahlke, C., et al. (2016). "Molecular physiology of EAAT anion channels." Pflugers Arch **468**(3): 491-502.

Feng, H. J., et al. (2006). "Delta subunit susceptibility variants E177A and R220H associated with complex epilepsy alter channel gating and surface expression of alpha4beta2delta GABAA receptors." J Neurosci **26**(5): 1499-1506.

Feustel, P. J., et al. (2004). "Volume-regulated anion channels are the predominant contributors to release of excitatory amino acids in the ischemic cortical penumbra." Stroke **35**(5): 1164-1168.

Fredriksson, R., et al. (2008). "The solute carrier (SLC) complement of the human genome: phylogenetic classification reveals four major families." FEBS Lett **582**(27): 3811-3816.

Gankam Kengne, F. and G. Decaux (2018). "Hyponatremia and the Brain." Kidney Int Rep **3**(1): 24-35.

Gebara, E., et al. (2016). "Heterogeneity of Radial Glia-Like Cells in the Adult Hippocampus." Stem Cells **34**(4): 997-1010.

Gensch, T., et al. (2015). Determination of Intracellular Chloride Concentrations by Fluorescence Lifetime Imaging. Advanced Time-Correlated Single Photon Counting Applications. Springer International Publishing Switzerland 2015. **111:** 189-211.

Gerkau, N. J., et al. (2018). "Reverse NCX Attenuates Cellular Sodium Loading in Metabolically Compromised Cortex." Cereb Cortex **28**(12): 4264-4280.

Glykys, J. and I. Mody (2007). "Activation of GABAA receptors: views from outside the synaptic cleft." Neuron **56**(5): 763-770.

Guastella, J., et al. (1990). "Cloning and expression of a rat brain GABA transporter." Science **249**(4974): 1303-1306.

Harris, K. D., et al. (2014). "Why are neurotransmitters neurotoxic? An evolutionary perspective." F1000Res **3**: 179.

Hatten, M. E., et al. (1984). "Two forms of cerebellar glial cells interact differently with neurons in vitro." J Cell Biol **98**(1): 193-204.

Heinemann, U., et al. (1992). "The dentate gyrus as a regulated gate for the propagation of epileptiform activity." Epilepsy Res Suppl **7**: 273-280.

Hertz, L., et al. (2015). "Roles of astrocytic Na(+),K(+)-ATPase and glycogenolysis for K(+) homeostasis in mammalian brain." J Neurosci Res **93**(7): 1019-1030.

Hilgemann, D. W. and C. C. Lu (1999). "GAT1 (GABA:Na+:Cl-) cotransport function. Database reconstruction with an alternating access model." J Gen Physiol **114**(3): 459-475.

Hotzy, J., et al. (2013). "Mutating a conserved proline residue within the trimerization domain modifies Na+ binding to excitatory amino acid transporters and associated conformational changes." J Biol Chem **288**(51): 36492-36501.

Hughes, F. M., Jr., et al. (1997). "Intracellular K+ suppresses the activation of apoptosis in lymphocytes." J Biol Chem **272**(48): 30567-30576.

Iwama, K., et al. (2018). "A novel mutation in SLC1A3 causes episodic ataxia." J Hum Genet **63**(2): 207-211.

Jabs, R., et al. (2005). "Synaptic transmission onto hippocampal glial cells with hGFAP promoter activity." J Cell Sci **118**(Pt 16): 3791-3803.

Jäkel, S. and L. Dimou (2017). "Glial Cells and Their Function in the Adult Brain: A Journey through the History of Their Ablation." Front Cell Neurosci **11**.

Jen, J. C., et al. (2005). "Mutation in the glutamate transporter EAAT1 causes episodic ataxia, hemiplegia, and seizures." Neurology **65**(4): 529-534.

Jentsch, T. J. and M. Pusch (2018). "CLC Chloride Channels and Transporters: Structure, Function, Physiology, and Disease." Physiol Rev **98**(3): 1493-1590.

Jiang, G., et al. (2005). "A Na+/Cl- -coupled GABA transporter, GAT-1, from Caenorhabditis elegans: structural and functional features, specific expression in GABA-ergic neurons, and involvement in muscle function." J Biol Chem **280**(3): 2065-2077.

Jin, X. T., et al. (2011). "Localization and Function of GABA Transporters GAT-1 and GAT-3 in the Basal Ganglia." Front Syst Neurosci **5**: 63.

Jungblut, M., et al. (2012). "Isolation and characterization of living primary astroglial cells using the new GLAST-specific monoclonal antibody ACSA-1." Glia **60**(6): 894-907.

Kafitz, K. W., et al. (2008). "Developmental profile and properties of sulforhodamine 101--Labeled glial cells in acute brain slices of rat hippocampus." J Neurosci Methods **169**(1): 84-92.

Kahle, K. T., et al. (2015). "K-Cl cotransporters, cell volume homeostasis, and neurological disease." Trends Mol Med **21**(8): 513-523.

Kalia, M., et al. (2021). "Ion dynamics at the energy-deprived tripartite synapse." bioRxiv: 2021.2003.2019.436129.

Kaneko, H., et al. (2002). "Determination of intracellular chloride concentration in dorsal root ganglion neurons by fluorescence lifetime imaging." Calcium-Activated Chloride Channels **53**: 167-+.

Kaneko, H., et al. (2004). "Chloride accumulation in mammalian olfactory sensory neurons." J Neurosci **24**(36): 7931-7938.

Katan, M. and A. Luft (2018). "Global Burden of Stroke." Semin Neurol **38**(2): 208-211.

Kettenmann, H., et al. (1987). "gamma-Aminobutyric acid opens Cl-channels in cultured astrocytes." Brain Res **404**(1-2): 1-9.

Kimelberg, H. K. (1981). "Active accumulation and exchange transport of chloride in astroglial cells in culture." Biochim Biophys Acta **646**(1): 179-184.

Kimelberg, H. K. (2004). "The problem of astrocyte identity." Neurochem Int **45**(2-3): 191-202.

Kofuji, P. and E. A. Newman (2004). "Potassium buffering in the central nervous system." Neuroscience **129**(4): 1045-1056.

Koncz, C. and J. T. Daugirdas (1994). "Use of MQAE for measurement of intracellular [Cl-] in cultured aortic smooth muscle cells." Am J Physiol **267**(6 Pt 2): H2114-2123.

Kovalchuk, Y. and O. Garaschuk (2012). "Two-photon chloride imaging using MQAE in vitro and in vivo." Cold Spring Harb Protoc **2012**(7): 778-785.

Kovermann, P., et al. (2020). "Increased glutamate transporter-associated anion currents cause glial apoptosis in episodic ataxia 6." Brain Comms **2**(1): 1-17.

Kritis, A. A., et al. (2015). "Researching glutamate - induced cytotoxicity in different cell lines: a comparative/collective analysis/study." Front Cell Neurosci **9**: 91.

Kuhn, H. G., et al. (1996). "Neurogenesis in the dentate gyrus of the adult rat: age-related decrease of neuronal progenitor proliferation." J Neurosci **16**(6): 2027-2033.

Kuner, T. and G. J. Augustine (2000). "A genetically encoded ratiometric indicator for chloride: capturing chloride transients in cultured hippocampal neurons." Neuron **27**(3): 447-459.

Lanjakornsiripan, D., et al. (2018). "Layer-specific morphological and molecular differences in neocortical astrocytes and their dependence on neuronal layers." Nat Commun **9**(1): 1623.

Lee, A., et al. (2016). "A novel splice variant of the Excitatory Amino Acid Transporter 5: Cloning, immunolocalization and functional characterization of hEAAT5v in human retina." Neurochem Int.

Lee, J. Y. (2019). "Normal and Disordered Formation of the Cerebral Cortex : Normal Embryology, Related Molecules, Types of Migration, Migration Disorders." J Korean Neurosurg Soc **62**(3): 265-271.

Lee, Y., et al. (2006). "Astrocyte heterogeneity revealed by expression of a GFAP-LacZ transgene." Glia **53**(7): 677-687.

Lehre, K. P. and N. C. Danbolt (1998). "The number of glutamate transporter subtype molecules at glutamatergic synapses: chemical and stereological quantification in young adult rat brain." J Neurosci **18**(21): 8751-8757.

Leroy, F., et al. (2019). "Input-Timing-Dependent Plasticity in the Hippocampal CA2 Region and Its Potential Role in Social Memory." Neuron **102**(1): 260-262.

Leung, A. W. and J. Y. H. Li (2018). "The Molecular Pathway Regulating Bergmann Glia and Folia Generation in the Cerebellum." Cerebellum **17**(1): 42-48.

Levy, L. M., et al. (1998). "Stoichiometry of the glial glutamate transporter GLT-1 expressed inducibly in a Chinese hamster ovary cell line selected for low endogenous Na+-dependent glutamate uptake." J Neurosci **18**(23): 9620-9628.

Liour, S. S. and R. K. Yu (2003). "Differentiation of radial glia-like cells from embryonic stem cells." Glia **42**(2): 109-117.

Lorente De Nó, R. (1934). "Studies on the structure of the cerebral cortex. II. Continuation of the study of the ammonic system. ." Journal für Psychologie und Neurologie **46**: 113-177.

Machtens, J. P., et al. (2015). "Mechanisms of anion conduction by coupled glutamate transporters." Cell **160**(3): 542-553.

Maeno, E., et al. (2000). "Normotonic cell shrinkage because of disordered volume regulation is an early prerequisite to apoptosis." Proc Natl Acad Sci U S A **97**(17): 9487-9492.

Maeno, E., et al. (2012). "Apoptotic Volume Decrease (AVD) Is Independent of Mitochondrial Dysfunction and Initiator Caspase Activation." Cells **1**(4): 1156-1167.

Marandi, N., et al. (2002). "Two-photon chloride imaging in neurons of brain slices." Pflugers Arch **445**(3): 357-365.

Marcu, L., et al. (2014). Fluorescence lifetime spectroscopy and imaging : principles and applications in biomedical diagnostics. Boca Raton, CRC Press/Taylor & Francis Group.

Martins, W. A., et al. (2016). "Dysplastic Cerebellar Epilepsy: Complete Seizure Control Following Resection of a Ganglioglioma." Cerebellum **15**(4): 535-541.

Matthias, K., et al. (2003). "Segregated expression of AMPA-type glutamate receptors and glutamate transporters defines distinct astrocyte populations in the mouse hippocampus." J Neurosci **23**(5): 1750-1758.

McManus, M. L., et al. (1995). "Regulation of cell volume in health and disease." N Engl J Med **333**(19): 1260-1266.

Meier, S. D., et al. (2008). "Developmental profile and mechanisms of GABA-induced calcium signaling in hippocampal astrocytes." Glia **56**(10): 1127-1137.

Mongin, A. A. (2016). "Volume-regulated anion channel--a frenemy within the brain." Pflugers Arch **468**(3): 421-441.

Mori, T., et al. (2006). "Inducible gene deletion in astroglia and radial glia--a valuable tool for functional and lineage analysis." Glia **54**(1): 21-34.

Moss, J., et al. (2016). "Fine processes of Nestin-GFP-positive radial glia-like stem cells in the adult dentate gyrus ensheathe local synapses and vasculature." Proc Natl Acad Sci U S A **113**(18): E2536-2545.

Nakanishi, T., et al. (1988). "Survey of osmolytes in renal cell lines." Am J Physiol **255**(2 Pt 1): C181-191.

Ndubaku, U. and M. E. de Bellard (2008). "Glial cells: Old cells with new twists." Acta Histochem **110**(3): 182-195.

Nieuwenhuys, R. (2013). "The myeloarchitectonic studies on the human cerebral cortex of the Vogt-Vogt school, and their significance for the interpretation of functional neuroimaging data." Brain Struct Funct **218**(2): 303-352.

Nimmerjahn, A., et al. (2004). "Sulforhodamine 101 as a specific marker of astroglia in the neocortex in vivo." Nat Methods **1**(1): 31-37.

Nolte, C., et al. (2001). "GFAP promoter-controlled EGFP-expressing transgenic mice: a tool to visualize astrocytes and astrogliosis in living brain tissue." Glia **33**(1): 72-86.

O'Keefe, J. and L. Nadel (1978). The Hippocampus as a Cognetive Map.

Oheim, M., et al. (2001). "Two-photon microscopy in brain tissue: parameters influencing the imaging depth." J Neurosci Methods **111**(1): 29-37.

Owens, D. F., et al. (1996). "Excitatory GABA responses in embryonic and neonatal cortical slices demonstrated by gramicidin perforated-patch recordings and calcium imaging." J Neurosci **16**(20): 6414-6423.

Payne, J. A., et al. (2003). "Cation-chloride co-transporters in neuronal communication, development and trauma." Trends Neurosci **26**(4): 199-206.

Porcelli, A. M., et al. (2004). "Apoptosis induced by staurosporine in ECV304 cells requires cell shrinkage and upregulation of Cl- conductance." Cell Death Differ **11**(6): 655-662.

Pyle, A., et al. (2015). "Exome sequencing in undiagnosed inherited and sporadic ataxias." Brain **138**(Pt 2): 276-283.

Rakic, P. (1971). "Neuron-glia relationship during granule cell migration in developing cerebellar cortex. A Golgi and electronmicroscopic study in Macacus Rhesus." J Comp Neurol **141**(3): 283-312.

Regan, M. R., et al. (2007). "Variations in promoter activity reveal a differential expression and physiology of glutamate transporters by glia in the developing and mature CNS." J Neurosci **27**(25): 6607-6619.

Reyes, N., et al. (2009). "Transport mechanism of a bacterial homologue of glutamate transporters." Nature **462**(7275): 880-885.

Ringel, F. and N. Plesnila (2008). "Expression and functional role of potassium-chloride cotransporters (KCC) in astrocytes and C6 glioma cells." Neurosci Lett **442**(3): 219-223.

Rothstein, J. D., et al. (1994). "Localization of neuronal and glial glutamate transporters." Neuron **13**(3): 713-725.

Russell, J. M. (2000). "Sodium-potassium-chloride cotransport." Physiol Rev **80**(1): 211-276.

Sadava, D., et al. (2011). Purves Biologie, Spektrum Akademischer Verlag.

Sattler, R. and J. D. Rothstein (2006). "Regulation and dysregulation of glutamate transporters." Handb Exp Pharmacol(175): 277-303.

Schreiner, A. E., et al. (2014). "Laminar and subcellular heterogeneity of GLAST and GLT-1 immunoreactivity in the developing postnatal mouse hippocampus." J Comp Neurol **522**(1): 204-224.

Seifert, G., et al. (2006). "Astrocyte dysfunction in neurological disorders: a molecular perspective." Nat Rev Neurosci **7**(3): 194-206.

Shepherd, G. M. (2011). "The microcircuit concept applied to cortical evolution: from three-layer to six-layer cortex." Front Neuroanat **5**: 30.

Shigetomi, E., et al. (2011). "TRPA1 channels regulate astrocyte resting calcium and inhibitory synapse efficacy through GAT-3." Nat Neurosci **15**(1): 70-80.

Sperk, G., et al. (1997). "GABA(A) receptor subunits in the rat hippocampus I: immunocytochemical distribution of 13 subunits." Neuroscience **80**(4): 987-1000.

Spigelman, I., et al. (2002). "Behavior and physiology of mice lacking the GABAA-receptor delta subunit." Epilepsia **43 Suppl 5**: 3-8.

Stoffel, W., et al. (2004). "Functional analysis of glutamate transporters in excitatory synaptic transmission of GLAST1 and GLAST1/EAAC1 deficient mice." Brain Res Mol Brain Res **128**(2): 170-181.

Stokum, J. A., et al. (2016). "Molecular pathophysiology of cerebral edema." J Cereb Blood Flow Metab **36**(3): 513-538.

Strominger N.L., D. R. J., Laemle L.B. (2012). Cerebral Cortex. In: Noback's Human Nervous System, Humana Press, Totowa, NJ.

Sultan, F. (2014). "From cerebellar texture to movement optimization." Biol Cybern **108**(5): 677-688.

Tanaka, M., et al. (2008). "Connexin43 and bergmann glial gap junctions in cerebellar function." Front Neurosci **2**(2): 225-233.

Untiet, V., et al. (2016). "Elevated Cytosolic Cl- Concentrations in Dendritic Knobs of Mouse Vomeronasal Sensory Neurons." Chem Senses **41**(8): 669-676.

Untiet, V., et al. (2017). "Glutamate transporter-associated anion channels adjust intracellular chloride concentrations during glial maturation." Glia **65**(2): 388-400.

Verkman, A. S., et al. (1989). "Synthesis and characterization of improved chloride-sensitive fluorescent indicators for biological applications." Anal Biochem **178**(2): 355-361.

Verkman, A. S. (1990). "Development and biological applications of chloride-sensitive fluorescent indicators." Am J Physiol **259**(3 Pt 1): C375-388.

Vogt, O. (1903). "Zur anatomischen Gliederung des Cortex cerebri." Journal Psychologie und Neurologie **2**: 160-180.

von Bartheld, C. S., et al. (2016). "The search for true numbers of neurons and glial cells in the human brain: A review of 150 years of cell counting." J Comp Neurol **524**(18): 3865-3895.

Wainwright, A., et al. (2000). "Expression of GABA(A) receptor alpha5 subunit-like immunoreactivity in human hippocampus." Brain Res Mol Brain Res **80**(2): 228-232.

Walz, W., et al. (1984). "Astrocytes in primary cultures: membrane potential characteristics reveal exclusive potassium conductance and potassium accumulator properties." Brain Res **292**(2): 367-374.

Walz, W. and S. Mukerji (1988). "Lactate production and release in cultured astrocytes." Neurosci Lett **86**(3): 296-300.

Walz, W. (2000). "Role of astrocytes in the clearance of excess extracellular potassium." Neurochem Int **36**(4-5): 291-300.

Watase, K., et al. (1998). "Motor discoordination and increased susceptibility to cerebellar injury in GLAST mutant mice." Eur J Neurosci **10**(3): 976-988.

Willford, S. L., et al. (2015). "Evidence for a Revised Ion/Substrate Coupling Stoichiometry of GABA Transporters." J Membr Biol **248**(4): 795-810.

Wilson, C. S. and A. A. Mongin (2019). "The signaling role for chloride in the bidirectional communication between neurons and astrocytes." Neurosci Lett **689**: 33-44.

Winter, N., et al. (2012). "A point mutation associated with episodic ataxia 6 increases glutamate transporter anion currents." Brain **135**(Pt 11): 3416-3425.

Wisden, W., et al. (1992). "The distribution of 13 GABAA receptor subunit mRNAs in the rat brain. I. Telencephalon, diencephalon, mesencephalon." J Neurosci **12**(3): 1040-1062.

Yamada, K. and M. Watanabe (2002). "Cytodifferentiation of Bergmann glia and its relationship with Purkinje cells." Anat Sci Int **77**(2): 94-108.

Yamauchi, A., et al. (1992). "Cloning of a Na(+)- and Cl(-)-dependent betaine transporter that is regulated by hypertonicity." J Biol Chem **267**(1): 649-652.

Yan, Y., et al. (2001a). "Expression of Na(+)-K(+)-Cl(-) cotransporter in rat brain during development and its localization in mature astrocytes." Brain Res **911**(1): 43-55.

Yan, Y. P., et al. (2001b). "Na+-K+-Cl- cotransporter in rat focal cerebral ischemia." Journal of Cerebral Blood Flow and Metabolism **21**(6): 711-721.

Zerangue, N. and M. P. Kavanaugh (1996). "Flux coupling in a neuronal glutamate transporter." Nature **383**(6601): 634-637.

Zhang, Y. and B. R. Bhavnani (2006). "Glutamate-induced apoptosis in neuronal cells is mediated via caspase-dependent and independent mechanisms involving calpain and caspase-3 proteases as well as apoptosis inducing factor (AIF) and this process is inhibited by equine estrogens." BMC Neurosci **7**: 49.

Zipfel, W. R., et al. (2003). "Nonlinear magic: multiphoton microscopy in the biosciences." Nat Biotechnol **21**(11): 1369-1377.

7 Danksagung

Letztlich möchte ich nun an dieser Stelle einen Dank an jeden aussprechen, der mich in den letzten Jahren unterstützt hat und somit einen Beitrag zu der Fertigstellung dieser Dissertation beigetragen hat.

Ich möchte mich bei meinem Doktorvater Herrn Prof. Dr. Christoph Fahlke bedanken, dass er mir die Möglichkeit geboten hat dieses spannende Forschungsprojekt in seinem Institut anfertigen zu dürfen, begonnen in einer Masterarbeit und letztlich resultierend in einer Promotion. Des Weiteren hat er mich dazu ermuntert an meine Ergebnisse zu glauben – seien sie noch so unerwartet und neu – und lehrte mich den wichtigsten Aspekt: die Forschung ist „lediglich“ die Beschreibung der Natur.

Ebenfalls bedanke ich mich bei Frau Prof. Dr. Christine R. Rose für die vielen Ratschläge und Ideen hinsichtlich meiner Experimente, die virtuellen Meetings und die Übernahme der Aufgabe als Zweitgutachterin dieser Dissertation.

Zusätzlich möchte ich mich bei meinem Betreuer Dr. Peter Kovermann bedanken für seine unentwegte Betreuung, sein stets offenes Ohr und seine fachliche Hilfe. Ein weiterer Dank gilt Dr. Thomas Gensch, welcher mir ebenfalls immer hilfsbereit zur Seite stand und mit mir meine FLIM-Daten auf Herz und Nieren geprüft hat.

Ebenso möchte ich mich bei meiner Bürokollegin Dr. Andrea Jansen - Grabowski bedanken für ihre magischen Hilfen am und um das Zwei-Photon-Mikroskop herum, die anregenden Diskussionen und erheiternde Spaziergänge. Meiner Kollegin Dr. Yulia Kolobkova möchte ich ebenfalls Danken für jegliche Zusammenarbeit, die mit den Versuchstieren zu tun hatte und für unsere gegenseitig unterstützenden Ergebnisse.

Darüber hinaus möchte ich meinen lieben Kolleg:innen – Inge, Nadine, Maike, Christoph, Arne, sowie allen Mitarbeitern des IBI-1 – für jede Art von Tipps und Tricks, die das Leben im Labor erleichtern haben, die angenehme Atmosphäre und die große Hilfsbereitschaft danken.

Zuletzt möchte ich ein großes Dankeschön an meine Familie richten, die mich immer unterstützt und ermuntert hat weiter zu machen und mich somit da hingebracht hat wo ich nun heute stehe, am Anfang von etwas großem Neuen.

8 Eidesstattliche Versicherung

Ich versichere an Eides Statt, dass die vorliegende Dissertation von mir selbstständig und ohne unzulässige fremde Hilfe unter Beachtung der "Grundsätze zur Sicherung guter wissenschaftlicher Praxis an der Heinrich-Heine-Universität Düsseldorf" verfasst worden ist. Textstellen oder Abbildungen, die wörtlich oder abgewandelt aus anderen Arbeiten stammen, habe ich mit einer Quellenangabe versehen.
Diese Arbeit wurde weder vollständig noch in Teilen einem anderen Prüfungsamt zur Erlangung eines akademischen Grades vorgelegt.

Jülich, 27. Mai 2021

_____

Miriam Engels